

Dissertation

submitted to the

Combined Faculties of the Natural Sciences and Mathematics
of the Ruperto-Carola-University of Heidelberg, Germany

for the degree of

Doctor of Natural Science

Put forward by

Diplom-Physikerin Maren Mohler-Fischer

Born in: Lehrte, Germany

Oral Examination: October 21, 2013

Search for extrasolar planets
around young stars in the presence
of stellar activity

Referees: Prof. Dr. Thomas Henning

Prof. Dr. Andreas Quirrenbach

Die Suche nach Planeten um junge Sterne in Gegenwart stellarer Aktivität

Zusammenfassung

Planeten entstehen in Scheiben um neugeborene Sterne. Die Zeitskalen, auf welchen ihre Entstehung und das Einnehmen eines langzeitstabilen Orbits ablaufen, stehen noch immer zur Debatte. Eine Abschätzung liefern Infrarotflussmessungen, die zeigen, dass sich die Scheibe binnen etwa 10 Millionen Jahren auflöst, weshalb die Entstehung und Entwicklung von Planeten innerhalb dieser Zeitspanne geschehen muss. Um diese von den aktuellen Theorien vorhergesagten Zeitskalen zu überprüfen, ist es wichtig, Planeten um Sterne von 1 bis 100 Millionen Jahre zu finden. Ebenso können aber auch Nichtentdeckungen dabei helfen, zwischen Theorien zu unterscheiden. Jedoch ist die Anzahl der bereits gefundenen Planeten um solch junge Sterne zu klein, um schlüssige Aussagen zur Planetenentstehung zu treffen. Der Grund dafür ist, dass junge Sterne im allgemeinen sehr aktiv sind, was Planetenentdeckungen erheblich erschwert.

Innerhalb dieser Arbeit wurde eine systematische Suche unter Verwendung der Radialgeschwindigkeitsmethode (RV) nach Planeten um 21 junge Sterne mit einem Alter zwischen ~ 3 and ~ 400 Myr und Spektraltypen von F6 bis M0 durchgeführt. Um die stellare Aktivität zu analysieren, wurden die beobachteten Sternspektren in Hinblick auf eine Vielzahl von Aktivitätsindikatoren untersucht. Dafür habe ich sowohl einzelne Spektrallinien als auch die Kreuzkorrelationsfunktion zur Ermittlung der RV verwendet. Ein klares periodisches RV-Signal, welches nicht durch die zeitliche Abfolge der Beobachtungen hervorgerufen worden sein kann, wurde in den Zeitreihen von drei Sternen gefunden. Auf Grund der Analyse von Photometrie und Aktivitätsindikatoren konnte jedoch ein Planet nicht bestätigt werden; vielmehr scheint stellare Aktivität als Ursache wahrscheinlich. Verschiedene Sternflecken und ihre Auswirkungen auf die relative Radialgeschwindigkeit wurden daraufhin simuliert, um mögliche Sternfleckszenarien als Ursache für die RV-Variation auszumachen.

Die Abhandlung über den Transitplaneten HATS-2b, welcher einen Stern mit Sternfleckenaktivität vom Spektraltyp K umkreist, zeigt die Herausforderungen auf, die bei den Nachfolgebeobachtungen und bei den Analysen von Transitplaneten im Beisein von stellarer Aktivität entstehen.

Die damit verbundenen Herausforderungen, RV-Signale unterschiedlicher physikalischer Ursachen (wie ein Begleiter im System und stellare Aktivität) zu trennen, ist des Weiteren in der Analyse der RV-Variabilität - und der damit verbundenen möglichen Existenz eines Begleiters - des jungen eruptiven Sterns EX Lupi diskutiert.

Obwohl im Rahmen der RV-Suche um 21 junge Sterne kein Planet nachgewiesen werden konnte, lässt sich zusammenfassend sagen, dass die detaillierten Analysen in dieser Arbeit es ermöglichen, Anforderungen an zukünftige Studien von Planeten um junge Sterne zu stellen. Dies schließt sowohl die Samplegröße und die Targetauswahl, als auch die Beobachtung und Auswertung ein.

Search for extrasolar planets around young stars in presence of stellar activity

Abstract

Planets form in circumstellar disks around newly born stars. The timescales of planet formation and migration remain poorly constrained and are a matter of ongoing debate. The disk dispersal timescale, which sets a limit to the duration of planet formation, was derived from infrared surveys to be less than 10 Myr. In order to test the predicted planet formation time scales described in current theories, it is important to find planets in the age range of 1 to 100 Myrs. In the same manner, non-detections can help to understand the current theories. However, the number of discoveries is still very small due to the challenging task to analyze RV signals contaminated by the high stellar activity .

Within this thesis, I performed a systematic radial velocity (RV) search for planets around 21 young targets with ages between ~ 3 and ~ 400 Myr and spectral types between F6 and M0. In order to account for the strong stellar activity, I analyzed the stellar spectra in terms of a variety of activity indicators, analyzing both single spectral lines and the RV cross-correlation function. For three targets, a strong radial velocity signal could be identified, which was not induced by measurement sampling. Due to the analysis of available photometric data and activity indicators, it was possible to exhibit stellar activity patterns such as cool stellar spots as origin of the signal. The simulation with a spot program allowed to reconstruct possible spot scenarios that could have caused the detected RV variability.

The challenge of the confirmation of a transit planet with follow-up observations in presence of stellar activity is shown in the discussion of HATS-2b, a transiting extrasolar planet orbiting a K-type star showing starspot activity.

Furthermore, the discussion of a possible companion around the young eruptive star EX Lupi is part of this thesis. The detailed RV and activity analyses show the challenging task to disentangle RV signals caused by a possible companions and by stellar activity.

Although no planet could be identified in the RV search around 21 young stars, it can in summary be stated that the detailed analyses in this thesis allow to put constraints on further RV surveys looking for exoplanets around young stars. This includes not only the sample size and target selection but also the observations and data analysis methods.

*To my beloved husband
my bastion of calm*

*The most exciting phrase to hear in science, the one that heralds new discoveries,
is not 'Eureka!' but 'That's funny...'*

Isaac Asimov

Contents

1	Introduction	5
1.1	Star formation, evolution and death	5
1.2	Planet formation and migration	11
1.3	Motivation and thesis outline	13
2	Methods	15
2.1	Determination of stellar parameters from observational data	15
2.1.1	SME - Spectroscopy made easy	17
2.1.2	Projected rotational velocity $v \sin i$	18
2.1.3	Veiling	20
2.2	Synthetic spectra	22
2.3	Age determination methods	23
2.4	Calculation of radial velocity changes	29
2.4.1	FEROS	30
2.4.2	HARPS	31
2.4.3	Analysis of RV periodicity	32
2.5	Stellar activity indicators	33
2.5.1	Analysis of spectral lines and features	33
2.5.2	Analysis of the CCF	36
2.5.3	The effect of stellar activity on the measured RV	40
3	The target sample	41
3.1	The target selection	41
3.1.1	Individual target description	44
3.2	Characterization of the sample	47
3.2.1	Stellar parameters	47
3.2.2	Age	47
3.2.3	Disk	48
4	RV and activity signals of the sample	53
4.1	Observations and available data	53
4.2	Radial velocity analysis and results	53
4.2.1	Detection limits	63
4.3	Stellar activity indicators	68
5	Characterisation of RV signals in terms of starspots	79
5.1	The starspot program	79
5.2	Application to target sample	82
5.3	Reproducibility of RV curves with spot scenarios	84

6	Radial velocity variation of EX Lupi	85
6.1	Introduction	85
6.2	Observations and data reduction	86
6.3	Radial velocity analysis	86
6.4	Radial velocity results	87
6.4.1	Analysis of FEROS radial velocity results	88
6.4.2	Combined analysis of FEROS and HARPS radial velocity results	88
6.5	Analysis of activity indicators	89
6.6	Starspot scenarios	92
6.7	Summary and discussion	93
7	The search for exoplanets with the HATSouth survey	95
7.1	The HATSouth Survey	95
7.2	HATS-2b: A transiting extrasolar planet orbiting a K-type star showing starspot activity	97
8	Summary and Conclusions	117
8.1	The young stars exoplanet RV search	117
8.1.1	Stellar parameters	117
8.1.2	Age determination	117
8.1.3	Circumstellar disks	118
8.1.4	Target observations and RV analysis	119
8.1.5	RV results	120
8.1.6	Detection limits	120
8.1.7	Stellar activity analysis	121
8.1.8	Starspot scenarios	122
8.1.9	Discussion of results for individual targets	122
8.2	Radial velocity variation of EX Lupi	129
8.3	The search for exoplanets with the HATSouth survey	130
9	Recommendations for future RV exoplanet surveys of young stars	131
A	Determined stellar parameters	133
B	Age determination	135
B.1	Isochrones	136
B.2	Moving group memberships	141
B.3	Lithium I EW	142
B.4	Gyrochronological ages	144
C	Disks	149
D	RV periodograms	157
	Bibliography	169

List of Figures

1.1	Evolution of a protostar in the Hertzsprung-Russell-Diagram	8
1.2	The Hertzsprung-Russell-Diagram	9
1.3	Mass distribution of confirmed extrasolar planets	12
1.4	Age distribution of known exoplanet host stars	14
2.1	Limb darkening coefficients for $v \sin i$ template stars	20
2.2	Artificially broadened $v \sin i$ template spectra with different limb darkening	21
2.3	Lithium I EW for different spectral types for age determination	25
2.4	Angular velocity over age	26
2.5	Schematic Keplerian orbit of a planet around its host star	29
2.6	Spectral line origins in the solar chromosphere during quiescence	34
2.7	Ca II K line at 3933 \AA for the S_{FEROS} index	34
2.8	CCF bisector	38
2.9	Stellar activity indicators in a FEROS spectrum	39
2.10	Effect of a cool stellar spot on an artificially created spectral line and the effective RV	40
3.1	Target selection process	42
3.2	Distribution of spectral type, stellar age and $v \sin i$ for selected targets . . .	44
3.4	Four-band WISE images for CD-37 13029	50
3.3	SED fits for HBC 603 and V2129 Oph	51
4.1	Periodograms and sampling test of CD-37 1123	57
4.2	GLS periodogram of RV residua for CD-37 13029	58
4.3	RV fit of CD-37 13029	58
4.4	De-aliasing of the RV signal of TYC 8654-1115-1 - window function	60
4.5	De-aliasing of the RV signal of TYC 8654-1115-1 - GLS periodogram	61
4.6	RV fit of TYC 8654-1115-1	62
4.7	RV fit of HD 140637	62
4.8	Detection limits for 20 targets	65
4.9	Median detection limit of the sample	65
4.10	Histogram of detected exoplanets in the Marcy et al. (2005) survey.	67
4.11	Detection limits in the Naef et al. (2005) survey.	67
4.12	GLS periodogram of the S_{FEROS} analysis of HD 139084	70
4.13	GLS periodogram of the BVD analysis of HD 183414	71
4.14	GLS periodogram of the CCF variance analysis of HD 216803	71
4.15	GLS periodogram of the BVD and CCF skewness analysis for 1RXSJ0434	72
4.16	GLS periodogram of the H_{α} EW analysis of CD-40 14901	73
4.17	GLS periodogram of the BVS and BC analysis of CD-37 13029	73
4.18	GLS periodogram of the BVS and CCF skewness analysis of TYC 8654-1115-1	74

4.19	GLS periodograms of the CCF moments and the CaH 2 spectroscopic index of HD 140637	75
4.20	Correlation plots between target RV and BVS	77
5.1	Phase-folded SuperWASP photometry of CD-37 13029 and HD 140637	80
5.2	Different starspot scenarios and their induced RV signal	84
6.1	Comparison of FEROS spectra of EX Lupi in quiescence and outburst	86
6.2	RV fit of FEROS data	88
6.3	RV fit of FEROS data with highlighted observation times	89
6.4	RV fit of FEROS and HARPS data with highlighted observation times	89
6.5	GLS periodograms of activity indicators	91
6.6	GLS periodograms of spectroscopic indices	91
6.7	Correlation between BVS and RV and BVS and RV residua, repectively, for EX Lupi	92
7.1	The three sites of the HATSouth survey	96
7.2	Phase-folded HATS-2 detection lightcurve	98
7.3	Phased follow-up transit light curves of HATS-2	100
7.4	Phase-folded high-precision RV measurments for HATS-2	102
7.5	YY-isochrones and stellar parameters of HATS-2	105
7.6	Normalized Lomb-Scargle periodogram of the combined HATSouth light curve of HATS-2	106
7.7	Combined four-colour transit light curves of HATS-2 obtained with the GROND imaging system	109
7.8	Phased GROND light curves of HATS-2b compared to the best GEMC fits	112
7.9	Spot temperature contrast with respect to the photospheric temperature in several dwarf stars	113
7.10	Correlation diagrams for confirmed transit planets	116
8.1	Fraction of stars with near-infrared disk emission as function of age	119
B.1	YY-isochrones of four Group A targets	136
B.2	YY-isochrones of four Group B target	137
B.3	YY-isochrones of five Group B targets	138
B.4	YY-isochrones of four Group C targets	139
B.5	YY-isochrones of four Group C targets	140
B.6	For veiling corrected Li I EWs over spectral type	143
B.7	GLS periodograms for SuperWASP photometry for four targets	145
B.8	GLS periodograms for SuperWASP photometry for four targets	146
B.9	GLS periodograms for SuperWASP photometry for three targets	147
C.1	SEDs of Group A targets including the best fitting stellar atmosphere model based on Kurucz models	151
C.2	SEDs of Group B targets including the best fitting stellar atmosphere model based on Kurucz models	152
C.3	SEDs of Group B targets including the best fitting stellar atmosphere model based on Kurucz models	153
C.4	SEDs of Group C targets including the best fitting stellar atmosphere model based on Kurucz models	154

C.5	SEDs of Group C targets including the best fitting stellar atmosphere model based on Kurucz models	155
D.1	RV GLS periodograms for four targets of Group A	158
D.2	RV GLS periodograms for four targets of Group B	159
D.3	RV GLS periodograms for four targets of Group B	160
D.4	RV GLS periodograms for one target of Group B	161
D.5	RV GLS periodograms for four targets of Group C	162
D.6	RV GLS periodograms for four targets of Group C	163
D.7	Measurement sampling test results for HD 96064	164
D.8	Measurement sampling test results for HD 139084	164
D.9	Measurement sampling test results for CD-37 1123	165
D.10	Measurement sampling test results for HD 217897	165
D.11	Measurement sampling test results for 1RXSJ0434	166
D.12	Measurement sampling test results for CD-40 14901	166
D.13	De-aliasing of the RV signal of HD 140637 - window function	167
D.14	De-aliasing of the RV signal of HD 140637 - GLS periodogram	168

List of Tables

2.1	Template stars for $v \sin i$ calculation	19
2.2	(Dis-)advantages of used age determination methods	28
2.3	Spectroscopic indices	37
2.4	Used stellar activity indicators	39
3.1	Stellar parameters of selected targets from literature	43
3.2	Determined ages for selected targets	49
4.1	Target observations	54
4.2	RV periods detected with GLS	55
4.3	RV fit parameters for CD-37 13029, TYC 8654-1115-1 and HD 140637 . . .	62
4.4	Detection limits for the target stars	64
4.5	Fraction f of stars hosting giant planets from literature	66
4.6	Periodicities of RV measurements and activity indicators on short timescales	69
4.7	Linear Pearson Correlation Coefficients R_{Pearson} for BVS vs. RV for all target stars	76
5.1	Parameters for the spot program	79
5.2	Input, derived and observed parameters for CD-37 13029, TYC 8654-1115-1 and HD 140637 of the spot program	83
6.1	Best fitting parameters for the FEROS RV analysis and the FEROS & HARPS RV analysis	90
7.1	Summary of photometric observations of HATS-2	101
7.2	Summary of spectroscopic observations of HATS-2	101
7.3	Relative RV and bisector span (BVS) measurements of HATS-2	103
7.4	Stellar parameters for HATS-2	104
7.5	Orbital and planetary parameters for the HATS-2 system for different fitting scenarios	108
7.6	Photometric parameters derived from the GEMC fitting of the GROND transit light curves	111
A.1	Stellar parameters for target stars determined with SME	134
B.1	Moving group memberships and according ages	141
B.2	Li I EW and veiling results	142
B.3	Rotational periods and gyrochronological age for 11 targets	144
C.1	Used magnitudes for SED fitting	150

List of Symbols

Symbol	Unit	Description
M_{core}	M_{\odot}	Mass of star formation core
T_{core}	K	Temperature of star formation core
ρ_{core}	kg m^{-3}	Density of star formation core
$v \sin i_{\star}$	km s^{-1}	Projected stellar rotational velocity
M_{\star}	M_{\odot}	Stellar mass
R_{\star}	R_{\odot}	Stellar radius
i	$^{\circ}$	Stellar inclination
$P_{\star, \text{rot}}$	d	Stellar rotational period
L_{\star}	W	Stellar bolometric luminosity
F_{\star}	Wm^{-2}	Stellar flux
$T_{\text{eff}\star}$	K	Stellar effective temperature
σ	$\text{Wm}^{-2}\text{K}^{-4}$	Stefan-Boltzmann constant
$\log g_{\star}$		Stellar surface gravity
G	$\text{m}^3\text{kg}^{-1}\text{s}^{-2}$	Gravitational constant
$[M/H]$		Stellar metallicity
N_{met}		Number of metal atoms
N_{H}		Number of hydrogen atoms
v_{mic}	km s^{-1}	Stellar microturbulence
v_{mac}	km s^{-1}	Stellar macroturbulence
$\mu = \cos \gamma$		Cosine of angle between line of sight and stellar surface normal
I_{μ}	Wm^{-2}	Stellar intensity at μ
I_0	Wm^{-2}	Stellar intensity without limb-darkening
LDC		Linear limb-darkening coefficient
V		Amount of veiling
EW_0	\AA	Line equivalent width of synthetic template
EW	\AA	Line equivalent width of observed spectrum
$R_{\text{TiO5},0}$		TiO5 index of synthetic template
R_{TiO5}		TiO5 index of observed spectrum
P_{abs}		Absorption profile of synthetic template
P'_{abs}		Absorption profile of artificially veiled template
EW_{Li}	\AA	Li EW of observed spectrum
$EW_{\text{Li},0}$	\AA	Veiling corrected Li EW of observed spectrum
$\log(gf)$		Spectral line oscillator strength
t	Myr	Stellar age
t_{iso}	Myr	Stellar age determined with isochrones

Symbol	Unit	Description
t_{MG}	Myr	Stellar age determined with moving group memberships
t_{LiEW}	Myr	Stellar age determined with Li EWs
t_{SFEROS}	Myr	Stellar age determined with the activity index S_{FEROS}
t_{gyro}	Myr	Gyrochronological stellar age
t_{W}	Myr	Stellar age from Weise (2010)
R_{HK}		Stellar chromospheric emission ratio
R'_{HK}		Stellar chromospheric emission ratio (corrected for photosphere contribution)
S_{FEROS}		FEROS activity index
$(B - V)$	mag	Stellar color from B - and V -band
K	km s^{-1}	RV semi-amplitude
a	AU	Semi-major axis
e		Orbital eccentricity
M_P	$M_{\text{J}} \equiv M_{\text{Jup}}$	Companion mass
f_m	M_{\odot}	Mass function
T_0	d	Time at periastron passage
Ω	$^{\circ}$	Ascending node
ω	$^{\circ}$	Periastron length
μ_2	$\overset{\circ}{\text{A}}^2$	Spectral line variance
μ_3	$\overset{\circ}{\text{A}}^3$	Spectral line skewness
μ_4	$\overset{\circ}{\text{A}}^4$	Spectral line kurtosis
λ_c	$\overset{\circ}{\text{A}}$	Observed central wavelength
R_{band}		Spectroscopic index
ΔI	mag	Photometric peak-to-peak amplitude
α	hrs:min:sec	Right ascension
δ	$^{\circ}$:min:sec	Declination
μ_{α}	mas yr^{-1}	proper motion in right ascension
μ_{δ}	mas yr^{-1}	proper motion in declination
P	d	Orbital period of the companion
$R = \lambda/\Delta\lambda$		Spectral resolution (of a spectrograph)
R_P	$R_{\text{J}} \equiv R_{\text{Jup}}$	Companion radius
$\log g_P$	cgs	Companion surface gravity
T_{eq}	K	Equilibrium temperature of the companion
k_B	JK^{-1}	Boltzmann constant

Abbreviations

2MASS	Two Micron All Sky Survey
AAT	Anglo-Australian Telescope
AAVSO	American Association of Variable Star Observers
ANU	Australian National University
APASS	AAVSO Photometric All-Sky Survey
BIS	Bisector inverse slope
BC	Bisector curvature
BVD	Bisector velocity displacement
BVS	Bisector velocity span
CCF	Cross-correlation function
CNO	Carbon-nitrogen-oxygen
CoRoT	Convection Rotation and planetary Transits (Satellite)
DRS	Data reduction system
ESA	European Space Agency
ESO	European Southern Observatory
ESPRI	Exoplanet Search with PRIMA
EW	Equivalent width
FAP	False-alarm probability
FEROS	Fiber-fed Extended Range Optical Spectrograph
FTS	Faulkes Telescope South
FWHM	Full width at half maximum
GEMC	Genetic Evolution Markov Chain
GLS	Generalised Lomb-Scargle (periodogram)
GROND	Gamma-Ray Burst Optical/Near-Infrared Detector
HARPS	High Accuracy Radial velocity Planet Searcher
HATnet	Hungarian-made Automated Telescope Network
HATSouth	Hungarian-made Automated Telescope South
HESS	High Energy Spectroscopic System
HRD	Hertzsprung-Russell diagram
IDL	Interactive Data Language
IR	Infrared
IRAS	Infrared Astronomical Satellite
KELT	Kilodegree Extremely Little Telescope
LCO	Las Campanas Observatory
LCOGT	Las Cumbres Observatory Global Telescope
LDC	Limb-darkening coefficient
LDR	Line depth ratio
LSO	La Silla Observatory
LTE	Local thermal equilibrium

MPG	Max Planck Gesellschaft
MS	Main sequence
NIR	Near infrared
PMS	Pre-main-sequence star
PRIMA	(Instrument for) Phase Referenced Imaging and Micro-arcsecond Astrometry
PRISM	Planetary Retrospective Integrated Star-spot Model
PUC	Pontificia Universidad Catolica de Chile
QES	Qatar Exoplanet Survey
RV	Radial velocity
SED	Spectral energy distribution
SME	Spectroscopy Made Easy
SNR	Signal-to-noise ratio (also S/N)
SOAP	Spot Oscillation And Planet (tool)
SpT	Spectral type
SSO	Siding Spring Observatory
SuperWASP	Super Wide Angle Search for Planets
TFA	Trend Filtering Algorithm
TTV	Transit timing variation
TrES	Trans-atlantic Exoplanet Survey
UV	Ultraviolet
VALD	Vienna Atomic Line Database
WD	White dwarf
WiFeS	Wide Field Spectrograph
WISE	Wide-field Infrared Survey Explorer

Chapter 1

Introduction

The new era of astronomy produces superlatives of telescopes with supersized mirrors, stable and precise instruments and effective algorithms to extract the smallest bit of information from the obtained data. Major questions that arose during centuries and are still not answered are the main driver. These are for example: “Where does mankind come from?”, “Are we unique?”, “Is a second Earth somewhere out there?” and “Why is the Solar System as it is?”. These questions are still not answered and maybe won’t be for the next centuries as well.

Although most physical processes in the universe take so long that evolution is not directly observable, many observations of different objects in different evolutionary phases deliver millions of snapshots and a global picture can be deduced. This fact has led to a commonly accepted picture of how stars and their planetary systems form, develop and finally die and scratches at least on the surface of the question, why the Solar System is, as we find it today.

1.1 Star formation, evolution and death

The universe as we find it today, was created by the Big Bang about 13.8 Gyrs ago (Planck 2013 results. I. Overview of products and scientific results, 2013). During the Big Bang, only hydrogen, helium and traces of lithium and deuterium were formed. All other different elements known today, including the main component of human bodies, carbon, was formed later. Most elements lighter than iron are formed in main-sequence and old stars, while elements heavier than iron have their origin in dying stars. As commonly accepted today, stars form in interstellar gas environments in galaxies. Approximately half of this gas consists of atoms (hydrogen, helium, lithium and heavier elements as remnants of dead stars), which is almost homogenously distributed with an average density of about one atom per cm^{-3} . The rest of the interstellar gas consists of molecules (mainly H_2) and is approximately 200 times denser than the atomic part. Due to the interaction of gravity and star formation processes, stable density waves are created in the galactic disk. When stars, which orbit the galactic center, cross these density waves, the crossed regions are locally condensed and visible as spiral arms. These compaction forces atomic hydrogen to form molecules and along the spiral arms large molecular clouds form, which are already gravitationally bound and are the main birth places of stars. In these clouds, gravitation is balanced by thermal processes (Brownian motion) and in addition often by turbulence and magnetic pressure and the cloud is stable. In case shock waves of close super novae or jets of newly formed stars in the near vicinity hit the balanced cloud, these perturbations destabilize the balance and the cloud starts to contract. A local core forms in the cloud,

in which density and temperature rapidly increase. The minimum mass M_{core} of such a core can be estimated using the *Jeans-criterion* and depends on the temperature T_{core} and density ρ_{core} as follows

$$M_{\text{core}} > \left(\frac{T_{\text{core}}}{50 \text{ K}} \right)^{3/2} \cdot \left(\frac{\rho_{\text{core}}}{10^{-20} \text{ kg m}^{-3}} \right)^{-1/2} \cdot 10^3 M_{\odot} \quad (1.1)$$

The equation is already normalized for the typical temperature and density values in star formation clouds.

Dust, which is mixed with the gas at an average mass ratio of about 1:100 (Milky Way), shields the core from the interstellar radiation field (ISRF) and re-emits the energy at infrared (IR) wavelengths. This cooling effect leads to a decrease of the inner thermal gas pressure and the core gravitationally collapses. The time scale of this protostellar collapse is about 10^5 years for a cloud core of 10^6 molecules/cm³. During collapse, the pressure rises and heats the core. The temperature leads to an increased motion of the hydrogen molecules. When energy is transported to dust particles via collisions with hydrogen molecules, these particles emit the energy at infrared wavelengths and the temperature is almost constant for a long time period at about 7-10 K. As soon as the density in the core reaches about 10^{10} molecules/cm³, the core becomes opaque for infrared wavelengths and energy emitted by dust particles can not leave the core area anymore - the core heats up. The increasing temperature leads to an enhanced gas pressure, which starts to slow down the gravitational collapse till it stops and a short-term hydrostatic equilibrium establishes inside the core. In case magnetic fields are involved, the mechanism of the gravitational collapse gets more complicated. Since many particles are already ionized by cosmic rays, these ions are limited to the movement along the magnetic field lines and influence the motion of the surrounding non-ionized particles. This leads to the fact that the gravitational collapse is unopposed in direction along the magnetic field lines, but is hampered perpendicular to it.

During the collapse, the core of several AU diameter accretes surrounding material. Due to this, its mass increases and the core heats up. As soon as the temperature reaches ~ 2000 K at the inside and the density 10^{16} molecules/cm³, molecular hydrogen starts to dissociate, what costs energy taken from the surrounding material. Therefore, the temperature and pressure can not balance the rising gravitation anymore and the core collapses a second time. As soon as the density inside the core reaches 10^2 g/cm³, the collapse slows down and the temperature starts to rise faster. At one million K core temperature, all atoms are completely ionized, the matter is in plasma state and surrounded by free electrons and protons. At this point, the fusion of deuterium and free protons to helium starts. This reaction is not efficient and does not free enough energy to stop the gravitational collapse. But it leads to convection in the outer shell of the protostar and to an inflation to about 3-6 solar radii. Since the protostar is still embedded in a thick gas cloud, the observation of this scenario is still only possible with infrared instruments.

One problem during both gravitational collapses is the angular momentum conservation. Each cloud is initially rotating and hence possesses an initial angular momentum. Due to the conservation of momentum and the contraction, the protostar spins up and the centrifugal force rises faster than gravity. This puts the stability of the protostar at risk and threatens to disrupt it. Hence, the angular momentum has to be redistributed in the whole system to prevent the disruption, which works via several of the following mechanisms:

Magnetic braking: surrounding material is captured by magnetic field lines as well as particles inside the protostellar core. This will cause the surrounding particles

to rotate along with the core as being part of a solid body. If ionized particles in this matter are blown away due to stellar wind, they take the angular momentum with them and finally escape, why the angular momentum of the protostellar system decreases.

Circumstellar disk: the material in the circumstellar environment is pressed to a disk due to the conservation of angular momentum. Due to friction and turbulence, mass is transported inwards from the outer regions, while angular momentum is carried outwards.

Bipolar jets: charged particles are blown away by centrifugal forces along magnetic field lines and take neutral gas particles and hence angular momentum with them.

Fragmentation: the core fragments into smaller cores, which individually evolve afterwards. In this scenario, the total angular momentum is split into orbital angular momentum and spin moments of the fragments. Although recent results show that about two-thirds of all main sequence stellar systems in the Galactic disk are singles (Lada, 2006), most stars can still initially be formed from multiple systems, which disintegrate due to dynamical interactions in early stages (e.g. Kroupa, 1995).

Planetary system: a part of the stellar angular momentum is converted to the rotation of planets formed from the circumstellar material and their orbital motion. In fact, most angular momentum of the Solar System is not located in the Sun, but in the orbit of Jupiter.

As soon as all available deuterium is completely burnt to helium, the protostar loses energy by radiation and the gravitational contraction increases again. This causes another increase of density and temperature inside the protostar. The time scale of the gravitational contraction depends on the stellar mass and radius as well as on the luminosity. In case of the Sun, this part of the evolution lasted about 1 Myr. The cloud shell dissolves in this time slowly and the protostar is visible in the end with optical telescopes as well. Since the luminosity of the protostar is not mainly caused by accretion of surrounding material anymore but by the contraction of the main celestial body and no stable hydrostatic equilibrium could be established until now, the body is now called a “pre-main-sequence star” (PMS). Its position in the *Hertzsprung-Russell diagram* (HRD) is now to the left side of the so called *Hayashi-line*, which separates stable stellar states from unstable ones. In this state, next evolutionary steps depend on the mass of the PMS: Low-mass stars, with masses typically less than $2 M_{\odot}$, are called T-Tauri stars and are observable with optical telescopes since their shell has dissolved. These stars are very active and reveal dark stellar spots due to strong magnetic fields. Many observed T-Tauri stars are very variable and undergo outbursts. Intermediate mass stars ($2 M_{\odot} < M < 8 M_{\odot}$) are called Herbig Ae/Be stars. As the name suggests, these stars have earlier spectral types than T-Tauri stars. Stars with masses $> 8 M_{\odot}$ reach the MS already before they become visible. When the star appears on the left side of the Hayashi-line, the energy transport from the protostellar core to the outside is dominated by convection. In this process, hot stellar plasma is transported to the outside, because it is less dense as the surrounding material. It cools then down in outer regions, its density increases again and the material sinks towards the protostellar core again. While the star contracts more and more, its luminosity decreases with decreasing stellar size and almost stable inner temperatures. In that process, the energy transportation changes from dominated by convection to radiative and the star approaches the main-sequence. As soon as the energy transportation is dominated by

radiation, the temperature of the protostellar core increases at almost constant luminosity in the state of almost hydrostatical equilibrium - it follows the Henyey track (Fig. 1.1).

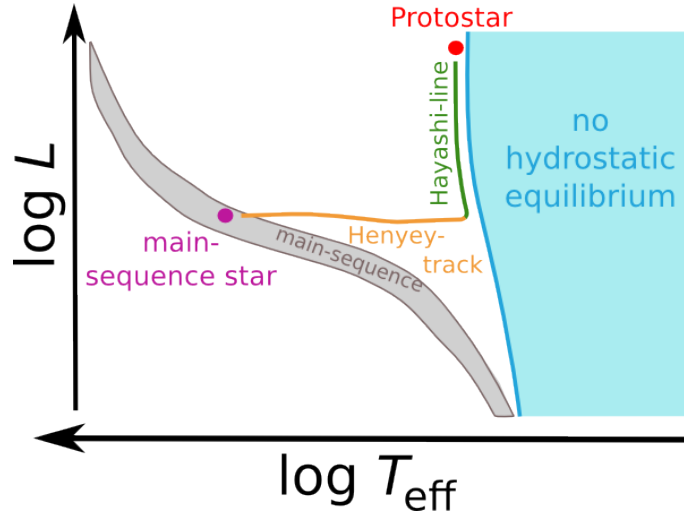
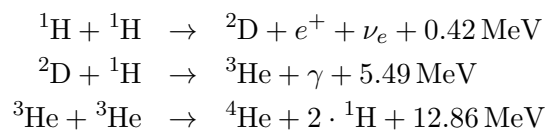


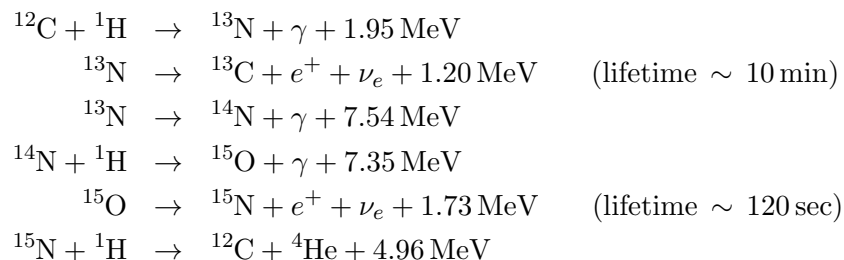
Figure 1.1: Evolution of a protostar in the Hertzsprung-Russell-Diagram

As soon as the temperature of the contracting protostar reaches several million Kelvin and the density in its central core adds up to several g/cm^3 , the protostar reaches the main-sequence and starts with the fusion from hydrogen to helium. Two main reactions dominate this scenario: the proton-proton chain reaction and the CNO cycle (carbon-nitrogen-oxygen).

Proton-proton chain reaction: this reaction starts at temperatures of about 3 million Kelvin and dominates at the beginning of the hydrogen fusion and for stars with masses of less than $1 M_{\odot}$. This reaction works slower as the CNO cycle. The reactions are as follows:



CNO cycle: this reaction is a catalytic cycle and is dominant for stars with masses larger than the Sun. It requires the existence of heavy elements and starts at temperatures of about 14 million Kelvin. The reactions are as follows:



Both the proton-proton chain reaction and the CNO cycle are so effective, that they more than compensate the energy loss caused by radiation. A hydrostatic equilibrium between gravitation and gas pressure is established and the contraction stops. The star is now

a stable main-sequence star and will be for a long time. How long a star stays on the main-sequence depends on the amount of available hydrogen that can be fused to helium, on the rate of energy conversion and on the luminosity of the star. Heavier stars convert their available hydrogen faster to helium as lower mass stars and therefore spend less time on the main-sequence.

The effective particle density inside the inner core decreases due to the nuclear fusion and the core contracts. This leads to an increasing temperature and furthermore to an increase of the luminosity - the star follows the main-sequence upwards (Fig. 1.2).

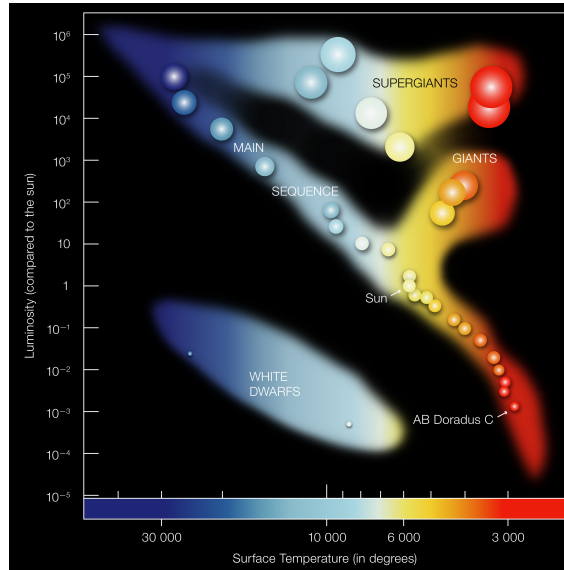
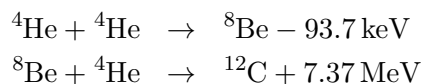
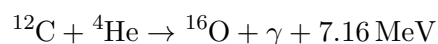


Figure 1.2: The Hertzsprung-Russell-Diagram, credit: ESO

Within time, the inner core consists of less and less hydrogen, while in outer shells, inactive hydrogen is still available. When the increase in temperature is not enough to start the fusion of helium to heavier elements, the produced energy is not enough to balance the gravitation, the star starts to contract again. It heats up until the gas pressure is able to balance the gravity again and the contraction stops. The significantly increased temperatures are now enough to start the fusion of hydrogen to helium in the outer shells. Although the temperature of the inner core still increases, the nuclear fusion in the outer shells leads to their inflation and therefore to a decrease in temperature in this regions. The luminosity increases rapidly while the surface gravity decreases and the star evolves to a red giant. Since a lot of material is puffed up, mass is started to get lost due to stellar winds. With time, the chemical composition of the inner core starts to be dominated by helium. At some point, the increasing temperature is sufficient to start the nuclear fusion of helium to carbon in the inner core. This is the so-called *Triple-alpha process*:



In further reactions, the produced carbon can be converted to oxygen:



The nuclear fusion of helium delivers new energy and starts soon after in the outer shells, which consist now mainly of helium as well. The reactions in the outer shells puffs the

star further up and already 1 Gyr after stopping the hydrogen fusion a solar like star has been swelled up by a factor of about 150. Its brightness increased in the meantime by a factor of about 2000 and it lost almost 30 % of its mass.

As soon as all helium is exhausted, the core - mainly composed of carbon - collapses and the inner density and temperature increases. In case the stellar mass exceeds $\sim 4 M_{\odot}$, temperatures of more than 500 million K can be reached and the carbon fusion to heavier elements can be started. This process works until iron is produced, since even heavier elements can only be produced by free neutron trapping. This usually occurs only in super giants and in super novae.

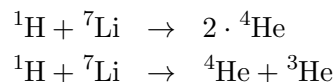
The way a stellar “life” finally ends depends again on its mass. Three different scenarios can be distinguished:

$0.075 M_{\odot} < M < 1.4 M_{\odot}$: If the stellar mass is smaller than the so-called *Chandrasekhar-mass*, the contraction of the star causes densities of up to 10^{10}kg/cm^3 and to a degeneration of the electron gas. The electron degeneration and the gravity balance out and the dying star reaches a stable state: a *White Dwarf* is born. The energy produced by the gravitational contraction is radiated and the White Dwarf slowly cools down and becomes fainter. They move in the HRD from mid-left to bottom-right to smaller temperatures and lower luminosities.

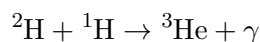
$1.4 M_{\odot} \leq M < 3.2 M_{\odot}$: In case of stars with masses higher than the Chandrasekhar-mass, the degeneration of the electron gas is not able to stop the contraction. Under high pressure, the electrons are pressed into the atomic nuclei and only neutrons remain outside as a neutron gas. Their degeneration finally stops the contraction and a *Neutron Star* has formed. The star is stripped from its outer shell by a large supernova explosion caused by the released energy of the gravitational collapse. The formation of heavier elements than iron is now possible in the leftover shells, since enough free neutrons are available. The persisting neutron star is very small (only several kilometers in diameter) and dense (typical 10^9kg/cm^3).

$M \geq 3.2 M_{\odot}$: If the stellar mass exceeds $3.2 M_{\odot}$, no degeneration of particles can stop the contraction and the whole core collapses to a *Black Hole*.

In case the mass of the protostar is smaller than about $0.075 M_{\odot}$, the core temperature produced by the contraction is not high enough to start the fusion of hydrogen to helium (a temperature of about $3 \cdot 10^6 \text{K}$ is necessary to start the proton-proton chain reaction, see above). These stars are called *Brown Dwarfs* and they never reach the MS. The fact, that the mass is too small to start hydrogen burning, does not imply that no nuclear reactions occur: For masses $0.065 M_{\odot} < M \leq 0.075 M_{\odot}$, the fusion of hydrogen to helium starts, but extinguishes quickly. For brown dwarfs with masses larger than about $0.06 M_{\odot}$, the fusion from hydrogen and lithium traces from the Big Bang is possible as follows:



Furthermore, the fusion of hydrogen and deuterium is possible as well as follows:



Of course do the lithium and deuterium reactions take place in heavier stars as well. Due to the fact that the amount of primordial lithium and deuterium are very limited, the

reactions are limited to time scales of several 100,000 yrs. Therefore, especially lithium can be used as a tracer for stellar age. The more lithium can be measured in the stellar spectrum, the younger the star is. Since the reaction rate heavily depends on the stellar temperature, this age determination method depends on the temperature of the star and its corresponding spectral type.

In case a collapsing cloud core exceeds about $100 M_{\odot}$, the contraction would produce enormous temperatures in the inner core and the radiation pressure would disrupt it. These constraints allow to define the mass regime of stars on the main-sequence as between about 0.075 and $100 M_{\odot}$.

1.2 Planet formation and migration

Circumstellar disks form in the process of star formation, which consist of gas and dust particles. Due to the conservation of angular momentum, the matter surrounding the star is pressed into a plane and therefore forms a disk, why most planets found so far orbit the star in that very plane (the exceptions are systems, in which a strong planet-star and/or planet-planet interaction forced one or more planets in orbits with higher inclination). These flat circumstellar disks, the so-called *protoplanetary disks*, are the birthplaces of planets and usually possess masses between 1 and 10% of the stellar mass. However, observations of our own Solar System revealed, that masses of the objects outside the Sun (as planets, plutoids, asteroids, comets etc.) only add up to about 0.1% of the whole system mass. This implies that about 90% of the protoplanetary disk was removed from the early Solar System at some point during the formation of the Sun, most likely by photoevaporation of the young blue Sun and to a smaller amount by accretion onto our host star.

Two theories of planet formation mechanisms currently exist, which are physically not yet fully understood. Furthermore, they have not been proven as valid, yet.

The core accretion model: This theory was initially postulated by the russian physicist V.S. Safronov. In this scenario, the disk mass is comparatively small and local self-gravitation can be neglected. Dust particles start to settle in the inner plane of the turbulent protoplanetary disk, collide during their migration and stick together. By this mechanism, constantly growing dust grains are located in the disk interior. A problem usually occurs during the simulation of cm-sized particles: if large particles meet small dust grains, the mechanism of hit and stick works and the particle grows. In case two large grains are hitting each other, fragmentation occurs too often to form enough larger than cm-sized particles to go on with the formation process. Recently published approaches use a distribution of orbit velocities for the large particles, which allows some particles to survive the encounter and to continue growing (Windmark et al., 2012). The surviving large particles are growing very fast by sweeping up smaller particles in the near environment. Doing so, objects up to about $0.1 M_{\text{E}}$ (the mass of Mars) form and dominate their environment by clearing out their orbit. At this point, gravitational interactions between these bodies lead to collisions, fragmentations, even ejections from the whole systems and Earth- and Venus-sized planets form. In case objects reach masses of about $10 M_{\text{E}}$, they start to accrete leftover gas particles and evolve to a Jovian planet.

The gravitational-instability model: In case of more massive disks, the assumption that local self-gravity is negligible is not valid anymore - the disk becomes gravita-

tionally unstable. Spiral arms of enhanced density evolve in the disk and work as traps for gas particles. Does the self-gravity of the trapped particle core exceeds the local pressure, the core collapses to a gas giant. This method allows the formation of gas giants without a solid core.

The fact that not many cm-sized particles survive the core accretion model favours the gravitational-instability scenario. Since the latter is not able to explain the formation of terrestrial planets like the Earth, the core accretion model is needed to at least form planets from Mercury to Mars. Since the planet formation scenarios are still heavily under discussion, the elaboration of different mechanisms in the future is possible.

By comparing confirmed extrasolar planets with the structure of the Solar System, one difference becomes quickly clear: The Solar System is lacking larger planets on inner orbits. This effect is especially visible, when taking Kepler exoplanet candidates into account (see Fig. 1.3).

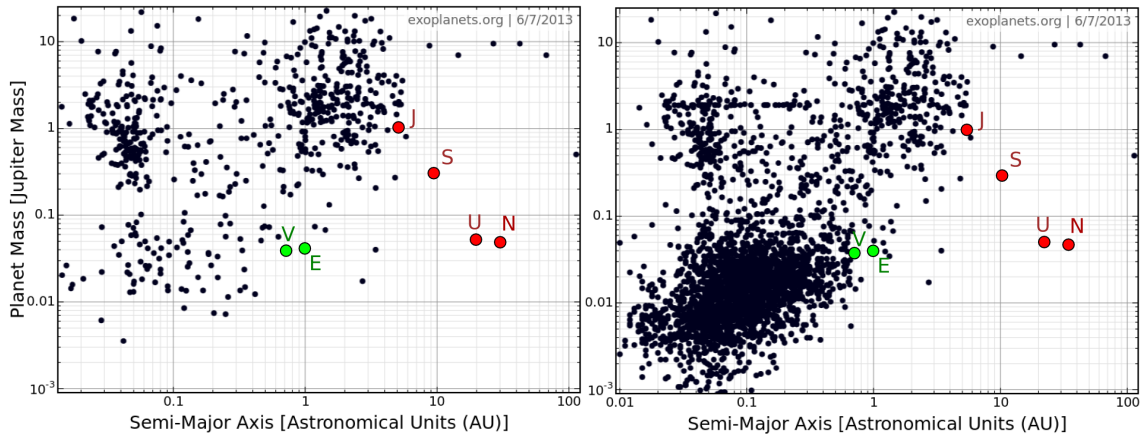


Figure 1.3: Left: Mass distribution of confirmed extrasolar planets over distance to the host star, right: same distribution for confirmed extrasolar planets and candidates detected with the *Kepler* satellite. In both panels, the Solar System planets Venus (V), Earth (E), Jupiter (J), Saturn (S), Uranus (U) and Neptune (N) are marked. The mass scale excludes the planets Mercury and Mars. The green color coding indicates terrestrial planets, whereas red color marks gas giants.

Most planets detected on inner orbits of extrasolar planetary systems are *Hot Jupiters*. They have the same characteristics as Jupiter in our Solar System, but have typically a higher mass and radius and a higher surface temperature due to the short distance to the host star. The detection of Hot Jupiters in other systems is favoured by the biases of the two main current detection methods:

The transit method: With this method, the existence of a second body in a system is analyzed, by looking for a periodic dimming of the stellar light, when the second body crosses the line-of-sight to the observer. The advantage is that the size of the planet can be determined, while on the other side the risk of observing a false-positive (e.g. a grazing eclipsing binary or a background binary) is always present. Furthermore, the event is only visible, if the observer looks edge-on onto the planetary orbit. This constraint of orbital inclination becomes more serious with increasing planet-star distance, why this method is biased towards planets on inner orbit additionally with

large radii. Since many stars at once can be observed simultaneously, the method is especially suited for large exoplanet search surveys.

The radial velocity method: This method uses the Doppler-shift of spectral lines due to the stellar motion around the star-planet barycenter. By measuring the periodic drift of spectral lines, it is possible to calculate the stellar radial velocity, i.e. the velocity directed along the line-of-sight to the observer. This signal is large for light stars with heavy planets. Since the inclination can not be determined with this method alone, only the determination of a minimum planet mass is possible. In case transit observations are complemented with RV measurements, possible false-positives can be ruled out. Furthermore, the combination of determined size, minimum mass and a good guess for the orbit inclination (if a transit is visible, the inclination has to be close to 90 deg), allows the derivation of the planet density.

Other methods as the transit-timing variation (TTV), pulsar timing, gravitational microlensing, direct imaging and astrometry are not mentioned here, since they don't produce or confirm extrasolar planet candidates on a large scale.

Current results of simulations show, that Hot Jupiters cannot have formed on their current orbits due to the lack of enough material on inner orbits. They are supposed to rather form on outer orbits beyond the stellar snow line (distance to the star, where temperatures are low enough to let hydrogen compounds as water, ammonia, and methane condense into solid ice grains) and then migrated inwards. Doing so, sweeping up smaller (terrestrial) planets is most likely, why the probability is high, that the Solar System was lacking a Hot Jupiter from the beginning.

1.3 Motivation and thesis outline

As mentioned above, the mechanisms of planet formation and evolution are not fully understood yet. Many open questions remain and the possibility is high that future research manages to refute current theories or produce new ones. One heavily discussed topic is the time scale of planet formation, which is of course closely related to different formation scenarios. While the gravitational-instability scenario takes place within about one orbit of the material around the star (H. Klahr, priv. comm.), the core accretion process is much slower. As upper limit of the planet formation time scale, the disk dispersal time is most often assumed. The disk disperses most likely around 10 Myr (Armitage, 1999), which leads to a lack of material for the planet formation and the process stops.

As shown in Fig. 1.4, do current exoplanet surveys target mainly main-sequence stars with ages of 100 Myr up to 10 Gyr. Since those targets usually do not exhibit as strong stellar activity signal as much younger stars do anymore, the data analysis is in general much easier. Nevertheless, exoplanet detections around those targets do not successfully target the age range of planet formation and therefore do not help to support or reject them.

In the framework of this thesis, I observed intensively a set of 21 young stars and looked for evidence for planets in the system with the radial velocity method. Fig. 1.4 shows that the targets analyzed in this thesis successfully target the era of planet formation in contrary to other surveys. Furthermore, I characterized the star itself, concerning stellar parameters, stellar age and especially signs of activity, which are very prominent due to the stellar youth.

The well-determined age of young stars and the discovery of extrasolar planets in their systems would place severe constraints on the models of planet formation. The same is

true for non-detections which can then be used with results of further young stellar objects surveys to make statistical inferences.

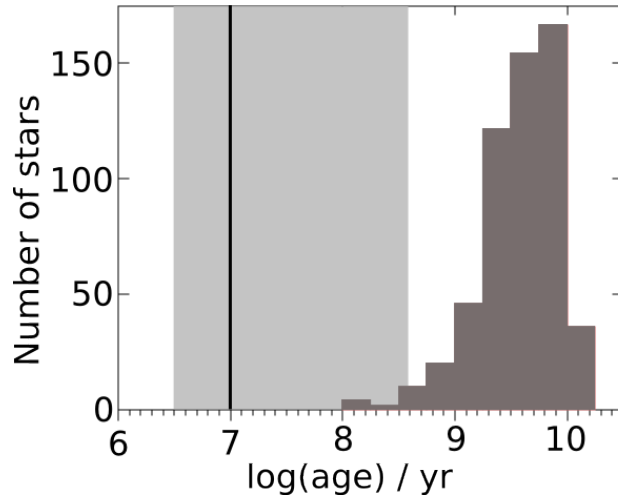


Figure 1.4: Age distribution of known exoplanet host stars. The black line indicates the upper limit to the planet formation time scale of 10 Myr (Armitage, 1999). The planets around the main-sequence stars (dark gray) between $\log(\text{age})=8.0-10.25$ were detections by using radial velocity, astrometry and the transit method. The light gray area from $\log(\text{age})=6.5-8.6$ marks the ages of the target sample in this thesis. (Last updated: July 27, 2013. Data taken from exoplanet.eu)

This thesis is organized as follows:

The second chapter gives a detailed overview of the used methods including stellar parameters and age determination, derivation of the radial velocity variation and stellar activity indicators.

Chapter 3 contains information about the target selection as well as results of the stellar parameters and age determination and additionally the system characterization.

Results of the analysis of the radial velocity variation and periodicity analysis are collected in Chapter 4. Furthermore, the results of the stellar activity analysis is listed.

Chapter 5 presents a simulation procedure for cool circular spots on stellar surfaces and the application of this software to stars of my sample.

One published and one submitted example of companions showing signs of activity are given in chapter 6 and 7. While chapter 6 discusses a possible companion in the young stellar EX Lupi-system, chapter 7 deals with the detection of a Hot Jupiter around a K-star showing starspot activity with the HATSouth transit network.

The summary and conclusion about the performed exoplanet search with RV and the analysis of stellar activity indicators is presented in chapter 8. This summary includes the results of the RV analysis of the young eruptive star EX Lupi and the confirmation of the planet around HATS-2 with follow-up observations as well.

Chapter 9 gives recommendations for future exoplanet surveys around young stars discussing lessons learned during the analysis.

Chapter 2

Methods

2.1 Determination of stellar parameters from observational data

The majority of stellar light that is detected at optical wavelengths (4000 - 7000 Å) is emitted by the stellar photosphere, which is the layer of the stellar atmosphere between the hot interior and the stellar chromosphere (Vernazza et al., 1973). In the Sun, the photosphere is about 1000 km thick. The observed spectral lines result from interactions of photons emitted by hot lower layers with particles in higher layers, e.g. atoms or molecules. There are several mechanisms that broaden spectral lines and give them their characteristic profile: In addition to the natural line broadening due to Heisenberg's uncertainty principle, thermal and pressure broadening also widen the spectral line: molecules and atoms in the gas of stellar atmospheres have a characteristic velocity distribution, both in absolute value and direction, and the emitted or absorbed spectral line is broadened due to red- and blueshifted photons emitted by particles. Furthermore, individual particles can change their emission and absorption behaviour if they collide with neighboring molecules or atoms. Magnetic fields lead to a splitting of spectral lines due to the Zeeman effect and to Zeeman broadening, which is usually much smaller than the thermal broadening due to Doppler shifted emission of particles (Zeeman, 1897). The Zeeman effect is best visible in cool stars, since they often have stronger magnetic fields and a smaller thermal broadening than hotter stars.

Due to the Doppler shift, the motion of a turbulent element, i.e. a group of particles in the stellar atmosphere, leads to spectral line broadening as well. If the turbulent element is smaller than the unit optical depth, one refers to *microturbulence* v_{mic} ; if the element is larger, the phenomenon is called *macroturbulence* v_{mac} (Gray, 1988, 2008). These effects cause the spectral lines to broaden to the commonly known spectral line shape - the *Voigt* profile.

All stars rotate around the axis of their angular momentum vector. If this axis is not parallel to the line of sight towards the observer, the stellar rotation causes a negative radial velocity of the stellar parts that are rotating towards the observer and a positive radial velocity of that parts that rotate away. This results in an additional line broadening due to the different Doppler shift of individual surface elements on the star. The stellar projected rotational velocity $v \sin i_*$ can be described using the stellar radius R_* , stellar rotational period $P_{\star, \text{rot}}$ and stellar inclination i_* as:

$$v \sin i_* = \frac{2\pi R_* \sin i_*}{P_{\star, \text{rot}}} \quad (2.1)$$

Additionally, the measurement process itself affects the observed spectral line shape as well. The finite resolution of the spectrometer and the spectral response function of individual spectrometer channels, as well as non ideal optics and wavelength dispersion, all must be taken into account when characterizing a star.

A star can be characterized by a variety of parameters extracted from stellar spectra. One parameter is the flux F_\star emitted by the stellar surface. It is defined as

$$L_\star = F_\star \cdot 4\pi R_\star^2 \quad (2.2)$$

with bolometric luminosity L_\star . This equation is valid only for isotropic irradiation and is already disturbed, if spots are involved. In the case of a circumstellar absorbing disk, the relation breaks down completely. Since stars are generally not spatially resolved, the observational estimation of R_\star and determination of F_\star using Eq. 2.2 is usually not possible.

The Stefan-Boltzmann law relates the total flux emitted by a blackbody to its temperature. This temperature is used to describe the effective temperature $T_{\text{eff}\star}$ of a star, which is actually not a perfect blackbody:

$$F_\star = \sigma T_{\text{eff}\star}^4 \quad (2.3)$$

with the Stefan-Boltzmann constant σ ($= 5.670373 \cdot 10^{-8} \text{ W m}^{-2} \text{ K}^{-4}$)¹. $T_{\text{eff}\star}$ is not only a proportion for the flux emitted by a star but also a mean temperature of the different layers of a stellar atmosphere.

Another useful quantity that can be derived from a stellar spectrum to characterize a star is the surface gravity:

$$\log g_\star = \log \left(\frac{GM_\star}{R_\star^2} \right) \quad (2.4)$$

with gravitational constant G ($= 6.67384 \cdot 10^{-11} \text{ m}^3 \text{ kg}^{-1} \text{ s}^{-2}$)². Typically g_\star is given in cgs units.

The chemical composition is another important stellar parameter that can be extracted from a stellar spectrum. The metallicity $[M/H]$ is defined as the abundance ratio of metals N_{met} (in astronomy all elements heavier than hydrogen and helium) to hydrogen N_{H} :

$$[M/H] = \log \left(\frac{N_{\text{met}}}{N_{\text{H}}} \right)_{\text{star}} - \log \left(\frac{N_{\text{met}}}{N_{\text{H}}} \right)_{\text{Sun}} \quad (2.5)$$

These equations for the derivation of stellar parameter are discussed and explained in more detail in Gray (2008).

In order to calculate an appropriate model atmosphere that can be used for the determination of radial velocity and activity indicators (see Sec. 2.4), it is important to determine a good estimation of the effective temperature $T_{\text{eff}\star}$, surface gravity $\log g_\star$, metallicity $[M/H]$, and projected rotational velocity $v \sin i_\star$ from the stellar spectrum. This can be done with various existing programs based on different calculation methods. One of them that has been used for the analysis in this thesis, is explained below.

¹<http://physics.nist.gov/cgi-bin/cuu/Value?sigma>, April 15, 2013

²<http://physics.nist.gov/cgi-bin/cuu/Value?bg>, April 15, 2013

2.1.1 SME - Spectroscopy made easy

The IDL-based **SME** (**S**pectroscopy **M**ade **E**asy, Valenti & Piskunov, 1996) fits a synthetic spectrum to an observed high-resolution spectrum using a nonlinear least-squares algorithm. **SME** assumes local thermal equilibrium (LTE) as well as a plane-parallel atmosphere geometry and a negligible magnetic field. Furthermore, it does not take into account bulk flows and molecular line opacities. **SME** comes as an IDL interface allowing to easily load observations and auxiliary files and to adjust necessary settings. The program requires manual input as described in detail below:

Spectral line lists: These lists are required for the determination of the best fitting synthetic spectrum and corresponding stellar parameters. They are the backbone of **SME** and decide which lines are fitted to the observed spectrum. They can be obtained from VALD³ using an initial guess of T_{eff} , $\log g$ and v_{mic} . A line list is then created for a given wavelength range and detection limit. Solar values are used as initial guess for the abundances for the whole analysis.

Observed spectra: Four different wavelength ranges have been chosen from the FEROS data, which are fitted simultaneously: 4160 – 4230 Å, 4250 – 4380 Å, 4400 – 4475 Å and 4500 – 4607 Å. These regions have been carefully chosen based on different lines sensitive to changes of the individual stellar parameters (Fe I and II) and to avoid telluric absorption lines. Before using them with **SME**, the FEROS spectra are cut to these wavelength ranges, continuum-normalized and stellar emission lines and emission line cores as well as incomplete lines at the range edges are excluded. This helps **SME** to focus on the spectral features that are fitable (the synthetic spectra do not exhibit emission lines as are typically observed in spectra of young stars).

Global and free parameters: Initial guesses for global parameters (T_{eff} , $\log g$, $[M/H]$, $v \sin i$, RV , v_{mic} , v_{mac}) have been adopted from spectral type determinations of the targets carried out by different research groups (Tab. 3.1, Sec. 3.1) and inserted into **SME**. In a first step, only $v \sin i$ and RV are set free to vary. Both are then solved as a global value and used as initial guess for the next iteration with T_{eff} , $\log g$, $[M/H]$, v_{mic} , v_{mac} , $v \sin i$ and RV as free parameters.

Model atmosphere: I assume a plane-parallel atmosphere geometry during the analysis with **SME** and therefore choose a MARCS 1D-LTE model (Gustafsson et al., 2008) already implemented in **SME**.

Instrumental profile: As mentioned above, each instrument leaves a characteristic imprint in the spectral data by broadening the spectral lines slightly due to effects of e.g. finite spectral resolution, wavelength dispersion and imperfect optical elements. This effect has to be taken into account to avoid ascribing the broadened lines to physical effects of the star itself as for example to stellar rotation or gravity. **SME** takes this into account by using a user-input instrumental resolution ($R_{\text{FEROS}} = 48\,000$, Kaufer et al., 1997; Stahl et al., 1999) and a Gaussian function.

³The **Vienna Atomic Line Database**, Kupka et al. (2000),
web interface: <http://www.astro.uu.se/~vald/php/vald.php>

Once the best-fitting synthetic spectrum is determined and the stellar parameters are derived, it is possible to refine the fit further. One can edit the used spectral ranges by dismissing parts containing contaminations such as leftover emission lines, regions with absorption lines in the stellar spectrum which are not listed in the line list or, regions with strong noise contamination. This easy method of masking spectral regions avoids editing the spectral line list directly, which is often time-consuming and unfortunately often needed for other programs (such as MOOG, Sneden et al., 2012). Furthermore, this method allows to exclude only parts of spectral lines (e.g. emission cores) and to fit the remaining parts (e.g. absorption line wings).

One drawback of the **SME** program is the error determination of the stellar parameters. The errors are calculated from the quality of the fit, namely the reduced χ^2 . Since **SME** was mainly developed to characterize main-sequence stars observed with a high S/N, the quality of the fit is mostly not optimal for noisy young stars with a medium S/N. This results in a significant underestimation of the actual uncertainties (e.g. a few K for T_{eff}). Therefore, I analyzed 5 individual spectra of each target with the best S/N ratio and calculated the average value for the stellar parameters using the S/N as a weight. The according uncertainty is then derived from the scatter of the 5 individual stellar parameters calculations. However, this method still ignores systematic effects and gives only an estimate of stochastic (measurement and stellar activity) noise.

All targets were fitted with **SME** and their stellar parameters were determined including final errors as explained above. The results are listed in Section A.

2.1.2 Projected rotational velocity $v \sin i$

In order to check if one of the main factors of line broadening, i.e. the projected rotational velocity $v \sin i$, is correctly determined using **SME**, I have applied another calculation method to the **FEROS** data. Following Tonry & Davis (1979), Basri et al. (2000), and Reiners et al. (2012), I use a cross-correlation method to calculate the $v \sin i$ for the targets. The method uses the direct comparison of artificially broadened observed spectra of slowly rotating stars as template spectra with the target spectra. Since both the template and the target spectrum are observed using the same instrument, i.e. **FEROS**, one need not correct for the instrumental broadening, because both spectra are affected in the same way. With this method, a spectrum of a slowly rotating star matching the spectral type of the target within approximately half a spectral class is cut into spectral chunks, carefully avoiding regions of telluric absorption. I choose the regions as 4600 – 4850 Å, 4850 – 5100 Å, 5200 – 5500 Å, 5500 – 5850 Å and 6000 – 6250 Å. These spectral chunks are then artificially broadened by using the **AVSINI**⁴-routine of the **SPECTRUM** package (Gray, 1999, cf. Section 2.2) and cross-correlated with the unbroadened spectral chunks. Therefore, it is important that the comparison star is slowly rotating, since the unbroadened spectrum has to be interpreted as $v \sin i = 0$ km/s. To justify this assumption, the intrinsic $v \sin i$ of the template star has to be below the detection limit, which depends on the spectral resolution of the used spectrograph. The detection limit, below which the $v \sin i$ can not be distinguished from the instrumental broadening anymore, was calculated for **FEROS** by Reiners et al. (2012) as about 3 km/s. By cross-correlating the artificially broadened template chunks with the unbroadened ones and measuring the FWHM of the cross-correlation function (CCF), one can determine a dependency of the FWHM from $v \sin i$ by applying a polynomial fit to the data. Afterwards, the target spectra with unknown rotational broadening are cut into the same chunks and cross-correlated with the unbroadened template

⁴available on <http://www.appstate.edu/~grayro/spectrum/spectrum.html>

spectral chunks. A Gaussian fit delivers the required FWHM with error and the $v \sin i$ can be estimated by the dependency between $v \sin i$ and FWHM of the CCF. This is repeated with all available target spectra. The error of the individual $v \sin i$ measurement is estimated by the quality of the polynomial fit in the individual chunk and a weighted average is calculated to get a $v \sin i$ estimation for the whole spectrum. The average $v \sin i$ for the target in total is then calculated using the weighted average of all individual spectra. The used template stars with known rotational velocity and spectral types (SpT) are listed in Table 2.1. Since the targets in this work do not cover all spectral types, template stars were needed only for certain SpT ranges.

Name	SpT	Ref.	SpT range	$v \sin i$ [km/s]	LDC				
					Reg.1	Reg.2	Reg.3	Reg.4	Reg.5
HD 88742	G0V	G06	F6-F9	2.7 ± 3.0	0.73	0.71	0.68	0.66	0.62
HD 140538	G2.5V	K89	G0-G4	1.8 ± 3.0	0.76	0.74	0.70	0.68	0.63
HD 14412	G8V	G06	G5-G9	2.7 ± 3.0	0.78	0.76	0.72	0.70	0.66
HD 154577	K2.5V	G06	K0-K5	2.7 ± 3.0	0.84	0.83	0.80	0.77	0.72
G1205	M1.5V	J09	M0-M4	0.9 ± 3.0	0.77	0.76	0.75	0.74	0.70

Table 2.1: Template stars with low $v \sin i$ for the $v \sin i$ -determination of targets stars, all $v \sin i$ -values have been taken from Glebocki & Gnacinski (2005). The last columns show the estimated linear limb darkening coefficients (LDC) for the individual regions used for the artificial line broadening of the template spectra as explained below. References: G06: Gray et al. (2006), K89: Keenan & McNeil (1989), J09: Jenkins et al. (2009).

The advantage of this method is the independence from theoretical spectral models, since only observed spectra are used. Because of this, the instrumental profile is automatically taken into account, since all involved measurements are affected in the same way. Furthermore, the usage of different spectral chunks provides a reasonable estimation of the uncertainties in $v \sin i$. The drawback is that a template star is needed. This has to fit the object spectrum by about half a spectral class, has to be a slow rotator, and has to be observed with the same spectrograph as the targets. In addition, strong lineblends lead to broad CCFs and therewith to high errors in the $v \sin i$ estimation. These line blends are especially a problem for M dwarfs. Since only one target used in this thesis is an M type star, the method was still very useful. Moreover, an assumption of the limb-darkening has to be made in order to artificially broaden the template spectral chunks. In order to determine an estimate of this parameter, limb darkening coefficients have been calculated for various filters for the stellar parameters of the template stars (Table 2.1) using the FORTRAN code JKTL⁵ and the linear limb darkening law (Russell, 1912)

$$\frac{I_{\mu}}{I_0} = 1 - LDC \cdot (1 - \mu) \quad (2.6)$$

with the linear limb darkening coefficient LDC and $\mu = \cos \gamma$, where γ is the angle between the line of sight of the observer and the normal to the stellar surface. JKTL⁵ interpolates linearly in T_{eff} and $\log g$, using the results of the study by Claret et al. (1995). The results for the limb darkening for each template star in the wavelength range of the used spectral chunks is shown in Figure 2.1. The data were fitted with a 2nd order polynomial and an average limb darkening was estimated to be used for the artificial line broadening for each region separately. The estimated linear limb darkening parameters for each region for the

⁵<http://www.astro.keele.ac.uk/jkt/codes/jktld.html>

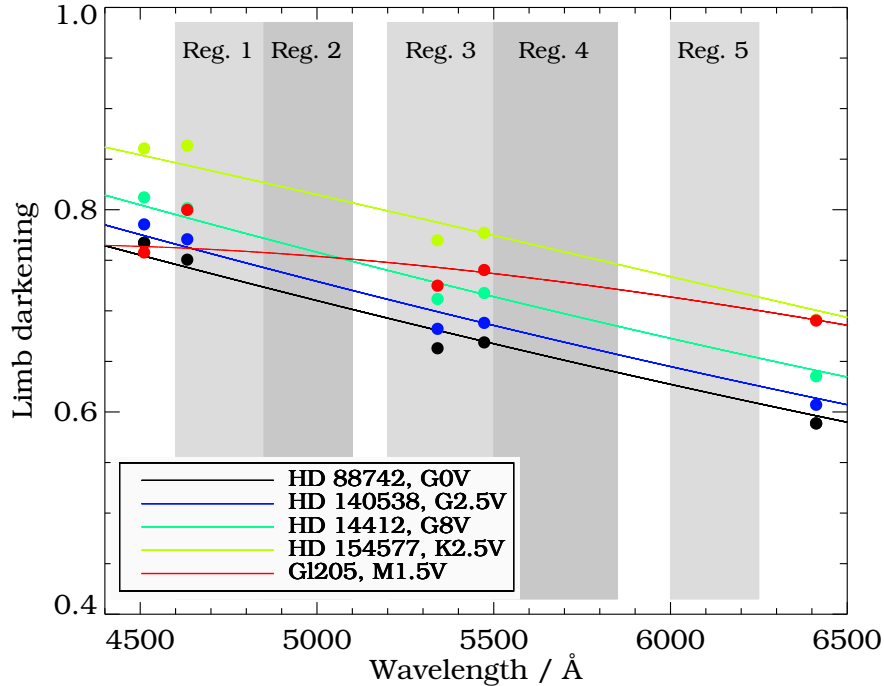


Figure 2.1: Linear limb darkening coefficients including a polynomial fit for the $v \sin i$ template stars (cf. Table 2.1) for the wavelength range between 4400 and 6500 Å. The five different regions for the $v \sin i$ -determination are marked.

individual template stars are listed in Table 2.1. As the figure shows, the polynomial fits are quite satisfying except for Gl205. The reason for this is that M dwarf atmospheres have more highly structured limb-darkening behavior than seen in earlier spectral types. Nevertheless, Figure 2.2 shows that the limb darkening estimation does not have a crucial impact on the artificially broadened template spectra legitimating the rough estimation of the limb darkening for the individual regions above.

2.1.3 Veiling

Young stars often reveal spectral lines with a lower line depth than expected from simple models. The reason for this is an additional continuum on top of the emitted photospheric spectrum of the star itself, that can have different causes. For instance, an active chromosphere of the star itself can have hot accretion spots (Calvet et al., 1984). Furthermore, it can be caused by disk material being accreted onto a star (Lynden-Bell & Pringle, 1974; Kenyon & Hartmann, 1987; Bertout et al., 1988), or a combination of both phenomena. This additional continuum changes the relative line depth (not the absolute), which becomes evident in normalized spectra as an apparently reduced absolute line depth.

The additional continuum fills up photospheric absorption lines and is therefore said to be “veiling” the spectral lines. This especially affects the determination of equivalent width (EW) of spectral lines by systematically underestimating them. When comparing relative EWs from different spectra of a single star, e.g. to check for temporal variations, this effect should affect all measurements and the derivation of the chronological evolution of the EW should not be affected (cf. Sec. 2.5). But if a temporal median EW is used to derive another parameter, e.g. the age estimation by using the Li I EW (see Sec. 2.3), this

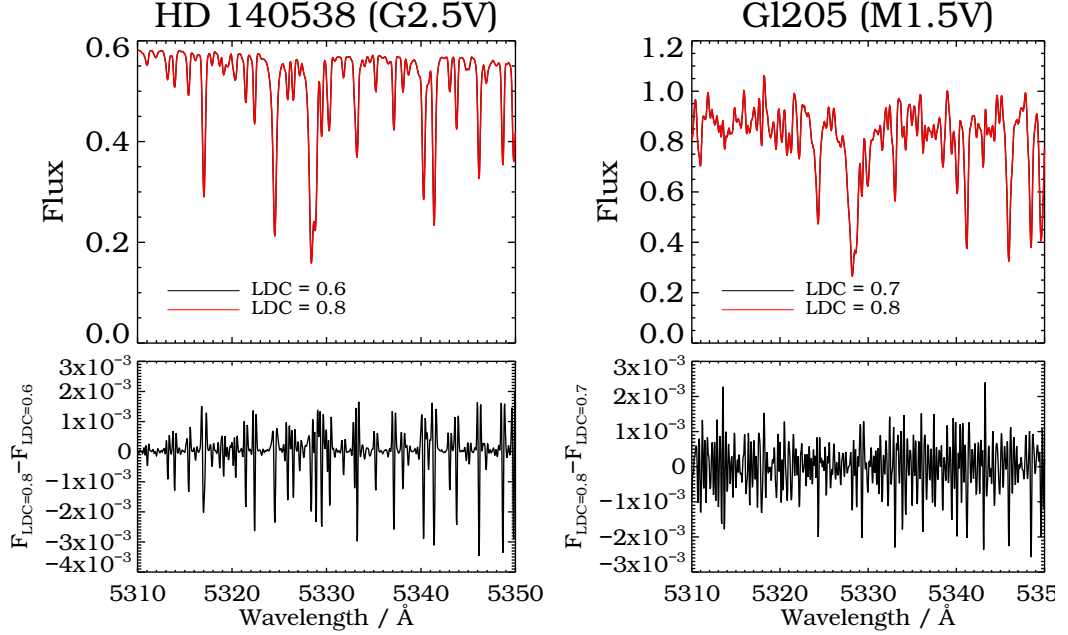


Figure 2.2: Spectra of HD 140538 (left panel) and G1205 (right panel) artificially broadened with 10 km/s using AVSINI for two different limb darkening coefficients representing the minima and maxima of Figure 2.1 (red and black curves are so similar that they almost perfectly overlay). The residua in the lower panels show the small impact of the LDC on the broadened spectra.

effect can lead to an underestimation of the Li I EW and therefore to an overestimation of the stellar age. Therefore, it is important to determine the veiling for each target separately and correct for it before deriving the Li I EW.

Two different methods are used for deriving the veiling: following the method of Johns-Krull & Basri (1997), a comparison of EWs of different spectral features is calculated for the stellar spectrum and for a synthetic template spectrum matching the derived stellar parameters. The veiling value V can then be determined as:

$$V = \frac{EW_0}{EW} - 1 \quad (2.7)$$

where EW_0 is the equivalent width of the spectral line of the synthetic template spectrum. Johns-Krull & Basri (1997) use four different photospheric features to derive V : the EWs of the spectral lines KI (7699 Å), Li I (6708 Å) and Ca I (6193 Å) as well as the TiO band head (7126 Å). Since Li I can not be compared with synthetic template spectra due to the youth of the targets, the analysis of this spectral feature has been neglected. For the TiO band head, I used the TiO 5 index $R_{\text{TiO}5}$ as described in Sec. 2.5. The determination of the veiling V by using the TiO 5 index has been done as follows (Johns-Krull & Basri, 1997):

$$V = \frac{R_{\text{TiO}5} - R_{\text{TiO}5,0}}{1 - R_{\text{TiO}5}} \quad (2.8)$$

with $R_{\text{TiO}5,0}$ the TiO 5 index of the unveiled template spectrum.

The EWs and the TiO 5 index, respectively, have been calculated for each spectrum separately and a weighted average has been derived by using the S/N as weighting factor.

Another possibility to derive the veiling V has been proposed by e.g. Hartigan et al. (1989) and Basri & Batalha (1990). There, a synthetic template spectrum matching the determined stellar parameters is artificially veiled in steps of 0.01:

$$P'_{\text{abs}} = \frac{P_{\text{abs}} + V}{1 + V} \quad (2.9)$$

with P_{abs} the absorption profile of the synthetic template spectrum and P'_{abs} the artificially veiled one. By subtracting the veiled synthetic spectrum from the target spectrum, an estimation of the best-fitting veiling-value V is possible. This analysis has been done in a 20 \AA region around Li I (6708 \AA) line, since this line has to be unveiled for a proper age analysis.

To unveil the Li I line and derive the true value for its EW for the age estimation, I used the equation by Johns-Krull & Basri (1997):

$$EW_{\text{Li},0} = EW_{\text{Li}} \cdot (1 + V) \quad (2.10)$$

with EW_{Li} the EW of the Li line from the observed spectrum and $EW_{\text{Li},0}$ the veiling corrected value.

2.2 Synthetic spectra

Synthetic spectra matching the stellar parameters of a target are used for a variety of analysis methods like radial velocity determination (Sec. 2.4), veiling or $v \sin i$ estimations (Sec. 2.1).

Two different methods have been tested to obtain these synthetic spectra: First the ‘‘Göttingen Spectral Library by PHOENIX’’⁶, which is described by Husser et al. (2013). The library is based on the stellar atmosphere code PHOENIX (Allard et al., 1995) and provides high-resolution synthetic spectra ($R = 500\,000$ at optical and near-infrared and $R = 100\,000$ at the mid-infrared wavelengths). It covers a large variety of stellar parameters ($2300 \leq T_{\text{eff}} \leq 12000 \text{ K}$, $0.0 \leq \log g \leq 6.0$, $-4.0 \leq [M/H] \leq 1.0$), but covers only the wavelength range between 0.5 and $5.5 \mu\text{m}$. Thus, it is not optimal for the analysis of FEROS data (spectral range $\sim 3500\text{-}9200 \text{ \AA}$).

Therefore, a different method to obtain synthetic spectra has been used throughout this thesis: the synthesis program SPECTRUM (Gray, 1999)⁷. SPECTRUM synthesizes stellar spectra assuming a plane-parallel atmosphere geometry and local thermal equilibrium (LTE). Therefore, it is able to use atmospheric models created by Castelli & Kurucz (Castelli & Kurucz, 2004), which are available on <http://kurucz.harvard.edu/grids.html>. Other models can be used as well, e.g. MARCS models (Gustafsson et al., 2008), if converted to the format used for the models of Castelli & Kurucz (2004).

To synthesize a spectrum including a set of spectral lines, line lists are needed, which can be either the ones provided in the download area of SPECTRUM or ones obtained elsewhere (e.g. from VALD) converted to the file structure of the former. SPECTRUM comes with four different lists of spectral line information like wavelength, species, energy of lower state, energy of upper state (in case the species is atomic) and $\log(gf)$ -value. The various spectral line information are collected from different sources like NIST⁸ or Kurucz linelists⁹.

⁶<http://phoenix.astro.physik.uni-goettingen.de/>

⁷available at <http://www.appstate.edu/~grayro/spectrum/spectrum.html>

⁸National Institute of Standard and Technology, http://physics.nist.gov/PhysRefData/ASD/lines_form.html

⁹<http://kurucz.harvard.edu/linelists.html>

In default mode, SPECTRUM synthesizes an intensity-normalized spectrum, integrated over the entire stellar disk, for a given T_{eff} and $\log g$ assuming $v \sin i=0$ km/s. The metallicity depends on the input atmospheric model as well as the usable T_{eff} - and $\log g$ -steps, usually $\Delta T_{\text{eff}}=250$ K and $\Delta \log g=0.5$ for the models of Castelli & Kurucz (2004). A variety of keywords usable in SPECTRUM help to customize the synthetic spectra, e.g. ignoring spectral lines and displaying merely the continuum or computing the flux as disk-integrated absolute flux as measured on the stellar surface instead of normalizing it. Furthermore, auxiliary programs allow for example the application of rotational broadening to the synthesized spectrum, smooth it or invert it in order to determine oscillator strength for individual spectral lines.

Synthetic spectra created with SPECTRUM have been used throughout this thesis for the determination of radial velocity shifts (Sec. 2.4) and activity indicators (Sec. 2.5).

2.3 Age determination methods

The stellar age is an important parameter to characterize a target in more detail and to better interpret analysis results. Different methods have been proposed in the past as useful especially for young stars up to 100 Myrs. Soderblom (2010) gives a detailed overview of the available age indicators, their advantages and drawbacks and their utility for very young stars up to 100 Myrs. Since my study is limited to the available data (observed spectra, photometry in data bases, previous studies), I selected several age determination methods, which are explained below including a list of advantages and drawbacks in Table 2.2.

Kinematic ages

The determination of kinematic ages traces back the motions of a group of stars to the past, when their spatial dispersion was at a minimum. This time is assumed to be the time of formation. All members of such group belong to a so called moving group. Due to tracing back stars to their origin, an age estimation can be obtained and targets identified as member of this special group are assumed to possess the same age as the other members. Although this concept is commonly used, it requires very accurate astrometry, which is not easy to obtain.

In order to identify possible memberships of my targets, I have looked up membership information on the astronomical database SIMBAD¹⁰ and looked through the literature for age estimations. This age determination method is relatively easy for targets which have been clearly identified as members of moving groups, since it is simply literature work. In case a target's assignment is uncertain, the resulting age estimation might be erroneous. In both cases, one strongly relies on results made by other groups, which are often not easily reproducible.

Stellar isochrones

One can also estimate the stellar age using isochrones based on stellar evolutionary models and the determined stellar parameters for a target. Therefore, I selected the isochrones calculated by Yi et al. (2001), which provide isochrones between 5 Myr and 20 Gyr for a variety of different metallicities. The isochrones up to 80 Myr are complete only until

¹⁰<http://simbad.u-strasbg.fr/simbad/>

the star reaches the main-sequence and thus focus on the pre-main-sequence evolution. For each individual target, a set of isochrones was calculated for the determined metallicity. The computed isochrones contain information about the model targets' effective temperature T_{eff} and surface gravity $\log g$. The targets' age can therefore be estimated by overplotting the stellar parameters determined with SME. Age determination via isochrones is straightforward in principle, since only one good spectrum is needed, for which the stellar parameters are then determined and compared to models. Nevertheless, the isochrone models can be very imprecise, especially for young stars, since physical mechanisms in the stellar evolution are not (yet) completely understood. Furthermore, restrictions to metallicity don't allow the application to all targets (see below). Due to large differences in different models, substantial systematic discrepancies can result. An additional problem arises in the determination of stellar parameters (see Sec. 2.1) and especially their error estimations. Therefore, the ages and their uncertainties are very affected by the quality of the stellar parameter determination.

Lithium depletion

An additional possibility is the determination of the stellar age by using the equivalent width of the lithium I spectral line at $\sim 6708 \text{ \AA}$. As e.g. Wallerstein & Conti (1969) summarize previous works in their review, the EW of this spectral line is a good age indicator. Traces of lithium were created during the Big Bang and are now included in the interstellar matter, from which a star is formed. If the initial stellar mass is larger than $0.06 M_{\odot}$, the lithium burning starts, burning lithium and Hydrogen to Helium. The reaction rates depends on the age and the mass of the star and its corresponding effective temperature. In younger stars, a larger amount of lithium is left than in older stars and therefore the Li I EW is larger, so it can be used for stellar age determination. In recent years, this stellar age indicator is more and more under discussion, since Baraffe & Chabrier (2010) showed that non-steady accretion in the early stages of star formation can affect the Li I depletion and so the usage of the Li I EW as age indicator can have a limited reliability. But, since the Li EW is still a commonly used age indicator (e.g. Thomann et al., 2013), I used this method for the sake of completeness for the targets in this thesis as well. Once the Li I EW is obtained, one has to use an age calibration of the EW value to determine the age. This has been done using the results of Zuckerman & Song (2004). They used members of eight different stellar associations with independently derived mean age and calculated Li EWs. These associations were NGC 2264 (4 Myr), TWA (8 Myr), η Cha (8 Myr), IC 2302 (30 Myr), TucHor (30 Myr), β Pic (30 Myr), Pleiades (90 Myr) and UMa (300 Myr). Since the Li I EW depends on the effective temperature of the star and hence its spectral type, Weise (2010) has created a diagram, plotting the Li I EW over spectral type for the members of the stellar associations analyzed by Zuckerman & Song (2004) (Fig. 2.3). To estimate the ages of the targets of this thesis, I determined the Li I EW of all spectra taken for these targets, calculated a weighted mean with error (using the S/N as a weight), corrected for the veiling and plotted them into Fig. 2.3 (see Sec. 3.2.2). In general, the age determination of stars using the Li I EW is relatively easy, since the calculation of one EW-value from a spectrum is fairly straight forward. Since the Li I spectral line is very prominent for most young stars, the measurement is easy to execute. Nevertheless, the derivations need a high-quality spectrum (high S/N and a high spectral resolution of the spectrograph) and a good correction for veiling. The determination of the position of a star in Fig. 2.3 delivers only a broad range or an upper limit of age and errors are difficult to derive.

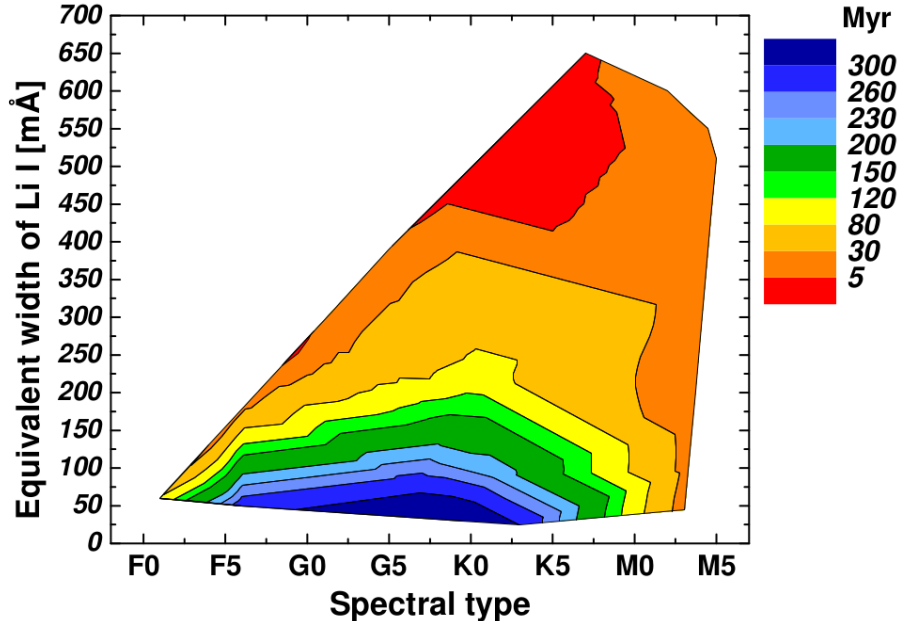


Figure 2.3: Lithium I EW for different spectral types after Zuckerman & Song (2004). The color-shades represent different ages.

Rotational spin-down and gyrochronology

In addition, one can use the fact that stellar rotation slows down with age (e.g. Wilson, 1963; Skumanich, 1972; Soderblom, 1983; Soderblom et al., 1991). This method is called gyrochronology and uses only stellar rotation periods and their colors (Barnes, 2007):

$$\log t_{\text{gyro}} = \frac{1}{n} [\log P_{\star, \text{rot}} - \log a - n \log((B - V) - 0.4)] \quad (2.11)$$

with t_{gyro} in Myr, the rotational period P in days and the constants $n = 0.5189 \pm 0.007$, $a = 0.7725 \pm 0.011$ and $b = 0.601 \pm 0.024$. Barnes (2007) claims an error of the gyrochronology age of about 28% for G, K and early M stars. Since a spectral analysis does not reveal directly the rotation period, the literature has been searched for photometric time series of the target e.g. taken by the large exoplanet transit survey SuperWASP (see Sec. 3.2.2). In general, the age determination using the rotational period can deliver reasonable age estimations. In case strong surface features are available, the analysis of well-sampled photometry can provide the stellar rotational period with good precision. If no stable surface features are detected on the stellar surface, the method of gyrochronology is apparently not applicable. The determination of the rotational period yields the danger to detect an alias of the rotation period (especially in case of bad measurement sampling) or to not detect the equatorial rotation period (differential rotation). Furthermore, Eq. 2.11 depends on the stellar color, which might be imprecise.

An additional drawback has been recently raised by Gallet & Bouvier (2013). As Fig. 2.4 shows, the angular velocity stellar rotational period exhibit substantial scatter for solar-type stars in young open clusters. Therefore, the rotational spin-down and the method of gyrochronology is most likely not useable for young stars. As the figure shows, the models converge for slow, median and fast rotators for targets older than 1 Gyr and so,

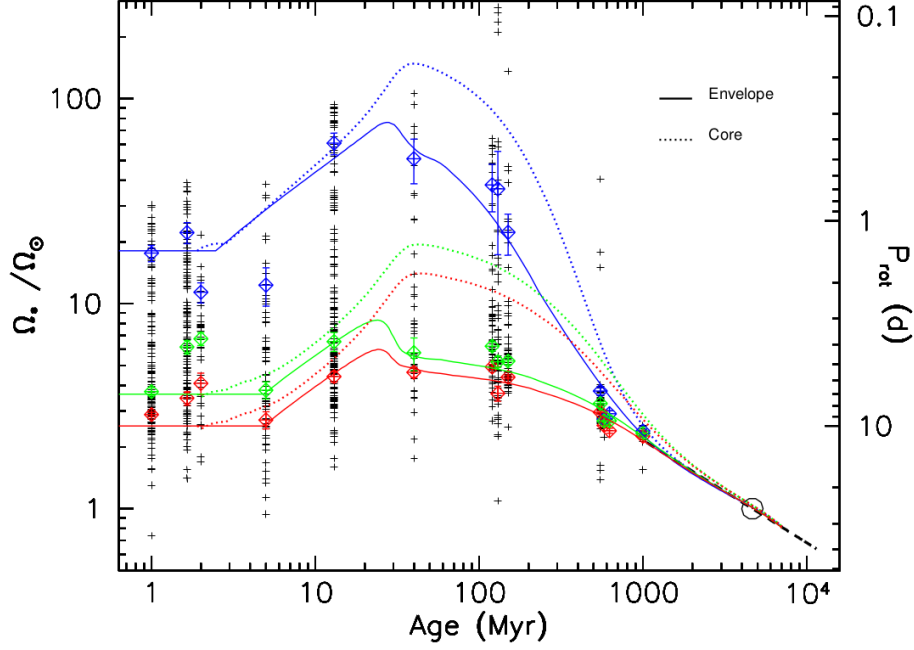


Figure 2.4: Angular velocity and rotational period over age for solar-like stars in open clusters near the Sun (\odot). Solid lines correspond to models of the convective envelope, while dashed lines describe the radiative core. Different rotator models are marked in colors: red (slow), green (median) and blue (fast). The position of the Sun and the dashed black line at the bottom right shows the Skumanich spin-down relation (Skumanich, 1972). The figure has been taken without changes from Gallet & Bouvier (2013).

the method is still applicable to older targets. Nevertheless, the method has been adopted to the targets of this thesis in order to compare the results with other methods.

Stellar activity

Finally, one can use the analysis of activity as an age indicator. This method has been proposed by Mamajek & Hillenbrand (2008) and bases on the relation between stellar activity and stellar rotation (e.g. Kraft, 1967; Noyes et al., 1984a,b). Following Mamajek & Hillenbrand (2008), the stellar age t is calculated by using the activity index R'_{HK} , which is corrected for the influence by the stellar photosphere:

$$\log t = -38.053 - 17.912 \cdot \log R'_{HK} - 1.6675 \cdot \log(R'_{HK})^2 \quad (2.12)$$

In order to derive the necessary quantity R'_{HK} to determine the stellar age, one calculates the activity index S_{FEROS} (see Sec. 2.5, Eq. 2.19) for each spectrum of a target and determines a median value, using the S/N as a weighting factor. By using the following equation of Noyes et al. (1984a), which is equivalent to the relation by Middelkoop (1982a),

$$R_{HK,\text{FEROS}} = 1.340 \cdot 10^{-4} C_{cf} \cdot S_{\text{FEROS}} \quad (2.13)$$

with $\log C_{cf}(B-V) = 1.13 \cdot (B-V)^3 - 3.91 \cdot (B-V)^2 + 2.84 \cdot (B-V) - 0.47$

one can convert the derived activity index S_{FEROS} to the activity index $R_{HK,\text{FEROS}}$.

By taking the influence of the stellar photosphere R_{phot} into account, one can calculate the necessary parameter $R'_{HK,FEROS}$ for the age estimation equation:

$$\begin{aligned} R'_{HK,FEROS} &= R_{HK,FEROS} - R_{\text{phot}} \\ &= R_{HK,FEROS} - 10^{-4.02-1.4 \cdot (B-V)} \\ \Rightarrow \log t_{S_{FEROS}} &= -38.053 - 17.912 \cdot \log R'_{HK,FEROS} - 1.6675 \cdot \log(R'_{HK,FEROS})^2 \quad (2.14) \end{aligned}$$

Eq. 2.12 (and accordingly Eq. 2.14) is only calibrated for stars fulfilling the criteria $0.5 < (B - V) < 0.9$ and $-5.1 < \log R'_{HK} < -4.0$ due to the selected stars in Mamajek & Hillenbrand (2008). This limits the range of usable spectral types to approximately F6 to K2, so some targets of this thesis could not be analyzed in terms of age using this method. Furthermore, equations by Noyes et al. (1984a) and Middelkoop (1982a) were derived for main-sequence stars. These limitations might be problematic for the age estimation of young stars, which has been confirmed by Song et al. (2004), who compared the age derived by the lithium abundance, X-ray activity and Galactic space motion with that derived by using the chromospheric activity indicator of 20 stars. Nevertheless, since the Ca II K is easily observed from the ground, the determination of the activity index is uncomplicated.

Other age estimation methods like asteroseismology (e.g. Lebreton, 2012) have not been used in this thesis and are not explained further here. For a very detailed overview of the used age indicators and of additional ones, I refer, as mentioned above, to Soderblom (2010).

During the recent *Protostars and Planets VI* in Heidelberg, Rob Jeffreys proposed the use of the deuterium depletion boundary as age indicator. This has been already analyzed in 2000 by Chabrier et al. Since the method has not been used and tested extensively, I do not consider it in this thesis.

Tab. 2.2 gives a general overview of the advantages and the drawbacks of the used age determination methods.

Method	Advantage	Disadvantage
Kinematic ages (Moving group memberships)	→ conceptionally simple	→ when membership not clear, age estimation ambiguous → moving group membership identification needs very precise astrometry
Isochrones	→ Just one good spectrum & well determined stellar parameters needed	→ models can vary systematically → restrictions to metallicity → large differences between different models → ages and their uncertainties rely heavily on quality of stellar parameter estimation
Lithium I EW	→ Li I feature easy to detect → EW straight forward to measure → analysis of many clusters provides good calibration	→ high-quality spectrum needed → age estimation only a broad range or upper limit → results questionable due to unclear accretion history
Gyrochronology	→ if well-sampled photometric data available, P_{rot} determination easy → large data bases of transit surveys can provide good photometric data	→ not applicable, if no rotational period P_{rot} available → P_{rot} only measurable in presence of stable surface features → risk to detect alias of P_{rot} → imprecise, in case stellar color is not well known → photometric observations with good sampling are expensive → recent studies show that method most likely not applicable to stars younger 1 Gyr due to large rotational period scatter over age
Stellar activity	→ Ca IIK easy to observe from the ground → calculation of activity index straight forward	→ limited to F6-K2 spectral types

Table 2.2: (Dis-)advantages of used age determination methods

2.4 Calculation of radial velocity changes

If a celestial body (stellar or substellar) is orbiting a star, the detected stellar light is Doppler shifted due to the stellar motion around the common center of mass. The velocity contribution of the star along the line of sight of the observer is called *radial velocity* (RV) and its semi-amplitude K_\star can be calculated by (e.g. Perryman, 2011):

$$K_\star = \frac{2\pi}{P} \frac{a_\star \sin i}{(1 - e^2)^{1/2}} \quad (2.15)$$

with orbital period P , semi-major axis a_\star of the stellar orbit, orbital inclination i and orbital eccentricity e .

The orbital period P is related to the companion mass M_P , the stellar mass M_\star and the gravitational constant G by

$$P^2 = \frac{4\pi^2}{G} a_\star^3 \cdot \frac{(M_\star + M_P)^2}{M_P^3} . \quad (2.16)$$

Squaring Eq. 2.15 and substituting P^2 with Eq. 2.16 leads to a description of the *mass function* f_m :

$$K_\star^2 = \frac{G}{(1 - e^2)} \frac{1}{a_\star \sin i} f_m \quad (2.17)$$

$$\text{with } f_m = \frac{M_P^3 \sin^3 i}{(M_\star + M_P)^2} = \frac{P \cdot K_\star^3 (1 - e^2)^{3/2}}{2\pi G} \quad (2.18)$$

The parameters above can be determined by fitting the obtained RV data with a Keplerian function with free parameters K_\star , a_\star , e , P , i , T_0 , which represents the time at periastron passage and Ω (ascending node) and ω (periastron length) describing the alignment of the orbit in space (Fig. 2.5).

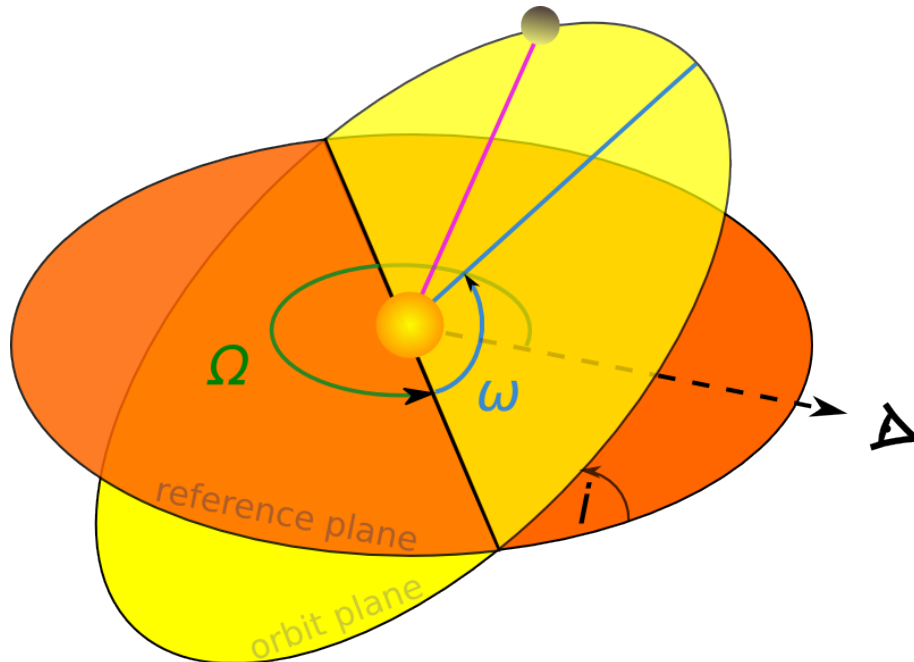


Figure 2.5: Keplerian orbit of a planet around its host star, showing the ascending node Ω , periastron length ω and inclination i . The planet moves in the orbital plane, while the observer's line-of-sight lies in the reference plane.

2.4.1 FEROS

All targets in this thesis were intensively observed with FEROS, the **F**iber-fed **E**xtended **R**ange **O**ptical **S**pectrograph mounted at the 2.2m MPG¹¹/ESO¹² telescope at La Silla Observatory in Chile (Kaufer et al., 1997; Stahl et al., 1999). FEROS is a high-resolution ($R=48\,000$) Échelle spectrograph covering the wavelength range between $\sim 3500\text{ \AA}$ and $\sim 9200\text{ \AA}$ in 39 different spectral orders and is environmentally controlled. Its large wavelength range allows to cover a variety of spectral features important for the analysis of targets in terms of stellar activity as described in detail in Section 2.5.

The wavelength calibration is done with a ThAr lamp and spectra can be obtained in object-cal (simultaneous exposure with the ThAr lamp during the target observation) and in object-sky mode (simultaneous sky exposure). The automatic reduction system (DRS) at the telescope¹³ follows the basic principle of the reduction of Échelle spectra: detection of spectroscopic orders, wavelength calibration and background subtraction, flatfield correction and order extraction. Furthermore, the DRS rebins the reduced spectra to constant wavelength steps in both logarithmic and linear regime and merges the individual orders if requested. Especially challenging for the reduction of FEROS raw spectra is the extraction of the highly curved and doubled orders due to the simultaneously taken object/sky and object/ThAr fibres, respectively, what is also implemented in the DRS. The DRS also applies the barycentric correction, which has been shown as to be not accurate enough, since the Earth's precession is neglected within (Müller et al., 2013). Therefore, a calculation of the barycentric velocity has been made outside the DRS using the IDL codes `calcpo.pro`¹⁴ to update coordinates for precession and proper motion and `baryvel.pro`¹⁵ to calculate the heliocentric and barycentric velocity of the Earth.

The RV has been determined from the spectra using the cross-correlation method. To do so, a template spectrum is needed, matching the stellar parameters, that have been determined with SME. This template has been synthesized with the FEROS resolution using SPECTRUM. The cross-correlation takes place orderwise. The spectral orders 1-7 are not used because of the high noise; Orders 32-33 and 36-39 were also avoided because of the contamination with telluric lines. The remaining orders (spectral range about $3970 - 7950\text{ \AA}$) were carefully trimmed avoiding strong spectral lines like H_α because of distortions due to stellar activity and emission lines, which are not part of the synthesized spectra. From the remaining 26 orders, a set was chosen for each target individually, dismissing orders with bad S/N or a small number of spectral lines, both causing a bad cross-correlation. To avoid systematic errors by choosing different subsets of analyzed orders for the individual spectra of the same object, the used set of orders is hard-coded for each target individually. The resulting subset of orders is then filtered for cosmic ray spikes, normalized and each order is individually cross-correlated with the equivalent of the synthetic spectrum. The velocity range for the correlation is fixed for each target as between ± 30 to $\pm 50\text{ km/s}$ with respect to its system velocity. This value is hard-coded as well to make sure that the same range is applied for all spectra of a target. The resulting CCF is then fitted with a Gaussian, the RV being the center of the Gaussian. The individual error of the RV in this order represents the quality of the fit.

¹¹Max Planck Gesellschaft

¹²European Southern Observatory

¹³offline version available on <https://www.eso.org/sci/facilities/lasilla/instruments/feros/tools/DRS.html>

¹⁴<http://www.astro.washington.edu/docs/idl/cgi-bin/getpro/library43.html?CALCPOS>

¹⁵<http://idlastro.gsfc.nasa.gov/ftp/pro/astro/baryvel.pro>

In order to correct for wavelength shifts due to instabilities of the instrument during the measurement, the simultaneously obtained ThAr+Ne spectra are cross-correlated with a binary template of ThAr+Ne lines. By subtracting the calculated RV of the ThAr+Ne spectrum from the target RV, instrumental shifts can be corrected. Other spectrographs like Coralie (Queloz et al., 2000) determine the mean instrumental shift during a single exposure, by using the same exposure time for ThAr as for the object. This is achieved by filters between detector and calibration lamp with different transparencies depending on the exposure time. Instead, FEROS takes a single ThAr+Ne exposure of 15-25 s (depending on the lamp brightness, which changes with the age of the lamp). This leads to the fact that the ThAr exposure does not represent the mean shift of the instrument during the whole exposure time but just for 15-25 s. But tests have shown that the instrumental shift is negligible even for longer exposure times (J. Setiawan, priv. comm.).

The final RV value per spectrum is then calculated taking the weighted average of the individual order measurements. This approach has the effect that orders with higher RV errors, representing spectral ranges with high noise and/or only a few spectral lines, do not carry much weight in the determination of an average RV value for an individual spectrum. In the end, the newly calculated barycentric correction was applied to the RV by subtracting the reduction pipeline value (given in the header) and adding the correction determined with baryvel.pro.

2.4.2 HARPS

In addition to the observed FEROS spectra, I have obtained HARPS data from the ESO archive. HARPS (**H**igh **A**ccuracy **R**adial velocity **P**lanet **S**earcher; Mayor et al., 2003) is a fibre-fed, high-resolution ($R = 115\,000$) optical Échelle spectrograph, mounted at the 3.6 m telescope at the La Silla Observatory, Chile. HARPS is optimized for mechanical stability and therefore achieves high accuracy RV measurements (e.g. Bonfils et al., 2007). Like FEROS, HARPS can be used in two different modes: either the simultaneous observation of the target and a ThAr calibration lamp, or the target and the background sky. The spectra are directly reduced on-site and the RV is determined by cross-correlating the target spectrum with a mask, matching the spectral type, and written in the file header. Since no additional data has been taken for the selected targets in the framework of this thesis, the analysis of the HARPS spectra relies on the already reduced and RV-analyzed spectra, so that no influence could be made on the selection of the cross-correlation template. Therefore, the quality of the reduction and the cross-correlation can not be tested or reproduced and I decided not to rely on the RV results given in the headers. In order to make RV results of the HARPS spectra comparable to the FEROS results, the reduced merged spectra were downloaded from the ESO archive and each was split into wavelength ranges corresponding to the FEROS orders. Due to the fact that HARPS has a smaller wavelength coverage than FEROS ($\sim 3780\text{-}6910\text{ \AA}$ for HARPS in comparison to $\sim 3500\text{-}9200\text{ \AA}$ for FEROS) not all FEROS orders could be reproduced. By selecting the same orders that have been previously used for the FEROS data for the individual targets, it is assured that no regions with emission lines or high noise were used for the analysis. In order to avoid inducing systematic errors, used orders for stars with both FEROS and HARPS spectra have been adjusted such that FEROS-orders which are out of the HARPS spectral range have been neglected. This procedure leads to a lower SNR by neglecting spectral ranges of intrinsically good quality and correspondingly higher RV errors, but new systematic errors are avoided, which was deemed more important.

Furthermore, this approach treats the spectra for the two instruments consistently. The same cross-correlation template as for the FEROS analysis was used, rebinned to the spectral resolution of HARPS. Otherwise, the RV determination is equivalent to the FEROS procedure described above (Sec. 2.4.1).

In contrast to the FEROS spectra, the barycentric correction for HARPS has proven to be precise enough, so that no additional correction has to be applied.

2.4.3 Analysis of RV periodicity

In order to look for periodicities in the obtained RV data of a target (and within the characterization of stellar activity indicators, see Sec. 2.5), two different programs have been used.

The program GLS (**G**eneralised **L**omb-**S**cargle periodogram, Zechmeister & Kürster, 2009) is based on the Lomb-scargle periodogram (Scargle, 1982) but includes also the analysis of Kepler periodograms by optimizing a fit of a Keplerian orbit to the RV data. It has been used for the period analysis of data taken by one instrument (i.e. FEROS) for the analysis of Keplerian orbits and stellar activity patterns on the stellar surface. The tool calculates detailed sine and Keplerian periodograms in a required frequency range (i.e. orbital period) and orbital parameters as eccentricity e , RV semi-amplitude K , periastron length ω , periastron passage T_0 as well as system velocity V_0 . Furthermore, it gives the false-alarm probability (FAP, Cumming, 2004) of the best-fitting period. By using the FAP, periods can be characterized in terms of significance (throughout this thesis, a FAP < 0.1% indicates a significant period, Martin Kürster, MPIA, priv. comm.). If a mass estimate of the host star is given, the program calculates physical parameters of the secondary and orbital parameters like mass function f_m , minimum mass ($M_P \sin i$) of the secondary and semi-major axis a . To do so, it solves Equation 2.17 iteratively by assuming $\sin i = 1 \Rightarrow i = 90^\circ$ to determine the minimum mass of the companion. Additionally, the program calculates the window function of the data set, which gives information about periods favoured to be found in the periodogram because of measurement sampling issues. One typical favoured period is that of 1 d, since observations are only taken during night time and due to visibility reasons often at the same time of night during an observing run. In order not to classify these periods as significant evidence of a companion, the combination of both the periodogram and the window function has to be examined. This has been done in detail in Sec 4.2.

If spectra taken by more than one instrument for one target are used (i.e. FEROS and HARPS) and the determined RV values shall be fitted simultaneously, the IDL program *RVlin.pro*¹⁶ (Wright & Howard, 2009) was used. Although it solves for the individual RV offset between the different instruments, it does not provide periodograms, since the best-fitting orbital period is determined by simply fitting an arbitrary number of Keplerian curves to the data set instead of analyzing in detail the frequency space as done within GLS. The uncertainties for the derived orbital and companion parameters are calculated using the bootstrap method implemented in the provided IDL program *boottran.pro* (Wang et al., 2012).

To obtain periodograms for a combined data set of different instruments, an analysis with *RVlin.pro* was first executed in order to calculate the RV offset between the instruments, which has then been corrected. Afterwards, periodograms were created with GLS using the combined data set.

¹⁶available on <http://exoplanets.org/old/code>

2.5 Stellar activity indicators

A subset of spectral lines was used to determine the spectral line distortion by stellar activity: calcium and hydrogen as well as spectral features such as line-depth ratios and spectroscopic indices. Since the chosen spectral features originate in different heights within the stellar atmosphere by radiative and collisional processes, one can analyze the influence of both chromospheric and photospheric activity. The majority of the spectral lines having their origin in the stellar chromosphere lie in the UV and at shorter wavelengths (Hall, 2008) and are therefore not observable with ground-based facilities. The exceptions are a limited set of lines; for example, the Ca II H & K lines, H $_{\alpha}$ and the Ca II infrared triple (Vernazza et al., 1981, see Fig. 2.6). Therefore, an analysis of the chromospheric activity, which is supposed to be closely related to the stellar dynamo, magnetism, and rotation rate (Middelkoop, 1982a,b; Rutten, 1984; Zhao et al., 2013), is executed on a selection of those spectral features (see below).

The analysis of the photospheric activity uses temperature-sensitive spectral lines as well as the CCF, representing an average line profile of the mainly photospheric lines in the stellar spectrum.

The analysis of these features is described below and a general overview of these indicators is given in Table 2.4. The distribution of indicators of the whole FEROS spectrum is shown in Figure 2.9. In order to achieve a consistent analysis of the various indicators, only FEROS spectra have been used, since some indicators use spectral ranges not covered by HARPS.

2.5.1 Analysis of spectral lines and features

Calcium II lines

Ca II lines have their origin in the stellar chromosphere (Vaughan et al., 1978; Vernazza et al., 1981). Representatives of these lines such as the Ca II H & K lines (at 3968 Å and 3933 Å, respectively) as well as the Ca II infrared triple (at 8498 Å, 8542 Å and 8662 Å) are good indicators for chromospheric activity (Larson et al., 1993). In order not to risk a possible blend of the Ca II H line with the H $_{\epsilon}$ line, I exclude this spectral line from the analysis as well as the Ca II lines at 8498 Å and 8542 Å, which can be blended with telluric water vapor lines (Moore et al., 1966). That is why I concentrated on the Ca II K (at 3933 Å) and the Ca II line at 8662 Å. Since Ca II H & K lines are collisionally dominated (Hall, 2008), they carry information of conditions in the plasma due to the fact that collisional effects increase with the electron temperature. This effect can be seen in the emission cores of these lines at hot temperatures in the chromosphere caused by shock fronts due to infalling material or flares. Therefore, they are a commonly used indicator for activity. The first activity indicator of Ca II lines is the so called S_{FEROS} -index (Vaughan et al., 1978) and is calculated by using the Ca II K line (Fig. 2.7). The flux of the core emission is integrated (F_e) and divided by the sum of the integrated flux of the blue (F_b) and red (F_r) line wing as follows:

$$S_{\text{FEROS}} = \frac{F_e}{F_b + F_r} = \frac{F_{3933 \text{ \AA} - 3935 \text{ \AA}}}{F_{3930 \text{ \AA} - 3933 \text{ \AA}} + F_{3935 \text{ \AA} - 3938 \text{ \AA}}} \quad (2.19)$$

Before the flux integration, the spectra are corrected for the radial velocity shift for each spectrum individually and the line wings fitted to avoid monitoring changes of the blending lines (Fig. 2.7). By monitoring the change of the S_{FEROS} index over time, a period

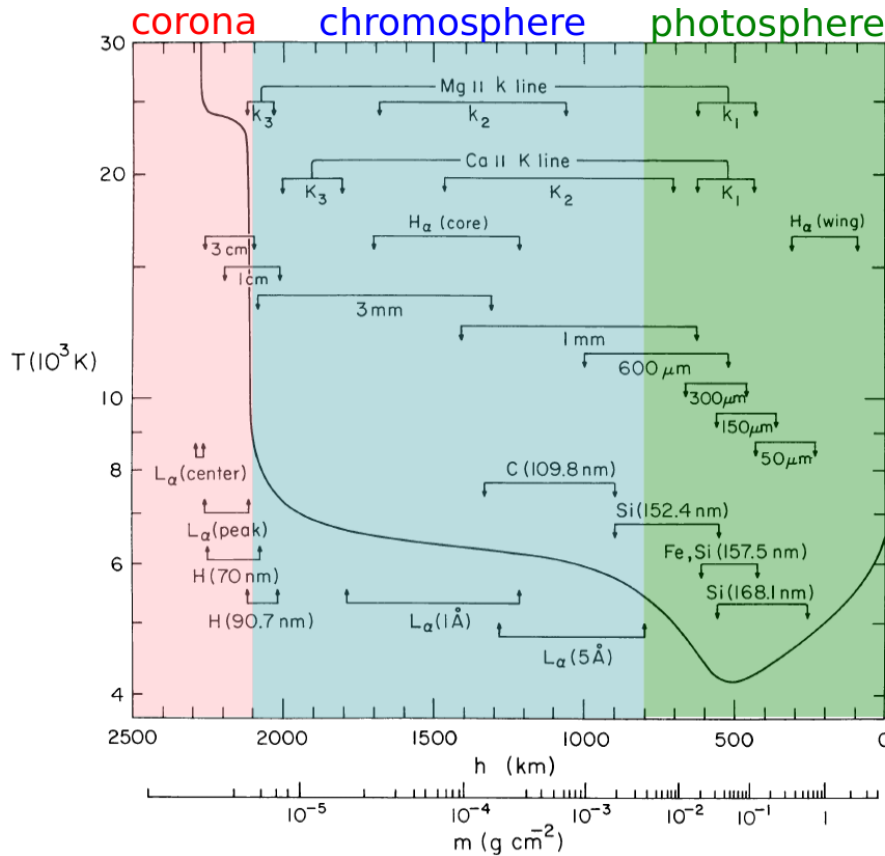


Figure 2.6: Spectral line origins in the solar chromosphere during quiescence. The x-axis shows the geometrical depth in km. 0 km corresponds to the lower layer of the stellar photosphere, which in this picture spans between 0 and about 800 km (green). Above lies the stellar chromosphere between about 800 and 2200 km (blue). Layers above belong to the stellar corona (red). The black line shows the temperature profile over geometrical depth. The figure has been adopted from Vernazza et al. (1981).

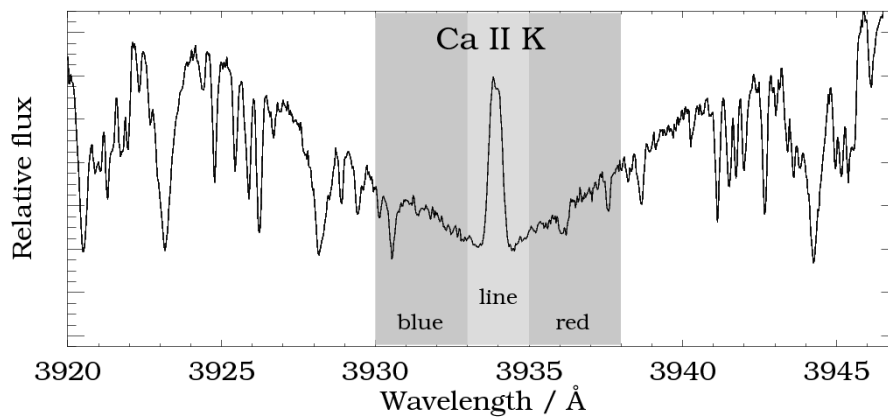


Figure 2.7: Ca II K line at 3933 Å for the S_{FEROS} index. The emission line center is marked light grey and the blue and red wings in dark grey.

analysis is possible (Sec. 2.4.3) and results can be compared with an obtained RV period. Furthermore, one can analyze the asymmetry of the emission core of the Ca IIR line. In case a spot is rotating on the stellar surface, it will cause a distortion only on one side of the emission core, depending on its position on the stellar surface. To analyze possible distortions, I calculated the slope on each point of the emission core and plotted it over wavelength. Afterwards, areas of positive A_p and negative slope A_n are integrated and the quotient $Q = A_p/A_n$ is calculated. In case the absolute value of Q is larger than 1, the line is distorted on the red part of the wing and vice versa. Again, the development over time of this parameter and a detailed period analysis can reveal, whether a connection exists between RV variations and activity.

Another possibility to monitor changes of spectral lines over time, is the calculation of the Ca IIR 8662 Å EW. For this, I calculated the EW of each spectrum of a target separately and examined the data for significant periods.

Helium

One of the strongest lines observable from ground at optical wavelengths is the Helium I line at 5876 Å. This has been found from the analysis of solar *flash spectra* of the Sun, i.e. a spectrum of the Sun observed during total eclipse (Bray & Loughhead, 1974). Analogous to Ca IIR, He I is a good tracer for infalling material via line core emission. To monitor changes over time, the EW of this line has been analyzed.

H $_{\alpha}$

As shown in Figure 2.6, the H $_{\alpha}$ core has its origin very high in the stellar chromosphere. In contrast, its line wings originate from much deeper layers. In case of hot conditions with a high density (e.g. during flares or in case of accretion), the line core can fill up or go into emission. Therefore, a H $_{\alpha}$ emission line is a good indicator for accretion. To analyze changes in the accretion process, I monitored the behavior of H $_{\alpha}$ using different criteria.

The first indicator used is the H $_{\alpha}$ EW analogous to the Ca IIR (@ 8662 Å) analysis. Furthermore, the line has been analyzed in terms of line distortions. For this, the asymmetry has been determined by analyzing the slope in each wavelength point of the line as has been explained for the Ca IIR emission core. A different way to describe the line asymmetry is the calculation of the statistical moments of the spectral line. For this, the wavelength of the balance point of the line λ_C is calculated by integrating the wavelength multiplied with the flux at each wavelength point and dividing by the integrated flux over the whole line. Afterwards the following statistical moments μ are calculated and monitored over time:

1. Line Variance μ_2

$$\mu_2 = \sum_i (\lambda_i - \lambda_C)^2 \quad (2.20)$$

2. Line Skewness μ_3

$$\mu_3 = \sum_i (\lambda_i - \lambda_C)^3 \quad (2.21)$$

3. Line Kurtosis μ_4

$$\mu_4 = \sum_i (\lambda_i - \lambda_C)^4 \quad (2.22)$$

Additionally, a spectroscopic index has been calculated following Reid et al. (1995). For this, Equation 2.23 (see below) has been used with the parameters $F_W=(6560-6266) \text{ \AA}$ and $F_{cont}=(6545-6555) \text{ \AA}$. The method of the determination of spectroscopic indices is explained below.

Temperature-sensitive lines VI and Fe I

If a cool spot is rotating along with the stellar surface, the average temperature over the stellar surface drops due to the much lower temperature of the stellar spot than that of the stellar surface itself, as soon as it comes into the line-of-sight. Depending on the spot size and the temperature ratio between spot and stellar surface, the impact on the stellar spectrum varies. In order to analyze the spectra for temperature changes over time, I followed Gray (1994) and Catalano et al. (2002) and calculated the line-depth ratio (LDR) of two spectral lines, which are VI (at 6268.87 \AA) and FeI (at 6270.23 \AA). The advantage of choosing this pair of lines is that they are close together so that the same setting of the continuum can be used. The depth of both lines increases with temperature, but the increasing depth is more rapid for low-excitation lines like VI as for FeI, so that temperature changes over time due to spots can be analyzed by monitoring the LDR of these two lines. The period analysis has been done once again using GLS (see Sec. 2.4.3).

Molecular bands

Since cool spots are usually at least a few hundred Kelvin cooler than the stellar photosphere, their spectrum is supposed to be similar to that of a cooler star. Therefore, features only visible in cooler stars should appear in the stellar spectrum when the spot rotates into the line-of-sight and disappear again as soon as the spot vanishes behind the star. In order to analyze this phenomenon, I calculated a variety of ‘‘spectroscopic indices’’ following Reid et al. (1995). Especially TiO features should become stronger as soon as a cool spot appears on the stellar surface, but also other molecular bands as CaOH and CaH. Therefore, the spectroscopic indices have been defined as flux ratio between the integrated flux over the molecular band F_W and pseudocontinuum flux F_{cont} - the mean flux in a sideband:

$$R_{\text{band}} = \frac{F_W}{F_{\text{cont}}} \quad (2.23)$$

The regions used for the different spectroscopic indices are listed in Table 2.3.

2.5.2 Analysis of the CCF

Most spectral lines contained in a spectrum taken with an instrument like FEROS have their origin in the stellar photosphere (Gray, 2008). By cross-correlating the target spectrum with a synthetic template matching the stellar spectral type, the cross-correlation function (CCF) represents the average line profile of the spectral lines in the spectral range used for the correlation. When many lines in an analyzed region are distorted due to e.g. cool spots on the stellar surface, the profile of the CCF will exhibit the same distortions.

Index	Band	cont [Å]	W [Å]
R_{TiO1}	TiO 1	6703-3708	6718-6723
R_{TiO2}	TiO 2	7043-7046	7058-7061
R_{TiO3}	TiO 3	7079-7084	7092-7097
R_{TiO4}	TiO 4	7115-7120	7130-7135
R_{TiO5}	TiO 5	7042-7046	7126-7135
R_{CaH2}	CaH 2	7042-7046	6814-6846
R_{CaH3}	CaH 3	7042-7046	6960-6990
R_{CaOH}	CaOH	6345-6354	6230-6240
$R_{\text{H}\alpha}$	H α	6545-6555	6560-6566

Table 2.3: Spectral ranges for the calculation of spectroscopic indices adopted from Reid et al. (1995).

Therefore, in addition to the analysis of single spectral lines and spectral features, the CCFs already available from the RV determination have also been used to characterize the stellar activity.

In order to analyze if a CCF is distorted, I followed the method described by Povich et al. (2001) and in the references therein. As illustrated in Fig. 2.8, the CCF is subdivided horizontally and the midpoints of the line segments are calculated. In the following, three different vertical regions have been defined in the CCF and a mean velocity has been calculated for each region: v_1 for $0.3 \leq \text{CCF} \leq 0.45$, v_2 for $0.45 \leq \text{CCF} \leq 0.6$ and v_3 for $0.6 \leq \text{CCF} \leq 0.9$. Three different quantities have been defined based on these three mean velocities:

1. The Bisector Velocity Span (BVS)

$$\text{BVS} = v_3 - v_1 \quad (2.24)$$

2. The Bisector Curvature (BC)

$$\text{BC} = (v_3 - v_2) - (v_2 - v_1) \quad (2.25)$$

3. The Bisector Velocity Displacement (BVD)

$$\text{BVD} = \frac{v_1 + v_2 + v_3}{3} - \lambda_c \quad (2.26)$$

with λ_c the observed central wavelength.

The development of these three parameters with time was monitored and the linear Pearson correlation-coefficient between BVS and RV was calculated in order to check if the observed RV variation might correlate with the spectral line distortion. Nevertheless, even in case of a clear correlation, the presence of a second body in the observed system cannot be excluded, because a scenario of an orbiting planet in a circumstellar disk inducing stellar activity (which occurs with the same period as the planet) by pushing surrounding material on the star is possible. Since the CCF represents an average spectral line, one can execute the same analysis methods as for individual spectral lines. Therefore, the CCF asymmetry and the statistical moments were calculated as well, Analogous to the calculation for H α .

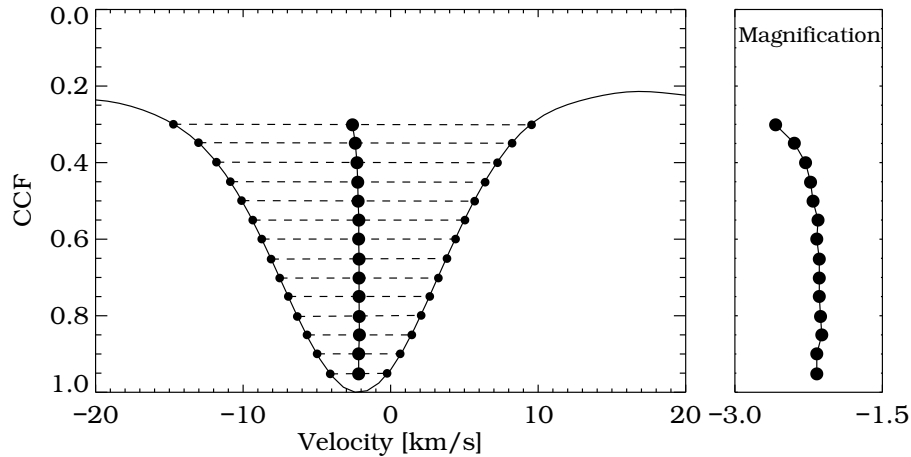


Figure 2.8: Schematic diagram of the characterization of the CCF distortion using the CCF bisector. (following Povich et al. (2001), illustration based on Gray (2008)).

Furthermore, Santos et al. (2010) have recently applied for K-dwarfs and Gomes da Silva et al. (2012) for M-dwarfs (both using HARPS), that the FWHM of the CCF is a good indicator for stellar activity. Therefore, this analysis has been used for FEROS data as well.

Different exoplanet surveys examine different stellar activity indicators. Santos et al. (2010) chose for their study the HARPS CCF parameters bisector inverse slope (BIS, analog to the BVS, Queloz et al., 2001) and CCF contrast and various line indicators as Ca II K & H, H_α and He I. Gomes da Silva et al. (2012) analyzed the same CCF parameters, but concentrated on the activity index using the Na I line (in contrary to the Ca II K activity index of this thesis). In general, most studies concentrate on the CCF profiles as shown by Boisse et al. (2011), who created a spot simulation software called *SOAP* (Boisse et al., 2012), which works similar to the spot program described in Sec. 5. Beneath the RV and photometric signals, *SOAP* simulates the variation of the spectral line shape while the spot is rotating in and out of view represented by the bisector velocity span (BVS). Since individual spectral lines provide information about activity in different stellar layers due to their different origin (see Fig. 2.6), I decided to include not only CCF parameters as BVS, BVD and BC but also single lines like He I and Ca II as well as comparative indicators as line-depth ratios and spectroscopic indices of molecular bands.

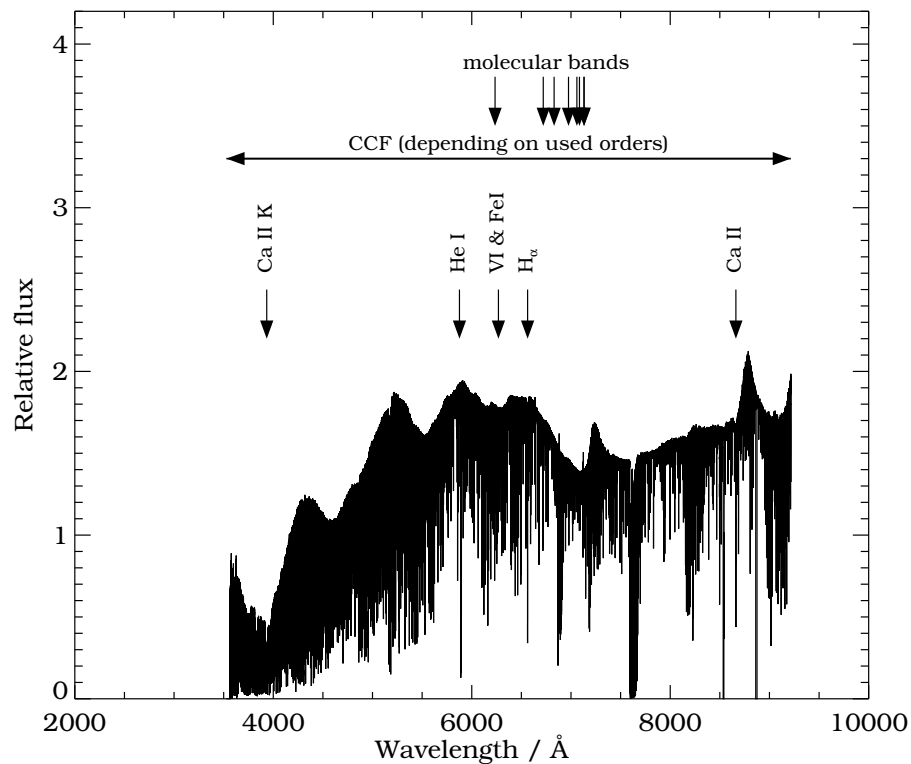


Figure 2.9: FEROS spectrum of the RV standard star HD 10700 with the positions of the used activity indicators overlotted.

(Spectral) Feature	origin	Indicator	wavelength [Å]
Ca II K	chromosphere	S_{FEROS} slope-analysis	3930-3938 3930-3938
Ca II	chromosphere	EW	8662
He I	chromosphere	EW	5876
H $_{\alpha}$	chromosphere	EW slope-analysis statistical moments spectroscopic index	6563 6563 6563 6560-6566
V I & Fe I	photosphere	LDR	6268-6271
Molecular bands	photosphere	spectroscopic indices	6230-7135
CCF	photosphere	BVS, BC, BVD FWHM slope-analysis statistical moments	used spectral orders used spectral orders used spectral orders used spectral orders

Table 2.4: Used stellar activity indicators for the characterization of chromospheric and photospheric activity

2.5.3 The effect of stellar activity on the measured RV

When a planet is orbiting its host star, the stellar spectral lines are Doppler shifted due to the stellar motion around the star-planet barycenter without changing their individual shapes.

In case of activity patterns on the stellar surface, i.e. cool spots, a Doppler shift of the spectral lines is induced as well, since the cool spot covers different longitudes of the stellar surface, and the center of light correspondingly moves. By blocking light of a red-shifted part of the surface, the stellar spectrum as detected on Earth is blue-shifted and vice versa. However, unlike a planet, inducing a Doppler-shift to the stellar light is not the only influence a spot has on a stellar spectrum. As already mentioned, the stellar rotation and other factors are responsible for the spectral line shape. If a spot appears on the stellar surface, the spectral lines can be distorted, which leads to a change in the effective RV. The impact of this effect depends on, where and how a spectral line forms.

Fig. 2.10 shows the impact of a cool stellar spot on an artificially created line and the resulting effective RV. The spot is 2000 K cooler than the limb-darkened stellar photosphere and rotates along with the stellar surface. Details on the simulation of cool spots on stars can be found in Section 5.

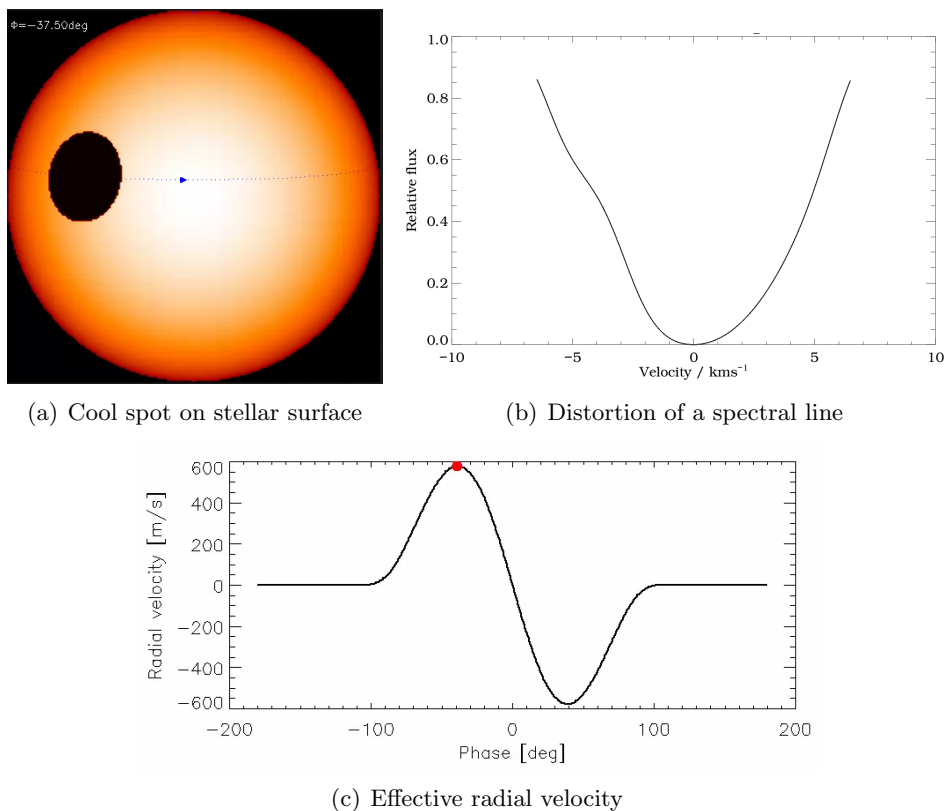


Figure 2.10: Effect of an cool stellar spot on an artificially created spectral line and the effective RV. Upper left panel: Illustration of cool spot on the limb-darkened stellar surface, upper right panel: distortions on a spectral line, lower panel: effective RV, produced by the cool stellar spot. The red dot indicates the effective RV for the upper scenario. The black line corresponds to the RV development with changing phase angle.

Chapter 3

The target sample

3.1 The target selection

An initial selection of suitable targets for the exoplanet search around young stars has been done by Weise (2010). He selected 206 stars from different publications on background of available Li I EW measurements for age estimation (selection criterium 1-100 Myr) and slow projected rotation ($v \sin i < 30$ km/s). He concluded, that small rotational velocities lead to a higher accuracy of the RV measurements, although the selection could eventually lead to a bias, preferring (close to) pole-on objects. Furthermore, the target selection was narrowed down by magnitude ($V \leq 11.5$ mag), spectral (F5 - M2) and system type (single stars or SB1), which was rated as important for a correct RV analysis. I identified 4 targets of the initial 206 stars overlapping with the ESPRI¹ target list. These have been analyzed in this thesis as targets of **Group A**. In case companions could be detected around these targets, they could be followed-up astrometrically with PRIMA after/within its commissioning run.

Out of these 206 stars, 100 stars have been observed with FEROS and/or HARPS on average about 6 times (1-66) by Weise (2010). He analyzed the spectra of these 100 targets and dropped 49 of them due to their high RV error and/or high activity signal. The remaining 51 targets were splitted into two groups. The first one consists of 26 targets all showing a clear RV variability. Two of them were published (HD 70573 and TW Hya; Setiawan et al., 2007, 2008), 12 could be excluded since the RV signal was revealed to be activity induced and 12 were investigated further. Out of these 12 targets, I selected a number of nine targets on background of magnitude and visibility from La Silla Observatory, Chile, which have been analyzed in this thesis as targets of **Group B**. They all had initially more than 5 FEROS data points.

The remaining 25 targets of the 51 stars showing a low RV error and low activity signal, didn't have enough data points (less than 5 initial FEROS data points) to characterize the RV variability. Out of these, 8 targets were selected on background of magnitude and visibility and have been analyzed as targets of **Group C**.

In order to optimize the planet search for these 21 targets, I observed them intensively between 2010 and 2013, taking at least two data points per observing night to estimate the short-term variability of these targets. For low-activity high-SNR stars, usually a number of about 21 data points is needed to derive a robust orbital solution. This corresponds to about 3 times the number of free fitting parameters for a Keplerian orbit. Since young stars show activity noise, at least the double amount of data points is needed, depending

¹ESPRI: Exoplanet Search with PRIMA (Launhardt et al., 2008; Sahlmann et al., 2013)

on the strength and the periodicity of the activity. The aim was to increase the number of data points for these targets significantly to reveal possible companions around the selected stars. Table 3.1 shows that the number of FEROS observations was increased such, that all but one target have more than 25 FEROS data points and therefore more than the criterium of 21 data points mentioned above. 15 targets fulfill as well the criterium of at least 42 data points.

Figure 3.1 shows the selection process of the targets and Table 3.1 shows their parameters known from the literature. From these, it is possible to plot the distribution of different parameters for the target selection. The histograms for spectral type, stellar age and $v \sin i$ on background of literature data (see Table 3.1) are shown in Figure 3.2.

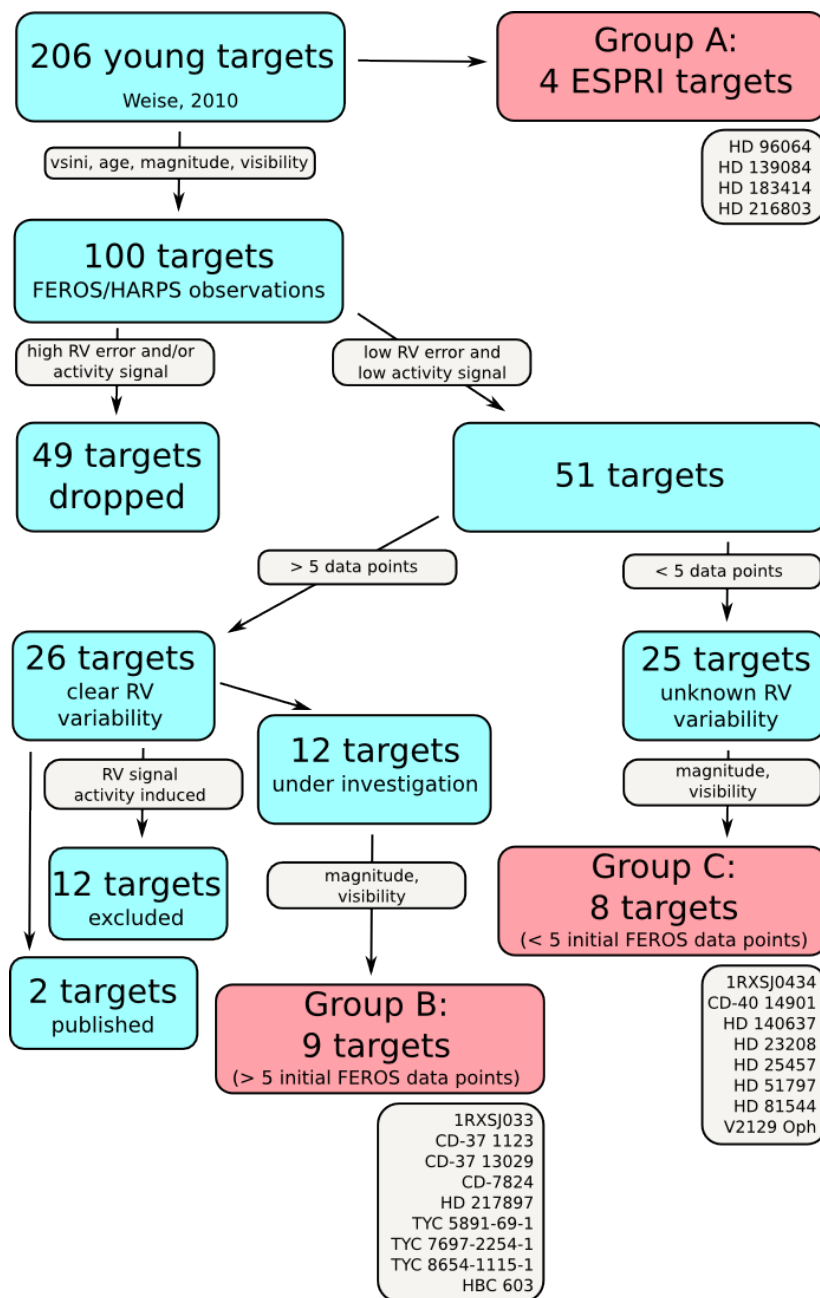


Figure 3.1: Target selection process

Target	RA	DEC	V-Mag	SpT	$v \sin i$ [km/s]	age [Myr]	#obs (W10) FEROS/HARPS	#obs (tw) FEROS/HARPS
Group A (ESPRI overlap targets):								
HD 96064	11 04 41.5	-04 13 16.0	7.6	G7V	6.1 ± 1.3	90 ± 10	... / ...	113 / 17
HD 139084	15 38 57.5	-57 42 27.3	8.0	G8V	18.2 ± 1.1	50 ± 15	... / ...	19 / 14
HD 183414	19 35 09.7	-69 58 32.1	7.9	G3V	9.6 ± 0.9	75 ± 15	... / ...	59 / 42
HD 216803	22 56 24.1	-31 33 56.0	6.5	K3V	4.5 ± 1.8	400 ± 50	... / ...	29 / 217
Group B (targets, with > 5 initial FEROS data points):								
1RXSJ033 ²	03 31 49.9	-63 31 53.6	10.9	K0V	18.1 ± 1.1	25 ± 15	13 / 7	60 / 7
CD-37 1123	03 00 46.9	-37 08 01.8	10.5	G9V	6.9 ± 1.2	30 ± 15	15 / 2	53 / 2
CD-37 13029	19 02 02.0	-37 07 43.5	10.5	G5	20.0 ± 2.0 (G05)	5 ± 2	6 / 0	65 / 0
CD-7824	00 42 20.3	-77 47 39.8	10.2	K3V	30.7 ± 2.3	15 ± 10	13 / 2	42 / 2
HD 217897	23 04 20.9	-34 24 52.4	9.7	K1	8.5 ± 1.2	30 ± 15	7 / 3	30 / 3
TYC 5891-69-1	04 32 43.5	-15 20 11.3	10.5	G4V	20.5 ± 1.3	10 ± 5	14 / 5	44 / 5
TYC 7697-2254-1	09 47 19.9	-40 03 09.8	10.9	K0V	9.0 ± 0.4	25 ± 10	18 / 12	36 / 12
TYC 8654-1115-1	12 39 38.0	57 31 40.7	10.1	G9V	19.4 ± 0.4	5 ± 3	6 / 5	57 / 5
HBC 603	15 51 47.0	-35 56 44.1	11.0	M0	5.9 ± 0.6	5 ± 3	7 / 7	42 / 7
Group C (targets, with < 5 initial FEROS data points):								
1RXSJ0434 ³	04 34 50.8	-35 47 21.3	10.9	K1V	11.3 ± 1.0	20 ± 15	2 / 0	45 / 0
CD-40 14901	22 46 33.5	-39 28 45.2	9.5	G5V	14.9 ± 1.0	75 ± 15	3 / 0	47 / 0
HD 140637	15 45 47.6	-30 20 55.7	9.4	K2V	9.8 ± 5.0 (G05)	5 ± 2	2 / 21	46 / 21
HD 23208	03 42 39.8	-20 32 43.6	9.2	G8V	9.3 ± 0.4	25 ± 10	3 / 3	43 / 3
HD 25457	04 02 36.8	00 16 08.1	5.4	F6V	18.5 ± 1.1	50 ± 15	3 / 18	38 / 18
HD 51797	06 56 23.5	-46 46 55.1	9.8	K0V	14.5 ± 0.5	30 ± 15	4 / 12	44 / 12
HD 81544	09 23 35.0	-61 11 35.9	10.0	K1V	12.9 ± 0.5	8 ± 3	3 / 4	40 / 4
V2129 Oph	16 27 40.3	-24 22 04.1	12.3	K5	13.5 ± 1.0	3 ± 2	4 / 25	37 / 25

Table 3.1: Parameters of selected targets. All parameters are taken from Weise (2010) and references therein. (G05): values taken from Glebocki & Gnacinski (2005), (W10): Weise (2010), (tw): this work, number of HARPS observations depends on the number of available reduced frames in the ESO archive. No number of observations for Group A is given in Weise (2010), since these objects were not included in the 100 target selected for observations.

² short for: 1RXS J033149.8-633155

³ short for: 1RXS J043451.0-354715

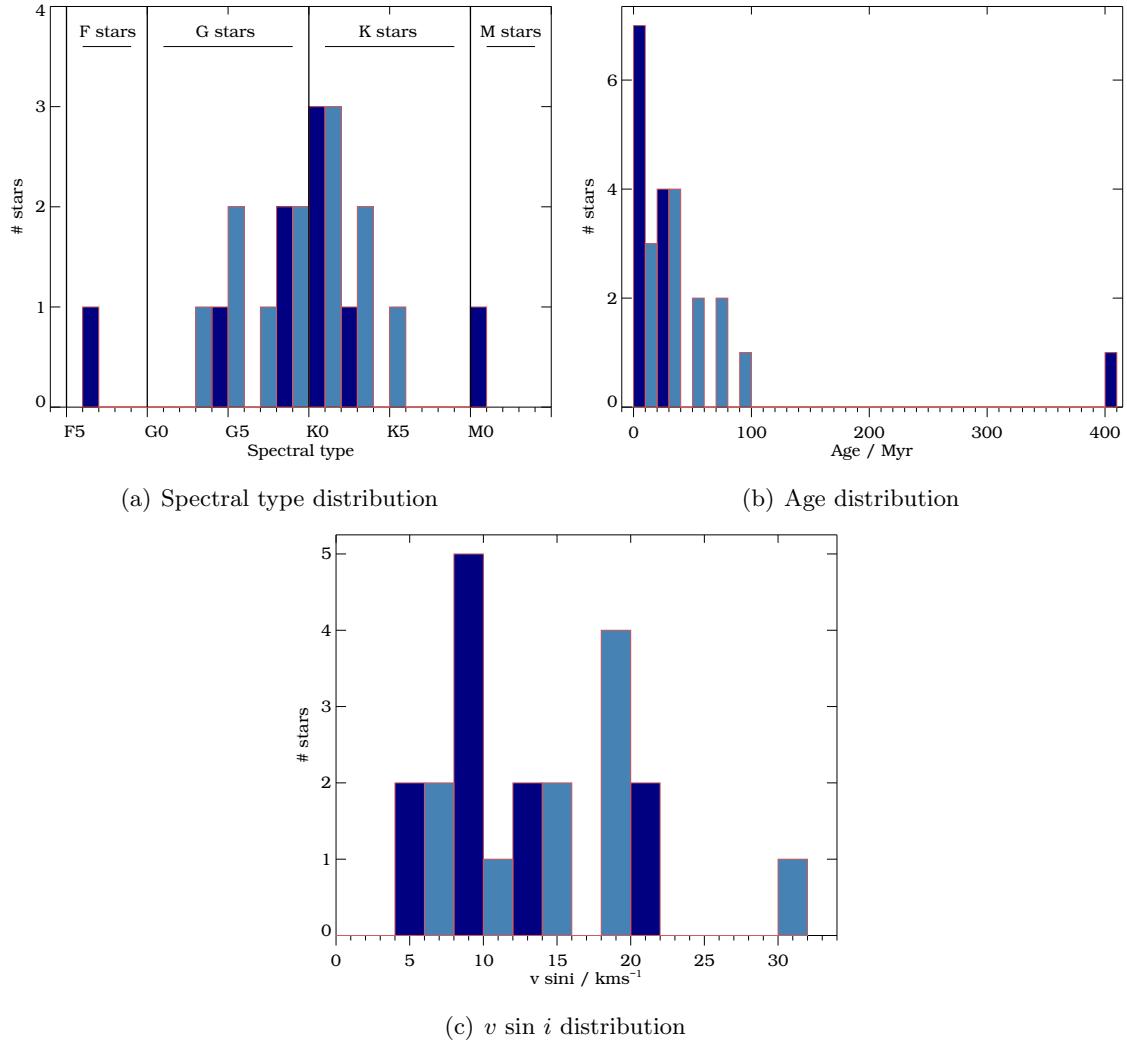


Figure 3.2: Distribution of (a) spectral type, (b) stellar age and (c) $v \sin i$ for the selected targets (c.f. Table 3.1).

3.1.1 Individual target description

In addition to the basic stellar parameters as listed in Table 3.1, most targets have been studied more intensively in terms of disk occurrence, system nature and other aspects. A short description of the known characteristics has been collected for the individual targets:

Group A (ESPRI overlap targets):

HD 96064 is a hierarchical triple stellar system at a distance of 26.3 pc from the Sun (van Leeuwen, 2008). The primary of the system, HD 96064 A, has a spectral type of G8V (Montes et al., 2001). The secondary component of the system is a binary of two M-type main-sequence stars. The separation between the component A and BC is ~ 11.4 arcsec, while the separation between the component B and C is ~ 0.3 arcsec. These translate to linear separations of 280 AU and 7.4 AU, respectively. HD 96064 BC orbits HD 96064 A with a period of ~ 3400 years, while the binary orbit of the B and C components has a period of ~ 23 years (Tokovinin, 2008). The

primary component A can be clearly distinguished from the components B and C with FEROS and HARPS. All observations have been made of HD 96064 A and the system name HD 96064 has been used from now on as shortcut for the primary component of the system HD 96064 A.

HD 139084 is a G8-dwarf located about 38.5 pc from the Sun (van Leeuwen, 2008) and has been studied extensively mainly in terms of chromospheric activity. Bopp & Hearnshaw (1983) list HD 139084 as one of the most chromospherically active stars visible from the southern hemisphere. Furthermore, they investigated that the H_α line is filled up. The spectral type has been reported to be K1III, but mean colors indicate that the star is too blue to be a K giant, why an early type companion is required (Cutispoto, 1993). Nevertheless, this companion was not found by RV measurements by Balona (1987). Zuckerman & Song (2004) identified HD 139084 as member of the β Pic moving group.

HD 183414 is a single star with spectral type G3V at a distance of about 23.4 pc (van Leeuwen, 2008). Henry et al. (1996) have identified HD 183414 as chromospherically active. HD 183414 was identified as field star (Soderblom et al., 1998).

HD 216803 , a K3-dwarf, is located about 7.6 pc away from the Sun (van Leeuwen, 2008) and could not yet be assigned to a known moving group. HD 216803 reveals a common proper motion with the A-star Formalhaut, which became famous for its dust-enshrouded planet detected by direct imaging (Kalas et al., 2005). Due to the common proper motion, HD 216803 is commonly assumed to be a companion of Formalhaut at the very large angular distance of $1^\circ.96$ (Fuhrmann & Chini, 2012).

Group B (targets, with > 5 initial FEROS data points):

1RXSJ033 , a K0-dwarf is located about 17.1 pc from the Sun (Perryman & ESA, 1997) and was identified to be chromospherically active by Bernhard et al. (2009). Weise (2010) classifies the RV shown by this target as most likely induced by stellar activity.

CD-37 1123 is a single star about 52.9 pc away from the Sun (Perryman & ESA, 1997) of spectral type G9V. Weise (2010) might have detected a planet around CD-37 1123, but more data was needed to verify the speculation.

CD-37 13029 , a G5-star, is a member of the extended R CrA association identified by Fernández et al. (2008). It is located about 6.4 pc away from the Sun (Perryman & ESA, 1997) and shows emission lines (Herbig & Bell, 1988). In the study for multiplicity of young stars in and around R Coronae Australis of Köhler et al. (2008), no companion to CD-37 13029 could be identified. Weise (2010) couldn't obtain enough data points to analyze the RV in terms of a companion in the system.

CD-7824 is a K3-dwarf star at a position 9.8 pc away from the Sun (Perryman & ESA, 1997). da Silva et al. (2009) identified CD-7824 as member of the Tucana-Horologium moving group. Using VLT/NACO, Chauvin et al. (2010) looked for substellar companions around nearby stars with separations larger than 10 AU, but could not identify a companion around CD-7824, though Weise (2010) claimed the detection of a brown dwarf companion of about $15 M_J$ at a distance of about 0.3 AU.

HD 217897 is a K1-star located about 78.7 pc away from the Sun. The star has so far not been part of any extensive observation campaigns.

TYC 5891-69-1 , a G4-dwarf at about 12.5 pc distance from the Sun. Silverstone et al. (2006) list TYC 5891-69-1 as field star and analyzed the target among 73 other young stars in terms of infrared excess using Spitzer/IRAC data, but no excess could be detected for TYC 5891-69-1. Weise (2010) claimed a significant detection of an about 4 M_J mass companion at 0.04 AU.

TYC 7697-2254-1 is a K0-dwarf. Its distance from the Sun was not correctly determined by the Hipparchos mission (Perryman & ESA, 1997) and the data was not part of the new reduction by van Leeuwen (2008). Reid (2003) identifies TYC 7697-2254-1 as potential member of the TW Hydrae moving group and list its distance with 56 pc. The results of Weise (2010) were ambiguous.

TYC 8654-1115-1 , a G9-dwarf, is located about 17.7 pc away from the Sun (Perryman & ESA, 1997). It is part of the Lower Centaurus Crux moving group (Hoogerwerf, 2000). The small number of available data points didn't allow a conclusion about the origin of the RV variation in Weise (2010).

HBC 603 is an M0-star and part of the Lupus I starforming region. It has been identified in the study by Ghez et al. (1997) as multiple system, revealing a companion at an angular separation of about 1.8 arcsec, which is so red that it is detectible at 2.2 μm, but missed at 0.9 μm. Weise (2010) detected a small positive trend of the BVS with RV, which he assigns to effects of this companion.

Group C (targets, with < 5 initial FEROS data points):

1RXSJ0434 is a K1-dwarf and part of the Columba moving group (Messina et al., 2010). Messina et al. (2011) identified a period of 2.29 ± 0.01 d by applying a Lomb-Scargle-periodogram to the SuperWASP data. They interpret this period as rotational period of the star, revealed by recurring surface patterns caused by stellar activity.

CD-40 14901 is a G5-dwarf located about 125 pc away from the Sun (Perryman & ESA, 1997).

HD 140637 , a K2V-star located at 40.4 pc distance from the star (van Leeuwen, 2008), is a member of the Upper Centaurus Lupus moving group (Song et al., 2012). Brandner et al. (1996) detected a companion with a separation of 0.67 ± 0.03 arcsec from HD 140637 with a brightness difference of primary (HD 140637) and secondary of more than 2 at the observing wavelength of 1 μm.

HD 23208 is a G8-dwarf at a distance of 50.3 pc from the Sun (van Leeuwen, 2008). HD 23208 was identified as possible member of the Octans moving group (Viana Almeida et al., 2009).

HD 25457 , a F6V star at a distance of 18.3 pc (van Leeuwen, 2008), is a member of the AB Dor moving group (Zuckerman & Song, 2004). Several studies tried to find companions around HD 25457 (Abt & Levy, 1976; Duquennoy et al., 1991) without success.

HD 51797 is a member of the Columba moving group (Messina et al., 2010) with a spectral type of K0V.

HD 81544 has a spectral type of K1V and is located as a member of the Carina moving group (Messina et al., 2010) at about 88 pc distance from the Sun.

V2129 Oph belongs to the Ophiuchus molecular cloud and has a spectral type of K5. Emission lines in the spectra have been revealed already in 1949 by Struve & Rudkjøbing as well as strong H and Ca II lines. Periodic variations ascribed to starspots have been analyzed by Bouvier et al. (1986), showing a period of about 6.3 d. Weaver (1987) calculated the stellar radius $R \sim 3.6 R_{\odot}$ and the inclination $i \sim 33.5^{\circ}$. Basri & Batalha (1990) calculated a veiling near H_{α} of $V = 0.0 \pm 0.1$. Ghez et al. (1993) identified a companion around V2129 Oph with a separation of 0.59 arcsec. The temperatures and masses of the two components were determined by as $T_1 = 4400$ K (what matches the spectral type K5) and $T_2 = 3230$ K and $M_1 = 1.3 M_{\odot}$ and $M_2 = 0.3 M_{\odot}$, respectively. Weise (2010) characterizes the mass accretion rate of V2129 Oph as about $1.2 M_{\odot}/\text{yr}$.

3.2 Characterization of the sample

3.2.1 Stellar parameters

As explained in Sec. 2.1, the determination of stellar parameters as T_{eff} , $\log g$, $[M/H]$ and $v \sin i$ is important for different purposes. While already determined spectral types by other research groups can be verified, a proper determination of these parameters can provide a good age estimation when combined with isochrones (see Sec. 2.3). Furthermore, a synthetic spectrum can be produced using these parameters, which is necessary e.g. for the RV analysis. Following the methods explained in Sec. 2.1, I determined T_{eff} , $\log g$ and $[M/H]$ using **SME**. Additionally, **SME** can provide estimations for $v \sin i$ as well as for micro- (v_{mic}) and macroturbulence (v_{mac}). In order to validate the $v \sin i$ -estimations of **SME**, I used the independent $v \sin i$ -determination following Reiners et al. (2012) and references therein. Therefore, I use the already available spectral type estimation of other research groups. The results for the determination of the stellar parameters are listed in Table A.1.

3.2.2 Age

As explained in Section 2.3, the stellar age can be estimated using different methods. First, I used the stellar parameters determined with **SME** and created YY-isochrones on background of the calculated $[M/H]$. Doing so, the alpha enhancement has been kept to solar. By overplotting the T_{eff} - and $\log g$ -values, at least the determination of an upper limit was possible for most of the targets.

Furthermore, the stellar age was estimated by memberships of different young moving groups. Different literature was used as listed in Table B.1.

Additionally, the Li I EW was used to derive the stellar age. As already mentioned in Sec. 2.3, the Li I EW is under debate as age indicator due to the unknown accretion history in the early stages of the evolution of the target (Baraffe & Chabrier, 2010). Nevertheless, the Li I EW has been used, since it is still used as a common age indicator. As described in Section 2.3, the Li I EW has been calculated by fitting the spectral line with a Lorentz profile to exclude the contamination with an Fe I line. Afterwards, the veiling V was calculated using different methods explained above (results listed in Table B.2) and the Li I EW accordingly corrected. By using the correlation of Li I EW and age from Zuckerman & Song (2004), an estimation of the stellar age was possible (Fig. B.6).

The activity index S_{FEROS} was used as an additional age indicator using the relations by Mamajek & Hillenbrand (2008) and Noyes et al. (1984a). As explained above, the intensity of the Ca K emission with respect to the spectral line wings was determined for each target and an estimation of the stellar age was derived.

Since the stellar rotation slows down with age (Sec. 2.3), one can also estimate the gyrochronological age on background of the stellar rotation period. Although this method is most likely not usable for young targets due to their large angular momentum scatter (see above), the ages have been calculated with this method for comparison purposes. The needed stellar rotation period is in general determined by using rotational modulation meaning period signals induced by stellar surface features. By monitoring the star photometrically, stellar surface features cause a period change of the stellar brightness and a rotation period can be estimated. Since no additional photometric data has been taken within this thesis, the determination of the rotation period depends on previous studies. One opportunity is the use of HIPPARCOS⁴ photometric data. Unfortunately, the sampling of these data is usually not ideal to monitor brightness changes on the timescales of days with high precision. Another possibility is the large data base of SuperWASP⁵ photometric data. In this data base, photometric time series have been successfully identified for 11 targets in total. Since each individual data set consists of several thousand data points, with hundreds taken at the same day, the light curves have been binned to one day. The binned light curves have been analyzed with GLS and to identify rotational periods. The obtained values and derived ages by following Barnes (2007) can be found in Table B.3.

All derived ages including literature values from Weise (2010) and references therein are summarized in Table 3.2.

3.2.3 Disk

Besides the determination of stellar parameters as mentioned above, the characterization of the circumstellar environment is important as well. As discussed in Section 1, the existence of circumstellar disks during the formation of a star by gravitational collapse is unavoidable to conserve the angular momentum within the system and prevent the protostar from disruption (Williams & Cieza, 2011). In the first stages of stellar evolution, the protostar accretes material from the disk. After some time, the rate of accretion decreases and the remnants of the disk stay in the circumstellar environment. These remnants are the birthplaces of planets.

Since most targets of this thesis are most likely younger than 50 Myr, it is reasonable to look for evidence of disk remnants in the circumstellar environment of the stars. Since disk remnants in the near vicinity of the star are heated up due to the irradiation by the stellar light, they leave a fingerprint in the spectral energy distributions (SED, the emitted energy per wavelength) of the stars as excess at infrared wavelengths. In case of a disk absence, the SED of the star is dominated by radiation from its photosphere and can be satisfyingly fitted with a blackbody curve. If a disk is present in the circumstellar environment, the detected flux from the star follows the blackbody curve in optical wavelength and exceeds it in the infrared. This phenomenon is called “infrared excess” and is a clear evidence of a disk (or remnants of it) around a star.

In order to look for infrared excess, I searched the literature for magnitudes and fluxes from different surveys. I used J , H and K magnitudes from the 2MASS⁶-catalog, magnitudes at $3.4\ \mu\text{m}$, $4.6\ \mu\text{m}$, $12\ \mu\text{m}$ and $22\ \mu\text{m}$ from the WISE⁷ and fluxes at $12\ \mu\text{m}$, $25\ \mu\text{m}$, $60\ \mu\text{m}$

⁴<http://www.rssd.esa.int/index.php?project=HIPPARCOS>

⁵<http://www.superwasp.org/>

⁶The **Two Micron All Sky Survey**,
<http://irsa.ipac.caltech.edu/Missions/2mass.html>, Cutri et al. (2003)

⁷**Wide-field Infrared Survey Explorer**,
http://www.nasa.gov/mission_pages/WISE/main/index.html, Cutri (2012)

Target	t_{iso} [Myr]	t_{MG} [Myr]	t_{LiEW} [Myr]	t_{SFEROS} [Myr]	t_{gyro} [Myr]	t_{W} [Myr]
Group A (ESPRI overlap targets):						
HD 96064	> 20	—	< 230	177 ± 13	—	90 ± 10
HD 139084	< 5	12^{+8}_{-4}	30-80	38 ± 4	—	50 ± 15
HD 183414	< 20	—	< 120	132 ± 7	—	75 ± 15
HD 216803	< 5	—	< 300	SpT	4 ± 1	400 ± 50
Group B (targets, with > 5 initial FEROS data points):						
1RXSJ033	< 20	—	< 120	26 ± 5	—	25 ± 15
CD-37 1123	< 35	—	< 120	45 ± 4	—	30 ± 15
CD-37 13029	< 5	~ 13	< 30	53 ± 12	27 ± 2	5 ± 2
CD-7824	< 5	~ 30	5-30	SpT	—	15 ± 10
HD 217897	met	—	~ 300	fail*	—	30 ± 15
TYC 5891-69-1	< 35	—	5-30	31 ± 5	—	10 ± 5
TYC 7697-2254-1	met	~ 8	30-80	12 ± 3	96 ± 6	25 ± 10
TYC 8654-1115-1	< 10	11-12	< 30	17 ± 3	—	5 ± 3
HBC 603	unclear	1.5-4.0	< 30	SpT	—	5 ± 3
Group C (targets, with < 5 initial FEROS data points):						
1RXSJ0434	< 35	~ 30	< 30	48 ± 23	53 ± 4	20 ± 15
CD-40 14901	< 35	—	~ 80	42 ± 5	63 ± 4	75 ± 15
HD 140637	< 5	~ 10	out	6 ± 14	22 ± 2	5 ± 2
HD 23208	< 35	~ 20	~ 30	23 ± 4	—	25 ± 10
HD 25457	unclear	~ 50	< 150	293 ± 18	—	50 ± 15
HD 51797	< 10	~ 30	30-80	4 ± 1	—	30 ± 15
HD 81544	< 20	~ 30	30-80	40 ± 8	—	8 ± 3
V2129 Oph	met	~ 2	out	SpT	—	3 ± 2

Table 3.2: Determined ages for selected targets.

t_{iso} : age estimation by using the determined stellar parameters and YY-isochrones (Yi et al., 2001), unclear: log g -error too large to determine age, met: $[M/H]$ exceed +0.2, which YY-isochrones can not handle.,

t_{MG} : stellar age estimated by the membership of young moving groups, no value is given in case no membership has been identified yet or the target has been classified as field star (memberships are listed in Table B.1),

t_{LiEW} : age determined by using veiling corrected Li I EW and the age-EW-SpT dependency by Zuckerman & Song (2004) (Table B.2, Figure B.6),

t_{SFEROS} : value determined by using the calculations of the FEROS S-index (see Sec. 4.3), SpT: analysis not possible, since method only varified for targets with spectral types between F6 and K2 (Mamajek & Hillenbrand, 2008), * analysis failed due to ambiguous shape of Ca II K line,

t_{gyro} : determined gyrochronological age on basis of SuperWASP photometric data, no value is given for stars with no available photometry,

t_{W} : age given by Weise (2010) and references therein for comparison.

and $100\ \mu\text{m}$ from the Infrared Astronomical Satellite (IRAS, Neugebauer et al., 1984). The magnitudes and fluxes for each target are listed in Table C.1.

To reveal evidence of a disk, I used the SED fitting tool by Robitaille et al. (2007) using a web interface⁸. This tool fits several thousand stellar photosphere models to the data and derives the best fit using the χ^2 . The individual fits are shown in the appendix (Figures C.1-C.5). For most of the targets, no evidence of a disk is visible in the SEDs, since the best fitting photospheric model matches the data almost perfectly. Two exceptions are HBC 603 and V2129 Oph. Their SED is not satisfyingly fitted with a simple stellar SED model. Therefore, their data has been fitted with a combination of a stellar SED model and a disk model (Fig. 3.3). These results show, that clear evidence for a disk exist in both stars. The best fit for the SED of HBC 603 assumes a stellar age of 3.36 Myr, a system inclination of 49.5° and a mass accretion rate of $5.39 \cdot 10^{-12} M_\odot/\text{yr}$. This result confirms Carpenter et al. (2009), who detected an accretion disk in this system. V2129 Oph is fitted best with a model of 1.78 Myr age, a system inclination of 81.4° and a mass accretion rate of $9.60 \cdot 10^{-9} M_\odot/\text{yr}$. The nature of an accretion disk was detected by Carpenter et al. (2009) as well and is confirmed here. However, since both fits have a significantly too high stellar mass ($2.09 M_\odot$ for the M0-dwarf HBC 603 and $2.94 M_\odot$ for the K5-dwarf V2129 Oph) for the spectral types, the accretion rates might not be correct.

Another exception is CD-37 13029. The plot shows that the WISE $22\ \mu\text{m}$ might suggest a disk inside the system. However, this data point is flagged as potentially induced by optical ghosting, which is confirmed by a direct look on the WISE images in the WISE archive⁹ (Fig. 3.4). Therefore, I conclude that the data does not show any evidence of a disk in the system.

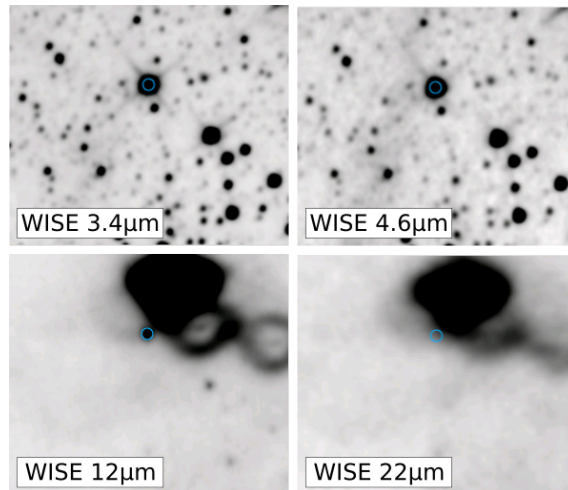


Figure 3.4: Four-band WISE images for CD-37 13029. The WISE $12\ \mu\text{m}$ and the $22\ \mu\text{m}$ data show clear evidence of optical ghosting.

⁸<http://caravan.astro.wisc.edu/protostars/sedfitter.php>

⁹<http://irsa.ipac.caltech.edu/applications/wise/>

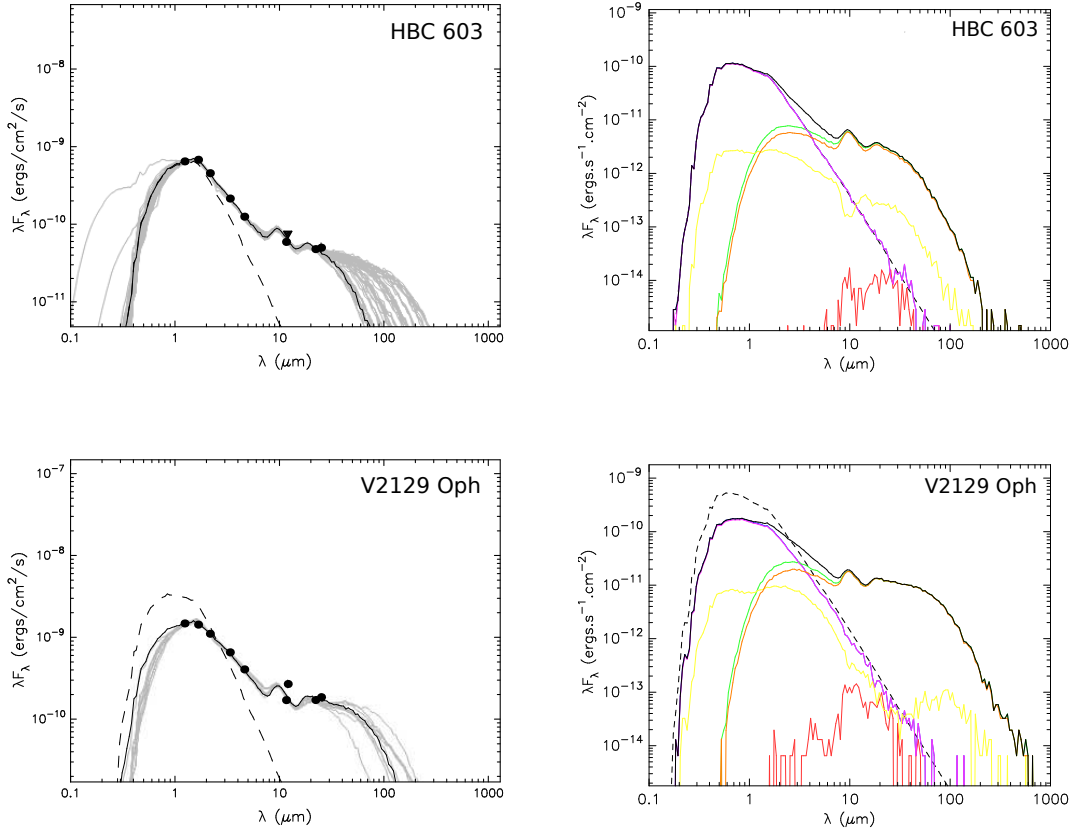


Figure 3.3: SED fits for HBC 603 (upper panels) and V2129 Oph (lower panels) including a best fitting disk model. Left panels: The filled circles show the input fluxes from 2MASS, WISE and IRAS, respectively. The black line shows the best fit, while gray lines show subsequent good fits. The dashed line shows the stellar photosphere corresponding to the central source of the best fitting model, as it would look in the absence of circumstellar dust (but including interstellar extinction). Right panels: composition parts of the final black disk model. Black: total flux, purple: stellar flux, green: disk flux, yellow: scattered flux, orange: thermal flux, red: envelope flux.

Chapter 4

RV and activity signals of the sample

4.1 Observations and available data

As already described in Section 3.1, the number of available FEROS data points per target has been increased significantly. Since no additional HARPS observations were carried out, some targets still lack these kind of observations. In order to find extrasolar planets around young stars, two different observing strategies have to be combined: at first, one needs a long time span of observations to confirm the long-term stability of the orbit solution of the claimed companion and furthermore, one needs at least one period with short-cadence observations (≥ 2 data points per night) to estimate the short-term variability due to stellar surface features like cool spots.

The amount of data points per target for both the FEROS and the HARPS instrument are listed with the overall time span of the observations in Table 4.1. The time span often contains longer gaps, where the target has not been observed. This is most often the case for targets with HARPS observation taken by other research groups within previous studies like HD 139084, where the first FEROS observations were executed almost one year after the last HARPS observations done by Eike Günther in the framework of his study of Hot Jupiters around young stars.

Within this chapter, the results of the RV analysis are presented. Furthermore, the careful analysis of several stellar activity indicators as listed above, is shown and the connection of both results is discussed.

4.2 Radial velocity analysis and results

As shown in Table 4.1 it is necessary to distinguish between 2 different types of data sets during the RV determination: 3 targets only have FEROS measurements (CD-37 13029, 1RXSJ0434 and CD-40 14901), while the remaining 18 do have HARPS data points as well. While the periodicity of the RV measurements for the 3 “FEROS-only-targets” can be analyzed using directly the program GLS as explained above, the RV analysis of the 18 “FEROS & HARPS-targets” needs an additional analysis step to compensate for the instrumental offset between FEROS and HARPS measurements. This is done with the IDL program *RVlin.pro* (see. Sec. 2.4.3).

Once the offset is calculated, the RV measurements of one instrument (here HARPS) can be corrected for it and be brought to the same level as the FEROS measurements. After-

Target	# FEROS observations	# HARPS observations	overall timespan of observations [yrs]
Group A (ESPRI overlap targets):			
HD 96064	113	17	8.1
HD 139084	19	14	7.3
HD 183414	59	42	7.2
HD 216803	29	217	8.2
Group B (targets, with > 5 initial FEROS data points):			
1RXSJ033	60	7	4.2
CD-37 1123	53	2	4.2
CD-37 13029	65	0	4.2
CD-7824	42	2	3.2
HD 217897	30	3	4.0
TYC 5891-69-1	44	5	4.2
TYC 7697-2254-1	36	12	4.0
TYC 8654-1115-1	57	5	3.3
HBC 603	42	7	4.3
Group C (targets, with < 5 initial FEROS data points):			
1RXSJ0434	45	0	4.0
CD-40 14901	47	0	4.0
HD 140637	46	21	7.4
HD 23208	43	3	4.0
HD 25457	38	18	7.4
HD 51797	44	12	4.0
HD 81544	40	4	5.3
V2129 Oph	37	25	4.2

Table 4.1: Number of observations with FEROS and HARPS and the overall timespan of the observations between the first data point and the last one.

wards, the GLS-periodograms can be calculated searching for significant periods indicating a stable signal caused by a companion and/or by stellar surface patterns over the whole observing time span. The period search was limited to periods ≤ 1000 d, due to the small timespan of observations for most targets. The periodograms including the corresponding window functions are shown in Sec. D for each target. One can notice from these plots that three different types of targets exist: 12 targets show no significant RV period at all (HD 183414, HD 216803, 1RXSJ033, CD-7824, TYC 5891-69-1, HBC 603, HD 23208, HD 25457, HD 51797, HD 81544, V2129 Oph), 6 targets exhibit one or more significant periods coinciding with window function peaks (HD 96064, HD 139084, CD-37 1123, HD 217897, 1RXSJ0434, CD-40 14901) and 3 targets show one or more significant periods with no corresponding window function peak (CD-37 13029, TYC 8654-1115-1, HD 140637). Table 4.2 lists the photometric periods (see Sec. 3.2.2) as well as the occurrence of significant periodic RV signals for the individual targets. Below, I will discuss the three groups of results.

Target	HARPS?	Phot. period [d]	RV period [d]	FAP
Group A (ESPRI overlap targets):				
HD 96064	✓	—	340.12 ± 0.01	$8.9 \cdot 10^{-7}$
HD 139084	✓	—	571.62 ± 5.37 65.59 ± 0.11 461.12 ± 5.07	$5.2 \cdot 10^{-9}$ $5.5 \cdot 10^{-6}$ $2.8 \cdot 10^{-5}$
HD 183414	✓	—	—	—
HD 216803	✓	1.29 ± 0.01 10.30^\dagger	—*	—*
Group B (targets, with > 5 initial FEROS data points):				
1RXSJ033	✓	—	—	—
CD-37 1123	✓	—	370.04 ± 0.02 182.21 ± 0.04	$1.3 \cdot 10^{-5}$ $1.2 \cdot 10^{-5}$
CD-37 13029	—	2.80 ± 0.01	2.83 ± 0.01	$1.3 \cdot 10^{-7}$
CD-7824	✓	—	—	—
HD 217897	✓	—	551.92 ± 5.15 45.16 ± 0.05 49.88 ± 0.08 398.82 ± 4.64	$2.0 \cdot 10^{-11}$ $1.1 \cdot 10^{-8}$ $8.6 \cdot 10^{-7}$ $8.5 \cdot 10^{-6}$
TYC 5891-69-1	✓	—	—	—
TYC 7697-2254-1	✓	4.00 ± 0.01	—	—
TYC 8654-1115-1	✓	—	2.43 ± 0.01	$1.5 \cdot 10^{-11}$
HBC 603	✓	—	—	—
Group C (targets, with < 5 initial FEROS data points):				
1RXSJ0434	—	2.00 ± 0.01	2.29 ± 0.01 1.77 ± 0.01	$4.6 \cdot 10^{-9}$ $6.1 \cdot 10^{-6}$
CD-40 14901	—	3.22 ± 0.01	46.83 ± 0.16 42.60 ± 0.09 564.73 ± 11.39	$1.9 \cdot 10^{-6}$ $4.0 \cdot 10^{-5}$ $8.2 \cdot 10^{-4}$
HD 140637	✓	2.75 ± 0.01	1.56 ± 0.01 2.76 ± 0.01	$2.3 \cdot 10^{-6}$ $4.5 \cdot 10^{-3}$
HD 23208	✓	—	—	—
HD 25457	✓	3.13^\dagger	—	—
HD 51797	✓	—	—	—
HD 81544	✓	—	—	—
V2129 Oph	✓	—	—	—

Table 4.2: RV periods detected with GLS with corresponding FAPs. The column “HARPS?” indicates if HARPS measurements are available, which decides if a correction for an instrumental offset between FEROS and HARPS measurements has to be executed. If not indicated otherwise, the photometric periods correspond to those obtained in the framework of the determination of the gyrochronological age (see Sec. 2.3). If no RV period is given, no significant period that is stable over the whole observation timespan could be identified. The periodograms for each target are shown in the appendix (Sec. B.4).

†: Wright et al. (2011)

*: HARPS data neglected, since 210 of 217 available data points were taken within 4 different days between 2004-9-27 and 10-02.

Targets showing no significant periods

The periodogram analysis with GLS shows, that 12 of 21 targets don't show a significant RV period, which is stable over the whole time span of the observations. This does not necessarily mean, that the targets don't possess any (with the used instruments and methods) detectable companion, but that the signal might be hidden. Involved stellar activity with a large amplitude and strong timely variations might distort the analyzed spectral lines such, that the Doppler-shift of the lines caused by a companion in the system are covered. For two of these targets, the determination of a rotational period was possible: Wright et al. (2011) detected a rotational period by the analysis of photometric data for HD 216803 and HD 25457 and an additional rotation period for HD 216803 could be determined by the analysis of SuperWASP data within this thesis. The fact that the identification of a significant RV period was not possible, shows that the stellar surface features that allow the determination of a rotational period by photometry are not stable over long time scales.

Targets showing significant periods, which are connected to window function peaks

By taking a closer look at the RV periodograms (Sec. D), it clearly visible that the window function (red) shows large peaks at the same periods, the periodogram (black) shows a significant peak. As explained in Sec. 2.4.3, the window function indicates if certain periods might be caused purely by the sampling function. In order to check if the significant periods are really caused by the sampling, I executed a simple test for these targets: I selected randomly about 20% of the data points from the sample and neglected them while calculating the generalised Lomb-scargle periodogram with GLS. Then, I noted the power and position for the initially as significant identified periods and repeated the calculation neglecting another set of randomly chosen data points. By repeating this 20 times, the development of the individual peaks can be monitored and in case of strong variations and the drop below the significance level, the period can be rejected, since it is being induced by the sampling function. Fig. 4.1 shows the initial RV periodogram, the test and the GLS periodogram for the RV residua for CD-37 1123 as representative example. The plots for the remaining targets are shown in Sec. D. Fig. 4.1 shows that the development over different iteration steps of both initially significant periods leads to a scatter in period space as well as to a large variation of the GLS power. Doing so, the scargle signal drops most often beneath the significance level of a FAP of 0.1%. This confirms, that the periods heavily rely on the sampling. The next step for CD-37 1123 is to look at the residua. By subtracting the signal with the period, which is apparently induced by the measurement sampling and had the highest significance in the initial calculation (in case of CD-37-1123 the period of about 370 d), one can make a statement about the other period: in case their signal vanishes, it is either also directly induced by the measurement sampling or it is an alias of the first. In case the period persists and potentially even strengthens, it was initially covered by the false signal and could be caused by physical processes. The bottom panel of Fig. 4.1 shows the GLS periodogram of the residua. The plot shows no period with $FAP < 0.1\%$, which indicates that no other long-term stable significant signal was covered by the sampling-induced signal. Therefore, the second initial period does not have most likely a physical origin, but is either induced by measurement sampling as well or an alias of the about 370 d period. Since ~ 370 d is about two times ~ 182 d, the latter explanation sounds more reasonable.

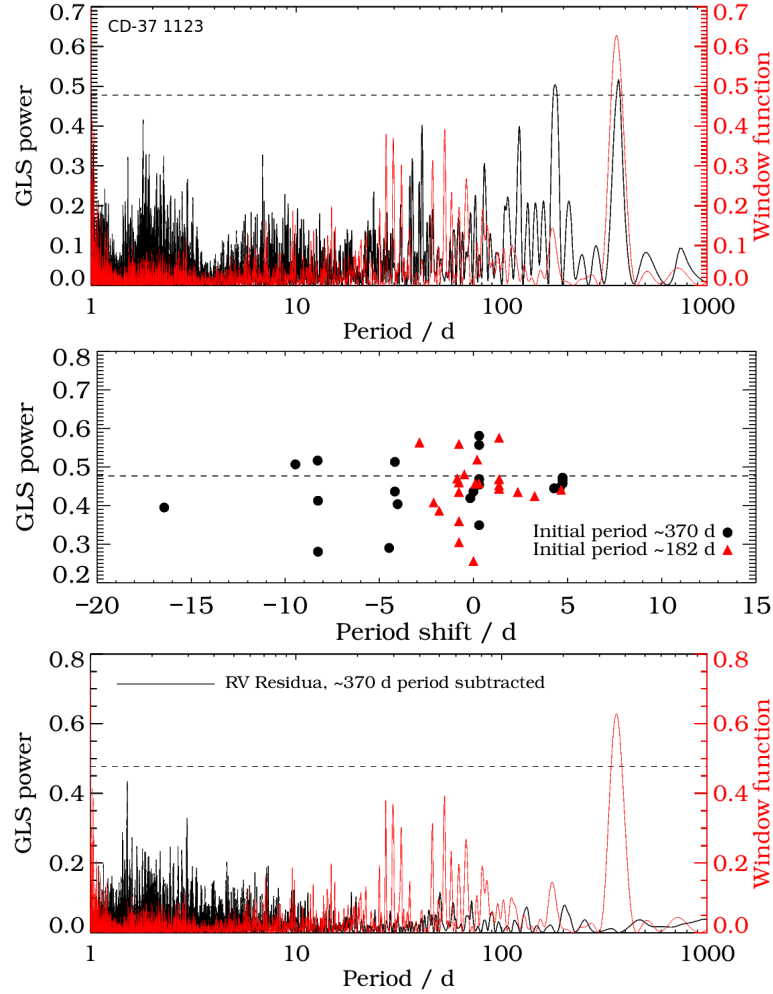


Figure 4.1: Upper panel: GLS periodogram of RV measurements for CD-37 1123 (black) with window function (red), the dashed line indicates the significance FAP level of 0.1%, middle panel: sampling test for CD-37 1123, the different colors indicate different initially detected periods, lower panel: GLS periodogram of RV residua (black) after the subtraction of the strongest period (~ 370 d) with window function (red).

HD 96064 had initially only one significant period. The test shows, that the period scatters in comparison to CD-37 1123 by a less amount in period space. However, the GLS power drops very often below the significance level, giving a hint, that the period is also most likely sampling-induced. After subtracting the ~ 340 d period, no period with FAP $< 0.1\%$ can be identified anymore. This leads to the same conclusion as for CD-37 1123 that no other long-term stable significant signal was covered by the sampling-induced signal. The same conclusion is valid for HD 139084 and 1RXSJ0434. Within the test, the initially detected periods strongly scatter in period and power space. After subtracting the strongest signal, no significant period can be found anymore. In contrast, the subtraction of the most likely sampling-induced periods from the data sets of HD 217897 and CD-40 14901 ($P=550$ d and 560 d, respectively) revealed other significant periods, which have been hidden before. However, Fig. D.10 and Fig. D.12 show that these periods have their origin most likely again in the measurement sampling indicated by the window function in red.

Targets showing one or more significant period with no corresponding window function peak

Three targets showed at least one significant RV period in the GLS periodogram, while the window function of the data set did not reveal large peaks at the same positions. The period analysis with GLS of the RV data of CD-37 13029 revealed a significant period of 2.83 ± 0.01 d with a FAP of $1.3 \cdot 10^{-7}$. By comparing the determined photometric period from the analysis of the SuperWASP data (2.80 ± 0.01 d, see Sec. 3.2.2) with this period, the probability is very high that they both have the same origin. Since periodic changes of photometric data can indicate spot patterns on the stellar surface, rotating in and out of view, the match of both periods indicates rotational modulation as the most likely origin of the ~ 2.8 d signal. However, since the signal of a spot rotating along with the stellar surface might cover another significant period caused by a companion in the system, I subtracted the 2.83 d period from the data and recalculated the GLS periodogram with the residua. The RV measurements fitted with GLS are shown in Fig. 4.3 and the fitting parameters are listed in Table 4.3.

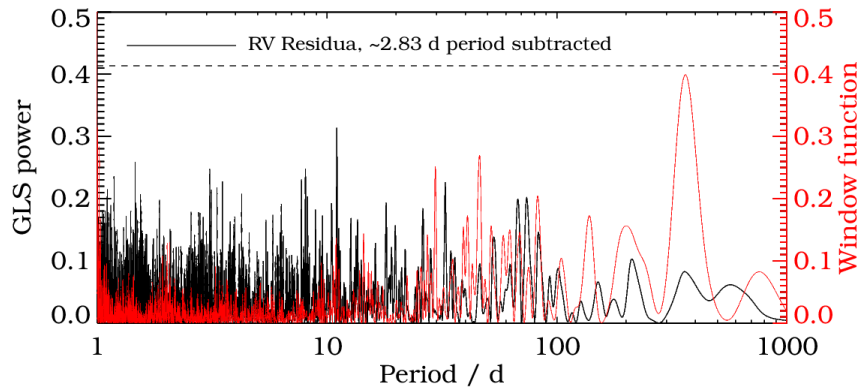


Figure 4.2: Periodogram of RV residua for CD-37 13029 after the significant 2.83 d period was subtracted from the RV measurements. The dashed line indicates the FAP level of 0.1 %.

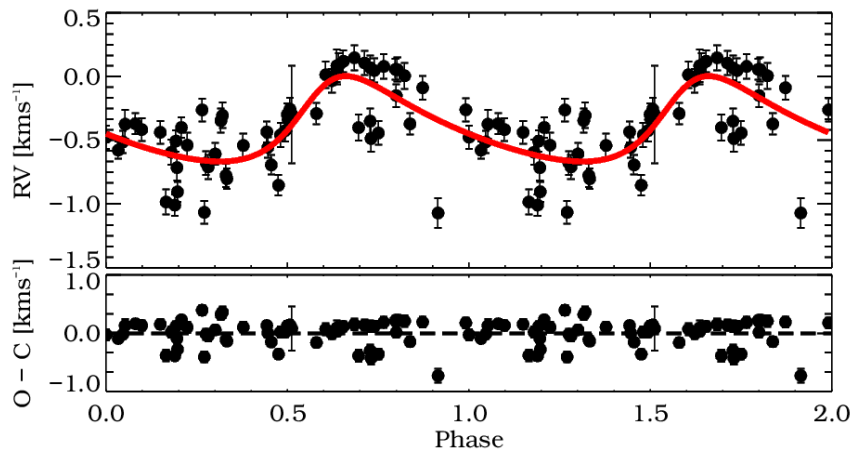


Figure 4.3: Upper panel: FEROS data points (black) with the best fitting Keplerian solution (red) for CD-37 13029. Lower panel: Residua of the fit (O-C: Observed black data points - Calculated red fit).

TYC 8654-1115-1 and HD 140637 are treated here in a different way, since the connection to stellar activity is not directly revealed by a matching photometric period. In order to identify if the highest peaks at 2.43 and 1.56 d are caused by physical processes (either stellar activity or a companion) and not by aliasing from the measurement sampling, I used the de-aliasing method published by Dawson & Fabrycky (2010).

As an example, I proceed with the method in detail for TYC 8654-1115-1 and give a summary of the results for HD 140637 below.

The first step is to inspect the window function (this time over frequency, not period) carefully for large peaks. They should be especially visible close to 1 year (0.0027 d^{-1}), 1 solar day (1 d^{-1}) and one sidereal day (1.007 d^{-1}). Fig. 4.4 shows a zoom in of the window function for different frequency ranges. These regions are short ones around 1 yr period, long ones covering the 1 d region and the frequency regions around the significant 2.43 d period and to an almost significant one around 1.69 d. The colored dashed lines mark major frequency peaks $f_{s,i}$ that could cause an alias peak in the periodogram with i begin the i -th sampling frequency.

66 different sampling periods $f_{s,i}$ were identified in the window function of TYC 8654-1115-1. An alias frequency $f_{a,i}$ appears now in the periodogram at $f_{a,i} = f_0 \pm f_{s,i}$, where f_0 is the assumed true frequency of the data. In case of TYC 8654-1115-1, two frequencies f_0 have been tested as true frequency: $410.846 \cdot 10^{-3} \hat{=} 2.434 \text{ d}$ and $591.716 \cdot 10^{-3} \hat{=} 1.690 \text{ d}$. These two different sets of alias frequencies $f_{a,i}$ are then marked in the periodogram. In case the major peaks in the periodogram can be reproduced using the period f_0 , this period has a physical origin and is not induced by measurement sampling. Fig. 4.5 shows the periodogram twice with the overplotted determined alias frequencies: upper figure using the period $2.434 \hat{=} 410.846 \cdot 10^{-3}$, lower figure using the period $1.690 \hat{=} 591.716 \cdot 10^{-3}$ as assumed true frequency.

Since the period of 2.434 d reproduces the scargle peaks better including the one at 1.690 d, this period is the real one and can be ascribed to a physical origin like a companion in the system or a stable starspot pattern. The 1.69 d period has to be an alias of the 2.43 d period, since it can be reproduced assuming the 2.43 d period as the true one.

The same analysis was performed for HD 140637. This target shows two significant periods at 1.56 and 2.76 d in the RV data. Furthermore, a significant period could be identified in the SuperWASP data (2.75 d). Although this case is very similar to CD-37 13029, for which the photometric and RV periods match, I have executed this de-aliasing method, since the period of 2.76 d is not the strongest in the RV data. Fig. D.13 and Fig. D.14 show the results. It is clearly visible that the 2.76 d period covers in contrast to the 1.56 d period all major large scargle peaks, unveiling it as the real period with a physical origin. Since the 1.56 d period can be reproduced using the 2.76 d period (Fig. D.14b), this period is most likely an alias of the 2.76 d period. Since the photometric period is matching the 2.76 d period, the probability is quite high, that the signal is induced by stable starspot patterns equivalent to CD-37 13029.

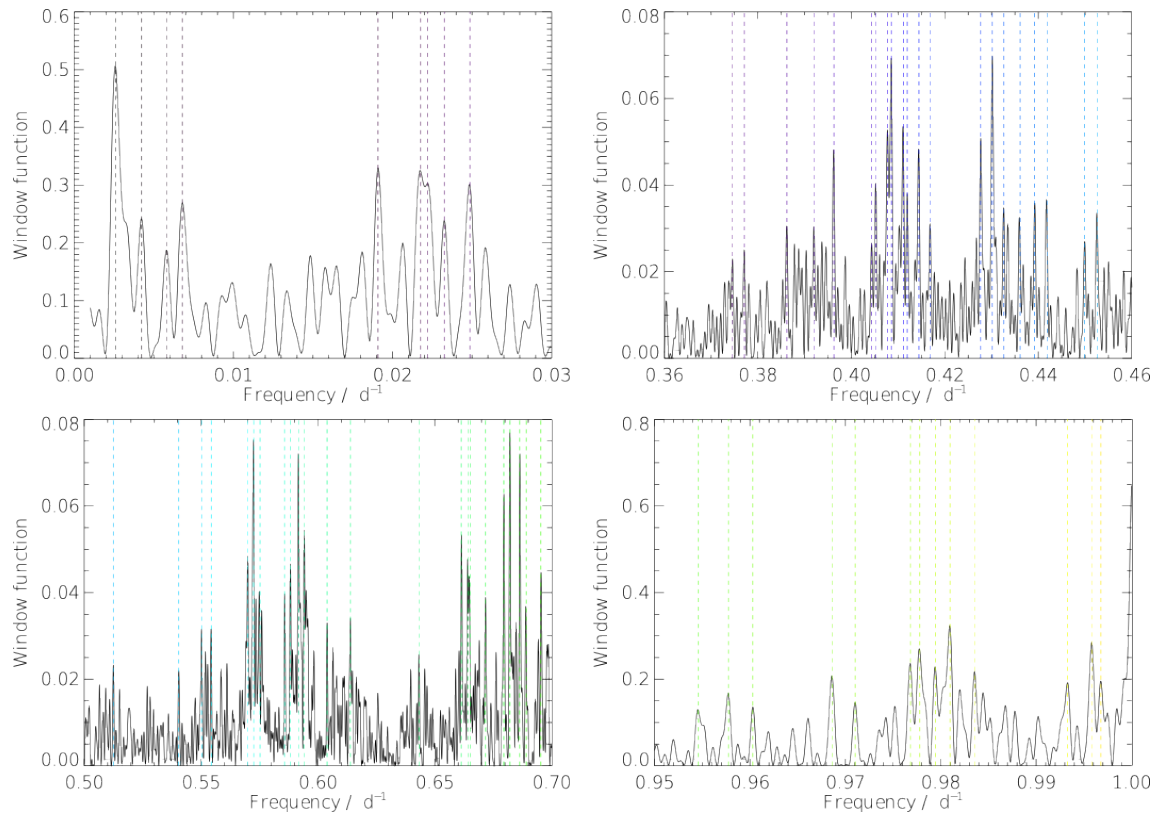


Figure 4.4: Different regions in the window function of TYC 8654-1115-1. Colored lines mark selected strong frequency peaks $f_{s,i}$.

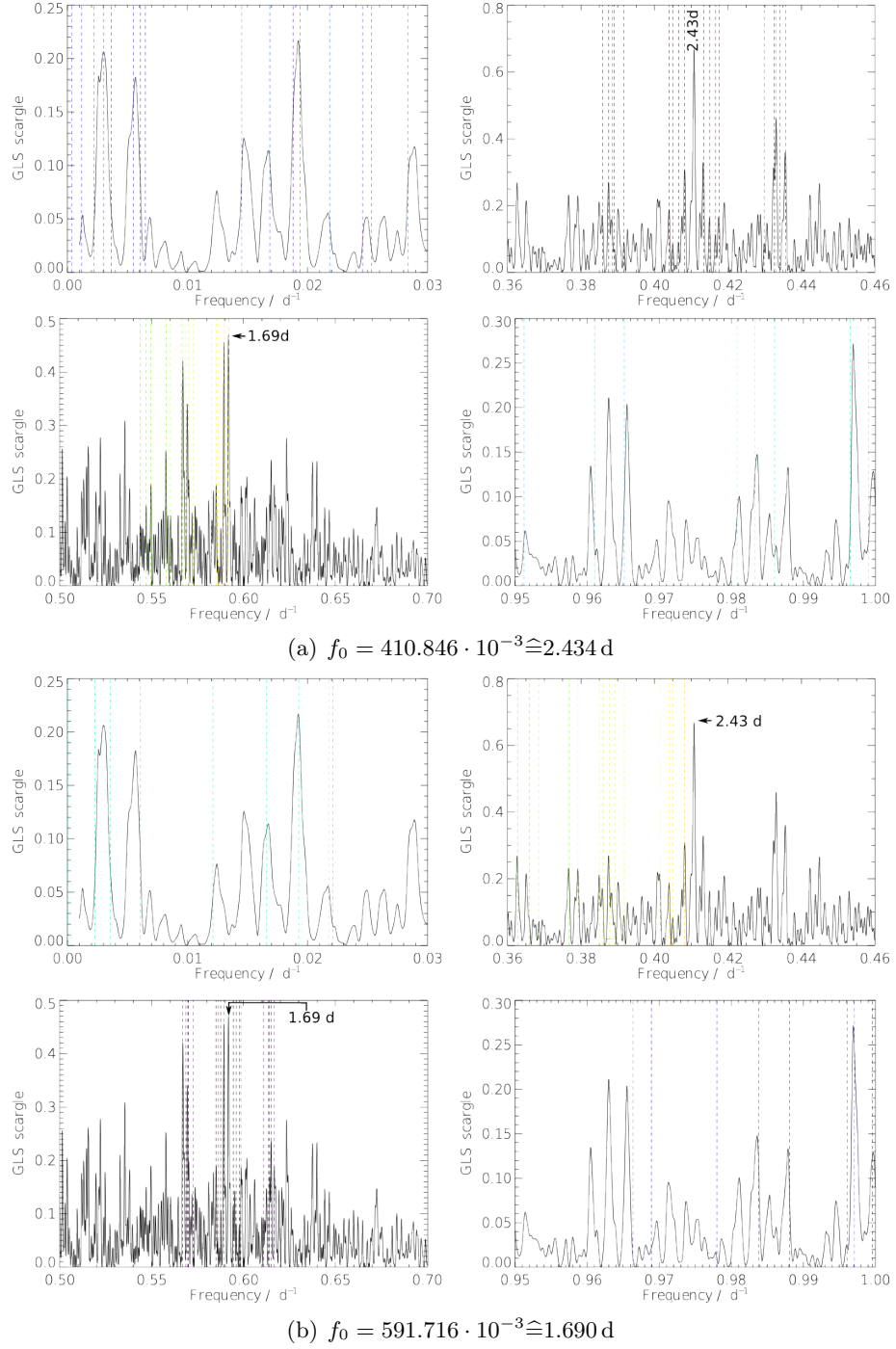


Figure 4.5: Different regions in the GLS scargle function of TYC 8654-1115-1 for two different f_0 . Colored lines mark calculated strong alias frequency peaks $f_{a,i}$ using selected strong sampling frequency peaks $f_{s,i}$ from the window function.

Parameter	CD-37 13029	TYC 8654-1115-1	HD 140637
Period P [d]	2.829 ± 0.001	2.434 ± 0.001	2.760 ± 0.001
RV semi-ampl. K [km/s]	0.335 ± 0.039	0.535 ± 0.051	0.304 ± 0.049
Eccentricity e	0.301 ± 0.002	0.057 ± 0.080	0.004 ± 0.001
Periastron length ω [deg] ^a	306.780	324.065 ± 130.126	353.209 ± 0.050
Per. passage time T_0 [d]	2454635.443 ± 0.006	2455766.373 ± 0.571	2453463.233 ± 0.300
System velocity γ [km/s]	-0.392 ± 0.028	13.059 ± 0.040	-4.637 ± 0.035
FAP (Cumming 2004)	$2.323 \cdot 10^{-10}$	$6.955 \cdot 10^{-13}$	$2.707 \cdot 10^{-8}$
Offset FEROS-HARPS	—	0.290 ± 0.003	0.089 ± 0.011
M [M_{\odot}] ^b	1.000 ± 0.100	0.800 ± 0.100	0.800 ± 0.100
$m \sin i$ [M_J]	1.919 ± 0.008	3.053 ± 0.280	1.809 ± 0.010
Semi-major axis a [AU]	0.004 ± 0.001	0.033 ± 0.002	0.036 ± 0.006

Table 4.3: RV fit parameters for CD-37 13029, TYC 8654-1115-1 and HD 140637. The analysis was done for CD-37 13029 directly using GLS due to the lack of HARPS observations. The other two objects were offset corrected using *RVlin.pro* results and afterwards analyzed with GLS.

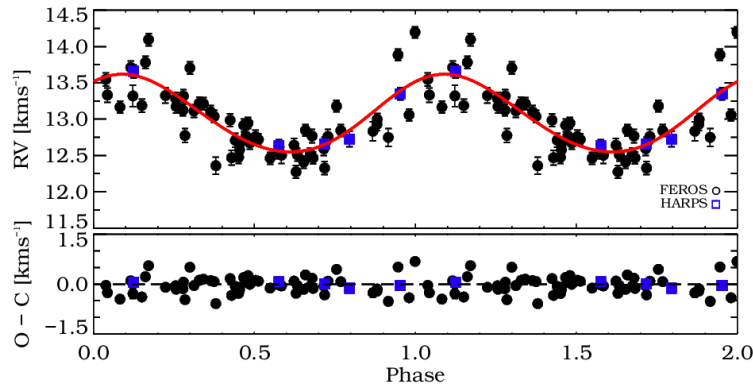


Figure 4.6: RV fit of TYC 8654-1115-1. Black filled circles mark the FEROS data points, while blue filled squares indicate HARPS ones. The red line shows the best Keplerian fit. The bottom panel shows the residua of the fit with the same color coding.

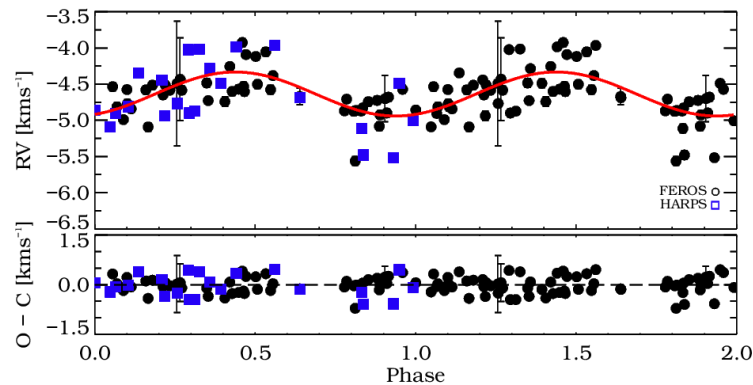


Figure 4.7: RV fit of HD 140637. Black filled circles mark the FEROS data points, while blue filled squares indicate HARPS ones. The red line shows the best Keplerian fit. The bottom panel shows the residua of the fit with the same color coding.

4.2.1 Detection limits

All targets of the sample show RV variations due to activity and for many targets no significant period could be determined. The question arises, which companion masses in which orbital separation can be detected in presence of the detected stellar activity. To answer this question, I evaluated the general detection limit due to quasi-stochastic activity noise neglecting the “blind” windows due to periodic rotational modulation. Doing so, I calculated the mass detection limits depending on orbital period for each target of the sample using the method of Zechmeister et al. (2009). Within this method, planetary signals in circular orbits are simulated over the observed time range and the data points are added as noise to the sine signal. The sine signal is calculated as follows:

$$RV(t) = K \cdot \sin\left(\frac{2 \cdot \pi}{P}t + \varphi\right) \quad (4.1)$$

with phase shift φ . The RV semi-amplitude K can be described as:

$$K = \sqrt{\frac{G}{1-e^2}} \frac{M_P \sin i}{\sqrt{(M_\star + M_P) \cdot a}} \quad (4.2)$$

$$\stackrel{(1)}{=} 28.4 \text{ m/s} \cdot \frac{M_P \sin i}{M_J} \cdot \left(\frac{M_\odot \text{ AU}}{M_\star a}\right)^{1/2}$$

Relation (1) assumes a circular orbit ($e = 0$) and $M_P \ll M_\star$. As initial semi-amplitude I assumed 50 m/s per target representing roughly the average RV uncertainty.

For each target, I simulated 201 periods between 1 and 1000 d (equally sampled in frequency space) and for each period 10 different phase shifts between 0.0 and 0.9. For each period, the generalised Lomb-Scargle periodogram was calculated with GLS for all 10 phases and the GLS power was determined at the period of the sine signal. In case the signal power is below the significance level (FAP of 0.1 %), the semi-amplitude K was increased and the periodogram recalculated. The simulated planet with a certain RV semi-amplitude K is treated as detected, when the signal power for each phase step is equal or above the significance level. The according RV semi-amplitude K represents the 99.9 % confidence level considered as the detection limit. This detection limit can be converted to the minimum secondary mass $M_P \sin i$ using equation 4.2 and the relation $a = \sqrt[3]{G \frac{M_\star \cdot P^2}{4\pi^2}}$ for circular orbits.

The calculated minimum mass $M_P \sin i$ for the 99.9 % detection limit over orbital period P is shown in Figure 4.8 for each target except for HD 217897, for which the analysis failed due to the large RV scatter. In order to compare the detection limits for the different stars more easily, Table 4.4 lists the number of available RV measurements, their standard deviation (stdev) and the average RV scatter per night (“night scatter”). Furthermore, the detection limits for 3 different orbital periods (2, 10 and 100 d) are listed.

In order to calculate a median detection limit for the whole sample, I calculated the median mass detection limit and corresponding standard deviation for each period step. Doing so, I neglected 4 targets, since their detection limits deviate significantly from the others due to their small amount of data points or/and their large RV scatter (HD 13908, CD-40 14901, V2129 Oph and HBC 603). The orbital period was converted to semi-major axis, assuming a median mass of $0.825 M_\odot$. Fig. 4.9 shows the median 99.9 % detection limit for this sample including the ± 1 -sigma error. This estimation of the detection sensitivity for this sample can now be compared to other studies to estimate the fraction of the stars of this

Target	# RV measurements*	RV stdev [m/s]	night scatter† [m/s]	M_{\star}^{\ddagger} [M_{\odot}]	$M_P \sin i_{2d}$ [M_J]	$M_P \sin i_{10d}$ [M_J]	$M_P \sin i_{100d}$ [M_J]
Group A (ESPRI overlap targets):							
HD 96064	130	74.3	32	0.9	0.4	0.5	1.7
HD 139084	33	1164.1	54	0.8	12.2	26.8	43.2
HD 183414	101	59.1	35	1.0	0.6	0.6	2.0
HD 216803	246	40.3	30	0.7	0.3	0.4	0.9
Group B (targets, with > 5 initial FEROS data points):							
IRXSJ033	67	125.7	50	0.8	0.7	1.5	2.7
CD-37 1123	55	72.6	35	0.8	0.5	1.1	1.9
CD-37 13029	65	327.5	65	1.0	2.5	4.6	10.0
CD-7824	44	221.8	75	0.7	1.3	2.5	4.6
HD 217897	33	4082.2	27	0.8	fail	fail	fail
TYC 5891-69-1	49	270.2	47	1.0	2.3	3.1	6.3
TYC 7697-2254-1	48	110.6	42	0.8	0.7	1.5	4.0
TYC 8654-1115-1	62	446.7	64	0.8	3.6	5.0	12.3
HBC 603	49	498.9	78	0.5	2.4	5.6	13.1
Group C (targets, with < 5 initial FEROS data points):							
IRXSJ0434	45	184.6	31	0.8	1.6	3.5	7.1
CD-40 14901	47	1443.7	39	0.9	7.6	20.4	74.4
HD 140637	67	347.4	39	0.8	2.6	3.3	8.1
HD 23208	46	172.4	33	0.8	1.3	2.5	8.5
HD 25457	56	34.9	50	1.2	0.4	0.6	1.9
HD 51797	56	126.5	50	0.8	0.7	1.5	3.4
HD 81544	44	517.0	47	0.8	2.0	2.3	10.5
V2129 Oph	62	925.7	99	0.6	3.8	10.2	15.2

Table 4.4: Number of RV measurements, their rms and the mass detection limits for the three different orbital periods 2d, 10d and 100 for the target stars, *: sum of FEROS and HARPS-measurments, ggf hd 140637 korrigieren, †: average of the nightly scatter for all nights with more than one measurement, ‡: Stellar mass estimation on background of spectral type.

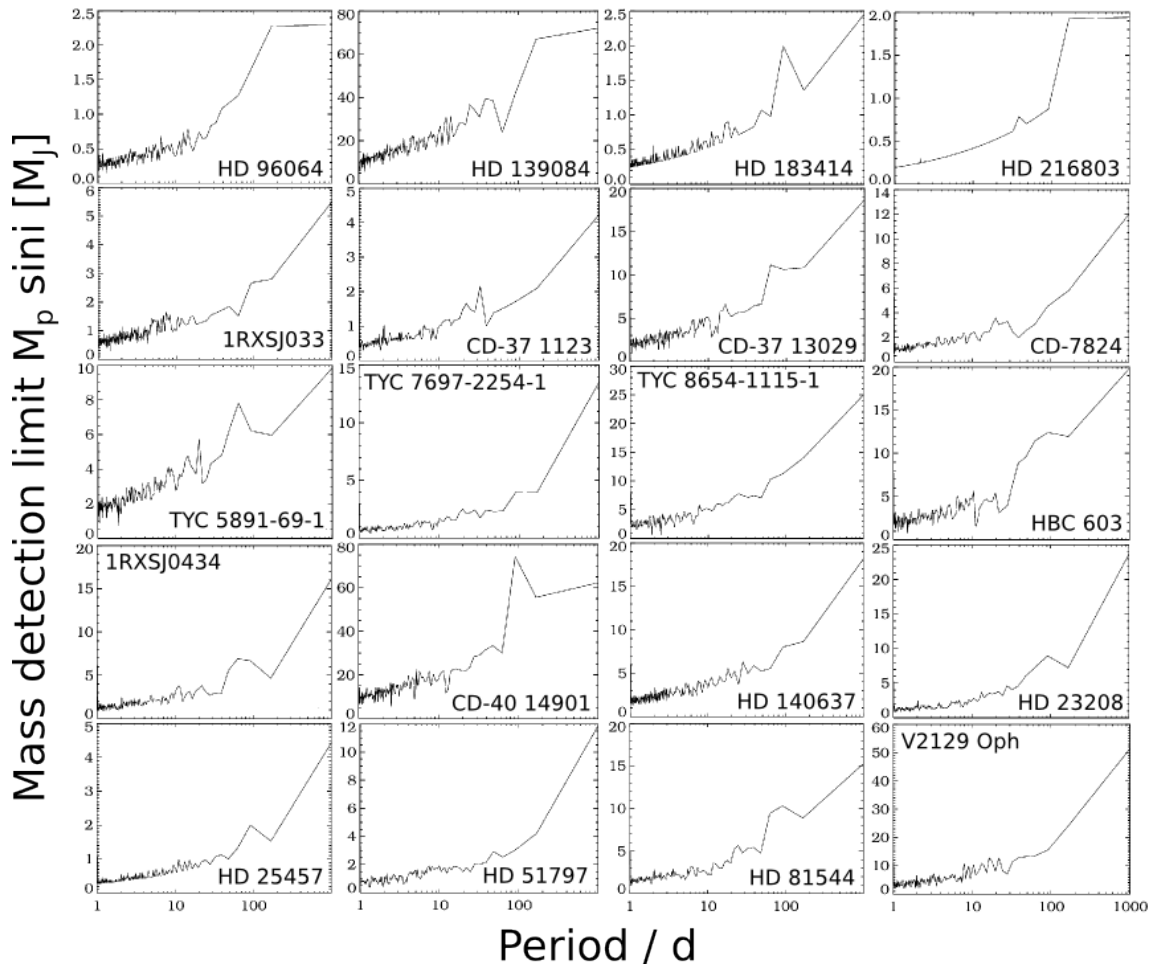


Figure 4.8: Companion mass detection limits in M_J over orbital period in days for 20 targets (the analysis of HD 217897 failed due to the large RV scatter).

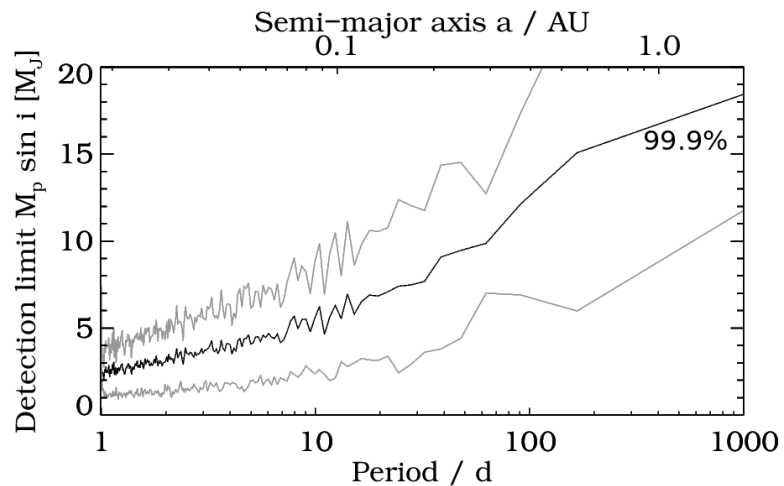


Figure 4.9: Median 99.9% detection limit of the sample (black). Grey lines indicate the 1-sigma error.

sample hosting detectable giant planets in orbits with period < 1000 d (corresponds to about 1.83 AU). The period upper limit of 1000 d was chosen, since most targets do not have a significantly longer time coverage of available spectra.

Naef et al. (2005) used a sample of 330 main sequence stars being observed with the ELODIE spectrograph. For 18 of them, a planet or even multiple system could be detected. Correcting their detection statistics for observational biases, they calculated the fraction f of stars hosting at least one giant planet with mass $M_P \geq 0.47 M_J$ depending on orbital period. A similar study was done by Marcy et al. (2005), who used a sample of 1330 solar type stars, observed with Lick, Keck and the AAT. 104 exoplanets could be detected in the sample. Using this sample, they calculated the fraction of stars hosting planets with $M_P \gtrsim 0.3 M_J$ (1 Saturn-mass). The derived values for both studies are listed in Table 4.5.

	Period range [d]	Semi-major axis range [AU]	fraction f [%]
Na05	< 5	$\sim 0.05^\dagger$	0.7 ± 0.5
	< 1500	$\sim 2.4^\dagger$	4.0 ± 1.1
	< 3900	$\sim 4.6^\dagger$	7.3 ± 1.5
Ma05	$\sim 12.7^\dagger$	< 0.1	1.2 ± 0.3
	$\sim 4500^\dagger$ (~ 12.3 yr)	< 5	≥ 6.6
	$\sim 36000^\dagger$ (~ 98.6 yr)	< 20	~ 12 (extrapolated)

Table 4.5: Fraction f of stars hosting giant planets from studies by Na05: Naef et al. (2005) and Ma05: Marcy et al. (2005). † : derived assuming $M_\star = 0.825 M_\odot$.

Using the statistics listed in Table 4.5, it is now possible to estimate, which fraction of the 21 targets of this thesis, could host detectable planets. Doing so, one can count the detected exoplanets in the survey of Marcy et al. (2005), which have orbital periods smaller than 1000 d, which corresponds to about 1.83 AU (Fig. 4.10), and compare them to the total target number of 1330, which results in a fraction f of about $4.8 \pm 1.5\%$. The error was estimated taking the errorbars of the histogram into account. The comparison with the detection limit plot by Naef et al. (2005) (Fig. 4.11) shows, that the estimated fraction has the correct order of magnitude, although the more realistic value is most likely closer to the lower end (approximately 3-3.5%). The comparison of the detection limit plot of Naef et al. (2005) and of this thesis shows, that the calculated detection limits are approximately a factor of 5 larger for this thesis than for Naef et al. (2005). One reason is that Naef et al. (2005) considered only MS stars, showing less variability than young stars. Furthermore, the detection limit calculated in the framework of this thesis, corresponds to the 99.9% detection limit, while Naef et al. (2005) show only the 90% detection limit. Therefore, the detection limits of this thesis have to be scaled down, even if not significantly. Doing so, I assume that both detection limits differ only by a factor of 4. Considering a fraction of about 3.5% of stars hosting planets with orbital periods shorter than 1000 d, the correction of a factor 4 gives a fraction of about 0.9% of targets in this sample hosting a detectable extrasolar planet in an orbit with period shorter than 1000 d and masses $\gtrsim 2.5 M_J$. This corresponds to a total number of about 0.2 stars hosting a giant planet in this sample. Therefore, future samples should be significantly larger than 100 targets.

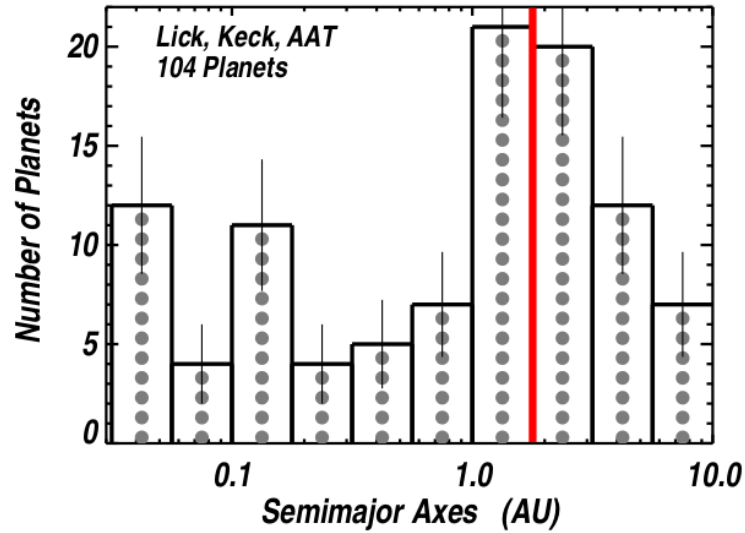


Figure 4.10: Histogram of detected exoplanets in the Marcy et al. (2005) survey. The red vertical line indicates the 1000 d period (corresponding to a semi-major axis of about 1.83 AU).

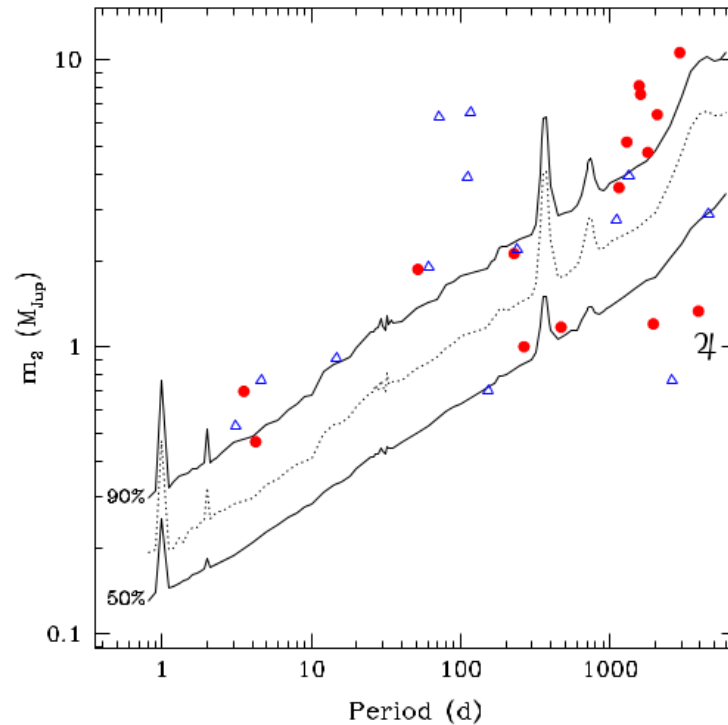


Figure 4.11: Detection limits in the Naef et al. (2005) survey. Solid lines are the detection limits of 50 and 90 %, respectively. The dotted line describes the 90 % detection limit neglecting non-photonic error sources. The filled red dots show the detected planets in the sample, while blue triangles indicate other planets detected with ELODIE around stars, which were not part of the sample. The symbol of Jupiter shows its position in the diagram.

4.3 Stellar activity indicators

The 21 targets are also analyzed in terms of stellar activity using a variety of activity indicators as described in Sec. 4.3. Doing so, single spectral lines as Ca I K, Ca II, He I and H $_{\alpha}$ were analyzed as well as ratios of single lines as VI and Fe I and different molecular bands. Furthermore, the detailed analysis of the CCF, which was created within the determination of the RV, gives a hint of the average line shape. This way, an examination of the chromospheric and the photospheric activity is possible.

Within the RV analysis, 12 of the 21 targets did not show a significant period at all. Additionally, another 6 targets revealed significant periods that could be traced back to the measurement sampling. For these 18 target, I performed a detailed periodicity analysis of the above mentioned activity indicators. The aim was to search for evidence of a stable period that can be interpreted as the rotational period. This period can then be compared to determined photometric periods (using SuperWASP data) or literature data (Wright et al., 2011) listed in Table 4.2. Furthermore, an age estimation for targets with no previously determined rotational period is possible using gyrochronology (Eq. 2.11). 13 of these 18 targets (HD 96064, 1RXSJ033, CD-37 1123, CD-7824, HD 217897, TYC 5891-69-1, TYC 7697-2254-1, HBC 603, HD 23208, HD 25457, HD 51797, HD 81544 and V2129 Oph) do not show a significant period in any of the activity indicators. This result suggests that no stable surface features survive over longer time intervals, which could be used as tracers for the rotational period of the targets.

In order to determine the rotational periods by looking for evidence of stellar surface features which are stable over short time scales, I selected a time interval for each target, during which many measurements have taken place in a short time span. Doing so, I estimated an upper length of the time interval using the oldest target of these 13 stars (HD 96064, < 250 Myr, Table 3.2) and derived the maximum rotational period for this target using the $(B - V)$ of 0.77 (SIMBAD) and the relation for the gyrochronological age (Barnes, 2007). This estimation leads to a maximum rotational period of 7–8 days and should be smaller for the remaining targets due to their younger age. After selecting a time interval of a length up to two times this maximal period (namely 14–16 days) of high measurement sampling for each target, I executed the period search in the RV data and all activity indicators for the 13 targets again. Even if the detected periods are not significant, I nevertheless executed the derivation of the gyrochronological age in order to compare the results with the remaining age determination methods. The results are listed in Table 4.6.

The remaining 5 of the 18 targets not showing a significant RV period (or only one that could be identified as caused by measurement sampling) reveal a significant period in one or more activity indicators and are therefore described in detail below:

HD 139084

For this target no photometric data was available from SuperWASP and no rotational period could be found in the literature. Furthermore, HD 139084 revealed 3 significant RV period between ~ 65 d and ~ 570 d, which could all be traced back to measurement sampling. The analysis of the activity indicators did not deliver any significant period in any of the indicators except for a ~ 1.5 d period in the S_{FEROS} analysis of the Ca I K line with a FAP of $1.350 \cdot 10^{-7}$ (see Fig. 4.12). Although the window function does not indicate the detected period of ~ 1.5 d as sampling induced, I executed the de-alias method of Dawson & Fabrycky (2010) on the data, which confirms that the period is real.

Target	# spectra	time interval	RV period [d]	other indicators	t_{gyro} [Myr]
Group A (ESPRI overlap targets):					
HD 96064	15	Apr 4 - Apr 24, 2012	~ 9.0	BVS, CCF skewness	~ 360
Group B (targets, with > 5 initial FEROS data points):					
1RXSJ033	12	Oct 5 - Oct 15, 2012	~ 1.25	BVS, BVD	~ 12
CD-37 1123	10	Oct 5 - Oct 15, 2012	~ 2	—	~ 20
CD-7824	9	Nov 26 - Dec 1, 2010	~ 4.0	BVD, CCF skewness	~ 40
TYC 5891-69-1	7	Dec 3 - 16, 2011	~ 2.2	BVS	~ 25
TYC 7697-2254-1	8	Jun 3 - Jun 12, 2009	~ 4.2	BVD, CCF skewness	~ 115
HBC 603	11	Jul 12 - Jul 28, 2011	~ 8.8	BVS, BVD, BC	~ 80
Group C (targets, with < 5 initial FEROS data points):					
HD 23208	17	Nov 22 - Dec 7, 2012	~ 2.0 ✓	bisectors, CCF skewness	~ 20
HD 25457	13	Nov 22 - Dec 6, 2012	~ 5.5	BVS, CCF variance	~ 630
HD 51797	16	Nov 22 - Dec 7, 2012	~ 2.4 ✓	bisectors, CCF moments	~ 25
HD 81544	10	Nov 27 - Dec 6, 2012	~ 1.3	BVS	~ 10
V2129 Oph	7	May 30 - Jun 6, 2012	~ 1.9 ✓	BVS, CCF var. & skew.	~ 30

Table 4.6: Periodicities of RV measurements and activity indicators for targets with no detected period that is stable over the whole observed time interval. The second column indicates the number of used measurements to determine a period stable on short timescales. The third column lists the used time ranges for the analysis. The detected RV periods on these timescales are listed in column four. A checkmark behind the period is given in case the detected period is significant. Column five lists the activity indicators, in which this specific period was detected as well, while the derived gyrochronological age t_{gyro} from this very period is given in the rightmost column. t_{gyro} was calculated also for non-significant periods for comparison purposes.

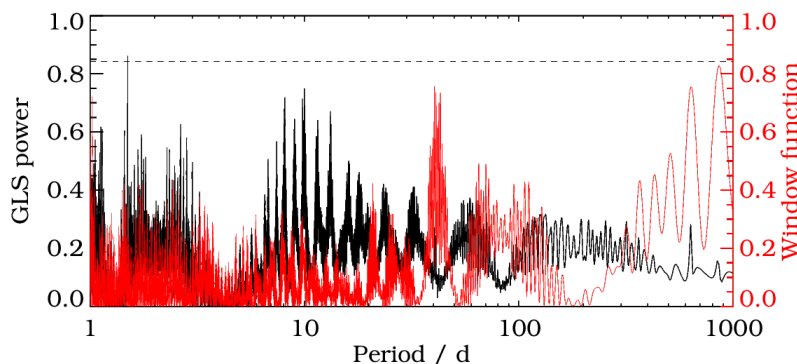


Figure 4.12: GLS periodogram of the S_{FEROS} analysis of HD 139084. The GLS power is plotted in black, the window function of the measurements in red. The dashed horizontal line marks the FAP level of 0.1%. The GLS power peaks at 1.497 ± 0.001 d with a FAP of $1.350 \cdot 10^{-7}$.

Assuming a period of 1.5 d as rotational period of the star, it is possible to estimate the stellar age using gyrochronology (Barnes, 2007). With a $(B - V)$ of 0.81 (SIMBAD), the age can be determined as about 10 Myr. This result matches the kinematic age estimation of 12_{-4}^{+8} Myr. Therefore, the 1.5 d period could indeed be the rotational period of the star.

HD 183414

HD 183414 did neither show a significant RV period nor could a photometric period be determined due to the lack of SuperWASP data and/or information in previous publications. The only activity indicator revealing a significant periodicity is the bisector velocity displacement (BVD). It changes with a period of 2.404 ± 0.001 d with a FAP of $1.865 \cdot 10^{-8}$ (see Fig. 4.13). Similar to HD 139084, the peak can not be traced back to measurement sampling issues consulting the window function. The de-alias method of Dawson & Fabrycky (2010) again supports the detected period as real, allowing the determination of a gyrochronological age of the target. Using a $(B - V)$ of 0.613 (SIMBAD), the age can be derived to be about 54 Myr. This does not match with the previously determined ages of about 100 Myr, indicating that the determined period is most likely not the rotational period of the star, although it could be classified as real.

HD 216803

HD 216803 showed a significant period of 1.29 ± 0.01 d in the SuperWASP photometry but none could be detected in the RV data. Furthermore, Wright et al. (2011) reported a photometric period of 10.30 d, which is significantly larger than the one determined in the framework of this thesis. The analysis of the activity indicators revealed a significant period of 1.215 d in the analysis of the statistical moments of the CCF, namely in the CCF variance μ_2 (Fig. 4.14). This period is similar to the SuperWASP photometry. The CCF variance period could be identified as sampling induced using both the window function criterion and the de-aliasing method by Dawson & Fabrycky (2010). The window function peaks could not be reproduced using the 10.30 d period as the original one, indicating that this period does not have a physical origin. Interpreting the 1.21 d period as rotation period of the star, the gyrochronological age can be calculated (using a $(B - V)$ of 1.1, SIMBAD) as about 3.5 Myr. Although the 10.30 d period of Wright et al. (2011) has been

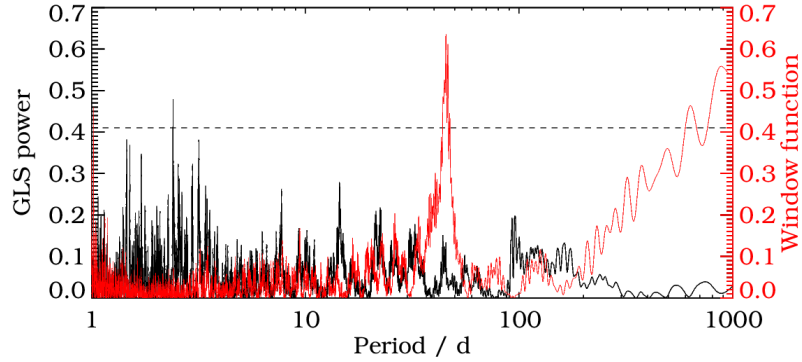


Figure 4.13: GLS periodogram of the BVD analysis of HD 183414. The GLS power is plotted in black, the window function of the measurements in red. The dashed horizontal line marks the FAP level of 0.1%. The GLS power peaks at 2.404 ± 0.001 d with a FAP of $1.865 \cdot 10^{-8}$.

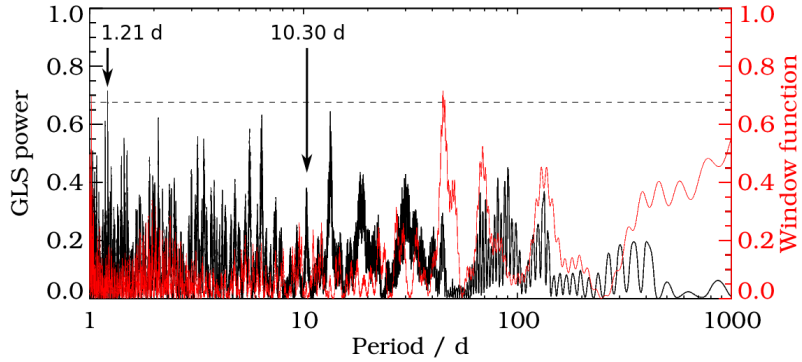


Figure 4.14: GLS periodogram of the CCF variance analysis of HD 216803. The GLS power is plotted in black, the window function of the measurements in red. The dashed horizontal line marks the FAP level of 0.1%. The GLS power peaks at 1.215 ± 0.001 d (left arrow) with a FAP of $4.035 \cdot 10^{-7}$. The second arrow marks the period of 10.30 d determined as rotational period by Wright et al. (2011).

ruled out as stellar rotational period, I calculated the gyrochronological age for comparing issues as about 220 Myr, which support the lithium age of < 300 Myr.

1RXSJ0434

This target revealed two significant RV periods of 2.29 and 1.77 d, which could however be traced back to sampling issues. The photometric period was derived from SuperWASP data as 2.00 d. The analysis of most activity indicators did not reveal a significant period that could be traced back to a physical origin, except for the analysis of the CCF skewness μ_3 and the BVD. The former showed a significant (FAP $7.236 \cdot 10^{-8}$) period of 2.180 ± 0.001 d, while latter exhibited a period of 2.480 ± 0.001 d with a FAP of $4.045 \cdot 10^{-9}$. Both periods are fairly close to the 2.29 d period extracted from the RV data, indicating that a connection between these phenomena is most likely. Fig. 4.15 shows the GLS periodograms of the CCF skewness and the BVD including the window function. In order to test the reproducibility of the largest peaks in the periodograms of the RV, the BVD and the CCF skewness periodogram, all four periods (2.18 BVD, 2.29 d RV, 1.77 d RV and 2.48 d CCF skewness) were used. Unfortunately, none of them was able to completely reproduce all large peaks.

The three periods between ~ 2.2 and ~ 2.5 d reproduced more peaks than the ~ 1.8 d period, indicating that the real period lies somewhere between 2.2 d and 2.5 d. By assuming a real period in this interval, it is possible to calculate the gyrochronological age using a $(B - V)$ of 0.94 (SIMBAD) as between 15 and 20 Myr, which is in fairly good agreement with the previous age estimations of ~ 30 Myr. The fact, that many significant periods with small uncertainties were detected which could not be identified as the true period, reflects the difficulties in this analysis. Complex spot structures on the stellar surface rotating (also differentially) on different latitudes wash out the true signal and can completely mask it.

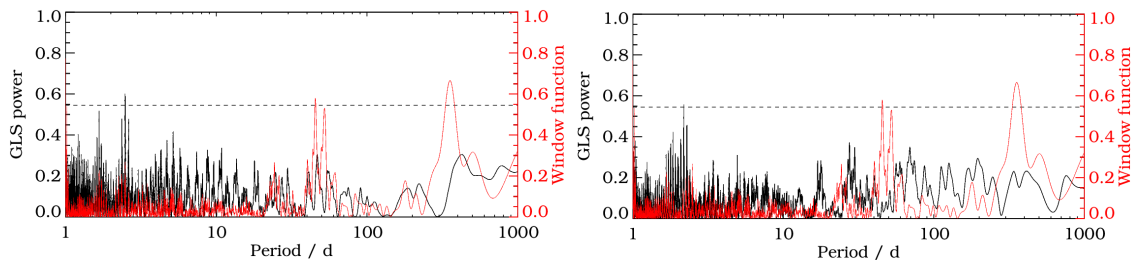


Figure 4.15: Left panel: GLS periodogram of the BVD analysis (left panel) and the CCF skewness analysis (right panel) of 1RXSJ0434. The GLS power is plotted in black, the window function of the measurements in red. The dashed horizontal lines mark the FAP level of 0.1%. The GLS power peaks at 2.480 d period (BVD) and 2.180 d period (CCF skewness), respectively.

CD-40 14901

CD-40 14901 shows evidence for 3 significant RV periods at about 43, 47 and 565 d. However, all of them could be traced back to measurement sampling. The photometric period was derived as 3.22 ± 0.01 d using SuperWASP data. The detailed activity analysis only showed a significant period in the H_α equivalent width (EW). This period is 1.647 ± 0.001 d and has a FAP of $9.703 \cdot 10^{-7}$. It is noticeable that this period is close to half of the photometric period suggesting a connection between both phenomena. Fig. 4.16 shows the GLS periodogram of the H_α measurements including the window function. Using the de-aliasing method, the 1.65 d H_α EW period can not reproduce the GLS periodogram peaks satisfyingly, while the 3.22 d period covers the very most of the large peaks. This indicates that the true rotational period of this star is most likely close to about 2x the H_α EW period ($= 3.22$ d), which corresponds to a stellar age of about 70 Myr (using a $(B - V)$ of 0.68 from SIMBAD). This age estimation supports the lithium method result of about 80 Myr.

Three of the 21 targets revealed a significant RV period that could not be traced back to measurement sampling issues. The activity analysis results of these three targets are discussed in detail below:

CD-37 13029

CD-37 13029 shows a significant photometric period of 2.80 d, which has been derived from the photometric SuperWASP data. Furthermore, the analysis of the RV exhibited almost the same period (2.83 d). Since the measurement sampling was ruled out as origin for both signals, a common physical origin of both signals stands to reason. In principle,

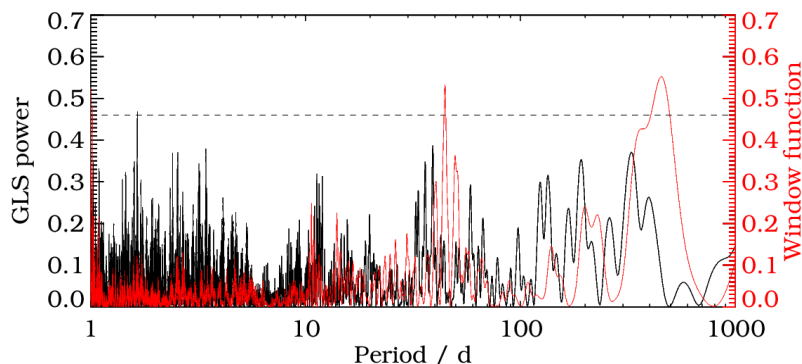


Figure 4.16: GLS periodogram of the H_α EW analysis of CD-40 14901. The GLS power is plotted in black, the window function of the measurements in red. The dashed horizontal lines mark the FAP level of 0.1%. The GLS power peaks at 1.647 d period.

a substellar companion of about $2 M_J$ at a semi-major axis of 0.004 AU could cause an RV signal of about 335 m/s as detected in the RV measurements (see Tab. 4.3). Nevertheless, a substellar companion can not cause a periodic photometric signal in sine shape. This result suggests stellar activity as origin of both signals, e.g. a cool starspot rotating along with the stellar surface. In order to confirm this assumption, the detailed analysis of the activity indicators is crucial. Within this analysis, significant periods were detected in the bisector velocity span (BVS) and the bisector curvature (BC) of the CCF. Fig. 4.17 show the GLS periodograms for the BVS and the BC analysis. The overplotted window function (red) rules out measurement sampling as origin of the signal. Once again, the de-alias method was executed on the RV, the photometric and the bisector measurements in order to proof or reject the 2.83 d period as the period causing the strongest periodogram peaks. Since this was successful for all periodograms, this period can be assumed as being caused by rotational modulation due to stellar surface features. The next step is to find a possible spot scenario (spot size, temperature difference to the stellar photosphere etc.), which is explained in Section 5.

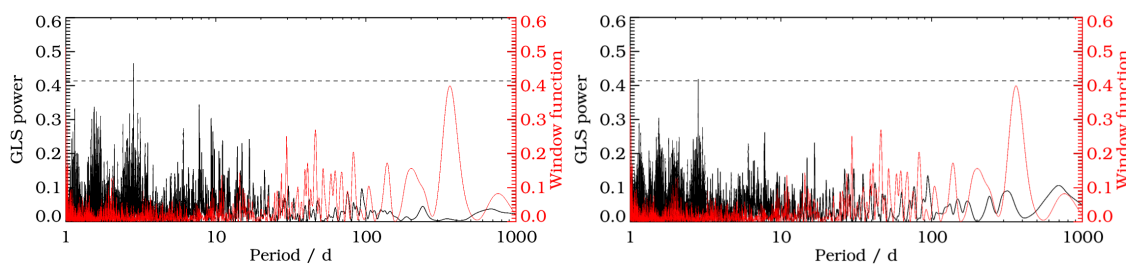


Figure 4.17: Left panel: GLS periodogram of the BVS analysis (left panel) and the BC analysis (right panel) of CD-37 13029. The GLS power is plotted in black, the window function of the measurements in red. The dashed horizontal lines mark the FAP level of 0.1%. In both panels, the significant period of 2.83 d is clearly visible.

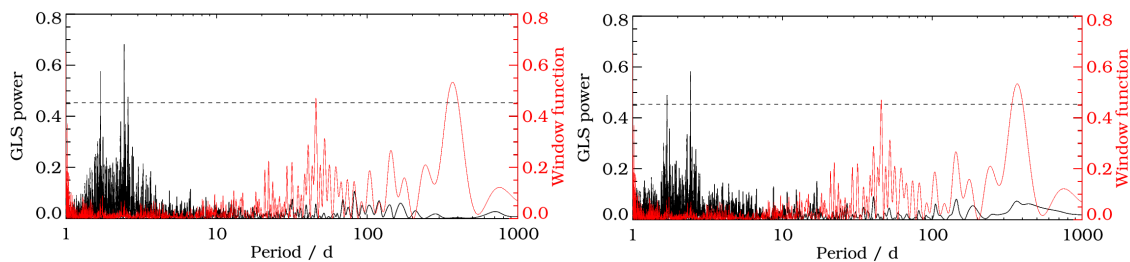


Figure 4.18: Left panel: GLS periodogram of the BVS analysis (left panel) and the CCF skewness analysis (right panel) of TYC 8654-1115-1. The GLS power is plotted in black, the window function of the measurements in red. The dashed horizontal lines mark the FAP level of 0.1%. In both panels, the significant period of 2.43 d is clearly visible as well as the 1.69 d period that have been identified as sampling induced within the RV analysis.

TYC 8654-1115-1

TYC 8654-1115-1 shows a significant (FAP $1.5 \cdot 10^{-11}$) 2.43 d RV period, while a photometric period could not be determined due to the lack of photometric SuperWASP data and previous publications. Due to the missing comparison of detected RV and photometrically determined rotational period, the involvement of a substellar companion ($\sim 3 M_J$, see Table 4.3) can not be as easily challenged as for CD-37 13029 and HD 140637. Therefore, a detailed analysis of the stellar activity is needed to confirm or reject the companion hypothesis. Most of the activity indicators do not show significant periods, which supports the substellar companion scenario. However, the CCF skewness μ_3 and the BVS reveal significant periods at 2.43 d which match the RV period (see Fig. 4.18). As can be seen in Fig. 4.18, a period of 1.69 d is significant as well. This period has been identified as alias and could therefore be ruled out as caused by a physical phenomenon within the analysis of the RV measurements (see Sec. 4.2). Since the periodic change of the BVS and the CCF skewness indicates a periodic change of the lineshape, the measured RV periodicity is most likely induced rather by line shape variations than by the Doppler shift of spectral lines due to the stellar motion around the star-companion barycenter. The de-aliasing method identifies the 2.43 d period as the origin of the largest periodogram peaks. The fact that the 2.43 d period can explain both the RV and the activity signals confirms that the signal is most likely caused by activity patterns on the stellar surface. Just as for CD-37 13029, a simulation using a spot program (see Sec. 5.2) can give an idea which spot scenario can induce the measured RV signal. Nevertheless, since the 2.43 d period is most likely the stellar rotation period, the estimation of the stellar gyrochronological age is possible using the relation by Barnes (2007). With the $(B - V)$ of 0.78 (SIMBAD) a stellar age of about 27 Myr can be calculated, which matches the upper limit of about 30 Myrs constrained by the Li I EW.

HD 140637

This target revealed a photometric period (analyzing the SuperWASP data) of 2.75 d, which was identified in the RV measurements only as second strongest but still significant period (2.76 d, FAP $4.5 \cdot 10^{-3}$). Within the RV de-aliasing analysis, the strongest RV period of 1.56 d (FAP $2.6 \cdot 10^{-6}$) could be identified as alias of the second strongest period of 2.76 d, while the 2.76 d period could be identified as true period induced by a physical phenomenon. Since identifying the same period within the RV and the photometric

measurements has a lot to commend that a substellar companion is unlikely the origin of the signal, the analysis of activity indicators is expected to reveal the same period. This is confirmed by the analysis, the same periods are exhibited even if not significant in the CCF statistical moments (kurtosis, skewness, variance) as well as in the CaH2 spectroscopic index (see Fig. 4.19). Just as CD-37 13029 and TYC 8654-1115-1, HD 140637 is an interesting target for the detailed spot analysis in order to find a possible scenario that could reproduce such RV and photometric signal.

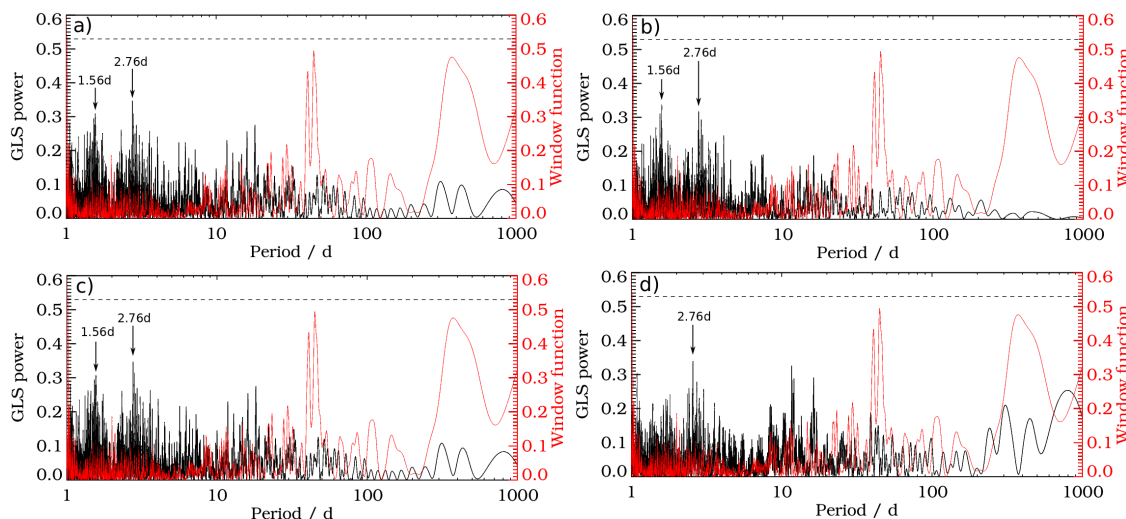


Figure 4.19: GLS periodograms of the a) CCF variance, b) CCF skewness, c) CCF kurtosis and d) the CaH2 spectroscopic index of HD 140637. The GLS power is plotted in black, the window function of the measurements in red. The dashed horizontal lines mark the FAP level of 0.1%. In all panels, the period of 2.76 d is clearly visible even if not significant. In the statistical moments of the CCF, the 1.56 d period is visible as well.

An additional estimation, if the detected RV variation is most likely induced by stellar activity, can be obtained by taking a closer look at the correlation of the BVS and the RV. The BVS represents the distortion of a line profile being the average of the photospheric lines. Its strength indicates, how much this average line is distorted. Subtracting the median of the BVS, one can distinguish between positive and negative distortions, describing, on which side of the line the distortion is largest. In case a clear correlation between this line distortion and the RV is noticed, the probability is very high that the detected RV shift is simply caused by the not satisfyingly fitted photospheric lines, which reveal the distortion due to activity. This can be analyzed using the Linear Pearson Correlation Coefficient R_{Pearson} (Pearson, 1920). This coefficient can adopt values between -1 and 1, while -1 indicates a 100% anticorrelation and 1 a 100% correlation of the two data sets. The R_{Pearson} for two data sets can be derived using the IDL function `correlate.pro`¹. In terms of the correlation of BVS and RV, both cases (-1 and 1) reveal a clear dependance of the RV from the BVS and therefore that the RV was induced by spectral line distortions cause by spots. In case the coefficient is close to 0, a dependance can be most certainly excluded. Values between 0 and 1 and 0 and -1, respectively, can not be treated definitely, but has to be seen in the context of e.g. equal significant periods appearing in both RV and activity indicators.

¹<http://www.astro.washington.edu/docs/idl/cgi-bin/getpro/library07.html?CORRELATE>

Table 4.7 shows the result for the correlation coefficient for all 21 targets. Fig 4.20 shows the correlation plots of RV vs. BVS for those targets, showing a clear correlation between both parameters.

Target	R_{Pearson}	Target	R_{Pearson}
Group A:		Group C:	
HD 96064	0.22	1RXSJ0434	0.50
HD 139084	0.24	CD-40 14901	0.50
HD 183414	0.35	HD 140637	0.49
HD 216803	0.62	HD 23208	0.65
		HD 25457	0.27
Group B:		HD 51797	0.37
1RXSJ033	0.19	HD 81544	0.58
CD-37 1123	-0.11	V2129 Oph	0.77
CD-37 13029	0.82		
CD-7824	0.44		
HD 217897	0.27		
TYC 5891-69-1	0.83		
TYC 7697-2254-1	0.31		
TYC 8654-1115-1	0.91		
HBC 603	-0.19		

Table 4.7: Linear Pearson Correlation Coefficients R_{Pearson} for all target stars. While $|R_{\text{Pearson}}| = 1.0$ describes a 100% (anti-)correlation of the two coefficients, I interpreted values of $|R_{\text{Pearson}}| > 0.6$ already as indicator for a possible (anti-)correlation (marked in orange). Results of $|R_{\text{Pearson}}| < 0.6$ are interpreted as not conclusive. Group A lists the ESPRI overlap targets. Group B consists of targets with initially more than 5 FEROS data points, which Group C contains the targets with initially less than 5 FEROS data points.

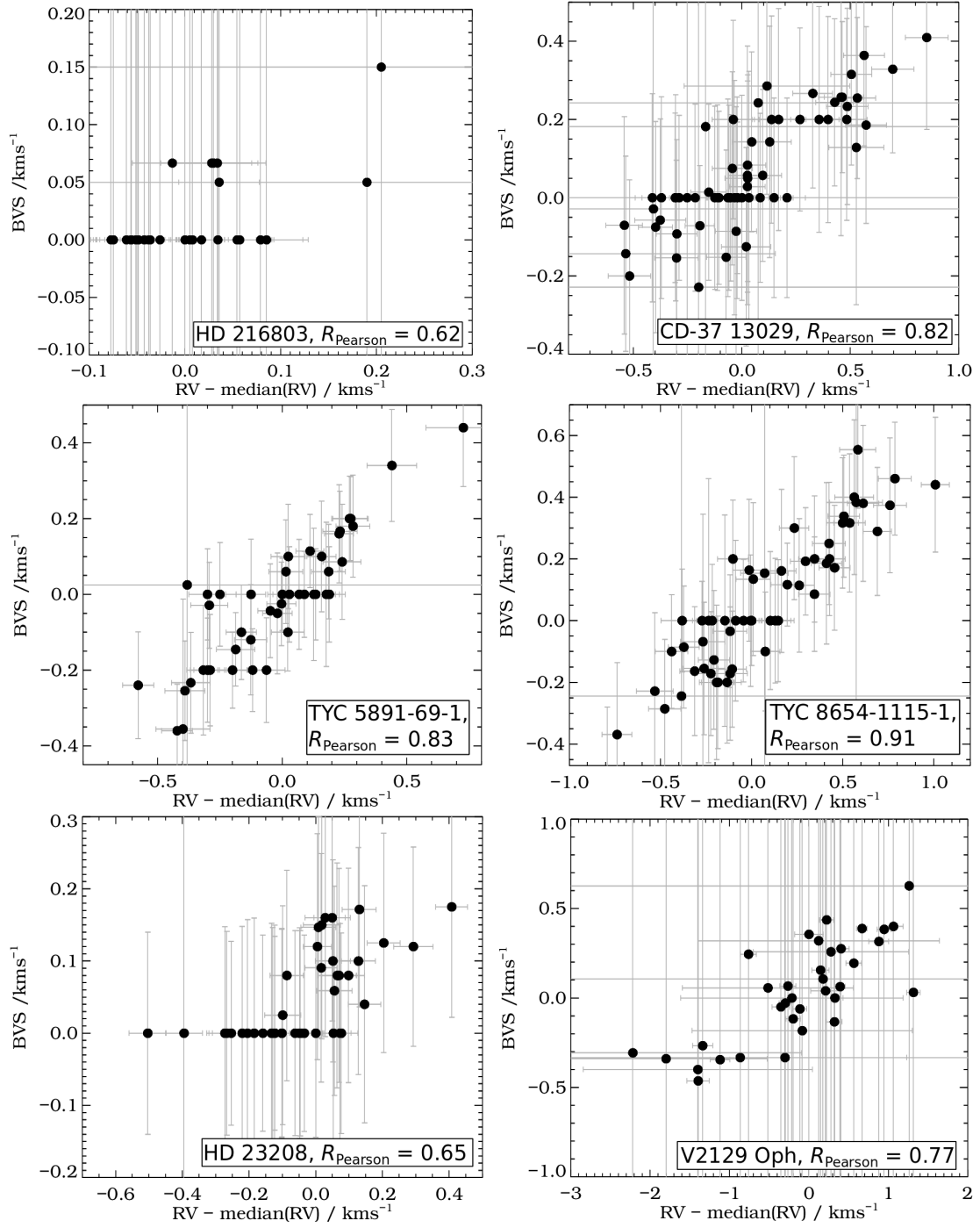


Figure 4.20: Correlation plots between target RV and BVS

Chapter 5

Characterisation of RV signals in terms of starspots

5.1 The starspot program

Within the analysis of RV and activity indicators, three objects, namely CD-37 13029, TYC 8654-1115-1 and HD 140637, revealed significant RV periods that could be retrieved from several activity indicators as well. Two objects have photometric SuperWASP measurements that vary with the detected RV period. Furthermore, the clear correlation of RV and BVS of two targets has shown that both signals have most likely the same origin. Therefore, I used a starspot program that has been modified in the framework of this thesis, in order to find possible spot scenarios that could cause the detected RV and photometric amplitudes. Table 5.1 shows the measured parameters as RV semi-amplitude K and photometric amplitude ΔI that are tried to be reproduced using the spot program (see below). Figure 5.1 shows the best fits of the photometric SuperWASP data for CD-37 13029 and HD 140637. All targets reveal a non-sinusoidal RV shape, which could be due to eccentricity if its origin was a companion, or which naturally arises from rotational modulation in case of starspots.

Target	K [km/s]	σ_K [km/s]	ΔI^* [mag]	$\sigma_{\Delta I}$ [mag]
CD-37 13029	0.335	0.039	0.084	0.014
TYC 8654-1115-1	0.535	0.051	—	—
HD 140637	0.304	0.049	0.074	0.010

Table 5.1: Parameters for the spot program, * peak-to-peak amplitude

The simulation of spots on stellar surfaces was done with a program, initially written by Dr. Ralf Launhardt, MPIA, which has been adjusted and modified in the framework of this thesis. The initial program was written in GILDAS and calculates the RV and photometric variation as well as the photocenter variation and its trajectory. Furthermore, it provides the change of the line bisectors over stellar rotation angles. The RV and bisectors are calculated using a thermal line spectrum and a fixed linear limb darkening coefficient LDC , which is provided by the user. In the framework of this thesis, the program has been modified in terms of the derivation of the RV and bisector shift. Instead of using a thermal line spectrum for the derivation of both parameters, it is possible to assign synthetic spectra to both the stellar photosphere and the starspot using different effective temperatures. Due to the fact that no astrometric measurements are used within this

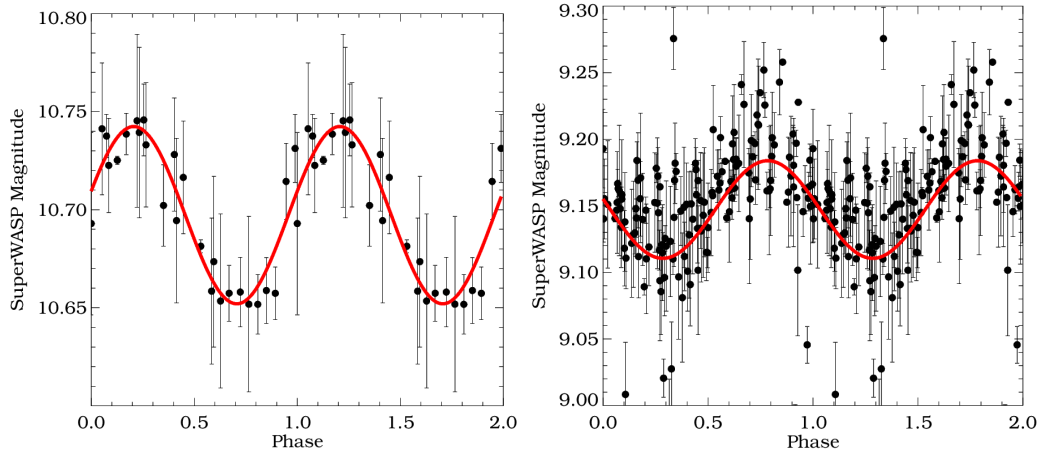


Figure 5.1: Phase-folded SuperWASP photometry of left CD-37 13029 ($P_{phot} = 2.80$ d) and right HD 140637 ($P_{phot} = 2.75$ d). The red lines shows the best fit solutions determined with GLS.

thesis, I concentrated on the implementation of the calculation of the RV shift and the photometric variation in the modified spot program and neglected photocenter shift and its trajectory.

The structure and operation mode of the optimized starspot program is explained below: Before the RV shift and other consequences due to the simulated spot scenario can be calculated, the user has to provide some information about the scenario. Besides the distance to the star d and stellar radius R_* , the projected rotational velocity $v \sin i$ and the stellar inclination i have to be defined. In order to create fitting synthetic spectra for the photosphere and the starspot, the effective temperature of the photosphere $T_{\text{eff,P}}$ and that of the spot $T_{\text{eff,S}}$ have to be fixed as well as the surface gravity $\log g$, metallicity $[M/H]$ and microturbulence v_{mic} . The last three parameters are adopted for both the stellar photosphere and the starspot. The spectral range, in which the RV and photometric variation shall be calculated is given via a wavelength range around a given central wavelength. In order to calculate the bisectors (BVS, BVD, BC), the different bisector heights (Eq. 2.24-2.26) have to be fixed in advance. Currently, the program can handle one single circular spot. Its size a_{spot} can be appointed by the user (in percent of hemisphere area) as well as the latitude Θ from stellar equator.

Using the stellar and spot parameter, synthetic spectra are created using SPECTRUM. Especially for wider wavelength ranges it is important to get a good estimation of the limb darkening coefficient LDC . This has been done by simulation a large grid of linear limb darkening coefficients LDC using JKTL D with Claret et al. (1995) models. The coefficients have been calculated for a large grid of stellar effective temperatures, surface gravities, metallicities and microturbulences for 10 different photometric filters. These are four Strömgren filters u , v , b , y between 352.8 and 547.3 nm, Johnson U , B , V (370 - 534.1 nm), Cousins R and I (641.2 and 786.5 nm) as well as the Teide J filter at 1248.8 nm. These 10 filters cover the FEROS wavelength range (~ 3500 - 9200 Å, Kaufer et al., 1997) well. For a given set of stellar parameters, the parameters from the grid can be fitted and the fit result provides a reasonable guess for the linear limb darkening coefficient LDC_λ at each wavelength.

The stellar image itself is created using a window of 201×201 px, where the star of radius 100 px lies in the middle, touching the box sides. The radial velocity RV_{px} for each pixel

is calculated using the input $v \sin i$ of the star and the provided stellar inclination i . Afterwards, the circular spot is projected onto the stellar surface at the selected latitude. The aim of this method is to calculate a final spectrum of the whole star as it would be observed from the ground with FEROS. This is done as follows: Since different regions in the pictures can now be distinguished (background, star, spot), it is possible to assign to all pixels an individual spectrum. In case the pixel falls onto the background, the resulting spectrum is zero over the whole wavelength range, since the background contribution to the detected stellar flux is neglected within this program. In case the pixel falls onto a region of the star that is not covered by the spot, the stellar flux for each wavelength λ at the current pixel $F_{\star,\lambda,px}$ is calculated as:

$$F_{\star,\lambda,px} = F_{\star,\lambda} \cdot (1 - LDC_{\lambda} \cdot (1 - \mu_{px})) \quad (5.1)$$

with $\mu_{px} = \cos \Theta_{px} = \sqrt{1 - (x_{px}^2 + y_{px}^2)}$, where Θ_{px} is the angle between the line of sight to the observer and the pixel vector and x_{px} and y_{px} are the coordinates at the current pixel in the 201x201 px frame.

In case the pixel falls onto the stellar spot, the flux is simply scaled by the ratio of the stellar and spot flux at a given wavelength:

$$F_{spot,\lambda,px} = \frac{F_{spot,\lambda}}{F_{\star,\lambda}} \quad (5.2)$$

The fluxes $F_{\star,\lambda}$ and $F_{spot,\lambda}$ are the fluxes at a certain wavelength from the simulated spectra.

The resulting spectrum at each pixel is then Doppler shifted using the calculated RV_{px} at each pixel:

$$\lambda_{RV,px} = \lambda + \left(\frac{RV_{px}}{c} \cdot \lambda \right) \quad (5.3)$$

By interpolating the flux onto the initial wavelength array, it is finally possible to sum up all 201x201 spectra and calculate the final spectrum that would be observable from Earth for the given snapshot. This final spectrum will show spectral line distortions that depend in strength and shape on the temperature difference between star and spot, on the spot size and its position.

The rotation of the star leads to the migration of the starspot over the surface and therefore to different final spectra. The spectral lines will be differently distorted depending on which part of the star is covered by the spot and the resulting RV shift caused by this can be calculated by cross-correlating the final spectrum with the synthetic stellar one. The line distortion can be analyzed using the bisectors of the CCF as has been described for real data in Sec. 2.5.

The photometric variation for the central wavelength λ_c is determined by calculating for each scenario the sum of all pixel fluxes at the central wavelength according to equations 5.1 and 5.2 and comparing the result with the sum over the undisturbed stellar surface. The maximal flux variation over the whole stellar rotation ΔF can be converted to the manageable unit "magnitude" via:

$$\Delta I = -2.5 \cdot \log_{10}(\Delta F) \quad (5.4)$$

where ΔI is the peak-to-peak amplitude of the photometric variation.

So far, the program does not take instrumental broadening into account.

5.2 Application to target sample

In order to find a possible spot scenario that would be able to produce the measured RV semi-amplitude K and photometric peak-to-peak amplitude ΔI for CD-37 13029, TYC 8654-1115-1 and HD 140637, respectively, I used the modified spot program. Since the number of free parameters (stellar inclination, spot temperature, size and latitude) and the according parameter space is very large, the calculation of a full grid of parameters and the according semi-amplitudes was not possible. Rather, I will give below one possible scenario for each target being able to reproduce the measured amplitudes to show, that it is in principle possible to explain the results with surface features. A short discussion about the general reproducibility of RV signals with spot scenarios is given in Sec. 5.3.

The parameters of one possible spot scenario for each target are listed in Table 5.2. All scenarios have been simulated in the wavelength range between 4990 and 5010 Å.

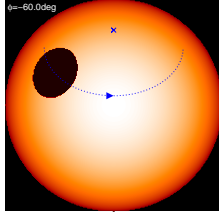
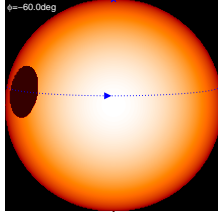
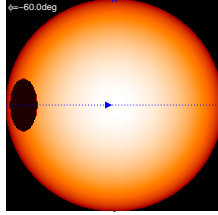
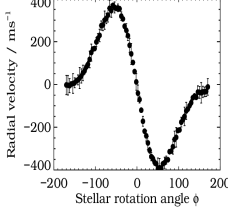
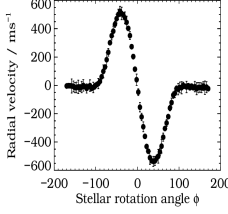
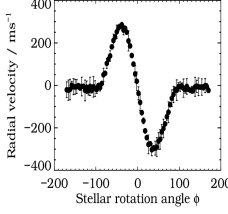
Parameter	CD-37 13029		TYC 8654-1115-1		HD 140637	
	Value	Reference	Value	Reference	Value	Reference
Input parameters:						
Distance d [pc]	6.45	Hip97	17.9	Hip97	41.7	vLe07
Stellar radius R_\star [R_\odot]	1.0	SpT	0.9	SpT	0.8	SpT
$v \sin i_\star$ [km/s]	20.68	Tab. A.1	20.30	Tab. A.1	10.05	Tab A.1
T_{phot} [K]	5500	SME	5500	SME	5000	SME
$\log g_\star$	3.5	SME	4.0	SME	4.0	SME
$[M/H]$	0.0	SME	0.0	SME	-0.2	SME
v_{mic} [km/s]	2.19	SME	1.90	SME	2.31	SME
T_{spot} [K]	3750		4000		3500	
Spot size a_{spot}	3		3		3	
Inclination i_\star [$^\circ$]	45.0		0.0		0.0	
Spot latitude Θ [$^\circ$]	50.0		10.0		0.0	
Derived parameters:						
RV semi-amplitude K [km/s]	0.373		0.525		0.288	
Phot. amplitude ΔI [mag]	0.072		0.070		0.075	
Scenario						
Radial Velocity Curve						
Observed parameters:						
RV semi-amplitude K [km/s]	0.335 ± 0.039		0.535 ± 0.051		0.304 ± 0.049	
Phot. amplitude ΔI [mag]	0.084 ± 0.014		—		0.074 ± 0.010	

Table 5.2: Input and derived parameters for CD-37 13029, TYC 8654-1115-1 and HD 140637 of the spot program. For comparison, the observed parameters K and ΔI are listed as well. The stellar radii are estimated using the known spectral types. The $v \sin i$ value has been taken from the analysis result using the method by Reiners et al. (2012). The plots show snapshots of the particular spot scenarios and the simulated RV curves.

5.3 Reproducibility of RV curves with spot scenarios

Sec. 5.2 has shown that a simple spot model with one circular spot on a limb darkened stellar sphere can reproduce the amplitude of a detected RV signal. Therefore, the question arises, if it is in principle possible to reproduce each measured RV curve with starspot scenarios. The application of the spot program to the three targets above showed that it does not need a complicated model to reproduce the amplitudes, but in order to reproduce the variation over time, some more considerations are needed. First of all, the application of different spot parameters (size, temperature, position) and stellar inclination can reproduce different shapes of the RV curve and by adding more spots to the system, the shapes become even more complex. But one problem arises in most of the cases: every time, the spot vanishes from the field of view, the radial velocity signal drops to zero. Conceivable exceptions are very large spots (larger than one 50 % of the star) and systems with (almost) pole-on orientation towards the observer (Fig. 5.2).

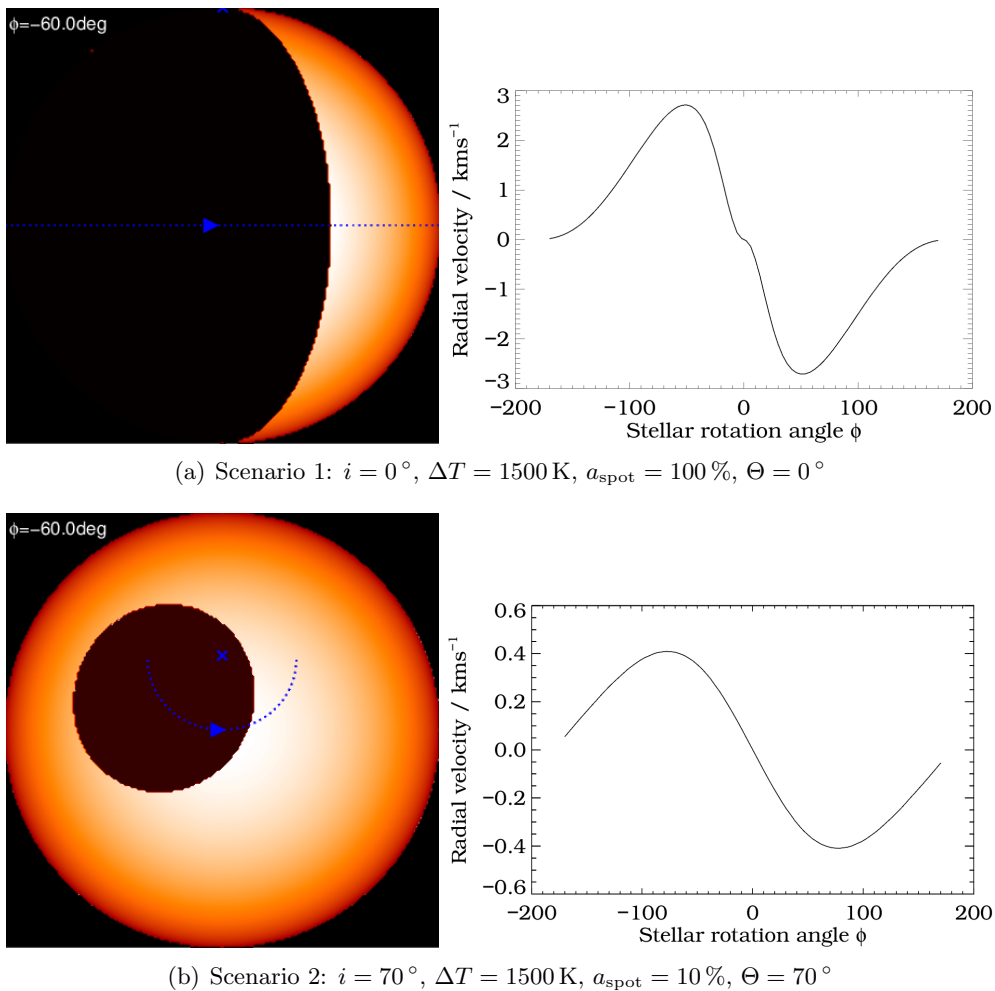


Figure 5.2: Different starspot scenarios and their induced RV signal

For extreme cases like a $K=2 \text{ km/s}$ RV signal, the program can still find a possible spot, which covers 50% of the stellar surface with a temperature of several thousand Kelvin below the photospheric temperature of the star. Nevertheless, in the end it is always a question of plausability, if the found solutions are really realistic.

Chapter 6

Radial velocity variations of EX Lupi¹

6.1 Introduction

EX Lupi is the prototype of the EXor class, a generic term for low-mass pre-main sequence stars, suffering regular optical outbursts between about 1 and 5 mag, which last for months or a few years and then decrease. Targets exhibiting longer and more intensive outbursts (in terms of brightness change) belong to the FUor class, named after the prototype FU Ori (Herbig, 2007).

EX Lupi has been intensively studied in both outburst and quiescence, e.g. in terms of accretion rate. Within outburst, the accretion is typically an order of magnitude higher than in quiescence, most likely due to an instability in the inner circumstellar disk at about 0.1 AU (Herbig, 1977, 2008; Lorenzetti et al., 2012). The origin of these outbursts is not yet clarified and still highly debated. Different mechanisms causing the postulated disk instability are discussed, and the existence of a possible companion causing the reoccurring outbursts could not be fully excluded. Wang et al. (2004) detected a companion at 225 AU projected distance with the direct imaging technique around FU Ori, which justifies an extensive companion search in the EX Lupi system as well.

EX Lupi was observed during several outburst of different magnitude. The latest outburst took place in 2008. Within outburst, the spectrum of EX Lupi changes significantly (e.g. Kóspál et al., 2011; Sicilia-Aguilar et al., 2012). Sicilia-Aguilar et al. (2012) show that during the outburst, strong emission from accretion-related spectral lines like Balmer and Paschen lines can be detected as well as emission of neutral metallic lines as Ca I. This emission of Ca I is clearly visible in FEROS spectra (Fig. 6.1). Ábrahám et al. (2009) analyzed the disk of EX Lupi during this outburst and discovered a crystallization of silicate grains. Most likely, the grain formation was caused by the increased luminosity and temperature during the outburst.

In the following sections I will present a radial velocity search for companions around EX Lupi using FEROS and HARPS spectra. Since EX Lupi is a very young star, the careful analysis of activity indicators is crucial, in order to exclude stellar activity as origin of any detected RV signal. These following sections represent my contribution to the publication of Kóspál et al. (2013, submitted to A&A).

¹This chapter contains the radial velocity and activity indicator analysis as well as the starspot discussion as in Kóspál et al. (2013, submitted to A&A)

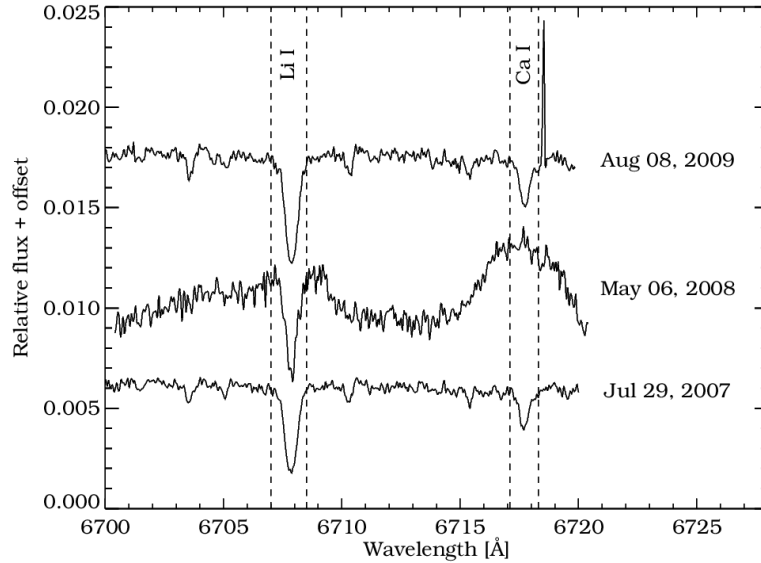


Figure 6.1: Comparison of FEROS spectra of EX Lupi in quiescence and outburst, showing the Li I line at 6708 \AA and a Ca I line at about 6718 \AA . The spectra at the top and bottom have been taken during quiescence, while the spectrum in the middle was taken during the 2008 outburst. It is clearly visible that the region around the Ca I line is completely filled up and the continuum is distorted, while the Li I region is less affected.

6.2 Observations and data reduction

Between 2007 and 2012 EX Lupi was observed in total 57 times with FEROS in the framework of different studies (PIs: Setiawan, Zechmeister, Weise, Launhardt, Gredel, Moór, Mohler-Fischer). The majority of the spectra (29) have been taken in object-calibration mode, including the simultaneous exposure to a ThAr calibration lamp, while the rest were observed in object-sky mode (simultaneous sky observation). Seven spectra were taken during the outburst in 2008 and could not be used for the radial velocity and activity indicator analysis (Sec. 6.3 and 6.5). Most on-site reduced spectra were available at our FEROS archive at MPIA, while some had to be downloaded from the ESO raw data archive² and reduced using the offline reduction pipeline, which is identical to the on-site software.

Furthermore, EX Lupi was observed 10 times with HARPS (PIs: Weise and Döllinger), with one spectrum taken in outburst. The reduced data have been downloaded from the ESO archive providing pipeline processed data³.

6.3 Radial velocity analysis

In order to obtain the radial velocities (RV) from both the FEROS and HARPS spectra, the cross-correlation method has been used. The basic principle of this method is to cross-correlate the object spectrum with an unshifted synthetic spectrum matching the spectral type of the object namely effective temperature T_{eff} and surface gravity $\log g$. The metallicity was fixed as solar. The effective temperature of EX Lupi has been estimated as

²http://archive.eso.org/eso/eso_archive_main.html

³<http://archive.eso.org/wdb/wdb/eso/repro/form>

~ 3750 K via the spectral type of M0.5 (Gras-Velázquez & Ray, 2005). The surface gravity of $\log g \approx 4.0$ has been determined by using the literature value of the stellar mass of $M = 0.6 M_{\odot}$ and of the stellar radius $R = 1.6 R_{\odot}$ (Aspin et al., 2010; Gras-Velázquez & Ray, 2005; Sipos et al., 2009). The template spectrum has been synthesized using the program SPECTRUM by David O. Gray⁴ (e.g. Gray, 1994).

In order to be able to achieve high RV precisions, it is necessary to broaden the synthetic spectrum to account for the rotational line broadening due to the stellar rotation in the object spectrum. Therefore, the $v \sin i$ has to be determined, which has been done by using the method described in Reiners et al. (2012). Our analysis revealed a $v \sin i$ for EX Lupi of less than 3 km/s. Unfortunately, a more accurate determination of the $v \sin i$ is not possible, because of the detection limit for FEROS of about 3 km/s. Reiners et al. (2012) argue that the threshold above which the rotational broadening can be seen in the spectral lines strongly depends on the resolving power of the instrument. The instrumental broadening dominates below this threshold of 3 km/s for FEROS and covers broadening effects in the spectral lines. The $v \sin i$ determination has been done using the HARPS data as well, which supported the result, but could not further constrain it.

FEROS and HARPS spectra were analyzed for radial velocity shifts in different ways. The FEROS spectra were already available in separate orders. For EX Lupi, I excluded the blue orders up to a wavelength of about 5580 Å, since the SNR was too low. In total I used 10 orders between 5580 Å and 7875 Å, carefully avoiding regions contaminated with telluric absorption features. I calculated the cross-correlation function of the observations with the synthetic spectrum for individual orders separately. By fitting a Gaussian to the CCF, I determined the radial velocity shift for each order and calculated the weighted average for each data point. The errors for the average values were calculated using the relation derived in Setiawan et al. (2003). Since the barycentric correction of the FEROS data calculated by the automatic reduction pipeline is not precise enough, I re-calculated the correction as described in Sec. 2.4.1 and applied the result to the RV data.

The ESO archive provides reduced HARPS spectra including the determination of the radial velocity stored in the file headers using a template mask. Since the RV analysis of HARPS is not very transparent and I wanted to carry out the analysis as similar to the FEROS analysis as possible, I did not use these pipeline results. Instead, I used the same method as for the analysis of the FEROS spectra. Therefore, I artificially splitted the merged HARPS spectra into 9 different orders in a wavelength range between 5450 Å and 6865 Å, again avoiding telluric absorption lines, and carried out the same radial velocity determination procedure by cross-correlating the object spectra with the synthetic template. Therefore, the RV analysis of both FEROS and HARPS data was done on the same spectral region. As mentioned above, both FEROS and HARPS observations taken during 2008 were not considered for the analysis due to significant changes in the spectra by EX Lupi being in outburst (e.g. Kóspál et al., 2011; Sicilia-Aguilar et al., 2012).

6.4 Radial velocity results

Using the method described above, I obtained in total 45 FEROS and 9 HARPS RV data points. Five FEROS spectra were not usable due to a very low SNR caused by bad weather or high airmass. Seven FEROS spectra and one HARPS spectrum were dismissed from the analysis since they were taken during the outburst in 2008 (see above).

⁴SPECTRUM is freely available on <http://www1.appstate.edu/dept/physics/spectrum/spectrum.html>

Since the number of available HARPS data points is not sufficient to carry out an independent radial velocity periodicity analysis, I first use only the FEROS results and afterwards conduct a combined analysis of both FEROS and HARPS results:

6.4.1 Analysis of FEROS radial velocity results

The 45 FEROS data points have been fitted using the Generalised Lomb-Scargle (GLS) method (see Zechmeister & Kürster, 2009). Figure 6.2 shows the data points phase-folded to the best-fitting period of (7.417 ± 0.001) days, while the orbital and system parameters determined with the fit are listed in Table 6.1. The periodogram in Fig. 6.2 shows two significant periods with a FAP of $< 10^{-3}$. One around 1 d, which has been confirmed as caused by the measurement sampling (cf. window function, Fig. 6.2, bottom panel), another at 7.417 d, which can not be assigned to sampling issues.

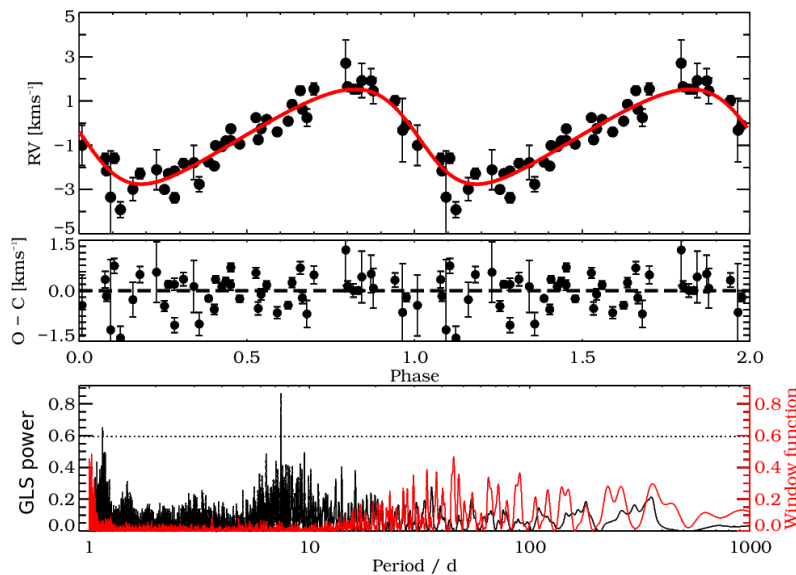


Figure 6.2: Best fit of the radial velocity data points obtained with FEROS. Upper panel: radial velocity phase-folded with a period of 7.417 d, middle panel: phase-folded residua of the fit including errors, bottom panel: GLS periodogram showing the best period of (7.417 ± 0.001) days and the sampling induced period at about 1 d. The horizontal line indicates the FAP level of 0.1%. The window function is overplotted in red.

In order to determine whether the radial velocity periodicity of 7.417 d has its origin in the outburst of 2008, I separately mark the data points obtained in the different years between 2007 and 2012 in Fig. 6.3, again excluding data from 2008, indicating that both data before and after the outburst are consistent.

6.4.2 Combined analysis of FEROS and HARPS radial velocity results

The obtained radial velocities always contain influences of the instrument itself which originate for instance in the different methods of data reduction. This usually results in a different offset velocity of the target, complicating the analysis of data sets from multiple instruments. That is why I used the IDL program *RVlin.pro* by Jason T. Wright⁵ (Penn

⁵<http://exoplanets.org/code/>

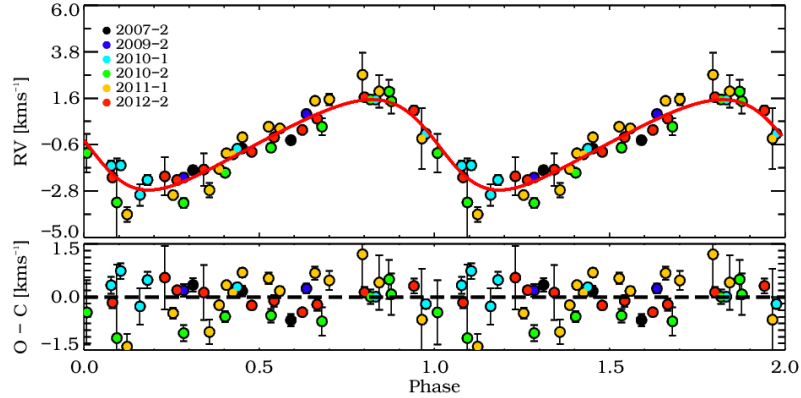


Figure 6.3: Best fit of FEROS radial velocity data highlighting the data points obtained in the single years from black (2007) to red (2012). The residua show the same color coding. The three data points from 2007 before the outburst match the fit solution dominated by the post-outburst measurements.

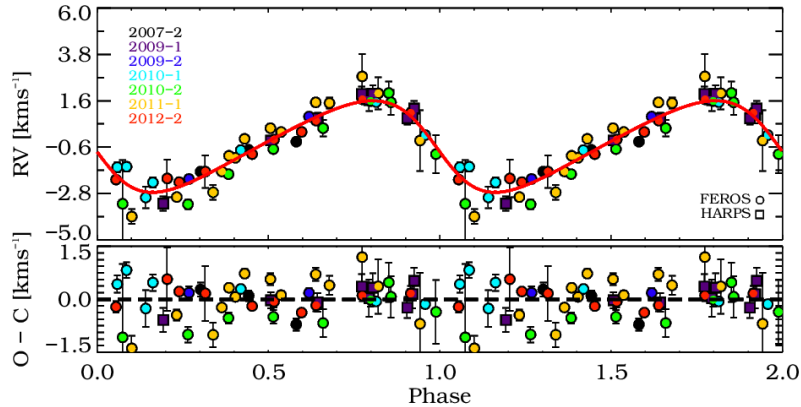


Figure 6.4: Best fit of FEROS and HARPS radial velocity data using the *RVlin.pro* IDL package. The different colors indicate the observation date, while filled circles represent FEROS and squares HARPS data points. The residuals show the same color and shape coding.

State University) which inserts an additional fitting parameter to correct for a relative offset velocity between both instruments. The errors of the fitting parameter can be determined using a bootstrap algorithm implemented in the IDL routine *boottran.pro* by Sharon Wang (Penn State University) (Wang et al., 2012).

Fig. 6.4 shows the best fit of the combined data sets indicating the observation dates. In Table 6.1 the values of the best fitting parameters for the Keplerian orbit solution are listed. By correcting the RV with the determined offset velocity from *RVlin.pro* it is possible to calculate a GLS periodogram for the combined data set of both instruments and determine with this the FAP of the 7.417 d period. The result is a significantly smaller FAP of $6.8780 \cdot 10^{-26}$ as for the FEROS RV data (Table 6.1).

6.5 Analysis of activity indicators

As already explained in Sec. 2.5 a (sub-)stellar companion induces a Doppler shift in the spectrum of its host star due to its motion around the common center-of-mass. In case

Parameter	FEROS		FEROS & HARPS	
	Value	Error	Value	Error
best fitting Keplerian period [d]	7.417	0.001	7.417	0.001
RV semi-amplitude [km/s]	2.154	0.103	2.175	0.099
eccentricity	0.229	0.042	0.23	0.05
longitude of periastron ω [°]	96.2	12.9	96.8	11.4
periastron passage [d]	2455583.108	0.256	2455405.112	0.224
Offset RV [km/s]	-0.519	0.071	-0.518	0.067
Offset FEROS-HARPS [km/s]	—		0.291	
FAP (see Cumming, 2004)	$1.276 \cdot 10^{-14}$		$6.696 \cdot 10^{-27}$	
$M_P \cdot \sin i$ [M_J]	14.55	0.75	14.68	0.73
semi-major axis a [AU]	0.063	0.005	0.063	0.005

Table 6.1: Best fitting parameter for the Keplerian solution of FEROS data analysis with GLS and of the combined FEROS and HARPS radial velocity data points obtained with *RVlin.pro*, the stellar mass was assumed to be $0.6 M_\odot$.

stellar activity patterns cover the stellar surface, i.e. stellar spots, not only a Doppler shift is induced but also spectral lines are distorted.

In order to test, whether the detected RV signal in both the FEROS and HARPS spectra is induced by stellar spots, the first step is to analyze a variety of activity indicators. This analysis has been done exclusively on the FEROS spectra, since some activity indicators are not covered by HARPS spectra. In case activity indicators show the same period as the RV data, stellar activity is most likely the origin of the detected RV signal and a companion hypothesis can be excluded. If activity indicators do not reveal the period of 7.417 d, the probability of a companion in the system increases. Many different activity indicators (as described in detail in Sec. 2.5) can be used as tracers for stellar activity. In case of EX Lupi, I have chosen the analysis of the CCF bisectors in terms of the BVS, the BVD and the BC as well as the asymmetry of the CCF. The last is calculated using the slope of the CCF at each velocity point. Furthermore, the following temperature-sensitive spectral feature were chosen: the line-depth ratio (LDR) of the V I line at 6268.87 \AA and the Fe I line at 6270.23 \AA . Additionally, spectroscopic indices have been calculated as described in Sec. 2.5. In order to analyze the chromospheric activity, the chromospheric activity index S_{FEROS} of the Ca II K line has been measured as well as the EW of the Ca I line at 8662 \AA . The calculation of the bisectors has been modified for EX Lupi by P. Ábrahám from Konkoly Observatory, Budapest. By carefully selecting only four spectral orders, he normalized the CCF and adjusted the CCF regions in which the bisectors are determined (Eq. 2.24-2.26, Sec. 2.5). This way, the individual errors were reduced. Since the comparison of the BVS and RV variation in the typical correlation diagram is then based on different spectral orders (4 for BVS, 10 for the FEROS RV), which might induce systematic errors, I abandoned the optimization of the bisectors for the 21 targets described earlier and used the optimized bisectors only for the periodicity analysis. The periodograms for the used activity indicators are shown in Fig. 6.5 and 6.6. The results show that the 7.417 d RV period is not evident in any of the activity indicators. The correlation diagram of BVS and RV and BVS and RV residua, respectively, are shown in Figure 6.7. The linear Pearson correlation coefficient R_{Pearson} was calculated as 0.08 for the correlation with the RV and as 0.27 for the correlation with the RV residua, indicating no strong correlation between the quantities.

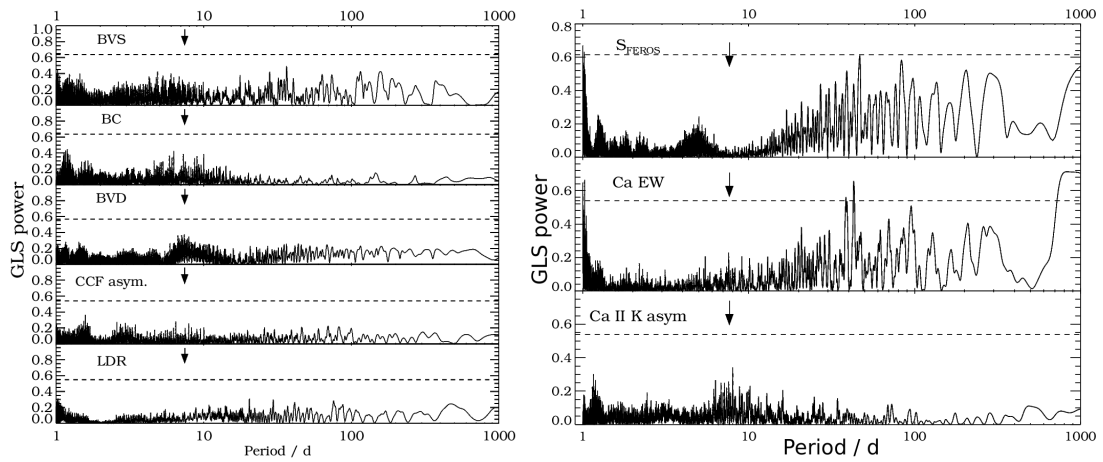


Figure 6.5: GLS periodograms of bisectors, CCF asymmetry, line-depth ratio (LDR), S_{FEROS} , Ca EW and Ca II K asymmetry. Dashed horizontal lines show the FAP level of 0.1%. The arrows mark the detected RV period of 7.417 d.

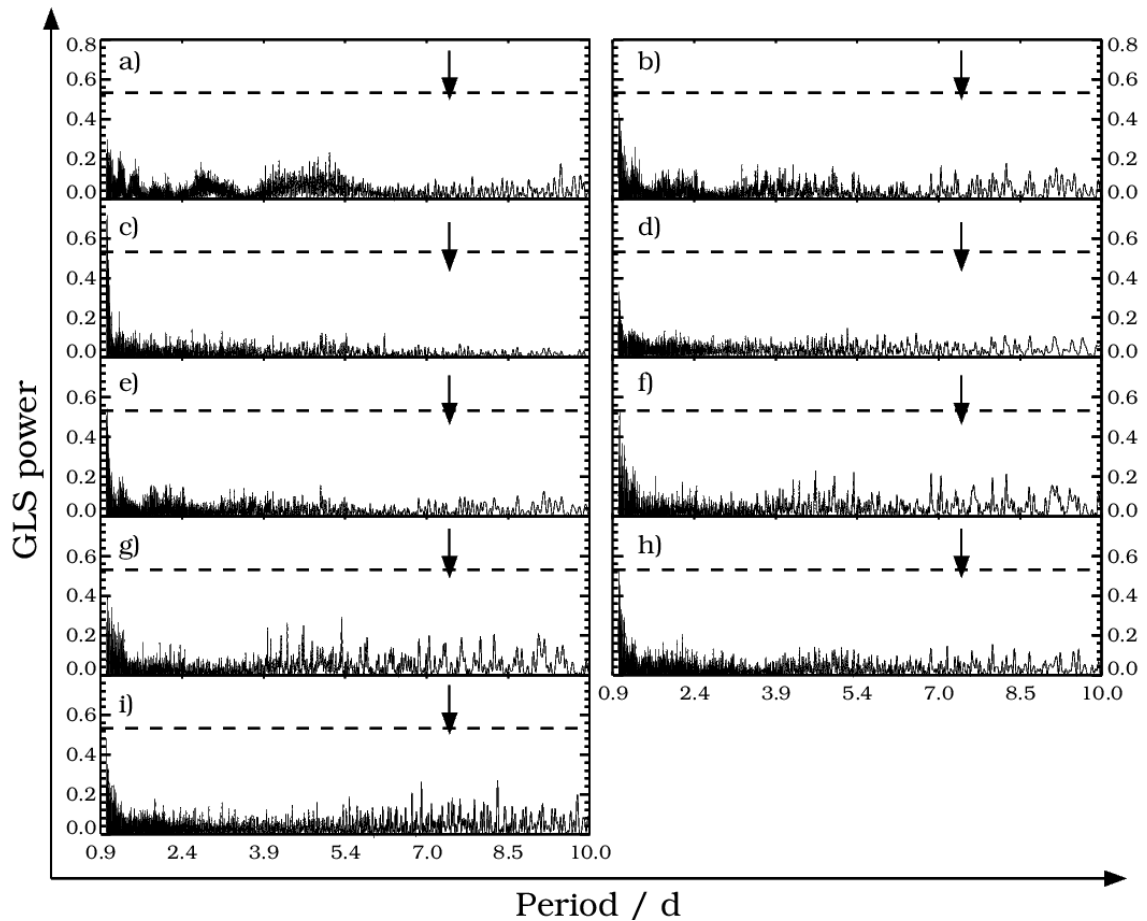


Figure 6.6: GLS periodograms of 9 spectroscopic indices. a) TiO 1, b) TiO 1, c) TiO 3, d) TiO 4, e) TiO 5, f) CaH 2, g) CaH 3, h) CaOH, i) H_{α} . Dashed horizontal lines mark the FAP level of 0.1%. Black arrows indicate the RV period of 7.417 d.

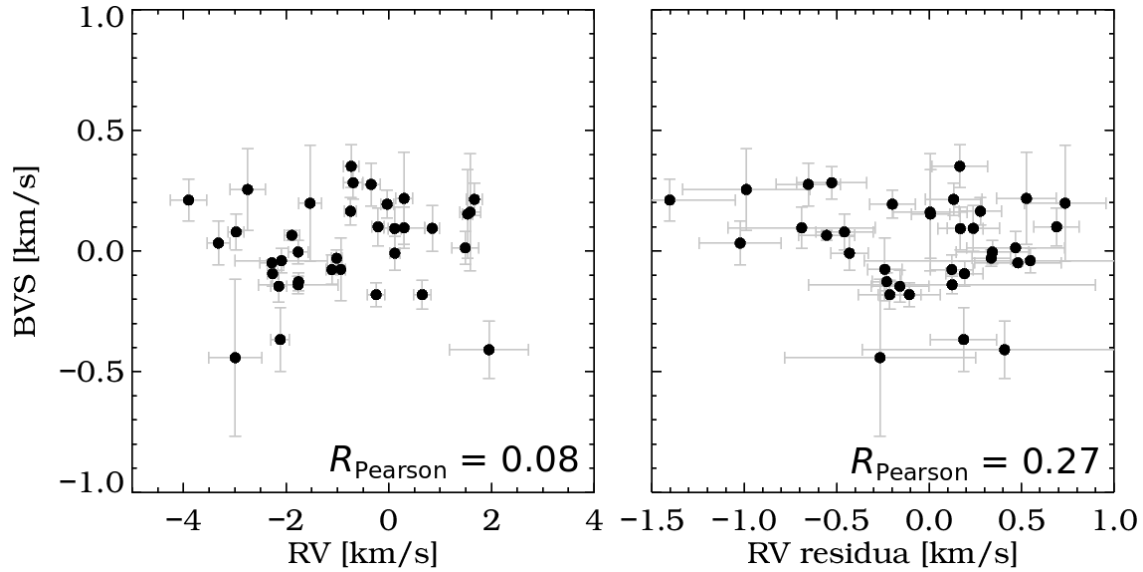


Figure 6.7: Correlation between BVS and RV and BVS and RV residua, respectively, for EX Lupi

6.6 Starspot scenarios

The analysis above has shown that the 7.417 d period was not evident in any of the stellar activity indicators and is therefore most likely not induced by activity patterns on the stellar surface.

In the following, I will however assume that the 7.417 d period identified in the RV analysis, is caused by stellar activity as spots on the surface and therewith represents the stellar rotational period. Using the previously described spot program, it is possible to simulate different spot scenarios, to identify one that could possibly cause an RV amplitude of about 2.2 km/s. Since the RV amplitude is in comparison to the measured $v \sin i$ of < 3 km/s very large, spots with a large filling factor and a large temperature difference to the stellar photosphere are expected.

One scenario being able to induce an RV amplitude of about 2.2 km/s is a large dark cool spot on the stellar surface. With a filling factor of 100 % of one stellar hemisphere, it covers half of the stellar surface. The temperature difference between spot and photosphere would be 2500 K. While the star is inclined by 30° in this scenario, the spot latitude is 30° . Since it is most unlikely that such a large cool spot is stable over long time scales (2007-2012), the companion scenario is more likely.

Another possibility is to simulate a hot spot on the stellar surface. One scenario being able to reproduce the detected RV amplitude is a spot with a temperature of 5500 K hotter than the stellar photosphere, again filling half of the stellar surface. The stellar inclination is 0° in this scenario and the spot is positioned directly at the equator. Nevertheless, one should note that this spot program was not designed for hot spots and the result is therefore not trustworthy and will be neglected during the following discussion.

6.7 Summary and discussion

Within my study of the FEROS and HARPS spectra of EX Lupi I have detected a stable (over the monitoring time of 5 yrs) RV signal with a period of 7.417 d and a RV semi-amplitude of ~ 2.2 km/s. The detection has been made using 45 FEROS and 9 HARPS measurements. The determined orbital solution is supported by measurements taken with both instruments after the outburst in 2008 and by three FEROS spectra taken before the outburst. This indicates that the detected RV signal already existed before the outburst and was not triggered by it. This further supports the hypothesis of a companion in the system, because stellar activity patterns are expected to change during the kind of large outburst that EX Lupi exhibited in 2008. Since the number of HARPS spectra was not sufficient to execute an independent RV analysis, I analyzed the RV twice, once for the FEROS measurements only and once for the joined analysis using both instruments measurements. The obtained results are consistent with each other.

In order to exclude stellar activity as cool spots on the stellar surface as origin of the signal, I analyzed a variety of activity indicators, looking for evidence of the 7.417 d RV period in the results. None of the indicators showed the RV period, indicating that the measured RV signal was induced by a line shift of the stellar spectrum rather than a line distortion induced by activity surface patterns.

In order to simulate which stellar spots could induce the detected RV amplitude, I used the spot program described in Section 5.1 to simulate the impact of different spot scenarios on the RV semi-amplitude. The results showed that a very large spot, covering half of the stellar surface, with a very low temperature (about 2500 K cooler than the stellar photosphere) is necessary to induce a ~ 2.2 km/s RV amplitude. Furthermore, the influence of a hot spot was tested. Since the program was not designed to deal with hot spots, the obtained results are not trustworthy.

Assuming an enormous dark cool spot as simulated above, several doubts arise. First of all, one would expect a significant signal in one or more of the activity indicators induced by this large spot. Especially the line-depth ratio (LDR) of VI and Fe I is very sensible to temperature changes on the stellar surface (Sec. 2.5) and its measurements should reflect the temperature changes caused by the spot. Also, the spectral lines should be significantly distorted by that kind of spot, what should be measurable in the bisectors as well as in the asymmetry of several lines. Furthermore, it is doubtful whether such a spot is physically plausible and whether it could be stable over 5 yrs. Another problem arising with that kind of spot is the photometric signal: such a spot would induce a photometric variation of more than 9 mag in V-band. As photometric measurements in Kóspál et al. (2013, submitted to A&A) show, no such strong variations could be detected in any photometric band. Further analyses using photometric data and emission lines detected in both FEROS and HARPS spectra are discussed in Kóspál et al. (2013, submitted to A&A), giving several new possibilities to explain the detected RV signal as for example a combination of a companion and accretion columns onto the star. Since this analysis has been done by collaborators and relies on more than just stellar spectra, I refer to Kóspál et al. (2013, submitted to A&A) and do not describe the different analysis steps and results in this thesis.

Chapter 7

The search for exoplanets with the HATSouth survey

7.1 The HATSouth Survey

In order to identify possible planet-hosting stars, large-scale surveys are of prime importance. Systematic transit surveys like HATNet (Bakos et al., 2011), WASP (Christian et al., 2006), TrES (Alonso et al., 2004) and now the Kepler mission (Borucki et al., 2010, 2011b; Batalha et al., 2013) have demonstrated the high return in terms of planet discoveries. However, it is not only the discovery that makes transit observations important, but the possibility to determine the planet mass, if precise radial velocity observations are added. The HATNet transit survey has already identified 43 exoplanets (exoplanet.eu, Jul 11 2013). The global southern counterpart of HATNet, HAT-South (Bakos et al., 2013), started in 2010 to produce exciting candidates, especially in the regime of relatively bright stars. These bright stars with transiting planets are not covered by Kepler and form ideal targets for follow-up transit spectroscopy. HAT-South is a transit network operated by Princeton University, Australian National University (ANU), Pontificia Universidad Catolica de Chile (PUC) and MPIA with three stations on three different continents: at Las Campanas Observatory (LCO) in Chile, South America, at H.E.S.S.¹ site in Namibia, Africa, and at Siding Spring Observatory (SSO) in Australia. It is the first homogenous global network in the southern sky and allows to near 24 hrs monitoring of selected fields due to the location of the selected sites (LCO \rightarrow SSO = 141° , SSO \rightarrow HESS = 133° , and HESS \rightarrow LCO = 86° , Bakos et al., 2013). Fig. 7.1 shows the location of the three HATSouth sites. Each location hosts two HATSouth units, which hold four 0.18 m diameter telescope tubes. The field-of-view on the sky is $8.2^\circ \times 8.2^\circ$. Four 4K \times 4K CCD cameras monitor the sky in Sloan r filter. The pixel scale corresponds to $3.7''$ /pixel. For detailed information on the HATSouth instruments and operations I refer to the instrument description paper by Bakos et al. (2013).

A variety of powerful instruments at different telescopes allows very effective follow-up observations for good candidates both photometrically and spectroscopically. So far four candidates could be confirmed, two (HATS-1 and -2) are published, one publication (HATS-3) is submitted and another one (HATS-4) is in preparation.

HATS-1b is a $1.86 M_J$ and $1.30 R_\odot$ planet in a 3.45 d orbit around a 12 mag G-dwarf star (Penev et al., 2013). The candidate was detected by all three stations between Jan

¹High Energy Spectroscopic System

2010 and Aug 2010. Partial transits observed by the SITE3 camera on Swope 1.0 m telescope at LCO and by the Spectral instrument on the 2.0 m Faulkes Telescope South (FTS) helped to revise the ephemeris, while the follow-up observations with GROND at the 2.2 m MPG/ESO telescope at La Silla Observatory (LSO), Chile, delivered a full transit taken simultaneously in three different filters (g , r and i). The high-precision RV follow-up was done with Coralie at the Euler 1.2 m telescope at LSO, the CYCLOPS spectrograph at the 3.9 m Anglo-Australian Telescope (AAT) at SS) and with FEROS. The latter were done mainly under my initiative and within MPG guaranteed time.

HATS-3 is an inflated hot Jupiter with $1.07 M_J$ and $1.38 R_\odot$ in a 3.55 d orbit around a 12.4 mag F-dwarf star (Bayliss et al., 2013). Analogous to HATS-1b, the detection has been done by all three HATSouth stations. The photometric and spectroscopic follow-up observations have been executed by the same instruments, allowing a consistent analysis in comparison to the previously published detections.

In the framework of my thesis, I'm responsible for the spectroscopic follow-up observations with FEROS within MPG guaranteed time. Doing so, I determine the stellar parameters using SME and calculate the radial velocity variation. Furthermore, I determine bisectors and other activity indicators if needed.

The following section is based on the work done by myself and collaborators which was published in A&A with myself as first author as Mohler-Fischer et al. (2013).



Figure 7.1: The three sites of the HATSouth survey: Las Campanas Observatory (LCO) in Chile, HESS site in Namibia and Siding Spring Observatory (SSO) in Australia

image credit: Bakos et al. (2013)

7.2 HATS-2b: A transiting extrasolar planet orbiting a K-type star showing starspot activity²

Abstract

We report the discovery of HATS-2b, the second transiting extrasolar planet detected by the HATSouth survey. HATS-2b is moving on a circular orbit around a $V = 13.6$ mag, K-type dwarf star (GSC 6665-00236), at a separation of 0.0230 ± 0.0003 AU and with a period of 1.3541 days.

The planetary parameters have been robustly determined using a simultaneous fit of the HATSouth, MPG/ESO 2.2 m/GROND, Faulkes Telescope South/Spectral transit photometry and MPG/ESO 2.2 m/FEROS, Euler 1.2 m/CORALIE, AAT 3.9 m/CYCLOPS radial-velocity measurements. HATS-2b has a mass of $1.37 \pm 0.16 M_J$, a radius of $1.14 \pm 0.03 R_J$ and an equilibrium temperature of 1567 ± 30 K. The host star has a mass of $0.88 \pm 0.04 M_\odot$, radius of $0.89 \pm 0.02 R_\odot$ and shows starspot activity. We characterized the stellar activity by analyzing two photometric-follow-up transit light curves taken with the GROND instrument, both obtained simultaneously in four optical bands (covering the wavelength range of 3860 – 9520 Å). The two light curves contain anomalies compatible with starspots on the photosphere of the host star along the same transit chord.

Introduction

The first detection of a planet orbiting a main-sequence star (51 Peg; Mayor & Queloz, 1995) started a new era of astronomy and planetary sciences. In the years since, the focus on exoplanetary discovery has steadily increased, resulting in more than 850 planets being detected in 677 planetary systems³. Statistical implications of the exoplanet discoveries, based on different detection methods, have also been presented (e.g. Mayor et al., 2011; Howard et al., 2012; Cassan et al., 2012; Fressin et al., 2013). Most of these planets have been detected by the transit and radial velocity (RV) techniques. The former detects the decrease in a host star’s brightness due to the transit of a planet in front of it, while the latter measures the Doppler shift of host star light due to stellar motion around the star-planet barycenter. In the case of transiting extrasolar planets, the powerful combination of both methods permits a direct estimate of mass and radius of the planetary companion and therefore of the planetary average density and surface gravity. Such information is of fundamental importance in establishing the correct theoretical framework of planet formation and evolution (e.g. Liu et al., 2011; Mordasini et al., 2012a,b).

Thanks to the effectiveness of ground- and space-based transit surveys like TrES (Alonso et al., 2004), XO (McCullough et al., 2005), HATNet (e.g. Bakos et al., 2012; Hartman et al., 2012), HATSouth (Penev et al., 2013), WASP (e.g. Hellier et al., 2012; Smalley et al., 2012), QES (Alsubai et al., 2011; Bryan et al., 2012), KELT (Siverd et al., 2012), COROT (e.g. Rouan et al., 2012; Pätzold et al., 2012) and Kepler (Borucki et al., 2011a,b; Batalha et al., 2013), one third of the transiting exoplanets known today were detected in the past 2 years. In some cases, extensive follow-up campaigns have been necessary to determine the correct physical properties of several planetary systems (e.g. Southworth et al., 2011; Barros et al., 2011; Mancini et al., 2013), or have been used to discover other planets by measuring transit time variations (e.g. Rabus et al., 2009b, Steffen et al., 2013). With high-quality photometric observations it is also possible to detect transit anomalies which are connected with physical phenomena, such as starspots (Pont et al., 2007; Rabus

²Section following Mohler-Fischer et al. (2013)

³exoplanet.eu, as at 2013, March 28

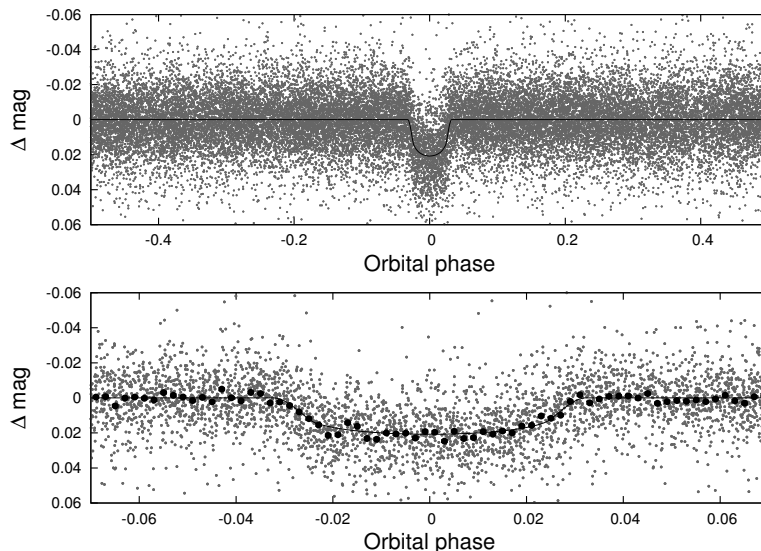


Figure 7.2: *Top panel:* Unbinned instrumental r -band light curve of HATS-2 folded with the period $P = 1.354133$ days resulting from the global fit described in Section 7.2. *Lower panel:* zoom in on the transit; the dark filled points show the light curve binned in phase using a bin size of 0.002. In both panels, the solid line shows the best-fit transit model (see Section 7.2).

et al., 2009a; Désert et al., 2011; Tregloan-Reed et al., 2013), gravity darkening (Barnes, 2009; Szabó et al., 2011), stellar pulsations (Collier Cameron et al., 2010), tidal distortion (Li et al., 2010; Leconte et al., 2011), and the presence of additional bodies (exomoons) (Kipping et al., 2009; Tusnski & Valio, 2011).

In this paper we report the detection of HATS-2b, the second confirmed exoplanet found by the HATSouth transit survey. HATSouth is the first global network of robotic wide-field telescopes, located at three sites in the Southern hemisphere: Las Campanas Observatory (Chile), Siding Spring Observatory (Australia) and H.E.S.S. (High Energy Stereoscopic System) site (Namibia). We refer the reader to Bakos et al. (2013), where the HATSouth instruments and operations are described in detail. HATS-2b is orbiting a K-type dwarf star and has characteristics similar to those of most hot-Jupiter detected so far. The photometric follow-up performed during two transits of this planet clearly reveals anomalies in the corresponding light curves, which are very likely related to the starspot activity of the host star.

Observations

Photometry

The star HATS-2⁴ was identified as a potential exoplanet host based on photometry from all the instruments of the HATSouth facility (HS-1 to HS-6) between January 19 and August 10, 2010 (details are reported in Table 7.1). The detection light curve is shown in Figure 7.2. This figure shows that the discovery data is of sufficient quality that it permits fitting a Mandel & Agol (2002) limb-darkened transit model. A detailed overview of the observations, the data reduction and analysis is given in Bakos et al. (2013). HATS-2 was

⁴GSC 6665-00236; $V = 13.562 \pm 0.016$; J2000 $\alpha = 11^{\text{h}}46^{\text{m}}57^{\text{s}}.38$, $\delta = -22^{\circ}33'46''.77$, proper motion $\mu_{\alpha} = -45.8 \pm 1.1 \text{ mas/yr}$, $\mu_{\delta} = -1.3 \pm 1.5 \text{ mas/yr}$; UCAC4 catalogue, Zacharias et al., 2012

afterwards photometrically followed-up three times by two different instruments at two different telescopes. On UT 2011, June 25, the mid-transit and the egress were observed with the “Spectral” imaging camera, mounted at 2.0 m Faulkes Telescope South (FTS), situated at Siding Spring Observatory (SSO) and operated as part of the Las Cumbres Observatory Global Telescope (LCOGT) network. The Spectral camera hosts a $4K \times 4K$ array of $0.15''$ pixels, which is readout with 2×2 binning. We defocus the telescope to reduce the effect of imperfect flat-fielding and to allow for longer exposure times without saturating. We use an *i*-band filter and exposure times of 30 s, which with a 20 s readout time gives 50 s cadence photometry.

The data is calibrated with the automated LCOGT reduction pipeline, which includes flat-field correction and fitting an astrometric solution. Photometry is performed on the reduced images using an automated pipeline based on aperture photometry with Source Extractor (Bertin & Arnouts, 1996). The partial transit observed is shown in Figure 7.3, and permitted a refinement of the transit depth and ephemeris. The latter was particularly important for the subsequent follow-up observations performed with the MPG⁵/ESO 2.2m telescope at the La Silla Observatory (LSO). Two full transits were covered on February 28 and June 1, 2012, using GROND (**G**amma-**R**ay **B**urst **O**ptical/**N**ear-**I**nfrared **D**etector), which is an imaging camera capable of simultaneous photometric observations in four optical (identical to Sloan *g*, *r*, *i*, *z*) passbands (Greiner et al., 2008). The main characteristics of the cameras and details of the data reduction are described in Penev et al. (2013). The GROND observations were performed with the telescope defocussed and using relatively long exposure times (80-90 s, 150-200 s cadence). This way minimises noise sources (e.g. flat-fielding errors, atmospheric variation or scintillation, variation in seeing, bad tracking and Poisson noise) and delivers high-precision photometry of transit events (Alonso et al., 2008; Southworth et al., 2009). The light curves and their best-fitting models are shown in Fig. 7.3. Distortions in the GROND light curves are clearly visible, which we ascribe to stellar activity. These patterns are analyzed in detail in Section 4. Table 7.1 gives an overview of all the photometric observations for HATS-2.

Spectroscopy

HATS-2 was spectroscopically followed-up between May 2011 and April 2012 by five different instruments at five individual telescopes. The follow-up observations started in May 2011 with high signal to noise (S/N) medium resolution ($\lambda/\Delta\lambda = 7000$) reconnaissance observations performed at the ANU 2.3 m telescope located at SSO, with the image slicing integral field spectrograph WiFeS (Dopita et al., 2007). The results showed no RV variation with amplitude greater than 2 km s^{-1} ; this excludes most false-positive scenarios involving eclipsing binaries. Furthermore, an initial determination of the stellar atmospheric parameters was possible ($T_{eff,\star} = 4800 \pm 300 \text{ K}$, $\log g_{\star} = 4.4 \pm 0.3$), indicating that HATS-2 is a dwarf star. Within the same month, high precision RV follow-up observations started with the fibre-fed echelle spectrograph CORALIE (Queloz et al., 2000) at the Swiss Leonard Euler 1.2 m telescope at LSO, followed by further high precision RV measurements obtained with the fibre-fed optical echelle spectrograph FEROS (Kaufer & Pasquini, 1998) at the MPG/ESO 2.2 m telescope at LSO. Using the spectral synthesis code *SME* (**S**pectroscopy **M**ade **E**asy, Valenti & Piskunov, 1996) on the FEROS spectra, it was possible to determine more accurate values for the stellar parameters (see Sect. 7.2). Further RV measurements were obtained with the CYCLOPS fibre-based integral field unit, feeding the cross-dispersed echelle spectrograph UCLES, mounted at the 3.9 m

⁵Max Planck Gesellschaft

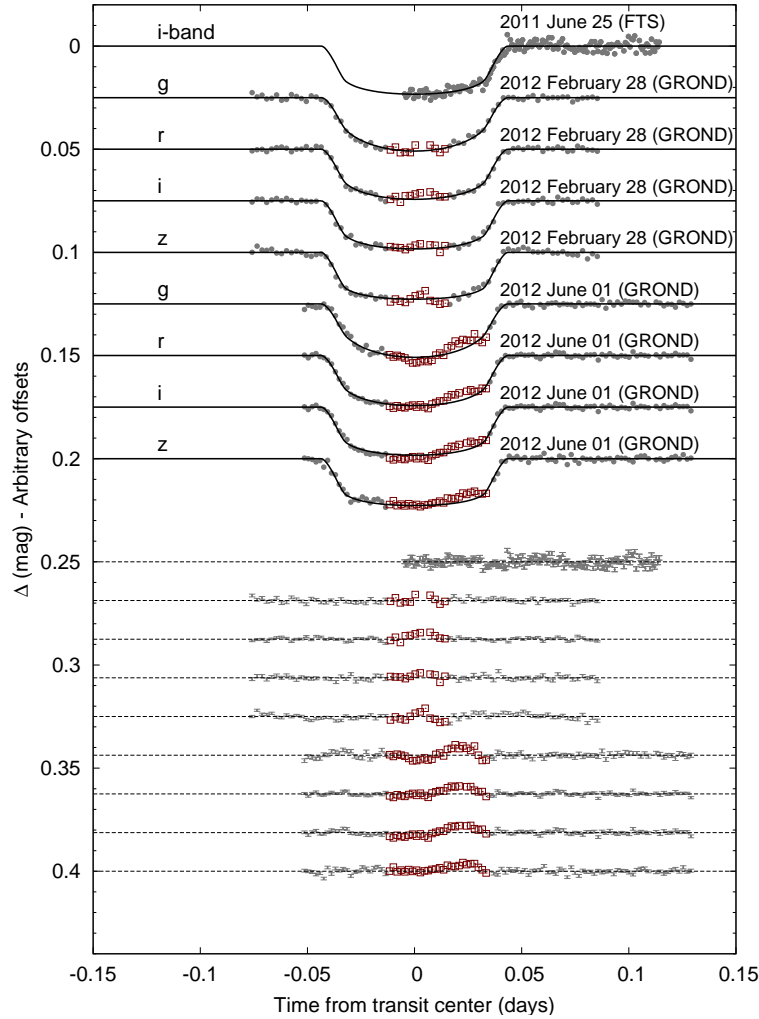


Figure 7.3: Phased transit light curves of HATS-2. The dates and instruments used for each event are indicated. The light curves are ordered according to the date and to the central wavelength of the filter used (Sloan g , r , i and z). Our best fit is shown by the solid lines (see Section 7.2). Residuals from the fits are displayed at the bottom, in the same order as the top curves. The GROND datapoints affected by anomalies are marked with red empty squares and were not considered in estimating the final values of the planetary-system parameters (see Sect. 7.2).

Anglo-Australian Telescope (AAT) at SSO, and with the fibre-fed echelle spectrograph FIES at the 2.5 m telescope at the Nordic Optical Telescope in La Palma. We refer to Penev et al. (2013) for a more detailed description of the observations, the data reduction and the RV determination methods for each individual instrument that we utilized.

In total, 29 spectra were obtained, which are summarized in Table 7.2. Table 7.3 provides the high-precision RV and bisector span measurements. Figure 7.4 shows the combined high-precision RV measurements folded with the period of the transits. The error bars of the RV measurements include a component from astrophysical/instrumental jitter allowed to differ for the three instruments (Coralie: 74.0 ms^{-1} , FEROS: 44.0 ms^{-1} , CYCLOPS: 193.0 ms^{-1} , see Sec. 3.3).

Facility	Date(s)	# of images	Cadence (s)	Filter
Discovery				
HS-1 (Chile)	2010, January 24 - August 09	5913	280	Sloan <i>r</i>
HS-2 (Chile)	2010, February 11 - August 10	10195	280	Sloan <i>r</i>
HS-3 (Namibia)	2010, February 12 - August 10	1159	280	Sloan <i>r</i>
HS-4 (Namibia)	2010, January 26 - August 10	8405	280	Sloan <i>r</i>
HS-5 (Australia)	2010, January 19 - August 08	640	280	Sloan <i>r</i>
HS-6 (Australia)	2010, August 06	8	280	Sloan <i>r</i>
Follow-up				
FTS/Spectral	2011, June 25	158	50	Sloan <i>i</i>
MPG/ESO 2.2 m / GROND	2012, February 28	69	80	Sloan <i>g</i>
MPG/ESO 2.2 m / GROND	2012, February 28	70	80	Sloan <i>r</i>
MPG/ESO 2.2 m / GROND	2012, February 28	69	80	Sloan <i>i</i>
MPG/ESO 2.2 m / GROND	2012, February 28	71	80	Sloan <i>z</i>
MPG/ESO 2.2 m / GROND	2012, June 1	99	80	Sloan <i>g</i>
MPG/ESO 2.2 m / GROND	2012, June 1	99	80	Sloan <i>r</i>
MPG/ESO 2.2 m / GROND	2012, June 1	99	80	Sloan <i>i</i>
MPG/ESO 2.2 m / GROND	2012, June 1	99	80	Sloan <i>z</i>

Table 7.1: Summary of photometric observations of HATS-2

Analysis

Stellar parameters

As already mentioned in Sect. 7.2, we estimated the stellar parameters, i.e. effective temperature $T_{eff\star}$, metallicity [Fe/H], surface gravity $\log g$ and projected rotational velocity $v \sin i$, by applying *SME* on the high-resolution FEROS spectra. *SME* determines stellar and atomic parameters by fitting spectra from model atmospheres to observed spectra and estimates the parameter errors using the quality of the fit, expressed by the reduced χ^2 , as indicator. Whenever the S/N is not very high, or the spectrum is contaminated with telluric absorption features, cosmics, or stellar emission lines, the reduced χ^2 does not always converge to unity, which leads to small errors for the stellar parameter values. To estimate of error bars, we used *SME* to determine the stellar parameters of each FEROS

Telescope/Instrument	Date Range	# of Obs.	Instrument resolution	Observing mode
ANU 2.3 m/WiFeS	2011, May 10-15	5	7000	RECON
Euler 1.2 m/Coralie	2011, May 20-21	4	60000	HPRV
ESO/MPG 2.2 m/FEROS	2011, June 09-25	9	48000	HPRV
ESO/MPG 2.2 m/FEROS	2012, January 12	1	48000	HPRV
ESO/MPG 2.2 m/FEROS	2012, March 04-06	2	48000	HPRV
ESO/MPG 2.2 m/FEROS	2012, April 14-18	3	48000	HPRV
AAT 3.9 m/CYCLOPS	2012, January 05-12	4	70000	HPRV
NOT 2.5 m/FIES	2012, March 15	1	46000	RECON

Table 7.2: Summary of spectroscopic observations of HATS-2.

Observing mode: HPRV = high-precision RV measurements, RECON = reconnaissance observations.

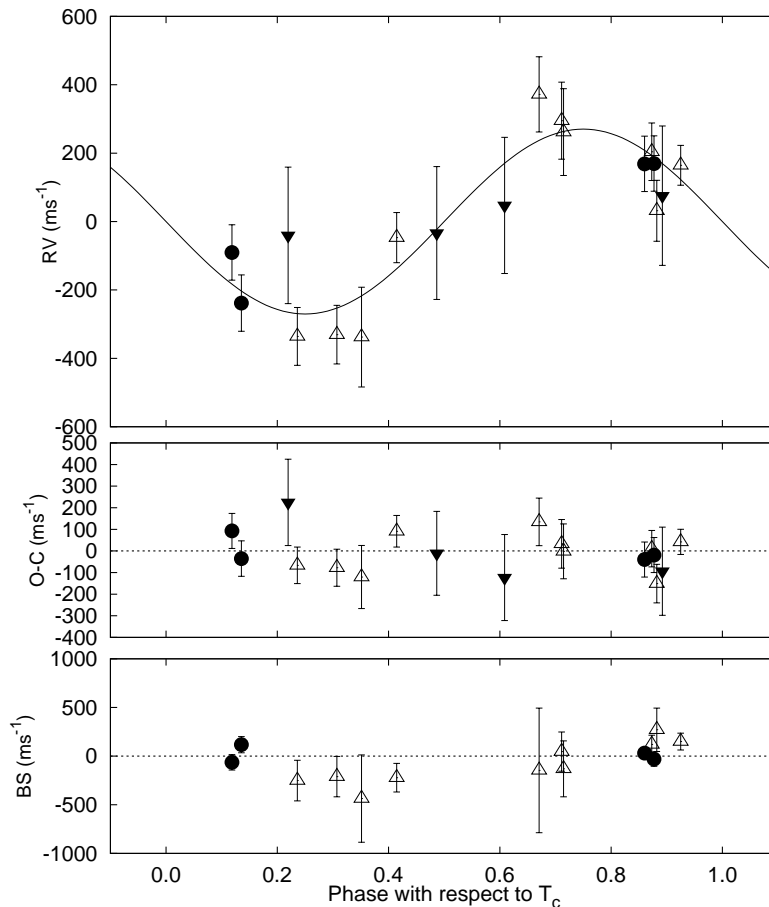


Figure 7.4: *Top panel:* high-precision RV measurements for HATS-2 from CORALIE (dark filled circles), FEROS (open triangles) and CYCLOPS (filled triangles) shown as a function of orbital phase, together with our best-fit model. Zero phase corresponds to the time of mid-transit. The center-of-mass velocity has been subtracted. *Second panel:* velocity O-C residuals from the best fit. The error bars include a component from astrophysical/instrumental jitter allowed to differ for the three instruments (see Sec. 3.3). *Third panel:* bisector spans (BS), with the mean value subtracted. Note the different vertical scales of the panels.

spectrum and calculated the weighted mean and corresponding scatter (weighted by the S/N of individual spectra). The results for the spectroscopic stellar parameters including the assumed values for micro- v_{mic} and macroturbulence v_{mac} of the SME analysis are listed in Table 7.4.

By modeling the light curve alone it is possible to determine the stellar mean density, which is closely related to the normalized semimajor axis a/R_{\star} (Sect. 7.2, when assuming a circular orbit). Furthermore, adding RV measurements allows the determination of these parameters for elliptical orbits as well.

To obtain the light curve model, quadratic limb-darkening coefficients are needed, which were determined using Claret (2004) and the initially determined stellar spectroscopic parameters. We used the Yonsei-Yale stellar evolution models (Yi et al., 2001; hereafter YY) to determine fundamental stellar parameters such as the mass, radius, age and luminosity. The light curve based stellar mean density and spectroscopy based effective temperature

BJD (-2454000)	Rel. RV (m s^{-1})	σ_{RV}^a (m s^{-1})	BVS (m s^{-1})	σ_{BVS} (m s^{-1})	Phase	Exp. Time (s)	S/N	Instrument
1701.52346	-90.37	33.00	-63.7	79.5	0.119	1800	9.0	Coralie
1701.54622	-238.37	36.00	117.7	83.3	0.135	1800	8.0	Coralie
1702.52760	168.63	33.00	31.3	58.6	0.860	1800	10.0	Coralie
1702.55065	169.63	33.00	-30.8	74.2	0.877	1800	9.0	Coralie
1721.50300	204.15	71.76	120.4	93.8	0.873	2400	14.0	FEROS
1722.58300	371.99	100.77	-146.9	640.0	0.671	2400	16.0	FEROS
1723.44500	-330.70	73.66	-211.0	207.2	0.307	2400	18.0	FEROS
1736.46900	164.63	38.18	149.3	86.4	0.925	2400	16.0	FEROS
1737.53800	261.69	119.02	-130.9	287.5	0.715	1044	17.0	FEROS
1738.48600	-47.00	58.61	-222.1	146.9	0.415	3000	12.0	FEROS
1932.22448	-33.63	21.80	1114.3	43.2	0.487	2400	22.7	CYCLOPS
1933.21669	-40.53	51.20	3464.1	19.9	0.219	2400	20.7	CYCLOPS
1934.12774	75.57	65.58	-4516.6	168.1	0.892	2400	17.6	CYCLOPS
1938.81200	-337.82	139.13	-436.4	449.1	0.351	2700	17.0	FEROS
1939.16016	47.07	49.44	9189.5	1723.7	0.608	2400	18.0	CYCLOPS
1990.75600	294.99	103.71	46.3	201.6	0.711	2700	15.0	FEROS
1992.82100	-335.90	72.26	-251.5	208.5	0.236	2700	19.0	FEROS
2035.67400	31.55	77.56	270.6	223.1	0.882	3600	22.0	FEROS

Table 7.3: Relative RV and bisector span (BVS) measurements of HATS-2 from various instruments used for high-precision RV measurements (c.f. Table 7.2). 5 data points determined with FEROS are not listed here and were not used for further analysis due to high error bars caused by bad weather conditions.

^a: The Coralie RV uncertainties listed here are known to be underestimated. Updated estimates are available, but we list here the values we used in the analysis. We note that in any case a jitter is included in the analysis to account for any additional scatter to that implied by the uncertainties, see Sec. 3.3 (cf. Table 7.5)

and metallicity, coupled with isochrone analysis, together permit a more accurate stellar surface gravity determination. To allow uncertainties in the measured parameters to propagate into the stellar physical parameters we assign an effective temperature and metallicity, drawn from uncorrelated Gaussian distributions, to each stellar mean density in our MCMC chain, and perform the isochrone look-up for each link in the MCMC chain. The newly determined value for $\log g_{\star} = 4.50 \pm 0.05$ is consistent with the initial value of $\log g_{\star} = 4.44 \pm 0.12$ thus we refrain from re-analyzing the spectra fixing the surface gravity to the revised value.

The spectroscopic, photometric and derived stellar properties are listed in Table 7.4, whereas the adopted quadratic limb-darkening coefficients for the individual photometric filters are shown in Table 7.5. To illustrate the position of HATS-2 in the H-R diagram, we plotted the normalized semi-major axis a/R_{\star} versus effective temperature $T_{\text{eff}\star}$. Figure 7.5 shows the values for HATS-2 with their 1- σ and 2- σ confidence ellipsoids as well as YY-isochrones calculated for the determined metallicity of $[\text{Fe}/\text{H}] = 0.15$ and interpolated to values between 1 and 14 Gyr in 1 Gyr increments from our adopted model.

Stellar rotation

We applied the Lomb-Scargle periodogram (Lomb, 1976; Scargle, 1982) to the HATSouth light curve for HATS-2 and found a significant peak at a period of $P = 12.46 \pm 0.02$ d with a S/N measured in the periodogram of 87 and a formal false alarm probability of

Parameter	Value	Source
Spectroscopic properties		
$T_{eff\star}$ (K)	5227 ± 95	SME
$[Fe/H]$	0.15 ± 0.05	SME
$v \sin i_{\star}$ (km s^{-1})	1.5 ± 0.5	SME
$\log g_{\star}$ (cgs)	4.44 ± 0.12	SME
v_{mic} (km s^{-1}) ^a	1.5	SME
v_{mac} (km s^{-1}) ^a	2.0	SME
Photometric properties		
V (mag)	13.562 ± 0.016	APASS ¹
B (mag)	14.490 ± 0.031	APASS
g (mag)	13.991 ± 0.012	APASS
r (mag)	13.260 ± 0.020	APASS
i (mag)	13.018 ± 0.021	APASS
J (mag)	11.906 ± 0.024	2MASS ²
H (mag)	11.475 ± 0.023	2MASS
K (mag)	11.386 ± 0.023	2MASS
Derived properties		
M_{\star} (M_{\odot})	0.882 ± 0.037	YY+a/ R_{\star} +SME
R_{\star} (R_{\odot})	0.898 ± 0.019	YY+a/ R_{\star} +SME
$\log g_{\star}$ (cgs)	4.48 ± 0.02	YY+a/ R_{\star} +SME
L_{\star} (L_{\odot})	0.54 ± 0.06	YY+a/ R_{\star} +SME
M_V (mag)	5.61 ± 0.13	YY+a/ R_{\star} +SME
M_K (mag)	3.64 ± 0.07	YY+a/ R_{\star} +SME
Age (Gyr)	9.7 ± 2.9	YY+a/ R_{\star} +SME
Distance (pc) ^b	360 ± 11	YY+a/ R_{\star} +SME
$P_{\star,rot}$ (d) ^c	30.32 ± 10.13	

Table 7.4: Stellar parameters for HATS-2

¹ The **AAVSO** (**A**merican **A**ssociation of **V**ariable **S**tars **O**bservers) **P**hotometric **A**ll-**S**ky **S**urvey

² **Two Micron All Sky Survey**

^a given values for micro- (v_{mic}) and macroturbulence (v_{mac}) are initial guesses, which were fixed during the analysis. Afterwards, the values were set free, but parameters were consistent with the fixed scenario within errorbars. Therefore, the stellar parameters given here and used throughout the following analysis are the ones determined with fixed micro- and macroturbulence

^b A_V corrected

^c upper limit of the rotational period of HATS-2 using the determined values for $v \sin i_{\star}$ and R_{\star} .

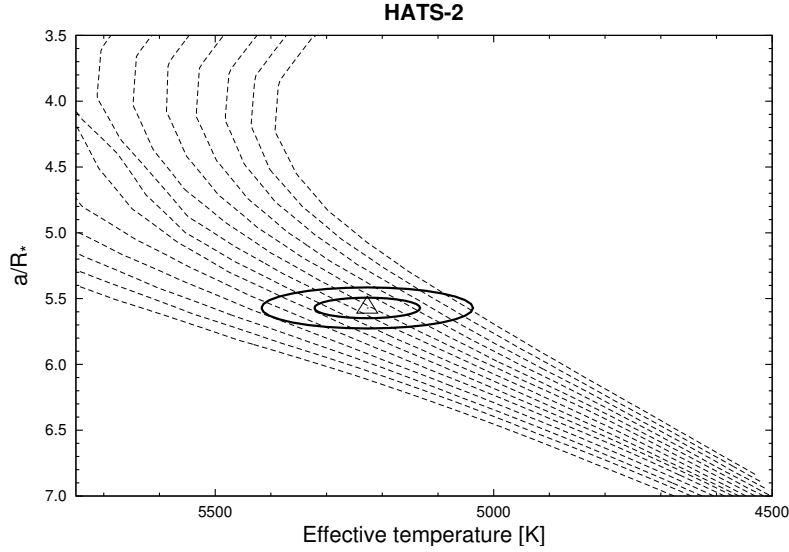


Figure 7.5: YY-isochrones from Yi et al. (2001) for the metallicity of $[\text{Fe}/\text{H}] = 0.15$. Isochrones are plotted for ages between 1 and 14 Gyr in steps of 1 Gyr (left to right). The ellipses mark the $1\text{-}\sigma$ and $2\text{-}\sigma$ confidence ellipsoids for the determined values of a/R_* and $T_{\text{eff}\star}$. The isochrones plotted here have a fixed metallicity for visualization purposes only, uncertainties on the metallicity are propagated into the uncertainties on the stellar mass and radius.

10^{-98} calculated following Press et al. (1992). Fig. 7.6 shows the normalized Lomb-Scargle periodogram of the HATSouth light curve. The peak-to-peak amplitude of the signal over the full 203 d spanned by the observations is 7.4 mmag. If we split the data into bins of duration 50 d, the amplitude in each bin varies from 3.6 mmag to 10.0 mmag. We interpret this signal as being due to starspots modulated by the rotation of the star. The stellar rotation period is thus ~ 12.5 d, or twice this value. As seen in many open clusters, an individual star often shows two minima per cycle so that the rotation period is double the value found from a periodogram analysis. Also owing to differential rotation and the unknown latitudinal distribution of spots on the star, the equatorial period may be as much as 10–20% shorter than the measured period. Both rotation periods (12.5 and 25 d) are consistent with the upper limit of $P_{\star,\text{rot}}$ of 30.32 ± 10.13 d derived from the determined $v \sin i$ and R_* (see Tab. 4). The rotation period of 12.46 d is comparable to that of similar-size stars in the 1 Gyr open cluster NGC 6811 (Meibom et al., 2011), which shows a tight period–color sequence. The spin-down rate for sub-solar-mass stars is poorly constrained beyond 1 Gyr, but assuming a Skumanich (1972) spin-down of $P \propto t^{0.5}$, the expected rotation period reaches ~ 25 d at an age of 4 Gyr. Based on this we estimate a gyrochronology age of either ~ 1 Gyr, or ~ 4 Gyr for HATS-2, depending on the ambiguous rotation period.

Excluding blend scenarios

To rule out the possibility that HATS-2 is actually a blended stellar system mimicking a transiting planet system we conduct a detailed modeling of the light curves following the procedure described in Hartman et al. (2011). Based on this analysis we can reject hierarchical triple star systems with greater than 4.5σ confidence, and blends between a foreground star and a background eclipsing binary with $\sim 4\sigma$ confidence. Moreover, the

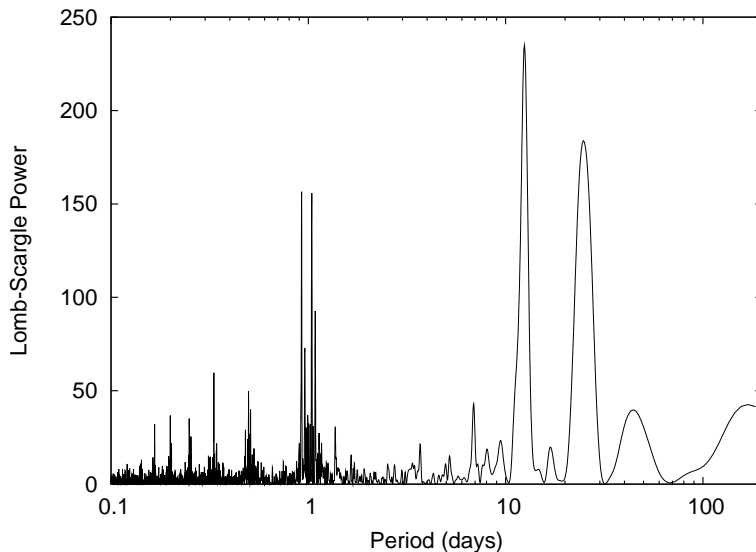


Figure 7.6: Normalized Lomb-Scargle periodogram of the combined HATSouth light curve of HATS-2. Transits have been removed from the data before applying the periodogram. A strong signal with a period of 12.46 days is detected in the data.

only non-planetary blend scenarios which could plausibly fit the light curves (ones that cannot be rejected with greater than 5σ confidence) are scenarios which would have easily been rejected by the spectroscopic observations (these would be obviously double-lined systems, also yielding several km s^{-1} RV and/or BVS variations). We thus conclude that the observed transit is caused by a planetary companion orbiting HATS-2.

Simultaneous analysis of photometry and radial velocity

Following Bakos et al. (2010) we corrected for systematic noise in the follow-up light curves by applying external parameter decorrelation and the Trend Filtering Algorithm (TFA) simultaneously with our fit. For the FTS light curve we decorrelate against the hour angle of the observations (to second order), together with three parameters describing the profile shape (to first order), and we apply TFA. For the GROND light curves we only decorrelate against the hour angle as the PSF model adopted for FTS is not applicable to GROND, and the number of neighboring stars that could be used in TFA is small. Following the procedure described in Bakos et al. (2010), the FTS and GROND photometric follow-up measurements (Table 7.1) were simultaneously fitted with the high-precision RV measurements (Table 7.3) and HATSouth photometry. The light curve parameters, RV parameters, and planetary parameters are listed in Table 7.5.

Table 7.5 also contains values for the radial velocity jitter for all three instruments used for high-precision RV measurements. They are added in quadrature to the RV results of the particular instrument. These values are determined such that χ^2 per degree of freedom equals unity for each instrument when fitting a fiducial model. If χ^2 per degree of freedom is smaller than unity for that instrument, then no jitter would be added. The RV jitters are empirical numbers that are added to the measurements such that the actual scatter in the RV observations sets the posterior distributions on parameters like the RV semi-amplitude.

Allowing the orbital eccentricity to vary during the simultaneous fit, we include the uncertainty for this value in the other physical parameters. We find that the observations are consistent with a circular orbit ($e = 0.071 \pm 0.049$) and we therefore fix the eccentricity to zero for the rest of this analysis. Table 7.5 shows that the derived parameters obtained by including the distorted regions of the light curves are consistent with those derived with these regions excluded, indicating that the starspots themselves are not affecting the stellar or planet parameters in a significant way.

The RMS varies from 1 to 1.6 mmag for the complete light curves and 0.8 to 1.3 mmag when then spot-affected regions are excluded, respectively. We scaled the photometric uncertainties for each of the light curves such that χ^2 per degree of freedom equals one about the best-fit model. We adopt the parameters obtained with the light curve distortions excluded in a fixed circular orbit.

Starspot analysis

Fig. 7.7 shows the combined four-colour GROND light curves for the two HATS-2 transit events that were observed with this imaging instrument. The slight difference in the transit depth among the datasets is due to the different wavelength range covered by each filter. In particular, the g , r , i and z filters are sensitive to wavelength ranges of 3860 – 5340 Å, 5380 – 7060 Å, 7160 – 8150 Å, and 8260 – 9520 Å, respectively.

Starspots and plages

From an inspection of Fig. 7.7, it is easy to note several distortions in the light curves. Such anomalies cannot be removed by choosing different comparison stars for the differential photometry, and we interpret them as the consequence of the planet crossing irregularities on the stellar photosphere, such as starspots. It is well known that starspots are at a lower temperature than the rest of the photosphere. The flux ratio should be therefore lower in the blue than the red. We thus expect to see stronger starspot features in the bluest bands.

The data taken on February 28, 2012, are plotted in the top panel of Fig. 7.7, where the *bump*, which is clearly present just after midtransit in all four optical bands, is explained by a starspot covered by the planet. In particular, considering the errorbars, the g , r , and i points in the starspot feature look as should be expected, whereas the feature in z is a bit peaked, especially the highest points at the peak of the bump at roughly BJD(TDB) 2455985.735. Before the planet crosses the starspot feature, it is also possible to note that the fluxes measured in the g and r bands are lower than those in the other two reddest bands, as if the planet were occulting a hotter zone of the stellar chromosphere. Actually, the most sensitive indicators of the chromospheric activity of a star in the visible spectrum are the emission lines of Ca II H λ 3968, K λ 3933, and H α λ 6563, which in our case fall on the transmission wings of the g and r GROND passbands. The characterization of the chromospheric activity by calculating the Ca activity indicator using FEROS spectra was not possible due to high noise in the spectra.

Within the transit observed on June 1, 2012, whose data are plotted in the lower panel of Fig. 7.7, we detected another starspot, which occurred near the transit-egress zone of the light curve. Again, before the planet crosses the starspot feature, we note another “hotspot” in the g band, which has its peak at roughly BJD(TDB) 2456079.681.

These hotspot distortions could be caused by differential color extinction or other time-correlated errors (e.g. red noise) of atmospheric origin. The g -band suffers most from the strength and variability of Earth-atmospheric extinction of all optical wavelengths covered

Parameter	LC distortions included, $e \equiv 0$	LC distortions included, free e	LC distortions excluded, $e \equiv 0$
Light curve parameters			
P (days)	1.354133 ± 0.000001	1.354133 ± 0.000001	1.354133 ± 0.000001
$T_c - 2455000$ (BJD) ^a	954.58576 ± 0.00008	951.87748 ± 0.00009	954.58576 ± 0.00009
T_{14} (days) ^a	0.0859 ± 0.0004	0.0859 ± 0.0004	0.0862 ± 0.0004
$T_{12} = T_{34}$ (days) ^a	0.0104 ± 0.0004	0.0107 ± 0.0004	0.0109 ± 0.0005
a/R_*	$5.57^{+0.06}_{-0.09}$	5.65 ± 0.32	5.50 ± 0.09
ζ/R_* ^b	26.48 ± 0.06	26.58 ± 0.07	26.52 ± 0.07
R_p/R_*	0.1317 ± 0.0007	0.1326 ± 0.0008	0.1335 ± 0.0010
$b \equiv a \cos i_p/R_*$	$0.214^{+0.061}_{-0.070}$	$0.265^{+0.053}_{-0.075}$	$0.271^{+0.055}_{-0.074}$
i_p (deg)	87.8 ± 0.7	87.4 ± 0.7	87.2 ± 0.7
Limb-darkening coefficients^c			
a_g (linear term)	0.7052	0.7052	0.7052
b_g (quadratic term)	0.1168	0.1168	0.1168
a_r	0.4756	0.4756	0.4756
b_r	0.2487	0.2487	0.2487
a_i	0.3617	0.3617	0.3617
b_i	0.2744	0.2744	0.2744
a_z	0.2861	0.2861	0.2861
b_z	0.2873	0.2873	0.2873
Radial velocity parameters			
K (m s ⁻¹)	272.2 ± 30.5	278.7 ± 33.0	268.9 ± 29.0
$e \cos \omega$	0.000	-0.033 ± 0.052	0.000
$e \sin \omega$	0.000	-0.023 ± 0.060	0.000
e^d	0.000	0.071 ± 0.049	0.000
ω (deg)	0.000	216 ± 77	0.000
RV jitter Coralie (m s ⁻¹) ...	74.0	74.0	74.0
RV jitter FEROS (m s ⁻¹) ..	44.0	44.0	44.0
RV jitter CYCLOPS (m s ⁻¹) .	193.0	193.0	193.0
Planetary parameters			
M_p (M _J)	1.369 ± 0.158	1.397 ± 0.171	1.345 ± 0.150
R_p (R _J)	1.139 ± 0.025	1.131 ± 0.065	1.168 ± 0.030
$C(M_p, R_p)^e$	0.11	-0.26	0.08
ρ_p (g/cm ³)	1.15 ± 0.15	1.20 ± 0.28	1.05 ± 0.14
$\log g_p$ (cgs)	3.42 ± 0.05	3.43 ± 0.08	3.39 ± 0.05
a (AU)	0.0230 ± 0.0003	0.0230 ± 0.0003	0.0230 ± 0.0003
T_{eq} (K)	1567 ± 30	1554 ± 57	1577 ± 31
Θ^f	0.062 ± 0.007	0.064 ± 0.009	0.060 ± 0.007
$\langle F \rangle$ (10 ⁸ erg s ⁻¹ cm ⁻²) ^g ...	1.36 ± 0.11	1.32 ± 0.20	1.40 ± 0.11

Table 7.5: Orbital and planetary parameters for the HATS-2 system for different fitting scenarios: including the light curve distortions with free and fixed eccentricity e as well as excluding the light curve distortions with a fixed circular orbit. The last scenario was adopted for further analysis steps (parameters are highlighted in bold font)

^a: T_C : Reference epoch of mid transit that minimizes the correlation with the orbital period. BJD is calculated from UTC. T_{14} : total transit duration, time between first to last contact; $T_{12} = T_{34}$: ingress/egress time, time between first and second, or third and fourth, contact.

^b: Reciprocal of the half duration of the transit used as a jump parameter in our MCMC analysis in place of a/R_* . It is related to a/R_* by the expression $\zeta/R_* = a/R_* \cdot (2\pi(1 + e \sin \omega))/(P\sqrt{1 - b^2}\sqrt{1 - e^2})$ (Bakos et al., 2010).

^c: Values for a quadratic law given separately for the Sloan g , r , i and z filters. These values were adopted from the tabulations by Claret (2004) according to the spectroscopic (SME) parameters listed in Table 7.4.

^d: the uncertainties on the eccentricity e incorporate the estimated RV jitter

^e: Correlation coefficient between the planetary mass M_p and radius R_p .

^f: The Safronov number is given by $\Theta = (1/2)(V_{esc}/V_{orb})^2 = (a/R_p) \cdot (M_p/M_*)$ (see Hansen & Barman, 2007).

^g: Incoming flux per unit surface area, averaged over the orbit.

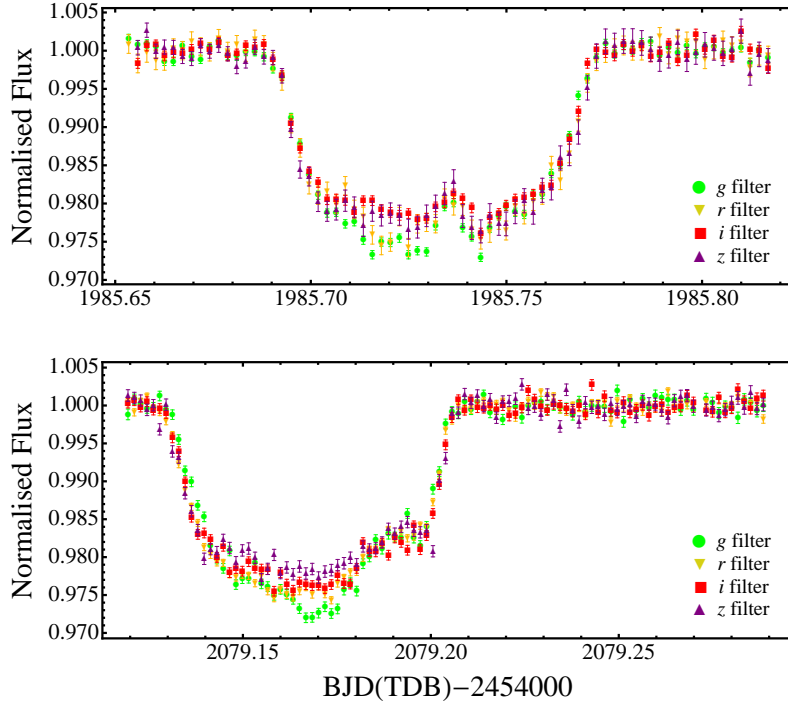


Figure 7.7: Combined four-colour transit light curves of HATS-2 obtained with the GROND imaging system. Green dots are for the data taken in the g band, yellow upside down triangles for the r band, red squares for the i band, and purple triangles for the z band. *Top panel:* transit observed on February 28, 2012. The *bump* observed just after the midtransit is interpreted as the covering of a “cold” starspot by the planet. *Lower panel:* transit observed on June 1, 2012. In addition to the bump occurred near the egress part of the light curve, a “hot” spot manifested in the g band, just before the starting of the covering of the starspot.

by GROND, which is why the distortions in the g -band could have an atmospheric origin. Discrepancies in blue filters have been noted by other observers, and are often ascribed to systematic errors in ground-based photometry with these filters (e.g. Southworth et al., 2012). However, our group has observed more than 25 planetary transits with the GROND instrument to date, and in no other case have we seen similar features in the g -band only. We consider it unlikely that a systematic error of this form would only appear near to other spot features in the HATS-2 light curve, and therefore conclude that a more plausible scenario is that of a “plage”. A plage is a chromospheric region typically located near active starspots, and usually forming before the starspots appear, and disappearing after the starspots vanish from a particular area (e.g. Carroll & Ostlie, 1996). Accordingly, a plage occurs most often near a starspot region. As a matter of fact, in the GROND light curves, our plages are located just before each starspot. One can argue that the plage in the second transit is visible only in the g band, but this can be explained by temperature fluctuations in the chromosphere, which causes a lack of ionized hydrogen, and by the fact that the CaII lines are much stronger than the H α line for a K-type star like HATS-2. Another argument supporting this *plage–starspot* scenario is that, for these old stars, a solar-like relation between photospheric and chromospheric cycles is expected,

the photospheric brightness varying in phase with that of the chromosphere (Lockwood et al., 2007).

We note, however, that if these are plages they must be rather different from solar plages, which are essentially invisible in broad-band optical filters unless they are very close to the solar limb. Detecting a plage feature through a broad-band filter near the stellar center suggests a much larger temperature contrast and/or column density of chromospheric gas than in the solar case.

Modelling transits and starspots

We modelled the GROND transit light curves of HATS-2 with the PRISM⁶ and GEMC codes (Tregloan-Reed et al., 2013). The first code models a planetary transit over a spotted star, while the latter one is an optimisation algorithm for finding the global best fit and associated uncertainties. Using these codes, one can determine, besides the ratio of the radii R_p/R_* , the sum of the fractional radii, $r_p + r_* = (R_p + R_*)/a$, the limb darkening coefficients, the transit midpoint T_0 , and the orbital inclination i_p , as well as the photometric parameters of the spots, i.e. the projected longitude and the latitude of their centres (θ and ϕ , these are equal to the physical latitude and longitude only if the rotation axis of the star is perpendicular to the line of sight), the spot size r_{spot} and the spot contrast ρ_{spot} , which is basically the ratio of the surface brightness of the spot to that of the surrounding photosphere. Unfortunately, the current versions of PRISM and GEMC are set to fit only a single starspot (or hotspot), so we excluded the g -band dataset of the 2nd transit from the analysis, because it contains a hotspot with high contrast ratio between stellar photosphere and spot, which strongly interferes with the best-fitting model for the light curve.

Given that the codes do not allow the datasets to be fitted simultaneously, we proceeded as follows. First, we modelled the seven datasets (1st transit: g, r, i, z ; 2nd transit: r, i, z) of HATS-2 separately; this step allowed us to restrict the search space for each parameter. Then, we combined the four light curves of the first transit into a single dataset by taking the mean value at each point from the four bands at that point and we fitted the corresponding light curve; this second step was necessary to find a common value for T_0, i_p, θ and ϕ . Finally, we fitted each light curve separately fixing the starspot position, the midtime of transit T_0 and the system inclination to the values found in the previous combined fit. While these parameters are the same for each band since they are physical parameters of the spot or the system and are therefore fixed during the analysis, other parameters as radius of the planet R_p , spot contrast ρ_{spot} and temperature of the starspots T_{spot} change according to the wavelength and hence according to the analyzed band and are therefore free parameters during the fit.

The light curves and their best-fitting models are shown in Fig. 7.8, while the derived photometric parameters for each light curve are reported in Table 7.6, together with the results of the MCMC error analysis for each solution.

Comparing Table 7.5 with Table 7.6 we find that the fitted light curve parameters from the analysis described in Section 7.2 are consistent with the parameters that result from the GEMC+PRISM model, except for the inclination which differs by more than 2σ . As already discussed in Section 7.2, the joint-fit analysis was performed both considering and without considering the points contaminated by the starspots, and the results are consistent with each other. So, our conclusion is that the spots themselves are not systematically affecting the stellar or planet parameters in a significant way; the differences

⁶PRISM (Planetary Retrospective Integrated Star-spot Model).

1 st transit				
Parameter Symbol	<i>g</i>	<i>r</i>	<i>i</i>	<i>z</i>
Radius ratio R_p/R_\star	0.1348 ± 0.0011	0.1324 ± 0.0011	0.13145 ± 0.00096	0.1352 ± 0.0010
Sum of fractional radii $r_p + r_\star$	0.2204 ± 0.0018	0.2232 ± 0.0018	0.2149 ± 0.0016	0.2161 ± 0.0015
Linear LD coefficient u_1	0.749 ± 0.060	0.593 ± 0.051	0.352 ± 0.057	0.298 ± 0.039
Quadratic LD coefficient u_2	0.171 ± 0.018	0.296 ± 0.043	0.218 ± 0.028	0.144 ± 0.024
Inclination ^a (degrees) i_p	85.26 ± 0.40	85.26 ± 0.40	85.26 ± 0.40	85.26 ± 0.40
Longitude of spot ^{a,b} (degrees) θ	5.78 ± 0.45	5.78 ± 0.45	5.78 ± 0.45	5.78 ± 0.45
Latitude of Spot ^{a,c} (degrees) ϕ	76.52 ± 1.94	76.52 ± 1.94	76.52 ± 1.94	76.52 ± 1.94
Spot angular radius ^d (degrees) r_{spot}	8.85 ± 0.61	10.01 ± 0.72	8.93 ± 0.65	8.72 ± 0.50
Spot contrast ^e ρ_{spot}	0.304 ± 0.035	0.546 ± 0.048	0.464 ± 0.052	0.251 ± 0.52
2 nd transit				
Radius ratio R_p/R_\star	–	0.1356 ± 0.0012	0.13411 ± 0.00093	0.1307 ± 0.0011
Sum of fractional radii $r_p + r_\star$	–	0.2108 ± 0.0019	0.2022 ± 0.0012	0.2039 ± 0.0017
Linear LD coefficient u_1	–	0.473 ± 0.057	0.399 ± 0.049	0.252 ± 0.044
Quadratic LD coefficient u_2	–	0.250 ± 0.038	0.230 ± 0.025	0.316 ± 0.049
Inclination ^a (degrees) i_p	–	85.89 ± 0.40	85.89 ± 0.40	85.89 ± 0.40
Longitude of spot ^{a,b} (degrees) θ	–	35.26 ± 1.20	35.26 ± 1.20	35.26 ± 1.20
Latitude of Spot ^{a,c} (degrees) ϕ	–	80.60 ± 2.10	80.60 ± 2.10	80.60 ± 2.10
Spot angular radius ^d (degrees) r_{spot}	–	20.14 ± 1.49	17.79 ± 2.17	18.28 ± 2.31
Spot contrast ^e ρ_{spot}	–	0.753 ± 0.046	0.780 ± 0.054	0.789 ± 0.047

Table 7.6: Photometric parameters derived from the GEMC fitting of the GROND transit light curves

^a: This is a common value and was found from the preceding fit of the combined data (see text).

^b: The longitude of the centre of the spot is defined to be 0° at the centre of the stellar disc and can vary from -90° to 90° .

^c: The latitude of the centre of the spot is defined to be 0° at the north pole and 180° at the south pole.

^d: Note that 90° degrees covers half of stellar surface.

^e: Note that 1.0 equals to the surrounding photosphere.

in the inclination between GEMC and our joint fit are most likely due to differences in the modeling.

Starspots discussion

The final value for the starspots angular radii comes from the weighted mean of the results in each band and is $r_{\text{spot}} = 9.02^\circ \pm 0.30^\circ$ for the starspot in the 1st transit (spot #1) and $r_{\text{spot}} = 19.16^\circ \pm 1.08^\circ$ for the starspot in the 2nd transit (spot #2), with a reduced χ^2_ν of 0.78 and 0.49 respectively, indicating a good agreement between the various light curves in each of the two transits. We note that the error of the angular size of the spot #2 is greater than that of the spot #1. While it may be that spot #2 is larger, we caution that its position near the limb of the star makes its size poorly constrained.

The above numbers translate to radii of $98\,325 \pm 3\,876$ km and $208\,856 \pm 11\,794$ km, which are equivalent 2.5% and 11% of the stellar disk, respectively. Starspot sizes are in general estimated by doppler-imaging reconstructions (i.e. Collier Cameron, 1992; Vogt et al., 1999) and their range is 0.1% to 22% of a stellar hemisphere, the inferior value being the detection limit of this technique (Strassmeier, 2009). Our measurements are thus perfectly reasonable for a common starspot or for a starspot *assembly*, and in agreement with what has been found in other K-type stars (e.g. TrES-1 (a K0V star) reveals a starspot of at least 42 000 km in radius, see Rabus et al. (2009a)).

Starspots are also interesting in terms of how the contrast changes with passband. In particular, we expect that moving from ultraviolet (UV) to infrared (IR) wavelengths the

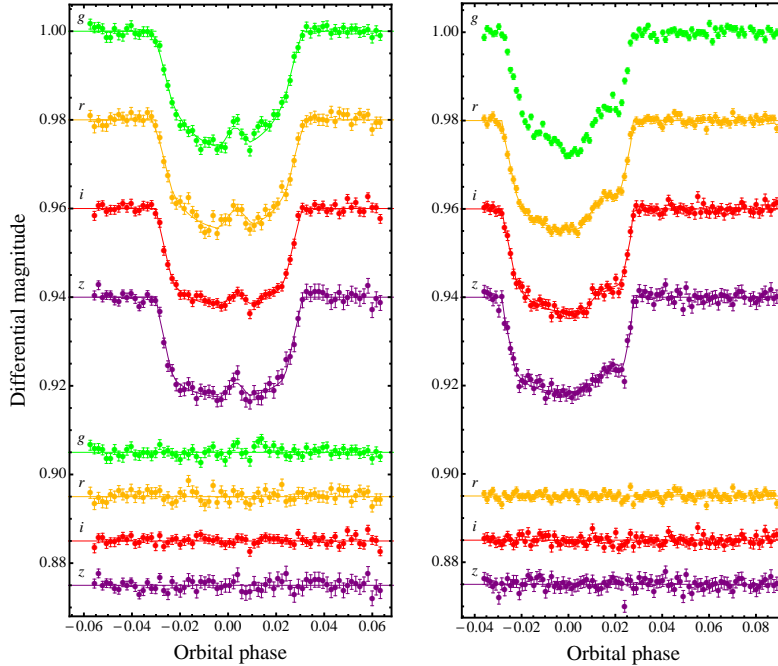


Figure 7.8: Phased GROND light curves of HATS-2b compared to the best GEMC fits. The light curves and the residuals are ordered according to the central wavelength of the filter used. *Left panel:* transit observed on February 28, 2012. *Right panel:* transit observed on June 1, 2012; due to presence of the hotspot, the *g* band was not analyzed with GEMC (see text).

spot becomes brighter relative to the photosphere. The contrast of starspot #2 decreases from *r* to *z*, even though this variation is inside the 1σ error (see Table 7.6). Considering that HATS-2 has an effective temperature $T_{eff\star} = 5227 \pm 95$ K and modeling both the photosphere and the starspot as blackbodies (Rabus et al., 2009a; Sanchis-Ojeda & Winn, 2011), we used Eq. (1) of Silva (2003) to estimate the temperature of the starspot #2 in each band:

$$f_i = \frac{\exp(h\nu/k_B T_e) - 1}{\exp(h\nu/k_B T_0) - 1} \quad (7.1)$$

with the spot contrast f_i , the Planck constant h , the frequency of the observation ν , the effective surface temperature of the star T_e and the spot temperature T_0 . We obtained the following values: $T_{\text{spot}\#2,r} = 4916 \pm 105$ K, $T_{\text{spot}\#2,i} = 4895 \pm 121$ K and $T_{\text{spot}\#2,z} = 4856 \pm 120$ K. The weighted mean is $T_{\text{spot}\#2} = 4891.5 \pm 66.2$ K.

Unlike starspot #2, the spot contrasts for starspot #1 are inconsistent with expectations. The spot is too bright in *r* relative to the other bandpasses, and too faint in *z*. If we estimate the starspot temperature in each band, we find $T_{\text{spot}\#1,g} = 4345 \pm 97$ K, $T_{\text{spot}\#1,r} = 4604 \pm 109$ K, $T_{\text{spot}\#1,i} = 4318 \pm 128$ K and $T_{\text{spot}\#1,z} = 3595 \pm 180$ K. While the temperature in *r* is in agreement with those of *g* and *i* at $1 - 2\sigma$ level, and slight differences could be explained by chromospheric contamination (filaments, spicules, etc.), the temperature in *z* seems physically inexplicable. This effect is essentially caused by the *z* points at the peak of the starspot, at phase ~ 0.004 (see Fig. 7.8), which are higher than the other points. However, one has also to consider that errorbars in this band are larger than those found in the other bands. This is due to the fact that, since the GROND system design does not permit to chose different exposure times for each band, we are

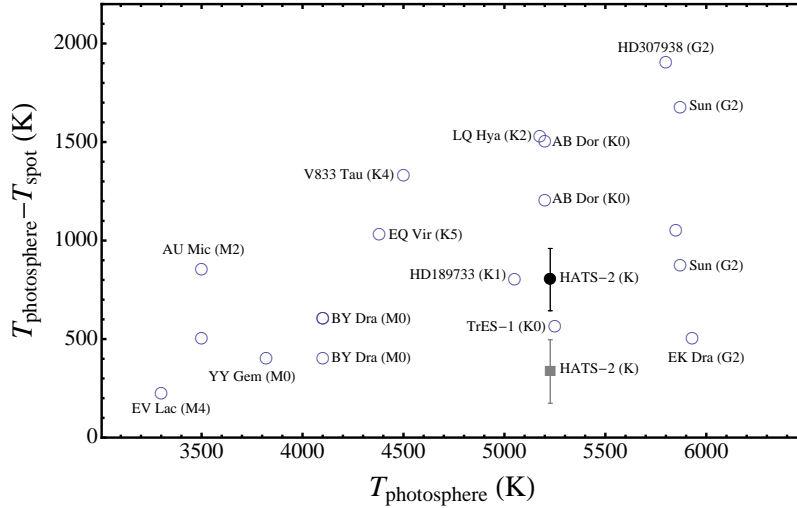


Figure 7.9: Spot temperature contrast with respect to the photospheric temperature in several dwarf stars. Gray square is from spot #2, black circle from spot #1, open circles from Berdyugina (2005), except TrES-1 (Rabus et al., 2009a) and HD189733 (Sing et al., 2011). The name of the star and its spectral type is also reported for most of them. Nameless targets do not have a name in the publication of Berdyugina (2005) as well. Note that some stars appear two times.

forced to optimize the observations for the r and i bands. Consequently, considering both the filter-transmission efficiency and the color and the magnitude of HATS-2, the SNR in these two bands is better than that in z , for which we have larger uncertainty in the photometry. Taking these considerations into account, we estimated the final temperature of starspot #1 neglecting the z -band value, and obtaining $T_{\text{spot}\#1} = 4425 \pm 63$ K. In Fig. 7.9 the final values of the temperature contrast of the two starspots are compared with those of a sample of dwarf stars, which was reported by Berdyugina (2005). The derived contrast for the HATS-2 starspots is consistent with what is observed for other stars. As already observed by Strassmeier (2009), the temperature difference between photosphere and starspots can be not so different for stars of different spectral types. Moreover, in the case of long lifetime, the same starspot could be seen at quite different temperature (Kang & Wilson, 1989). It is then very difficult to find any clear correlation between starspot temperatures and spectral classes of stars.

The achieved longitudes of the starspots are in agreement with a visual inspection of the light curves. The latitude of starspot #1, $76.52^\circ \pm 1.94^\circ$, matches well with that of starspot #2, $80.6^\circ \pm 2.1^\circ$, the difference being within 1σ .

Multiple planetary transits across the same spot complex can be used to constrain the alignment between the orbital axis of the planet and the spin axis of the star (e.g. Sanchis-Ojeda et al., 2011). Unfortunately, from only two transits separated by 94 days we cannot tell whether or not the observed anomalies are due to the same complex. It is possible that they are. Following Solanki (2003) we estimate a typical lifetime of ~ 130 days for spots of the size seen here. Moreover the rotation period of $P_{\text{rot}} = 31 \pm 1$ d that is inferred assuming they are the same spot is consistent with the value of $P_{\text{rot}} = (30 \pm 10 \text{ d}) \sin i_\star$ estimated from the spectroscopically-determined sky-projected equatorial rotation speed. If they are the same spot complex, then the sky-projected spin-orbit alignment is $\lambda = 8^\circ \pm 8^\circ$, which is consistent with zero. We caution, however, that this value depends entirely on this assumption which could easily be wrong. Continued photometric monitoring of HATS-2,

or spectroscopic observations of the Rossiter-McLaughlin effect, are necessary to measure the spin-orbit alignment of this system.

To test whether the spot parameters inferred from modelling the transits are consistent with the amplitude of variations seen in the HATSouth photometry, we simulate a light curve using the Macula starspot model (Kipping, 2012) and the model parameters determined from the first GROND r -band transit. We find that such a spot gives rise to periodic variations with a peak-to-peak amplitude of ~ 5 mmag, which is within the 3.6 to 10.0 mmag range of amplitudes observed in the HATSouth light curve. The fact that the amplitude changes by a factor of ~ 3 over the course of the HATSouth observations indicates, however, that the spot(s) observed by HATSouth is(are) likely to be unrelated to the spot(s) observed with GROND.

Conclusions

In this paper we have presented HATS-2b, the second planet discovered by the HATSouth survey. This survey is a global network of six identical telescopes located at three different sites in the Southern hemisphere (Bakos et al., 2013). The parameters of the planetary system were estimated by an accurate joint fit of follow-up RV and photometric measurements. In particular, we found that HATS-2b has a mass of $1.369 \pm 0.158 M_J$, and a radius of $1.139 \pm 0.025 R_J$. To set this target in the context of other transit planet detections, we plotted 4 different types of correlation diagrams for the population of transiting planets (Fig. 7.10). We analyzed the location of determined parameters for HATS-2b and its host star HATS-2 in the following parameter spaces: planetary radius R_p vs. stellar radius R_* , planetary mass M_P vs. planetary equilibrium temperature $T_{eq,P}$, planetary radius R_p vs. planetary equilibrium temperature $T_{eq,P}$, planetary radius R_p vs. stellar effective temperature $T_{eff,*}$, and planetary radius R_p vs. planetary mass M_P . As illustrated in Fig. 7.10, the analyzed parameter relations lie well within the global distribution of known exoplanets.

Within each correlation diagram, at least one well characterized exoplanet can be found, whose parameters are consistent with those of the HATS-2 system within the error bars. When looking at the correlation between planetary and stellar radius, the HATS-2 system is almost like the HAT-P-37 system (Bakos et al., 2012). Comparing the planetary equilibrium temperature and planetary mass, HATS-2b is similar to TrES-2b (O’Donovan et al., 2006). The relation between planetary equilibrium temperature and planetary mass shows an agreement with WASP-32b (Maxted et al., 2010), while the relation between stellar effective temperature and planetary radius points out that HATS-2b agrees well with WASP-45b (Anderson et al., 2012) within the error bars. The focus on the planetary parameters radius and mass reveals a similarity to the transiting planet TrES-2. Comparing the atmospheres of exoplanets with similar physical parameters will be especially important to pursue with e.g. the future ECHO space mission (Tinetti et al., 2012).

Very interesting is the detection of anomalies in the two multi-band photometric-follow-up light curves obtained with the GROND imaging instrument. We recognize the anomalies as starspots covered by HATS-2b during the two transit events, and used PRISM and GEMC codes (Tregloan-Reed et al., 2013) to re-fit the transit light curves, thereby measuring the parameters of the spots. Both the starspots appear to have associated hot-spots, which appeared in the 1st transit in the g and r bands, and only in the g band in the 2nd transit. These hotspots could be physically interpreted as chromospheric active regions known as *plages*, which can be seen only in the GROND’s bluest bands. We estimated the size and

the temperature of the two starspots, finding values which are in agreement with those found in other G-K dwarf stars.

acknowledgements

Development of the HATSouth project was funded by NSF MRI grant NSF/AST-0723074, operations are supported by NASA grant NNX09AB29G, and follow-up observations receive partial support from grant NSF/AST-1108686. Data presented in this paper is based partly on observations obtained with the HATSouth Station at the Las Campanas Observatory of the Carnegie Institution of Washington. This work is based on observations collected at the MPG/ESO 2.2m Telescope located at the ESO Observatory in La Silla (Chile), under programme IDs P087.A-9014(A), P088.A-9008(A), P089.A-9008(A), 089.A-9006(A) and Chilean time P087.C-0508(A). Operations of this telescope are jointly performed by the Max Planck Gesellschaft and the European Southern Observatory. GROND has been built by the high-energy group of MPE in collaboration with the LSW Tautenburg and ESO, and is operating as a PI-instrument at the MPG/ESO 2.2m telescope. We thank Timo Anguita and Régis Lachaume for their technical assistance during the observations at the MPG/ESO 2.2 m Telescope. A.J. acknowledges support from Fondecyt project 1130857, Anillo ACT-086, BASAL CATA PFB-06 and the Millenium Science Initiative, Chilean Ministry of Economy (Nucleus P10-022-F). V.S. acknowledges support from BASAL CATA PFB-06. R.B. and N.E. acknowledge support from Fondecyt project 1095213. N.N. acknowledges support from an STFC consolidated grant. M.R. acknowledges support from FONDECYT postdoctoral fellowship N°3120097. L.M. thanks Jeremy Tregloan-Reed for his help in using of the PRISM and GEMC codes, and John Southworth and Valerio Bozza for useful discussions.

This paper also uses observations obtained with facilities of the Las Cumbres Observatory Global Telescope. Work at the Australian National University is supported by ARC Laureate Fellowship Grant FL0992131. We acknowledge the use of the AAVSO Photometric All-Sky Survey (APASS), funded by the Robert Martin Ayers Sciences Fund, and the SIMBAD database, operated at CDS, Strasbourg, France. Work at UNSW has been supported by ARC Australian Professorial Fellowship grant DP0774000, ARC LIEF grant LE0989347 and ARC Super Science Fellowships FS100100046.

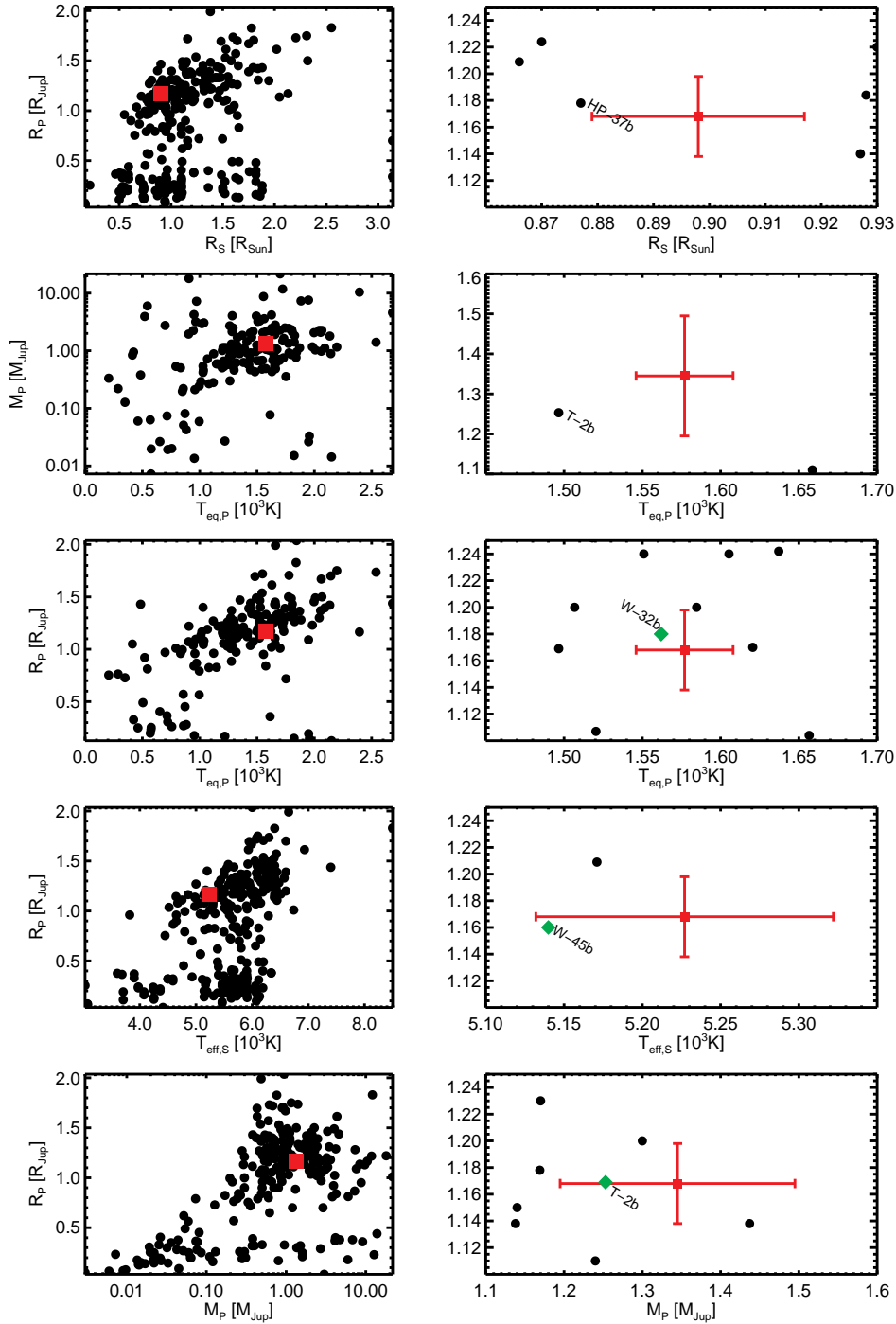


Figure 7.10: Correlation diagrams for confirmed transit planets (exoplanet.eu, last updated January 10 2013). From top to bottom: planetary radius R_p vs. stellar radius R_* , planetary mass M_P vs. planetary equilibrium temperature $T_{eq,P}$, planetary radius R_p vs. planetary equilibrium temperature $T_{eq,P}$, planetary radius R_p vs. stellar effective temperature $T_{eff,\star}$ and planetary radius R_p vs. planetary mass M_P . The position of the HATS-2 and HATS-2b parameters, respectively, are marked in red squares. Left panels give a general overview of the position of HATS-2 and HATS-2b in the population of known transit planets (black filled circles). Right panels illustrate a zoom in; green diamonds represent known exoplanets which fall within the errorbars of the HATS-2 system parameters. Short cuts: HP = HAT-P, W = WASP, T = TrES.

Chapter 8

Summary and Conclusions

8.1 The young stars exoplanet RV search

The formation and evolution of extrasolar planets and the corresponding time scales in particular are still not well known and a matter of ongoing debate.

Within this thesis I executed a radial velocity search for planets around young stars in order to put constraints on theoretical proposed planet formation timescales. Doing so, I selected 21 targets in total for extensive observations and detailed analyses. 17 targets have been selected from the young stellar objects survey of Weise (2010), taking $v \sin i$, age, magnitude, visibility and RV error into account. Four additional targets have been selected as overlap targets with the ESPRI program. The targets cover spectral types between F6 and M0 and show a $v \sin i$ of < 25 km/s, while one target shows a $v \sin i$ of more than 30 km/s. The stellar ages were determined by Weise (2010) by using the lithium depletion criterium as below 100 Myr. One target is most likely much older (~ 400 Myr).

8.1.1 Stellar parameters

The stellar parameters T_{eff} , $\log g$, $[M/H]$, $v \sin i$, v_{mic} and v_{mac} have been determined with SME individually for each target. SME provides an easy-to-use gui, which allows the user to comment out contaminated spectral regions, which are afterwards excluded from the analysis. However, it does not provide reasonable parameter errors, if the fit of a synthetic spectrum to the observed one is not absolutely perfect, which is expected for young active stars. In order to account for this, I analyzed several spectra with good S/N for each target and calculated the weighted average of the stellar parameters results with according error using the spectral S/N as a weight. Nevertheless, this just gives only an estimate of stochastic (measurement and stellar activity) noise and can not account for systematic errors. Therefore, the results should be treated carefully. In order to test SME, I calculated the $v \sin i$ using the method of Reiners et al. (2012). The results showed that both methods provide consistent results.

8.1.2 Age determination

The stellar ages of the 21 targets have been determined using different methods. These were kinematic ages using moving group memberships as well as the age determination using YY-isochrones and the determined stellar parameters with SME. Additionally, the stellar ages have been estimated using the lithium depletion criterium (Li I EW @ 6708 Å) and the activity criterium (S_{FEROS}). Although the method is under high debate, the stellar

ages have also been determined using gyrochronology to compare the results with the other methods.

Although lithium is a very commonly used age indicator, it can only provide rough estimations or upper limits. In most cases, the lithium age estimation agrees with those made by Weise (2010). Only the targets HD 216803 (Weise (2010): 400 ± 40 Myr, this thesis: < 300 Myr), HD 217897 (Weise (2010): 30 ± 15 Myr, this thesis: ~ 300 Myr) and HD 81544 (Weise (2010): 8 ± 3 Myr, this thesis: $30 - 80$ Myr) show large differences between the results. The reason for this disagreement is not clear, but might be due to a different veiling correction of the Li spectral line in both theses. Furthermore, I think it is problematic to claim errors of only a few Myrs on Li ages (as been done by Weise, 2010), since the ages are simply derived by a comparison to cluster ages (Fig. 2.3).

The accuracy of the age determination using isochrones is strongly limited for unprecise stellar parameters (T_{eff} and $\log g$) and for stars with metallicity > 2.0 . Therefore, isochrone ages could not be derived for five targets due to the above mentioned limitations of the method.

For 13 targets, a membership in a young moving group could be identified.

Stellar ages could be calculated for 17 targets, using stellar activity (S_{FEROS}). Three targets belong to late spectral types and could therefore not be analyzed with this method. The analysis failed for the remaining target, since a clear Ca IIR emission core could not be identified in any of the spectra.

For six targets, photometric data from the SuperWASP survey was available and revealed a significant period, which allowed the calculation of gyrochronological ages. The derived ages are in the same order of magnitude as those derived with other methods except for TYC 7697-2254-1 ($T_{\text{gyro}} = 96 \pm 6$ Myrs, other methods give younger ages). By trying to derive a rotational period from the radial velocity measurements over shorter timescales, I was able to derive gyrochronological ages for additional 11 targets for which not photometric data was available. Since most periods shown in the periodograms were not significant, it is no wonder that the results do not match the age estimations of the other indicators. To summarize the age estimation one can say that the disadvantages of most age indicators are clearly visible in this analysis. The isochrone method strongly suffers from unprecise stellar parameter estimations and metallicities. Kinematic ages provide a good and in most cases quite precise age estimation, but is of course not available for targets with no identified membership. The Li EW method needs a careful veiling correction and can only produce rough estimations and upper limits. The activity method is often far off from the other guesses, nevertheless showing small errorbars. In case of strong stellar activity, the line can suffer a variety of perturbations and might not be able to fulfill the activity-age-relations. Gyrochronology suffers from the selection of the right period and is in general under heavy debate, why not much weight should be put on those results.

8.1.3 Circumstellar disks

For all targets, the search for infrared excess was possible using 2MASS and WISE magnitudes. For 10 targets, additional IRAS data was available. The magnitudes were analyzed with the SED fitting tool by Robitaille et al. (2007). The fit revealed possible disks for three targets. The existence of a disk around HBC 603 could be confirmed by fitting a disk model to the data. The same worked for V2129 Oph. These results agree with Carpenter et al. (2009), who claim evidence for an accretion disk in both systems. CD-37 13029 showed evidence of a disk in the SED as well, but this could be traced back to optical ghosting with a look on the WISE images from the data base. In principle, the

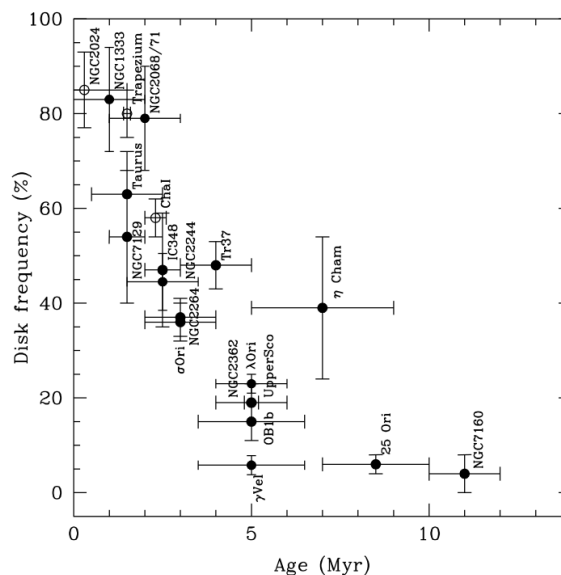


Figure 8.1: Fraction of stars with near-infrared disk emission as function of age of stellar groups. Figure adopted from Hernández et al. (2008).

presence of a disk can be used as age indicator (Hernández et al., 2008, , Fig. 8.1), which characterizes both targets as most likely younger than 10 Myrs. Nevertheless, the results should be treated carefully, since underlying disk dispersal timescales are not yet totally clarified. There might not even be one universal disk dispersal time, since different disk types in different environments may exist longer than others. The age estimations by the fitted SEDs match the determined ages of other methods very well.

8.1.4 Target observations and RV analysis

All targets have been extensively observed using FEROS at the 2.2 m MPG/ESO telescope at La Silla Observatory, Chile. The number of available data points has been increased significantly for each target in comparison to the thesis by Weise (2010). Additionally, HARPS spectra were available from the data base, being used for the analysis as well. The spectra were already reduced on-site (in case of FEROS) or could be downloaded as reduced data products from the ESO archive (in case of HARPS). Since HARPS spectra were only available as merged spectra, the spectra have been cut to the same spectral orders FEROS provides. The analysis in terms of RV has been done for both instruments analogously: Using the determined stellar parameters, I created a synthetic spectrum using SPECTRUM and cross-correlated it orderwise with the observed spectrum. For both the FEROS and the HARPS analysis, the same spectral orders have been used in order to not induce systematic errors. The cross-correlation functions have been fitted using a Gaussian function and the RV including error was determined. Since the error includes the fit quality, it automatically accounts for the quality of the spectrum. The final RVs were obtained by calculated the weighted mean of the RVs of the individual orders. Since the barycentric correction is not precise enough in case of FEROS, I applied the pipeline correction backwards, calculated the more precise value using IDL routines and applied this correction to the RV results.

8.1.5 RV results

In case both FEROS and HARPS data was available, the instrumental offset between the corresponding RVs has to be taken into account. Therefore, I used the IDL-program *RVlin.pro* to fit both data sets simultaneously including the instrumental offset. This offset then has been applied to the HARPS data. The resulting data could then be analyzed with GLS, treated as data from one single instrument. The advantage of this procedure is that GLS provides in contrast to *RVlin.pro* periodograms, which can be analyzed in terms of significant periods (both sine and Keplerian) in the data.

The GLS analysis identified 12 of the 21 targets showing no long-term stable period over the whole observing time. This does not automatically imply that no companion exists in the system, but more that the stellar activity might cover its signal. Another possibility is that the signal of a possible companion might be below the detection limit.

Six targets revealed significant periods in the periodograms, but these could be identified as induced by measurement sampling.

The remaining three targets (CD-37 13029, TYC 8654-1115-1 and HD 140637) revealed strong significant periods, which could not be traced back to measurement sampling. Nevertheless, photometric data of CD-37 13029 and HD 140637 showed the same significant period, which is an indicator for stellar surface features rotating along with the stellar surface. Stellar activity as origin of the RV signal could be identified for TYC 8654-1115-1 as well due to the careful analysis of a variety of stellar activity indicators.

8.1.6 Detection limits

In order to analyze, which minimum companion masses would in principle be detectable in the 21 data sets, I calculated the detection limit using the method described in Zechmeister & Kürster (2009). Doing so, the RV measurements are interpreted as noise, being added to a sine wave with known amplitude. The new data set consists then of data of the same sampling as before, but with an additional hidden sine wave with known amplitude and period. By calculating the GLS periodogram of this data set, the GLS power for the known period can be evaluated over amplitude. By systematically increasing the amplitude, the period becomes at some point significant and can then converted to the minimum mass of the corresponding (artificial) companion. The analysis for the different targets shows that the different detection limits heavily depend on the number of measurements (since the FAP significance level decreases with increasing number of measurements, Zechmeister & Kürster, 2009). Furthermore, it is self-explaining that the detection limit increases in case the RV measurements (here treated as noise) show a large scatter. Furthermore, the nightly scatter increases the detection limit as well.

The influence of the measurement sampling can simply be guessed, since there is no direct possibility to compare different measurement samplings with this method. In case of a homogenous sampling, the reproducibility should be certainly easier.

The comparison of the median detection limit to other studies revealed that a fraction of about 0.9% of the targets in this sample are expected to host detectable planets with masses $> 2.5 M_J$ in orbits with period ≤ 1000 d. This corresponds to a number of 0.2 detectable giant planets in this sample. This result shows that significantly more targets (ideally at least a few hundred) are needed to perform a realistic RV search for exoplanets around young stars.

8.1.7 Stellar activity analysis

Within the RV analysis, 18 of 21 targets did not show a significant period or one that could be traced back to measurement sampling. For these targets, I calculated a variety of activity indicators derived from the CCF, individual spectral lines and whole spectral regions. Using GLS, it was possible to search for periodicities for each individual indicator in order to try to identify the rotational period of the targets. Eight targets (HD 23208, HD 51797, V2129 Oph, HD 139084, HD 183414, HD 216803, 1RXSJ0434 and CD-40 14901) revealed a significant period in several indicators. HD 23208 showed an about 2 d period in all bisectors as well as in the CCF skewness. An about 2.4 d period was identified for HD 51797 as well in all bisectors, but additionally as well in all CCF statistical moments (variance, skewness, kurtosis). V2129 Oph exhibited a ~ 1.9 d period in the BVS and the CCF variance and skewness. A significant 1.5 d period was identified in the S_{FEROS} analysis for HD 139084 and a significant period of about 2.4 d in the BVD analysis of HD 183414. HD 216803 revealed a significant period of about 1.2 d in the CCF variance, while 1RXSJ0434 showed significant periods of about 2.5 d in the BVD and of about 2.2 d in the CCF skewness. The last target, CD-40 14901 revealed a significant 1.6 d period in the H_{α} EW analysis. For seven of these eight targets, the detected period could be traced back to a physical origin namely rotational modulation due to spots on the stellar surface. 1RXSJ0434, however, showed a variety of different periods around 2 d in different activity indicators, photometry and RV. It was not possible to identify the underlying real period with the de-aliasing method. The reason for this are most likely the influence of many different stellar surface features, inducing a variety of signals which wash out the true signal of the rotational period.

The three remaining targets reveal a significant RV period that could not be assigned to measurement sampling. The signal of two targets (CD-37 13029 and HD 140637) could be connected to a detected photometric signal and therefore as most likely not caused by a companion in the system. While CD-37 13029 shows the same period of about 2.8 d in the BVS and BC, the signal of 2.76 d of HD 140637 could not be identified as significant signal from any of the activity indicator periodograms. Nevertheless, all CCF statistical moments and the CaH 2 spectroscopic index showed evidence of the period.

TYC 8654-1115-1 reveals a strong RV signal as well, but the lack of photometric data still raised hope for a companion induced nature of the signal. Since the BVS and the CCF skewness showed significant evidence of the period of 2.43 d as well, the signal is most likely as well as for the other two targets activity induced.

Although a variety of activity indicators has been analyzed in terms of periodicity, it is recognisable that mainly only the bisectors BVS, BC, and BVD as well as the CCF statistical moments helped to identified RV signals as most likely activity induced. H_{α} helped to identify the signal as activity induced in fewer cases. Although the periods were strongly recognisable in the RV as well as the bisectors and the CCF shape, individual lines like Ca IIR do not seem to be strongly affected by the activity so that they don't reveal the period. An additional typical indicator for stellar activity influences in the RV signal is the correlation between BVS and RV. For the analysis I calculated the linear Pearson coefficient R_{Pearson} . Six targets revealed an obvious correlation between BVS and RV with correlation coefficients between 0.62 and 0.91. Two of the six targets were CD-37 13029 ($R_{\text{Pearson}} = 0.82$) and TYC 8654-1115-1 ($R_{\text{Pearson}} = 0.91$), which strongly supports the suspicion that the detected RV signal is indeed caused by stellar activity.

All detected RV (short- and long-term) signals of all targets could be detected in stellar activity indicators and for some targets in photometric measurements as well. Therefore, one can conclude, that all detected RV variabilities can be assigned to activity-related rotational modulation. Nevertheless, it is possible, that these signals simply cover the signals of companions in the system.

8.1.8 Starspot scenarios

Since the RV signals of the most promising three targets in the sample were identified as most likely induced by stellar activity, I tried to find possible starspot scenarios, which can cause the detected RV and photometric amplitude. I used a modified version of the starspot program initially coded by R. Launhardt. The analysis showed that relatively easy starspot scenarios (just one spot with small size) can reproduce the RV semi-amplitude and the detected photometric signal. The given examples showed that it is in principle possible to reproduce a variety of RV curves of different shape and amplitude. But even if it is possible to find a fitting spot scenario for each possible RV curve, the major question is always, if the found spot solution is reasonable, i.e. physically possible (stable). Furthermore, since the parameter space of all free parameters is never completely monitored in this program, the found solution is never unique.

8.1.9 Discussion of results for individual targets

Group A (ESPRI overlap targets):

HD 96064: Since the two individual FEROS fibres have an aperture of 2 arcsec and a separation of 2.9 arcsec (FEROS manual¹), the primary component could be observed without a contamination of the binary in orbit (separation A-BC: 11.4 arcsec). The age of the target was given by Weise (2010) as 90 ± 10 Myrs. The isochrone analysis gave a lower limit of 20 Myrs, while the age determination using lithium depletion defined an upper limit of 230 Myrs. The activity age using S_{FEROS} was calculated as 177 ± 13 Myrs. The gyrochronological age could not be determined due to a lack of a rotational period. Furthermore, since a membership to a young moving group is not identified for this target, no kinematic age could be estimated.

Since the period of the BC component around A is very large (~ 3400 yrs), I did not find an evidence of a long term trend in the spectroscopic data covering more than eight years. The RV analysis bases on 130 spectra from FEROS and HARPS in total, but the only significant period of about 340 d could be traced back to measurement sampling.

Due to the large amount of measurements and low RV scatter, the detection limits for companions around the A-component is pretty low ($< 1.7M_{\text{J}}$ for a period < 100 d). The short-term analysis of the RV and of stellar activity indicators showed a periodicity of the BVS and the CCF skewness of about 9 d, which was identified as not significant.

HD 139084: The determined lithium and activity age agree both with the age determined by Weise (2010) of about 50 ± 15 Myr. The isochrones suggest an age of younger than 5 Myrs, and the kinematic age classifies the corresponding moving group as 12_{-4}^{+8} Myrs, which is not far off from the isochrone estimation. The 33 RV data points cover in total a time span of more than 7 yrs, and show three different significant periods. These could unfortunately be identified as being sampling induced. Due to the small number of data points

¹www.eso.org/sci/facilities/lasilla/instruments/feros/doc/manual/P78/FEROSII-UserManual-78.0.pdf

and a large RV scatter, the detection limits are very high ($12.2 M_J$ for a companion in a 2 d orbit and increasing towards longer periods).

The S_{FEROS} analysis revealed a significant period of ~ 1.5 d, which was identified as most likely real with the de-aliasing method of Dawson & Fabrycky (2010). Assuming this period as the rotational period of the target, the gyrochronological age corresponds to about 10 Myr, matching the kinematic age.

HD 183414: The results for the different age determination methods do not well agree for this target. While the isochrones give an upper limit of 20 Myr, the lithium analysis defines an upper limit of 120 Myr. The age determined using S_{FEROS} was calculated as 132 ± 7 Myr, not matching both limits. Weise (2010) determined the age as 75 ± 15 Myr, matching roughly the lithium value of this thesis.

101 spectra were available in total, covering a timespan of more than 7 yrs. Nevertheless, no significant long term stable period at all could be identified in the periodograms. The detection limits for companions in the system are due to the small RV scatter and large amount of measurements quite low ($< 2 M_J$ for a period < 100 d).

The only activity indicator revealing a significant period over the whole time span is the BVD, showing a period of ~ 2.4 d. The period was tested with the de-aliasing method and was identified as most likely not measurement sampling induced. The corresponding gyrochronological age is about 54 Myr, which does not really match with any of the previously calculated ages.

HD 216803: The age determination of this target shows splitted results. While the lithium age suggests an upper limit of 300 Myr, the gyrochronological age agrees with the isochrones of an age of less than 5 Myr. By looking on the isochrones it is clear that a large shift in $\log g$ and/or T_{eff} would be necessary to shift the isochrone age to about 300 Myr. The shift would correspond to $\Delta \log g \sim 1$ dex, which would have been most likely recognisable in the SME analysis. One possible solution is that the lithium EW calculation was influenced by a non-optimal veiling correction. The S_{FEROS} -age could not be calculated due to the late spectral type, which is not covered by the method.

HD 216803 was observed 29 times with FEROS and 217 times with HARPS over a time span of more than 8 yrs. Since the HARPS data points were all taken within 4 days, they have been neglected from the RV periodicity search. In the remaining FEROS data, no significant period could be identified. SuperWASP data revealed a significant period of 1.29 d, which could be interpreted as the rotational period of the target. Wright et al. (2011) identified the rotational period as 10.3 d, not matching the SuperWASP period. Due to the very large amount of data points, the detection limits are all very low. However, the sampling of the data is not ideal, why an identification of low-mass planets does not seem likely despite the low detection limits.

The activity indicator analysis revealed a significant period in the CCF variance of 1.21 d, which is pretty similar to the discovered rotational period in the SuperWASP data. Assuming the 1.21 d period as rotational period, the corresponding gyrochronological age is about 3.5 Myr, supporting the isochrone results. In case the 10.3 d period of Wright et al. (2011) is the correct rotational period, the gyrochronological age would correspond to about 220 Myr, supporting the lithium age.

The linear Pearson correlation coefficient of 0.62 between BVS and RV shows that the RV is most likely induced by activity.

Group B (targets, with > 5 initial FEROS data points):

1RXSJ033: While the isochrone age and the S_{FEROS} -age were in a good agreement (about 20 Myr), the lithium age proposed the target as being younger than 120 Myrs, which is a very unprecise value in comparison the the other age indicators.

67 RV data points were analyzed in total taken over a timespan of more than 4 yrs, but no long-term stable significant period could be identified. The analysis of shorter timescales of the RV revealed a non significant but prominent period of 1.25 d, which was found in the BVS and BVD as well. Although the period is not significant, it can be assumed as rotational period of the target. The period is of the right order of of magnitude so that the gyrochronological age (about 12 Myrs) matches the values of the isochrone and S_{FEROS} age analysis.

CD-37 1123: The age determination for this target revealed again a problem with the lithium EW result. While the estimations of the isochrone method and the S_{FEROS} age have the same order of magnitude as the Weise (2010) result of 25 ± 15 Myr, the lithium estimation just gives an upper limit of 120 Myr.

55 RV data points taken over more than four years revealed two different significant periods (~ 370 d and ~ 180 d), which could not be traced back to a real origin. Due to the low RV scatter, the detection limits are relatively low and a detection of a companion with mass of about $2 M_J$ should have been possible for period < 100 d.

No significant (not even prominent) period could be identified in the RV data on short timescales and in any of the analyzed activity indicators, indicating that certainly available stellar activity signals (due to the youth of the target) wash out over the timespan of four years and even on shorter timescales.

Weise (2010) proposed a substellar companion in the system, which existence could not be confirmed.

CD-37 13029: The different age indicators for this targets point all to a target age of less than about 60 Myr. While the S_{FEROS} age gives the upper limit of the age range with 53 ± 12 Myr. The gyrochronological age corresponding to a significant 2.8 d period in the SuperWASP data, matches the other age estimations. Hints for a circumstellar disk have been found in the SED analysis, but could be traced back to optical ghosting in the WISE images.

65 FEROS spectra taken in a timespan of more than four years have been analyzed in terms of RV periodicity. The detected significant 2.83 d period matches the detected photometric one and is most likely representing the stellar rotational period uncovered by a stable starspot corotating with the stellar surface. The activity analysis supports this assumption, since the the bisectors show significant variations with the same period. A correlation coefficient of 0.82 between BVS and RV confirms the suspicion that the RV signal might be caused by stellar activity.

The analysis with a spot program revealed a possible scenario that could cause both the RV and photometric amplitude. So can a starspot covering 6% of the stellar surface, 1750 K cooler than the stellar photosphere cause both signals, if the system is inclined by 45° and the spot is located at a latitude of 50° from the equator.

The results of this thesis confirm the suspicions of other groups of no (detectable) companion in this system.

CD-7824: The age of this target is most likely younger than 30 Myrs, in which all the age methods agree. The calculation using the activity index S_{FEROS} was not possible, since the method is not tested for these late spectral types.

44 spectra have been analyzed, which cover only a quite short timespan of about three years. Unfortunately, no significant period could be detected in the data. The analysis of stellar activity indicators (BVD and CCF skewness) and the RV on shorter timescales revealed a non significant but prominent period of about 4 days. This period would correspond to a gyrochronological age of about 40 Myr, matching roughly the previous age estimations.

These results do not confirm the claim of Weisse (2010) of a brown dwarf companion of about $15 M_{\text{J}}$ at about 0.3 AU in the system. The primary mass of CD-7824 is about $0.7 M_{\odot}$, so that the orbital distance of the companion corresponds to an orbital period of about 70 d. The calculated detection limits show, that in case the proposed companion existed in the system, it should have been easily detected given the available number of measurements, measurement sampling and RV scatter.

HD 217897: The age determination of this target was not successful. While the determination using isochrones was not possible due to the high metallicity of the target, the S_{FEROS} age could not be retrieved due to the late spectral type. The lithium result gives an upper limit of 300 Myrs, which is not in good agreement with the result of Weisse (2010), who list 30 ± 15 Myrs for this target.

Only 33 RV measurements cover a quite short time range of about four years. Nevertheless, four significant periods could be identified in the data between 45 d and 550 d. Unfortunately, all of them could be traced back to measurement sampling issues. The calculation of detection limits failed due to the very large scatter in the RV measurements of about 4 km/s over the whole timespan.

No significant period could be detected in any of the analyzed activity indicators.

TYC 5891-69-1: All age determination methods are in quite good agreement for this target and propose all together a target age of less than 35 Myr. This result matches the one from Weisse (2010) roughly (10 ± 5 Myr).

The analyzed 49 RV measurements cover a timespan of about four years and show no significant period at all. Furthermore, no photometric data was available to put constraints on the rotational period of the target.

A short term analysis of the RV and the activity indicator analysis (especially the BVS) revealed a non significant but prominent period of about 2.2 d. This period corresponds to a gyrochronological age of about 25 Myrs, matching the estimations of the other age indicators. The clear correlation between BVS and RV (correlation coefficient of 0.83) shows that the detected RV signal is most likely induced by stellar activity.

Weisse (2010) proposed a $4 M_{\text{J}}$ companion in an inner 0.04 AU orbit. This result could not be confirmed within the analysis of this thesis. The calculated detection limits based on the available measurements show, that such companion in a 0.04 AU orbit (which corresponds to a period of about 3 d assuming a stellar mass of $1 M_{\odot}$ on background of the spectral type) would be easily detectable.

TYC 7697-2254-1: The results of the different age determination methods were quite ambiguous, while all agree on an age of less than 100 Myr.

In total 48 spectra of FEROS and HARPS taken over a timespan of almost four years were used for the companion search. Unfortunately, no significant period could be detected.

The analysis of available SuperWASP data shows a significant 4 d period, which could be interpreted as the rotational period of the target. The corresponding gyrochronological age is about 96 Myr, being the oldest guess of all age results.

The RV has been analyzed on short timescales which revealed a non significant but prominent 4.2 d period. The activity indicator analysis revealed the same period in the BVD and the CCF skewness, supporting the 4 d photometric period.

TYC 8654-1115-1: The age estimations indicate clearly a stellar age of less than 30 Myr. 62 RV measurements in total over a timespan of about 3.5 yrs revealed a significant period of 2.43 d, which could not be identified as measurement sampling induced. No photometric data were available in order to look for evidence of the stellar rotational period. This RV signal corresponds to a substellar companion with an orbital distance of 0.033 AU with a mass of about $3 M_J$. The eccentricity of the orbit is small with 0.057. Nevertheless, although most activity indicators do not show any significant period at all, the CCF skewness and the BVS reveal significant the significant period at 2.43 d. Since a substellar companion would not affect the shape of the stellar spectrum, the probability is very high, that the 2.43 d period belongs to a corotating spot on the stellar surface inducing the detected RV signal. This suspicion is supported by the clear correlation of the BVS and RV with a correlation coefficient of 0.91.

Since no photometric data is available for this target, the search for a possible starspot scenario which can reproduce the detected RV amplitude, is fairly easy. Doing so, a starspot covering 6% of the stellar surface with a temperature difference of 1500 K to the stellar photosphere at a latitude of 10° with no stellar inclination can cause the detected signal.

HBC 603: The age estimation of this target is just possible using two different age determination methods, since the isochrones do not provide a clear guess due to the large errors of the stellar parameters and the age estimation using S_{FEROS} can not be applied due to the late spectral type. The kinematic age of it gives a guess of 1.5-4 Myr.

The analysis of 2MASS, WISE and IRAS data revealed the existence of a circumstellar disk in the system, which matches the results of Carpenter et al. (2009), who detected an accretion disk in the system. The careful analysis of 49 spectra taken over a timespan of about 4.5 years do not reveal any significant periods. The periodicity analysis of shorter timespans revealed a non significant but prominent period of 8.8 d, which was identified in the bisectors as well. Interpreting this as the rotational period of the star, the gyrochronological age corresponds to about 80 Myr not matching the kinematic age at all. Therefore, the identified period is most likely not the rotational period of the star.

Ghez et al. (1997) claimed a companion at about $1.8''$ distance in the system. Since the fibre aperture of FEROS is 2 arcsec, the companion should have been observed simultaneously. No evidence of this companion has been identified, though. This is not surprising since Ghez et al. (1997) characterized it as too red to be visible in $0.9 \mu\text{m}$ and only detectable in $2.2 \mu\text{m}$ wavelengths. Therefore, evidence of the companion in visual spectra were not expected. Due to the large orbital distance, RV trends would also be very small an over a long timespan, certainly not covered by the used measurements.

Group C (targets, with < 5 initial FEROS data points):

1RXSJ0434: The age estimations using different methods are all in good agreement, all pointing towards an age of probably less than 50 Myr. In total 45 FEROS measurements over a timespan of 4 yrs have been used for the companion search, revealing two significant

periods at 2.29 d and 1.77 d, which could be identified as both measurement sampling induced. SuperWASP data revealed a significant 2 d period, which lies approximately in the middle of both RV periods.

The activity indicator analysis revealed significant periods of 2.18 d and 2.48 d in the CCF skewness and the BVD, respectively. Both periods are close to the detected RV periods. The de-aliasing method has been used to identify the original period causing the others. Unfortunately, none of the detected periods could reproduce all peaks in the periodogram, indicating that none of them is the original period. Since the longer periods could reproduce more peaks, it can be expected that the original period lies between 2.2 d and 2.5 d. The proposed rotational period by Messina et al. (2011) of about 2.29 d period falls in this expected regime.

CD-40 14901: The determined age with the variety of methods all scatter between 35 and 100 Myrs. While the isochrones give 35 Myr as upper limit, all other age estimations lie above this threshold indicating an error in the isochrone age estimation.

The RV companion search bases on 47 FEROS spectra observed over almost four years. Three significant periods could be identified in the RV data between 42 and 565 d. Unfortunately, all could be traced back to measurement sampling issues. The analysis of SuperWASP data revealed a significant period of 3.22 d, which can be interpreted as rotational period of the star. The corresponding gyrochronological age is about 63 Myr.

The activity indicator analysis revealed a significant peak at 1.65 d, which is close to one half of the photometric period. The de-aliasing method identified the 3.22 d period as being most likely the true one, while the 1.65 d is just an alias of it.

HD 140637: All age determination methods classify this targets as very young (<25 Myr).

The lithium age determination failed, since the calculated Li EW was out of range.

46 FEROS and 21 HARPS measurements were used for the companion search taken over a timespan of more than seven years. The period analysis revealed two significant periods, the stronger at 1.56 d, the other at 2.76 d, which could not be traced back to the measurement sampling. The analysis of SuperWASP photometry showed a significant peak at 2.75 d period, which is within errorbars equal to the less strong RV period. The de-aliasing method revealed that indeed the larger period of 2.76 d can reproduce all large periodogram peaks, while the 1.56 d period fails, indicating the 2.76 d period as the true one although its signal is smaller.

The analysis of the activity indicators support the suspicion that both the photometric and the RV signal have most likely their origin in stellar activity patterns corotating with the stellar surface: The CCF statistical moments as well as the spectroscopic index CaH 2 show both periods, though not significant but prominent.

In order to reconstruct a possible starspot scenario, which could cause the detected photometric and RV signals, I used analogous to CD-37 13029 and TYC 8654-1115-1 the starspot program. The application of the program, that a spot covering 6% of the stellar surface, 1500 K cooler than the stellar photosphere could cause the measured photometric and RV signals, in case of no system inclination and the spot location at the stellar equator.

Although the detected companion by Brandner et al. (1996) with orbital separation of 0.67 arcsec can not resolved by FEROS (fibre aperture 2 arcsec) and the signal of the companion should be contained in the primary spectrum, I can not find evidence for it. Since they detected a brightness difference of primary and secondary of more than 2 at 1 μm , this was not expected.

HD 23208: The age of this target could be pretty consistently nailed down to be less than 35 Myr. The RV period analysis bases on 46 spectra in total taken within almost four years. Nevertheless, no significant period could be detected in the data.

While looking on shorter timespans of RV data, a significant 2 d period could be found, which was identified as well in all bisectors and the CCF skewness. Assuming this period as the rotational period of the star, the gyrochronological age corresponds to about 20 Myr, which matches the other estimations.

HD 25457: The age determination for this targets was quite unclear. The isochrone method failed, most likely due to unprecisely determined stellar parameters. The moving group membership of AB Dor gives an age of about 50 Myr, which lies significantly below the lithium age (<150 Myr) and the S_{FEROS} -age (293 ± 18 Myr). In total 56 spectra taken over more than seven years have been analyzed in terms of RV. Within the data, no significant period, which is stable of the whole seven years could be identified. Wright et al. (2011) determined the rotational period of the star as 3.13 d.

By looking on shorter timescales, a non significant but prominent period of 5.5 d could be identified, which was found in the BVS and CCF variance as well.

HD 51797: Comparing the different results of the age determination methods, two different age guesses exist. While the isochrone method and the S_{FEROS} method suggest ages younger than 10 Myr, the lithium age gives a range between 30 and 80 Myrs. This result is supported by the Carina moving group membership, which assigns an age of about 30 Myrs to the target.

In total 56 spectra were analyzed in terms of RV variability. The spectra cover a timespan of about four years. However, no significant period stable over the whole four years could be identified. Furthermore, due to the lack of photometric measurements, the determination of a rotational period independently from the spectra was not possible. By looking on shorter timespans, it was possible to identify a 2.4 d significant period in the RV data, which was detected in the bisectors and the CCF statistical moments as well. If assuming this period as the rotational period of the target, the corresponding gyrochronological age is about 25 Myr, supporting the kinematic and lithium age.

HD 81544: This target is most likely about 30 Myrs old. This is supported by the kinematic age of its moving group Carina, the lithium EW measurements and the S_{FEROS} -age. The isochrone analysis proposes an age of younger than 20 Myrs. The difference to the other results could be due to a non accurate determination of the stellar parameters. The RV periodicity analysis was done using 44 spectra which have been taken over a timespan of about 5.5 years and no significant period could be identified. Analogous to HD 51797, no photometric measurements were available to put constraints on the stellar rotational period. The analysis of short timescale variation revealed a non significant but prominent 1.3 d period, which was identified in the BVS measurements as well. The corresponding age determined with gyrochronology is about 10 Myrs, which does not agree with the kinematic age and the lithium depletion age but with the isochrone guess.

V2129 Oph: The age estimation of V2129 Oph bases simply on the kinematic age of its moving group Ophiuchus of about 2 Myr. The age determination using isochrones was not possible due to the high metallicity. Furthermore, the lithium EW was out of range so that no age could be determined as well. Additionally, the age estimation using S_{FEROS} was not possible due to the late spectral type of the target.

A circumstellar disk was detected in the system using 2MASS, WISE and IRAS data. This confirms the result of Carpenter et al. (2009) who detected an accretion disk.

The executed RV periodicity search using 62 spectra taken over about four years did not reveal a significant period stable over the whole timespan. Nevertheless, the period search on short timescales showed a significant period of 1.9 d, which was identified as well in the BVS and the CCF variance and skewness.

Bouvier et al. (1986) found a 6.3 d period, which was ascribed to starspots. However, this period was not found in the RV analysis on short and long timescales. Furthermore, no evidence of a companion in the system was detected, although the second body at a separation of 0.59 arcsec proposed by Ghez et al. (1993), should fall within the same fibre as the primary.

The analysis has shown that it is of great importance to always analyze the full set of activity indicators for young stars. Companions would have easily been claimed especially in the absence of photometric measurements. The best example for this is TYC 8654-1115-1. The radial velocity analysis showed the clear evidence of a long-term stable signal with a period of 2.43 d indicating a $3 M_{\text{J}}$ planet in a close-in orbit. The careful analysis of the stellar activity indicators has quickly exposed this signal as being most likely activity induced. Especially the correlation of BVS and RV identifies the RV signal as most likely activity induced.

Please note that conclusions on gyrochronological ages within this thesis have been made under the assumption that the method is still valid even for young stars. Recent results have shown that this assumption might be wrong.

The usually large scatter of determined ages with different methods shows that there currently does not exist a completely valid and fully tested age determination method that can be used for stars younger than 100 Myr. The hope lies now in newly proposed methods like the Deuterium depletion boundary. This method still has to be verified and fully tested, though.

8.2 Radial velocity variation of EX Lupi

This chapter describes the data analysis of FEROS and HARPS spectroscopic data of EX Lupi in terms of RV variability, periodicity and activity indicators. The aim was to reveal evidence of a companion in the system of the young eruptive star. The descriptions follow the publication of Kóspál et al. (2013, submitted to A&A) but are limited to my contribution (spectroscopic analysis of RV, activity indicators, spot scenarios) to the work. The detailed analysis of the RV variability visible in FEROS and HARPS data of EX Lupi has revealed a clear periodicity with a period of 7.417 d. The semi-amplitude K of the signal is about 2.2 km/s and indicates a companion of about $15 M_{\text{J}}$ in the system. The star exhibited a large outburst in 2008, during which the stellar spectra completely changed. The fact that RV measurements taken before the outburst agree well with the best fitting orbit solution supports the assumption of a companion in the system, since the structure of stable surface features are expected to change significantly during an outburst.

A variety of activity indicators were carefully analyzed to search for evidence of an activity origin of the signal. Since none of the analyzed indicators shows the detected RV period as significant in the individual GLS periodograms, stellar activity as origin of the detected RV

signal seems unlikely. The simulation with the spot program revealed that a very large spot covering a complete hemisphere significantly colder than the stellar photosphere would be necessary to reproduce the detected RV amplitude. The fact that such spot is most likely not stable over the observed timespan of five years, supports the companion hypothesis.

8.3 The search for exoplanets with the HATSouth survey

In this chapter, I have presented the detection and confirmation of HATS-2b, the second detection from the HATSouth survey. HATS-2 is a K-type star showing starspot activity, while its companion HATS-2b is a planet with a mass of $\sim 1.4 M_J$ and a radius of $\sim 1.1 R_J$. The follow-up observations were executed with a variety of instruments located at different observatories. The photometric observations with GROND revealed evidence of starspots. By modeling these features in the lightcurve, it was possible to estimate the size and temperature of the spots. The conjecture that both detected spots are in fact the same could neither be completely excluded nor confirmed.

The chapter followed the publication Mohler-Fischer et al. (2013) of which I am first author. For this paper I provided most of the FEROS spectra taken within MPG guaranteed time. I determined the corresponding RV as described in Section 2.4.1 and determined the stellar parameters with SME using the FEROS spectra. Furthermore, I calculated the bisectors to analyse the influence of stellar activity on the detected RV signal.

Chapter 9

Recommendations for future RV exoplanet surveys of young stars

This thesis has shown that the search for exoplanets around young stars is by any means not trivial. This chapter briefly summarizes the most important consequences for future surveys that can be drawn from the results of this thesis.

The first difficulty arises in the sample size. As shown during the detection limit calculation, approximately 0.9% of the targets in this sample host a detectable giant planet of $> 2.5 M_J$ in an orbit with orbital period < 1000 d. This corresponds to a target number of about 0.2 stars. Therefore, future RV exoplanet surveys of young stars should be executed on a sample significantly larger than the target sample of this thesis, ideally several hundreds of stars.

Another challenge is the selection of suitable targets for future surveys. Within this survey, targets have been selected using $v \sin i$ values amongst other criteria by Weise (2010), rejecting targets with fast rotation. Doing so, on one hand it is possible to avoid targets showing broad spectral lines due to the fast rotation, which makes the analysis in terms of RV and activity much easier. On the other hand, the risk is high to be biased towards targets being aligned almost pole-on towards the observer. Since planets usually orbit the star in its (or close to) its equatorial plane, the RV signal of planets in these systems is very low and makes detections problematic. Therefore, a rejection of targets showing evidence of fast rotation should be done carefully in future surveys.

Furthermore, it might be helpful to limit the target selection towards objects with previously known photometric period. This can help to identify the possible rotation period and its aliases in the RV periodograms. The drawback is certainly, that such targets are already known to have prominent surface features caused by activity, which complicates the search for (sub-)stellar companions in those systems. In case no photometric data is available for candidates of a survey, the photometric monitoring before the RV measurements is a time intensive and expensive procedure. Furthermore, if a known rotational period is wanted for survey targets, the risk persists that a large number of targets have to be set aside before the RV observations because no clear period can be identified, although an extensive photometric monitoring was executed. Nevertheless, the target selection on background of available photometric data and a known rotational period is recommended.

For those targets being selected for a future survey, a large amount of spectroscopic measurements is necessary to decrease the noise of orbit solutions. Furthermore, the long-term

monitoring of the targets over decades is absolutely crucial since (until now) starspots as origin of the RV signal can not for sure be excluded completely. In order to decide, how long a signal should be stable to not be able to be caused by a starspot anymore but in fact by a planet, the theory of starspot stability has to be studied pretty extensively in the future.

Another difficulty arises in the determination of stellar parameters in noisy spectra for the sample targets. Programs like **SME** are not designed to handle extremely noisy data including emission lines and significant line distortions. One possibility to optimize the stellar parameters estimation is to choose only not heavily distorted individual lines and to fit synthetic spectra to those in contrast to fitting synthetic spectra to whole spectral regions as has been done in this thesis. The careful selection of lines sensitive to the different stellar parameters is a time consuming and challenging task. In the future, the program by Casey Deen called *MoogStokes* (Deen, 2013), which is currently adopted for optical wavelengths, might be of great use. This program allows to fit for the magnetic field, providing a potential new activity indicator. In case a spot is rotating in and out view, the measured magnetic field should increase as soon as it appears and decrease as it vanishes from view. By analyzing periodic changes of the magnetic field, it could be possible to trace spots on the stellar surface. Since the influence of spots on the stellar spectra is wavelength-dependent, one possibility for the future would be to analyze RVs and activity indicators depending on wavelength or on origin of spectral lines, i.e. formation in different layers of the stellar atmosphere. One problem occurring in this approach is that the wavelength dependence of the spot signal can be covered by the Zeeman effect (A. Reiners, priv. comm.).

Furthermore, another problem arises in the age estimation of young stars. Since non of the currently available age determination methods seems to be suited for stars younger than 100 Myr, the age estimation can only be done roughly. New hopes lie in new ideas like the deuterium depletion boundary as proposed by R. Jeffreys at the recent *Protostars and Planets VI* conference in Heidelberg.

In general one can say, that the search for planets around young stars is essential to understand the timescales of planet formation and evolution. Although the necessary observations are (time) expensive and the analysis is challenging, the efforts are absolutely crucial to confirm or reject proposed planet formation scenarios. Since the telescope, instruments, computational equipment and the knowledge about the proper design and execution of large surveys will improve significantly in the near future, the question if planets can be detected around very young stars should just by a matter of time.

Appendix A

Determined stellar parameters

In this appendix, the determined stellar parameters T_{eff} , $\log g$, $[M/H]$, $v \sin i$, v_{mic} and v_{mac} using SME are listed. Furthermore, the $v \sin i$ -results using the method by Reiners et al. (2012) are given.

Target	SME							Re2012
	T_{eff} [K]	$\log g$	$[M/H]$	$v \sin i$ [km/s]	v_{mic} [km/s]	v_{mac} [km/s]	$v \sin i$ [km/s]	
Group A (ESPRI overlap targets):								
HD 96064	5501 ± 38	4.51 ± 0.10	-0.01 ± 0.02	4.98 ± 1.76	2.02 ± 0.22	1.95 ± 0.92	6.71 ± 0.19	
HD 139084	5488 ± 62	3.74 ± 0.29	-0.08 ± 0.02	15.16 ± 0.72	1.88 ± 0.43	11.64 ± 0.58	15.02 ± 0.81	
HD 183414	5840 ± 47	4.03 ± 0.17	-0.03 ± 0.04	10.76 ± 0.81	1.56 ± 0.32	9.69 ± 0.71	10.08 ± 0.42	
HD 216803	4707 ± 32	4.01 ± 0.14	-0.27 ± 0.06	0.11 ± 0.62	1.09 ± 0.41	3.82 ± 1.19	3.38 ± 0.81	
Group B (targets, with > 5 initial FEROS data points):								
IRXSJ033	5620 ± 35	4.15 ± 0.18	-0.05 ± 0.10	18.76 ± 1.23	2.01 ± 0.19	13.88 ± 1.82	13.02 ± 0.22	
CD-37 1123	5610 ± 32	4.37 ± 0.17	-0.12 ± 0.08	7.11 ± 1.29	1.92 ± 0.79	1.71 ± 1.24	5.72 ± 1.16	
CD-37 13029	5568 ± 74	3.51 ± 0.23	-0.07 ± 0.12	24.05 ± 3.22	2.19 ± 0.32	3.87 ± 0.83	20.68 ± 0.36	
CD-7824	4879 ± 47	3.64 ± 0.29	-0.23 ± 0.13	11.96 ± 1.94	1.82 ± 0.43	20.07 ± 2.36	16.04 ± 1.41	
HD 217897	5075 ± 69	3.14 ± 0.18	0.42 ± 0.07	0.12 ± 3.21	1.91 ± 0.22	8.66 ± 1.08	3.58 ± 0.89	
TYC 5891-69-1	5869 ± 72	4.11 ± 0.21	-0.02 ± 0.03	11.68 ± 2.51	2.72 ± 0.29	17.71 ± 0.83	15.39 ± 0.58	
TYC 7697-2254-1	5836 ± 51	4.41 ± 0.14	0.23 ± 0.05	6.11 ± 3.32	1.68 ± 0.28	11.33 ± 3.27	10.11 ± 0.43	
TYC 8654-1115-1	5577 ± 43	3.77 ± 0.20	0.03 ± 0.02	18.71 ± 2.31	1.90 ± 0.22	19.06 ± 0.79	20.30 ± 0.51	
HBC 603	3765 ± 121	4.60 ± 0.31	-0.11 ± 0.15	7.20 ± 1.82	1.67 ± 0.49	3.43 ± 0.76	5.78 ± 0.42	
Group C (targets, with < 5 initial FEROS data points):								
IRXSJ0434	5380 ± 25	4.25 ± 0.25	-0.18 ± 0.12	9.60 ± 0.45	1.92 ± 0.32	2.27 ± 0.66	9.43 ± 0.31	
CD-40 14901	5836 ± 41	4.17 ± 0.23	-0.07 ± 0.08	17.15 ± 1.42	1.76 ± 0.22	2.83 ± 3.16	14.23 ± 0.64	
HD 140637	4972 ± 81	3.77 ± 0.22	-0.25 ± 0.07	7.69 ± 3.40	2.31 ± 0.21	13.84 ± 0.52	10.05 ± 0.71	
HD 23208	5573 ± 48	4.34 ± 0.12	-0.07 ± 0.06	12.83 ± 2.35	1.99 ± 0.32	2.17 ± 0.34	10.71 ± 0.75	
HD 25457	6539 ± 52	4.03 ± 0.17	0.08 ± 0.04	13.18 ± 3.65	2.30 ± 0.61	20.43 ± 1.76	16.86 ± 0.54	
HD 51797	5531 ± 86	3.93 ± 0.21	-0.17 ± 0.09	18.46 ± 4.64	2.41 ± 0.80	7.05 ± 2.63	13.52 ± 1.13	
HD 81544	5503 ± 46	4.13 ± 0.16	-0.10 ± 0.03	15.63 ± 3.54	2.26 ± 0.21	8.67 ± 0.50	12.22 ± 0.89	
V2129 Oph	4380 ± 35	3.72 ± 0.18	0.21 ± 0.06	13.11 ± 0.64	1.60 ± 0.15	8.54 ± 1.33	14.18 ± 0.78	

Table A.1: Stellar parameters for target stars determined with SME . Furthermore, the independently determined $v \sin i$ of the targets following Reiners et al. (2012) is listed in the rightmost column (Re2012).

Appendix B

Age determination

This appendix contains the results of a variety of age determination methods.

In Sec. B.1, the YY-isochrones (Yi et al., 2001) for each target are shown sorted by the three different target groups.

Within Sec. B.2, known moving group memberships for the single targets are listed together with the corresponding age estimations.

The results for the veiling determination using different methods are listed in table B.2 in Sec. B.3. The veiling corrected Li EW can then be used to determine the stellar age, by plotting it over spectral type (Fig. B.6).

Section B.4 lists the results for the determination of the gyrochronological ages (Barnes, 2007). The rotation periods were estimated on background of SuperWASP photometric data. Fig. B.7-B.9 show the GLS periodograms of the available data.

B.1 Isochrones

Group A (ESPRI overlap targets):

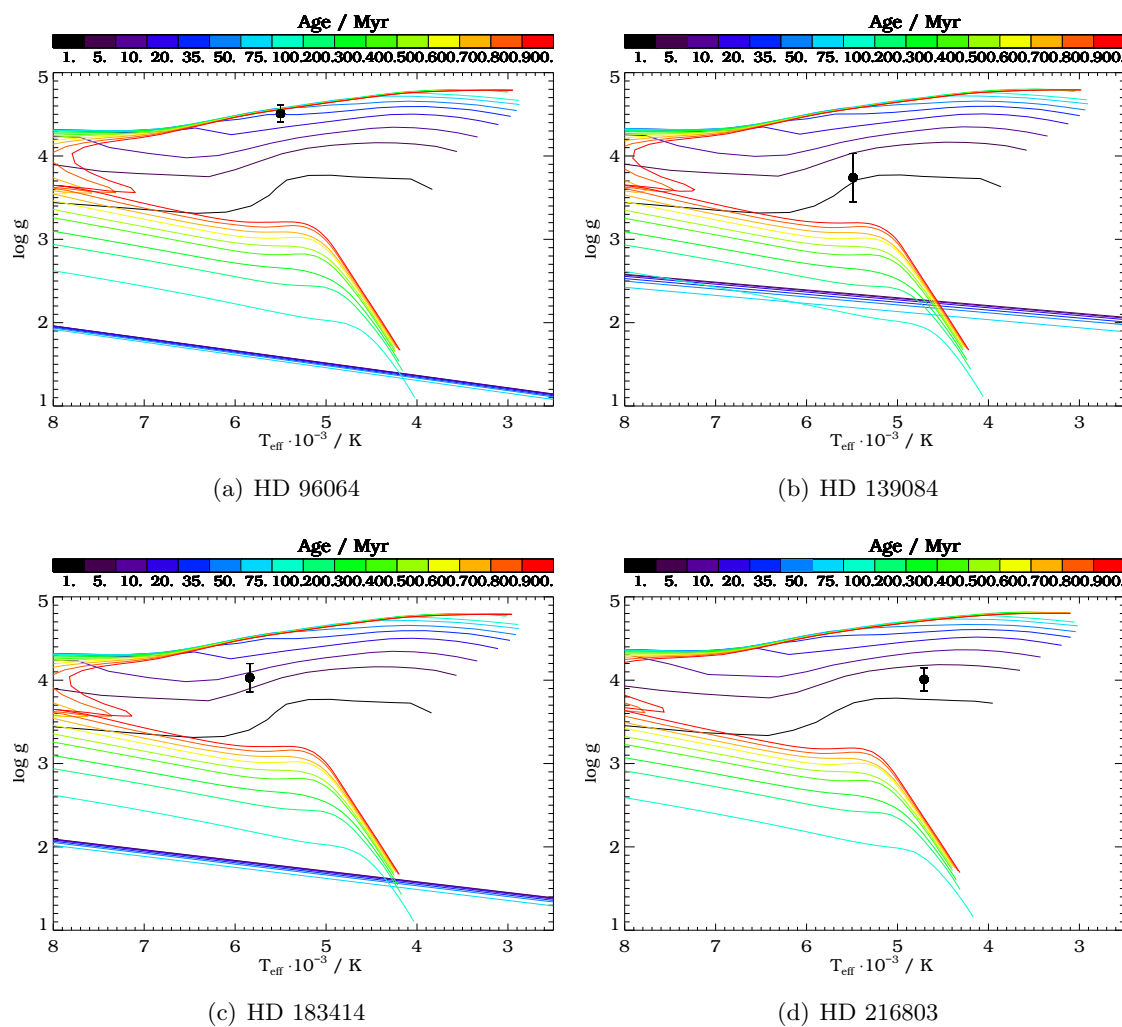


Figure B.1: YY-isochrones of Group A targets with overlotted stellar parameters T_{eff} and $\log g$ determined with SME.

Group B (targets, with > 5 initial FEROS data points):

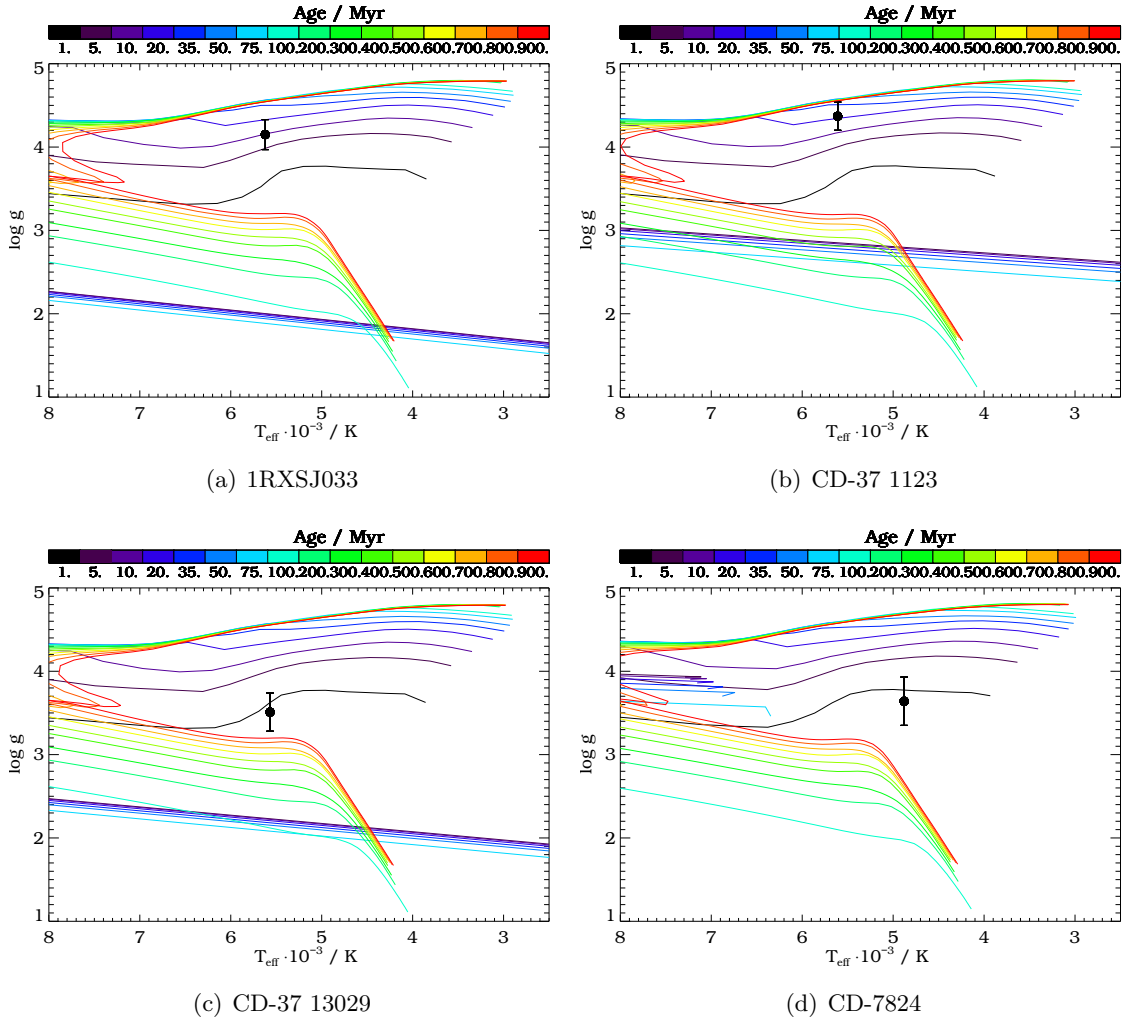


Figure B.2: YY-isochrones of Group B targets with overplotted stellar parameters T_{eff} and $\log g$ determined with SME.

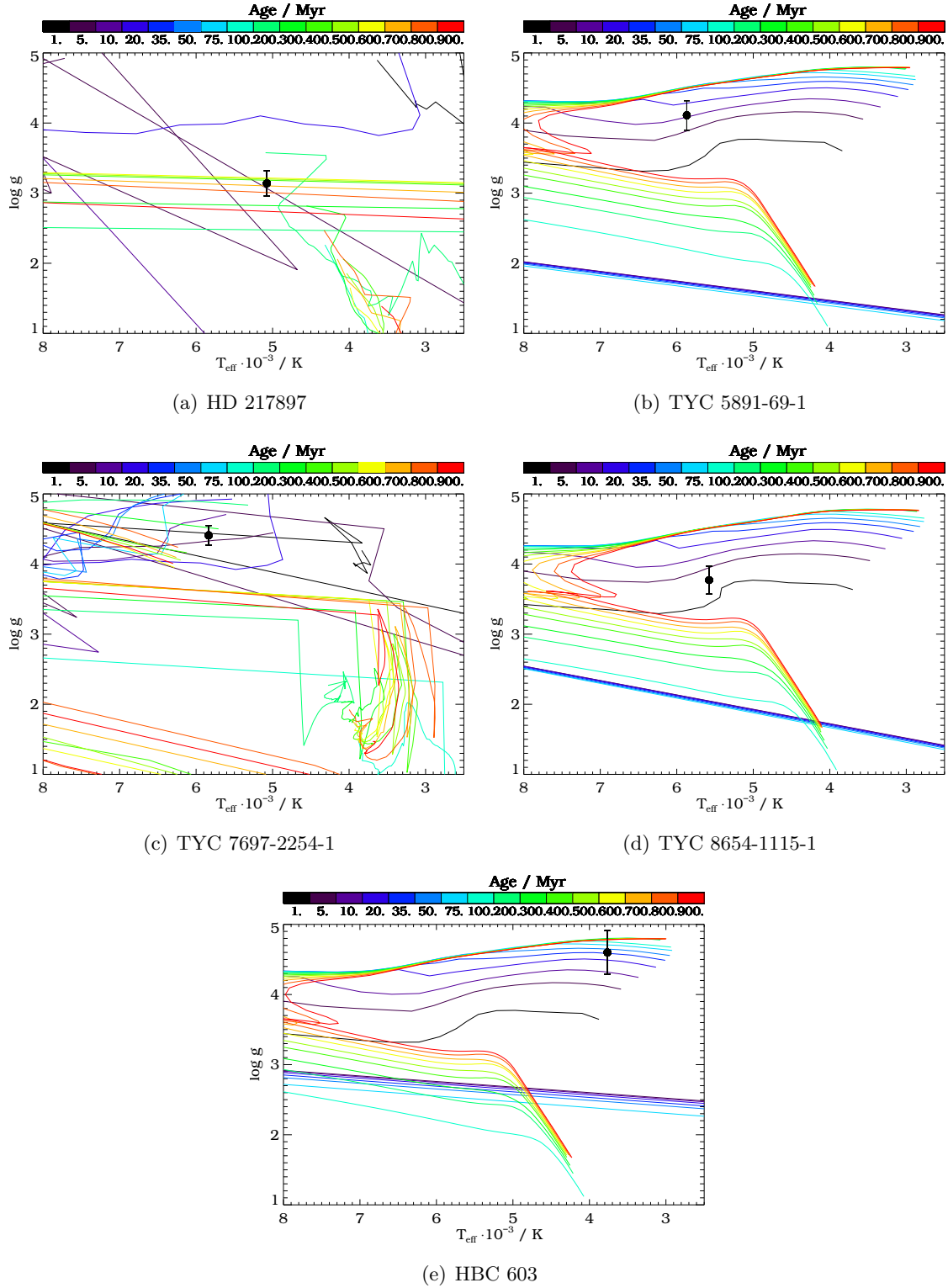


Figure B.3: YY-isochrones of Group B targets with overplotted stellar parameters T_{eff} and $\log g$ determined with SME. Panels a) and c) show, that the YY-isochrones can not be correctly calculated for stellar metallicities $[M/H] > +0.2$.

Group C (targets, with < 5 initial FEROS data points):

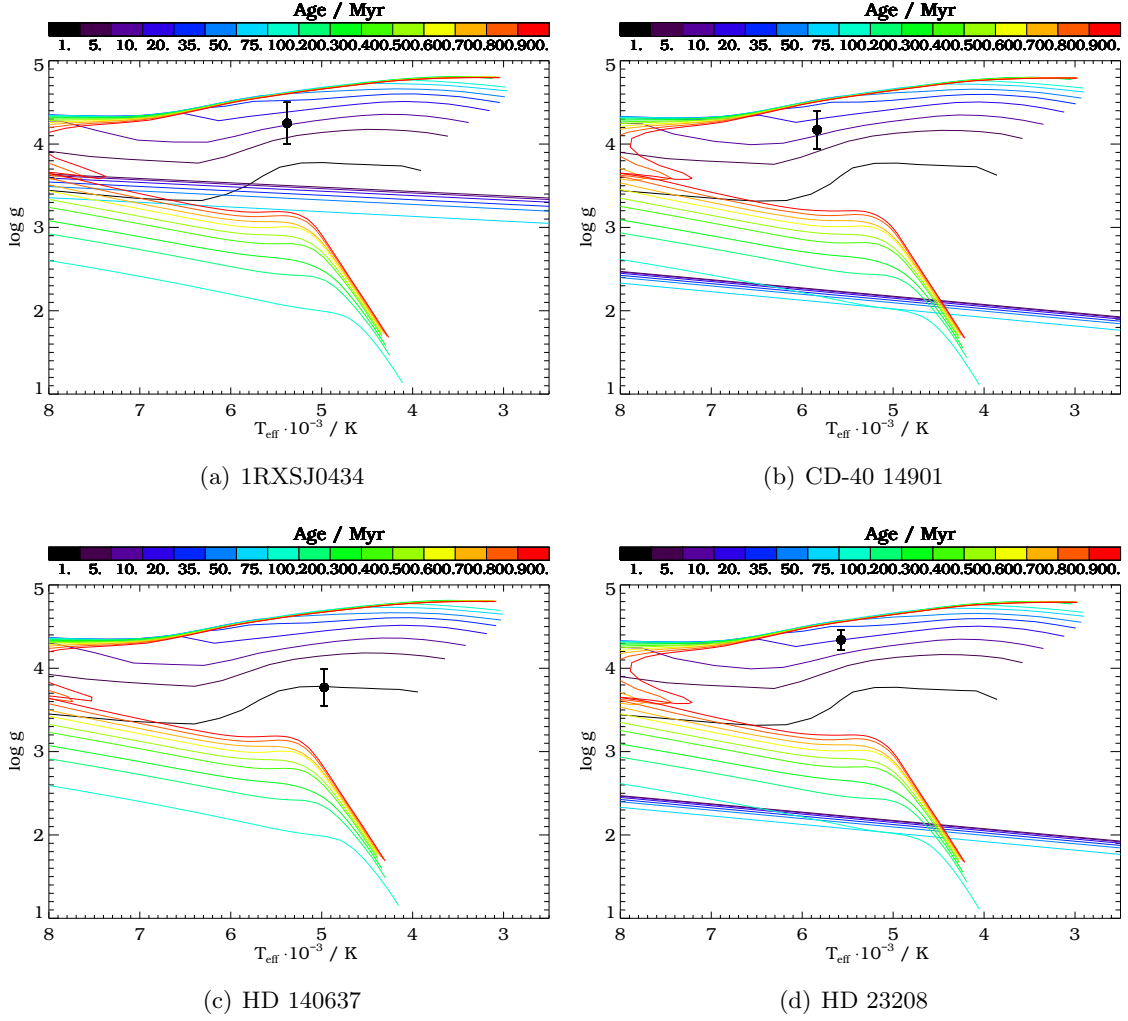


Figure B.4: YY-isochrones of Group C targets with overplotted stellar parameters T_{eff} and $\log g$ determined with SME.

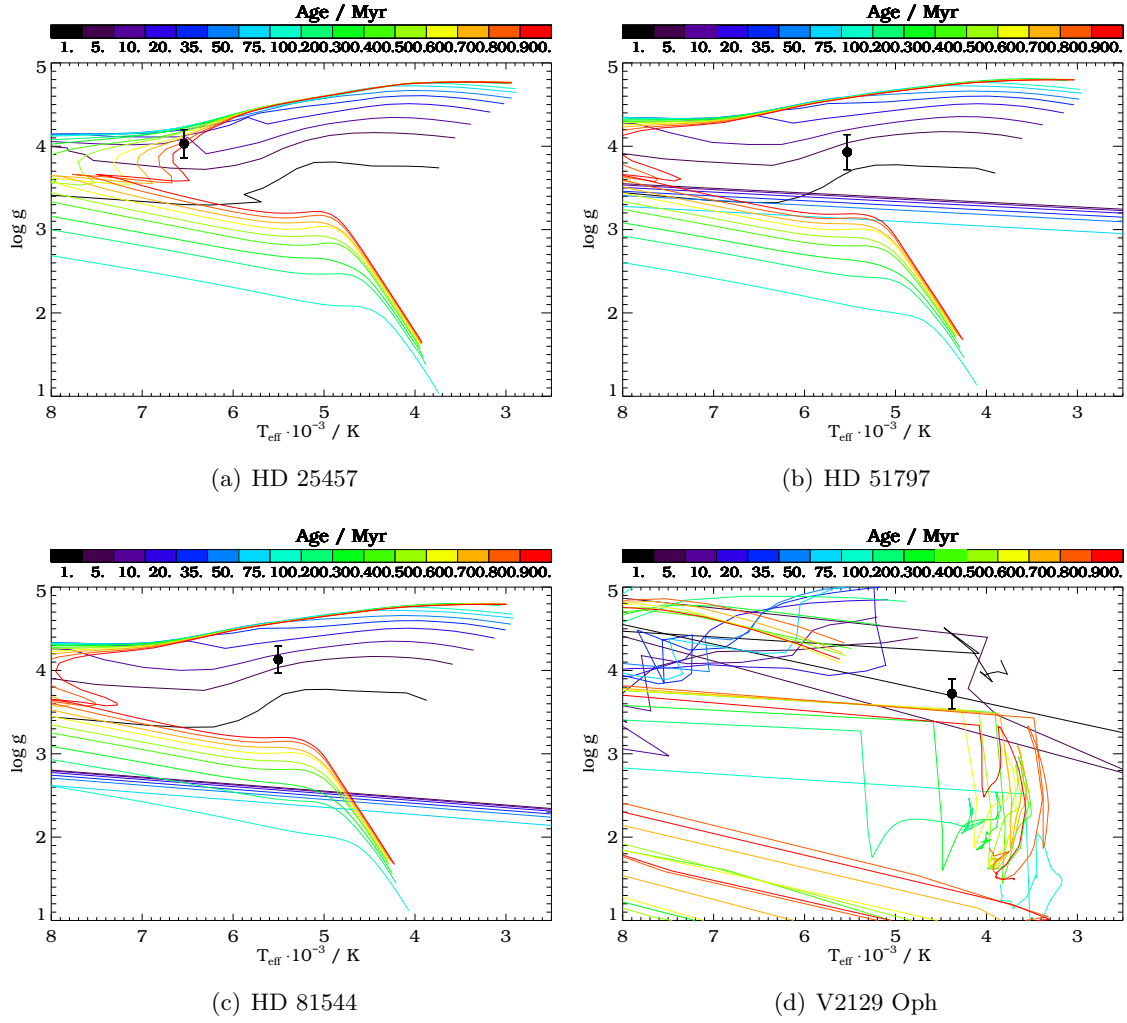


Figure B.5: YY-isochrones of Group C targets with overplotted stellar parameters T_{eff} and $\log g$ determined with SME. Panel d) shows, that the YY-isochrones can not be correctly calculated for stellar metallicities $[M/H] > +0.2$.

B.2 Moving group memberships

Target	Moving group (MG)	Reference	Estimated age of MG [Myr]	Reference
Group A (ESPRI overlap targets):				
HD 96064	nM	Wi03	—	—
HD 139084	β Pic	Zu04	12^{+8}_{-4}	Zu01
HD 183414	nM	So98	—	—
HD 216803	uM	—	—	—
Group B (targets, with > 5 initial FEROS data points):				
1RXSJ033	uM	—	—	—
CD-37 1123	uM	—	—	—
CD-37 13029	extended R CrA	Fe08	~ 13	Fe08
CD-7824	Tuc/Hor	dS09	~ 30	dS09
HD 217897	uM	—	—	—
TYC 5891-69-1	nM	Si06	—	—
TYC 7697-2254-1	possible TW Hydrae	Re03	~ 8	So03
TYC 8654-1115-1	Sco OB2.4 (Lower Centaurus Crux)	Ho00	11 – 12	dG89
HBC 603	Lup I	Gh97	1.5-4.0	Hu04
Group C (targets, with < 5 initial FEROS data points):				
1RXSJ0434	Columba	Me10	~ 30	Me10
CD-40 14901	uM	—	—	—
HD 140637	Upper Centaurus Lupus	So12	~ 10	So12
HD 23208	possible Octans	Vi09	~ 20	To08
HD 25457	AB Dor	Zu04	~ 50	Zu04b
HD 51797	Columba	Me10	~ 30	Me10
HD 81544	Carina	Me10	~ 30	Me10
V2129 Oph	Oph	—	~ 2	Ev09

Table B.1: Moving group (MG) memberships and according ages. (nM): no membership found and star identified as field star, (uM): unknown membership. Targets which could be identified as (possible) members of young moving groups are highlighted.

Wi03: Wichmann et al. (2003), **Zu04:** Zuckerman & Song (2004), **Zu01:** Zuckerman et al. (2001), **So98:** Soderblom et al. (1998), **Fe08:** Fernández et al. (2008), **dS09:** da Silva et al. (2009), **Si06:** Silverstone et al. (2006), **Re03:** Reid (2003), **So03:** Song et al. (2003) **Ho00:** Hoogerwerf (2000), **dG89:** de Geus et al. (1989), **Gh97:** Ghez et al. (1997), **Hu04:** Hughes et al. (1994) **Me10:** Messina et al. (2010), **So12:** Song et al. (2012), **Vi09:** Viana Almeida et al. (2009), **To08:** Torres et al. (2008), **Zu04b:** Zuckerman et al. (2004), **Ev09:** Evans et al. (2009)

B.3 Lithium I EW

Object	Li I EW _{uc} [mÅ]	V_{cont}	V_{KI}	V_{CaI}	V_{TiO}	V	Li I EW _c [mÅ]	age [Myr]
Group A (ESPRI overlap targets):								
HD 96064	112 ± 9	0.13 ± 0.05	eld	0.31 ± 0.12	0.45 ± 0.16	0.18 ± 0.05	133 ± 13	< 230
HD 139084	291 ± 29	0.01 ± 0.06	eld	0.01 ± 0.02	0.32 ± 0.22	0.01 ± 0.06	294 ± 35	30-80
HD 183414	144 ± 10	0.07 ± 0.10	0.03 ± 0.04	0.15 ± 0.02	0.50 ± 0.01	0.41 ± 0.01	204 ± 15	< 120
HD 216803	28 ± 4	0.47 ± 0.05	0.55 ± 0.03	0.12 ± 0.12	0.59 ± 0.05	0.53 ± 0.03	43 ± 7	< 300
Group B (targets, with > 5 initial FEROS data points):								
1RXSJ033	249 ± 10	0.02 ± 0.02	eld	0.10 ± 0.02	0.50 ± 0.28	0.06 ± 0.02	264 ± 12	< 120
CD-37 1123	211 ± 13	0.15 ± 0.03	0.47 ± 0.09	0.04 ± 0.06	0.50 ± 0.05	0.17 ± 0.02	247 ± 16	< 120
CD-37 13029	305 ± 33	0.12 ± 0.01	0.41 ± 0.09	0.15 ± 0.25	0.50 ± 0.02	0.20 ± 0.01	366 ± 40	< 30
CD-7824	282 ± 9	0.34 ± 0.05	0.47 ± 0.03	0.08 ± 0.05	0.50 ± 0.05	0.39 ± 0.03	392 ± 16	5-30
HD 217897	31 ± 4	0.74 ± 0.04	0.22 ± 0.04	0.27 ± 0.04	0.48 ± 0.09	0.41 ± 0.03	44 ± 6	~ 300
TYC 5891-69-1	266 ± 14	0.19 ± 0.07	0.37 ± 0.21	0.22 ± 0.24	0.53 ± 0.22	0.23 ± 0.07	327 ± 26	5-30
TYC 7697-2254-1	241 ± 6	0.50 ± 0.08	0.42 ± 0.03	0.07 ± 0.02	0.50 ± 0.02	0.31 ± 0.02	316 ± 10	30-80
TYC 8654-1115-1	301 ± 24	0.10 ± 0.14	0.40 ± 0.14	0.08 ± 0.22	0.50 ± 0.02	0.49 ± 0.02	448 ± 37	< 30
HBC 603	551 ± 76	0.10 ± 0.08	0.18 ± 0.09	0.67 ± 1.61	0.03 ± 0.03	0.05 ± 0.03	579 ± 82	5-30
Group C (targets, with < 5 initial FEROS data points):								
1RXSJ0434	283 ± 15	0.03 ± 0.05	0.55 ± 0.09	0.12 ± 0.04	0.51 ± 0.04	0.27 ± 0.03	359 ± 21	< 30
CD-40 14901	177 ± 9	0.00 ± 0.02	0.37 ± 0.07	0.11 ± 0.05	0.51 ± 0.02	0.25 ± 0.02	221 ± 12	~ 80
HD 140637	432 ± 19	0.20 ± 0.05	0.12 ± 0.30	0.42 ± 0.05	0.52 ± 0.03	0.43 ± 0.03	618 ± 31	out
HD 23208	259 ± 7	0.02 ± 0.03	0.43 ± 0.02	0.11 ± 0.05	0.50 ± 0.01	0.44 ± 0.01	373 ± 11	~ 30
HD 25457	104 ± 5	0.01 ± 0.05	0.05 ± 0.02	0.12 ± 0.01	0.46 ± 0.02	0.16 ± 0.01	120 ± 6	< 150
HD 51797	295 ± 19	0.02 ± 0.07	0.10 ± 0.03	0.02 ± 0.02	0.44 ± 0.05	0.08 ± 0.02	319 ± 22	30-80
HD 81544	311 ± 15	0.01 ± 0.04	0.03 ± 0.01	0.13 ± 0.03	0.52 ± 0.06	0.05 ± 0.01	327 ± 17	30-80
V2129 Oph	518 ± 56	0.21 ± 0.11	0.13 ± 0.06	0.41 ± 0.13	0.55 ± 0.04	0.40 ± 0.04	725 ± 82	out

Table B.2: Li I EW results as well as the veiling determined using different methods are listed. The corresponding age estimations are shown in the rightmost column.

eld: enhanced line depth, veiling could not be calculated, out: Li I EWs lie out of covered range (see Fig. B.6).

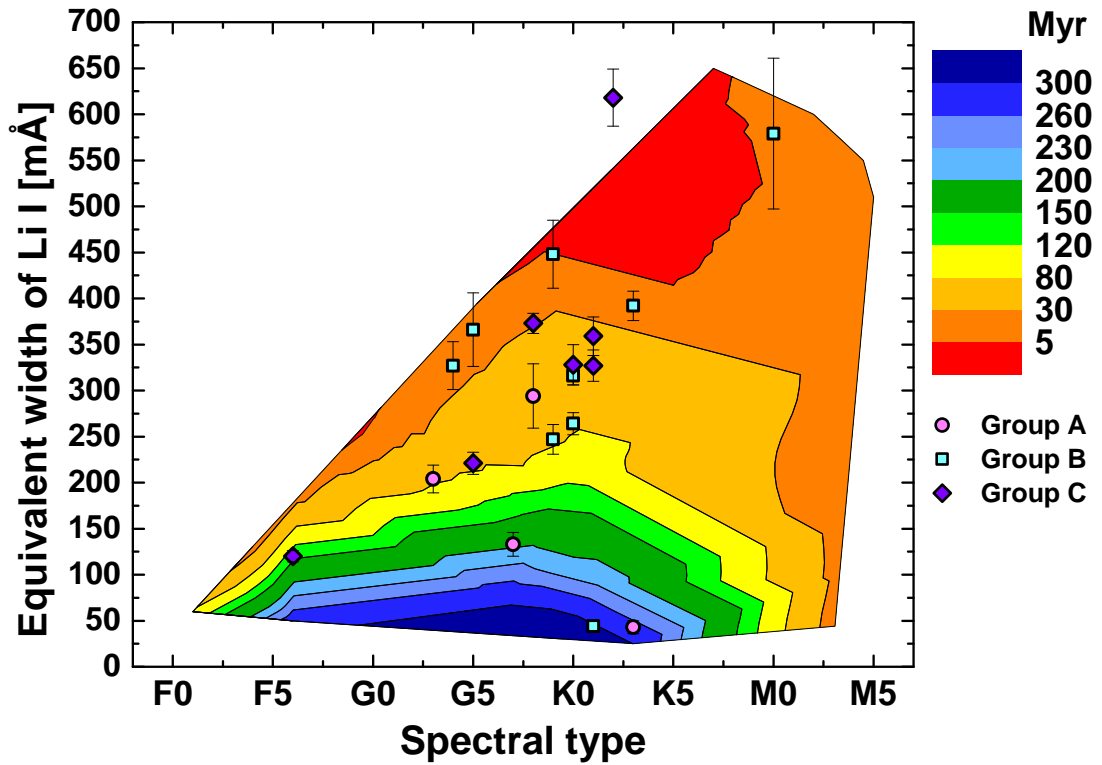


Figure B.6: For veiling corrected Li I EWs over spectral type. Pink circles mark the targets of Group A, cyan square these of Group B and purple diamonds the targets of Group C. V2129 Oph is missing, since its corrected Li I EW is 725 \AA and hence not part of the figure. The target outside the shaded contours is HD 140637. The contours are adopted from Weise (2010) by using Zuckerman & Song (2004) values for known moving groups.

B.4 Gyrochronological ages

Target	Rot. Period [d]	$(B - V)$ [mag]	t_{Gyro} [Myr]
Group A (ESPRI overlap targets):			
HD 216803	1.29 ± 0.01	1.1 ± 0.1	4 ± 1
Group B (targets, with > 5 initial FEROS data points):			
CD-37 1123	nsp	—	—
CD-37 13029	2.80 ± 0.01	0.9 ± 0.1	27 ± 2
HD 217897	nsp	—	—
TYC 7697-2254-1	4.00 ± 0.01	0.7 ± 0.1	96 ± 6
HBC 603	nsp	—	—
Group C (targets, with < 5 initial FEROS data points):			
1RXSJ0434	2.00 ± 0.01	0.9 ± 0.1	53 ± 4
CD-40 14901	3.22 ± 0.01	0.7 ± 0.1	63 ± 4
HD 140637	2.75 ± 0.01	0.97 ± 0.05	22 ± 2
HD 23208	nsp	—	—
V2129 Oph	nsp	—	—

Table B.3: Rotational periods determined by the analysis of photometric Super-WASP data, $(B - V)$ values (taken from SIMBAD¹) and derived gyrochronological ages following Barnes (2007). nsp = no significant period identified

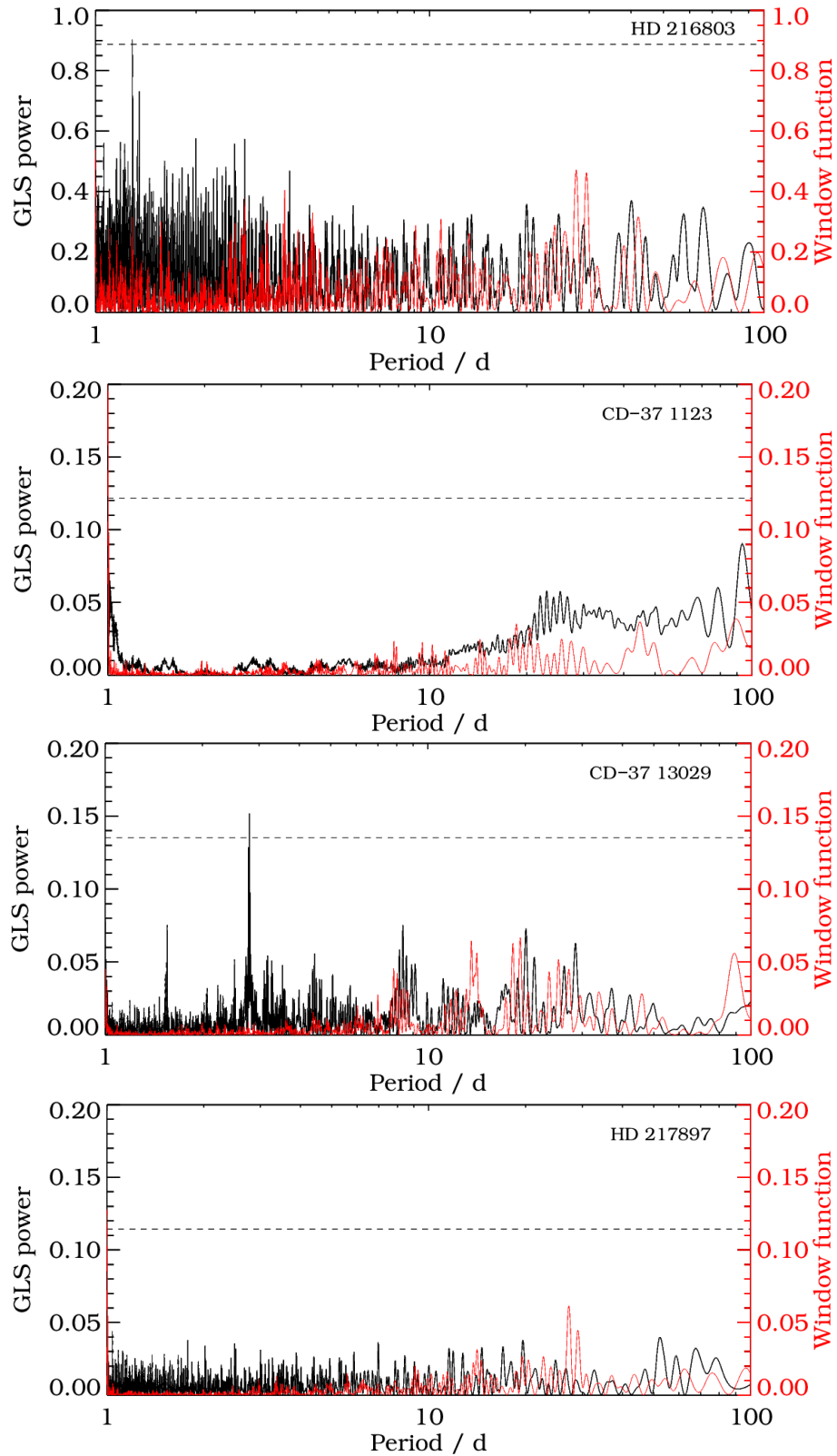


Figure B.7: GLS periodograms for SuperWASP photometry. The dashed line shows the FAP level of 0.1%. A clear significant period can be identified for HD 216803 and CD-37 13029.

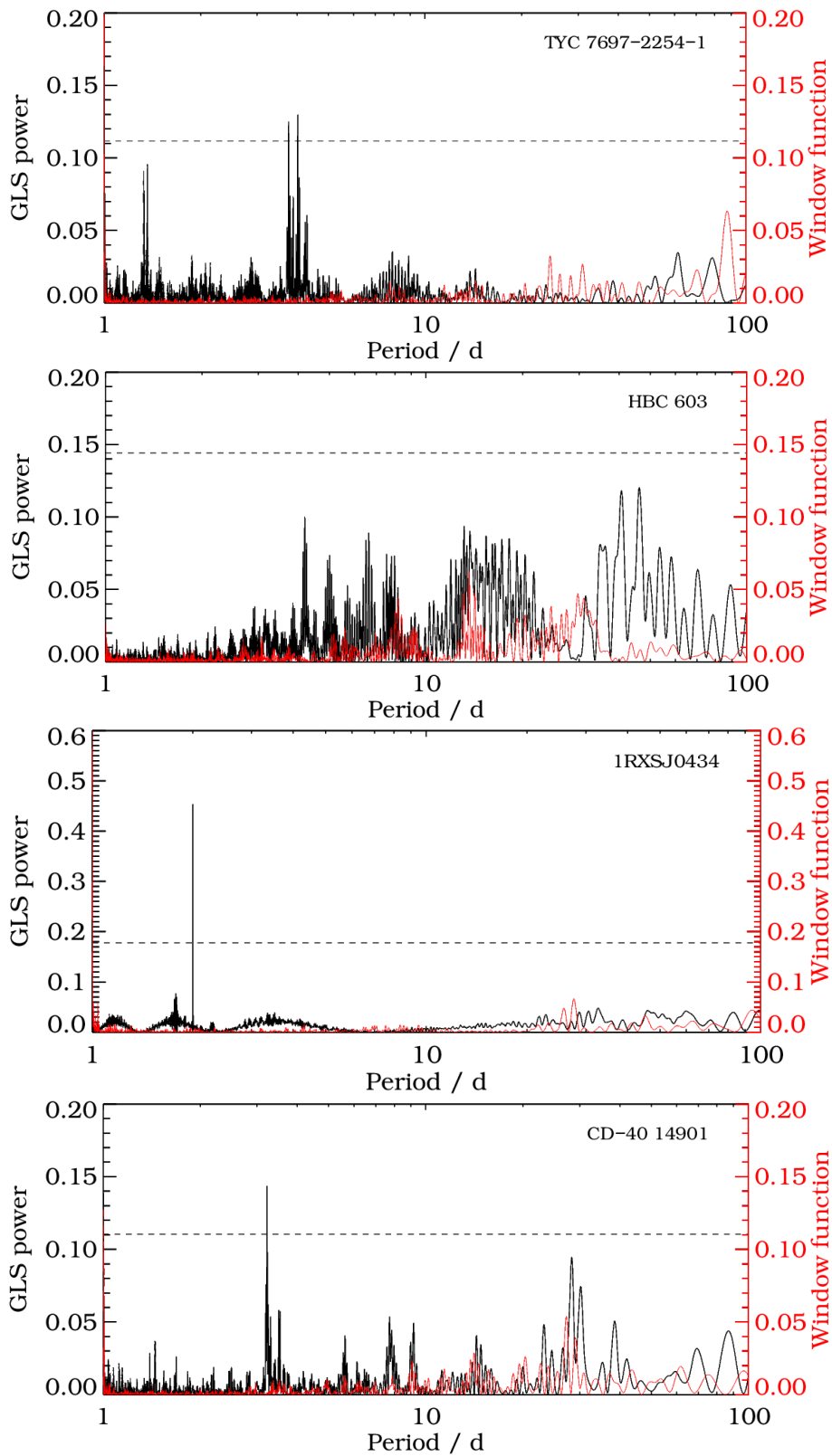


Figure B.8: GLS periodograms for SuperWASP photometry. The dashed line shows the FAP level of 0.1%. A clear significant period can be identified for 1RXSJ0434 and CD-40 14901. Two close periods could be identified for TYC 7697-2254-1.

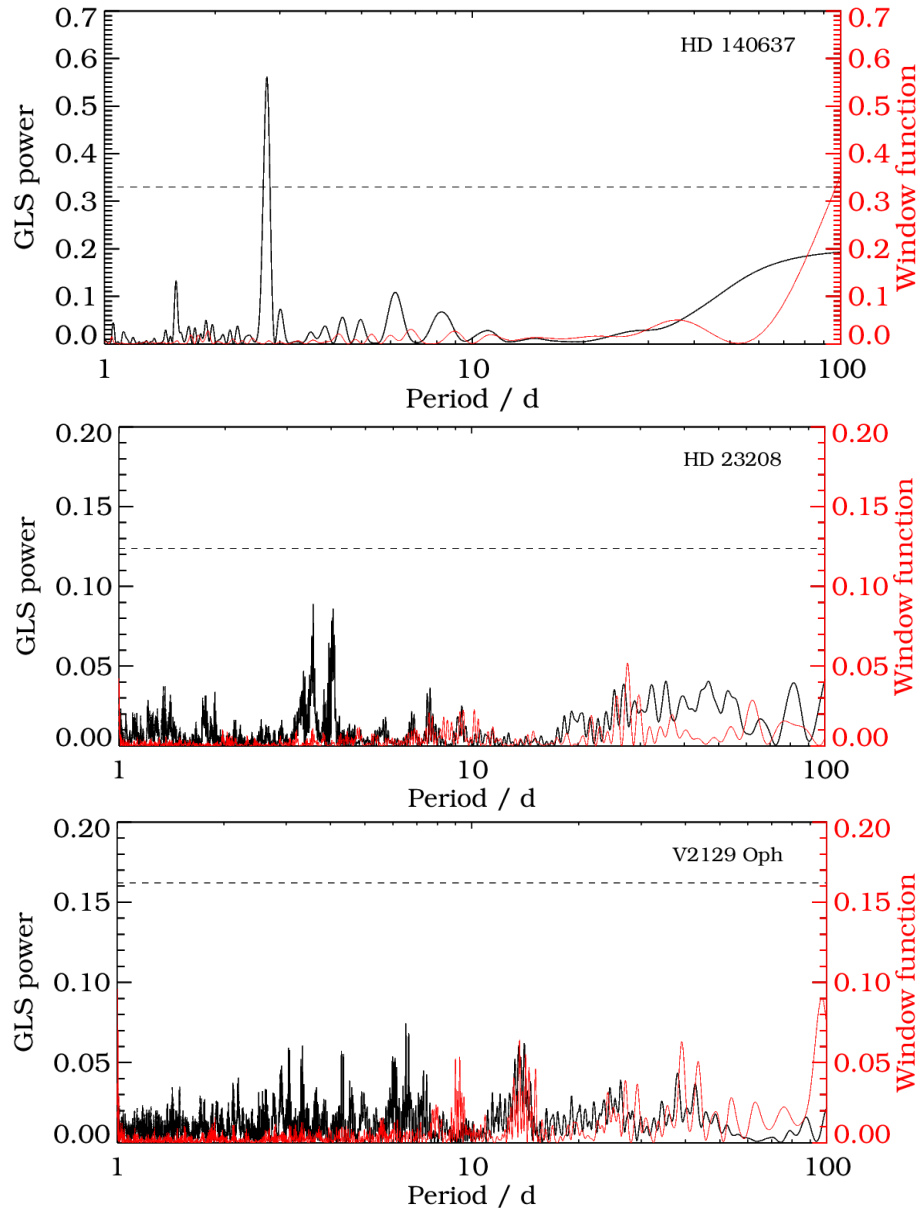


Figure B.9: GLS periodograms for SuperWASP photometry. The dashed line shows the FAP level of 0.1%. A pretty broad significant signal could be identified for HD 140637.

Appendix C

Disks

By using 2MASS, WISE (and in some cases IRAS) magnitudes, the analysis of the stellar SED in terms of disk presence was possible. This appendix contains the used magnitudes as well as the SED fits obtained with the SED fitter¹ by Robitaille et al. (2007).

¹<http://caravan.astro.wisc.edu/protostars/sedfitter.php>

Target	2MASS [mag]			WISE [mag]					IRAS [mJ]			
	J	H	K	3.4 μm	4.6 μm	12 μm	22 μm	12 μm	25 μm	60 μm	100 μm	
Group A (ESPRi overlap targets):												
HD 96064	6.302	5.903	5.801	5.284	4.653	5.102	5.314 ^u	352.4 ^u	255.9 ^u	400.0 ^u	100.0	
HD 139084	6.382	5.994	5.852	5.912	5.727	5.816	5.795	533.0	257.0	390.0	4220.0	
HD 183414	6.718	6.397	6.298	6.189	6.244	6.315	6.250	172.0 ^u	100.5	142.2 ^u	1029.0 ^u	
HD 216803	4.533	3.804	3.805	3.732	3.206	3.736	3.769	1250.0	307.0	400.0 ^u	100.0 ^u	
Group B (targets, with > 5 initial FEROS data points):												
IRXSJ033	9.402	9.021	8.904	8.790	8.824	8.722	8.527	—	—	—	—	
CD-37 1123	9.086	8.704	8.600	8.518	8.560	8.492	8.134	—	—	—	—	
CD-37 13029	8.903	8.478	8.354	8.257	8.288	7.934	6.080	—	—	—	—	
CD-7824	8.220	7.659	7.529	7.461	7.489	7.425	7.509	88.77	62.17 ^u	126.8 ^u	599.9 ^u	
HD 217897	7.723	7.144	7.044	6.907	7.050	6.957	6.796	—	—	—	—	
TYC 5891-69-1	9.128	8.734	8.630	8.571	5.605	8.534	8.309	—	—	—	—	
TYC 7697-2254-1	9.412	8.982	8.881	8.772	8.805	8.691	8.627	78.12 ^u	90.83 ^u	501.4 ^u	3621.0 ^u	
TYC 8654-1115-1	8.711	8.239	8.133	8.032	8.059	8.001	7.865	—	—	—	—	
HBC 603	9.444	8.590	8.271	7.777	7.378	5.358	3.441	302.0 ^u	419.0	—	—	
Group C (targets, with < 5 initial FEROS data points):												
IRXSJ0434	9.295	8.755	7.592	8.480	8.521	8.443	8.588	—	—	—	—	
CD-40 14901	8.210	7.897	7.769	7.656	7.689	7.640	7.847	—	—	—	—	
HD 140637	7.178	6.640	6.458	6.397	6.391	6.336	6.201	120.2	190.8 ^u	379.5 ^u	2684.0 ^u	
HD 23208	7.706	7.305	7.200	7.125	7.141	7.118	6.658	—	—	—	—	
HD 25457	4.712	4.342 ^u	4.181 ^u	9.654 ^u	6.076	5.645	6.318	1020.0	275.0 ^u	295.0 ^u	5510.0 ^u	
HD 51797	8.390	7.893	7.803	7.630	7.655	7.601	7.505	—	—	—	—	
HD 81544	8.557	8.064	7.964	7.792	7.829	7.780	7.932	—	—	—	—	
V2129 Oph	8.546	7.778	7.306	6.565	6.101	4.204	2.054	1084.0	1555.0	—	—	

Table C.1: Used magnitudes for SED fitting, ^u: upper limits

Group A (ESPRI overlap targets):

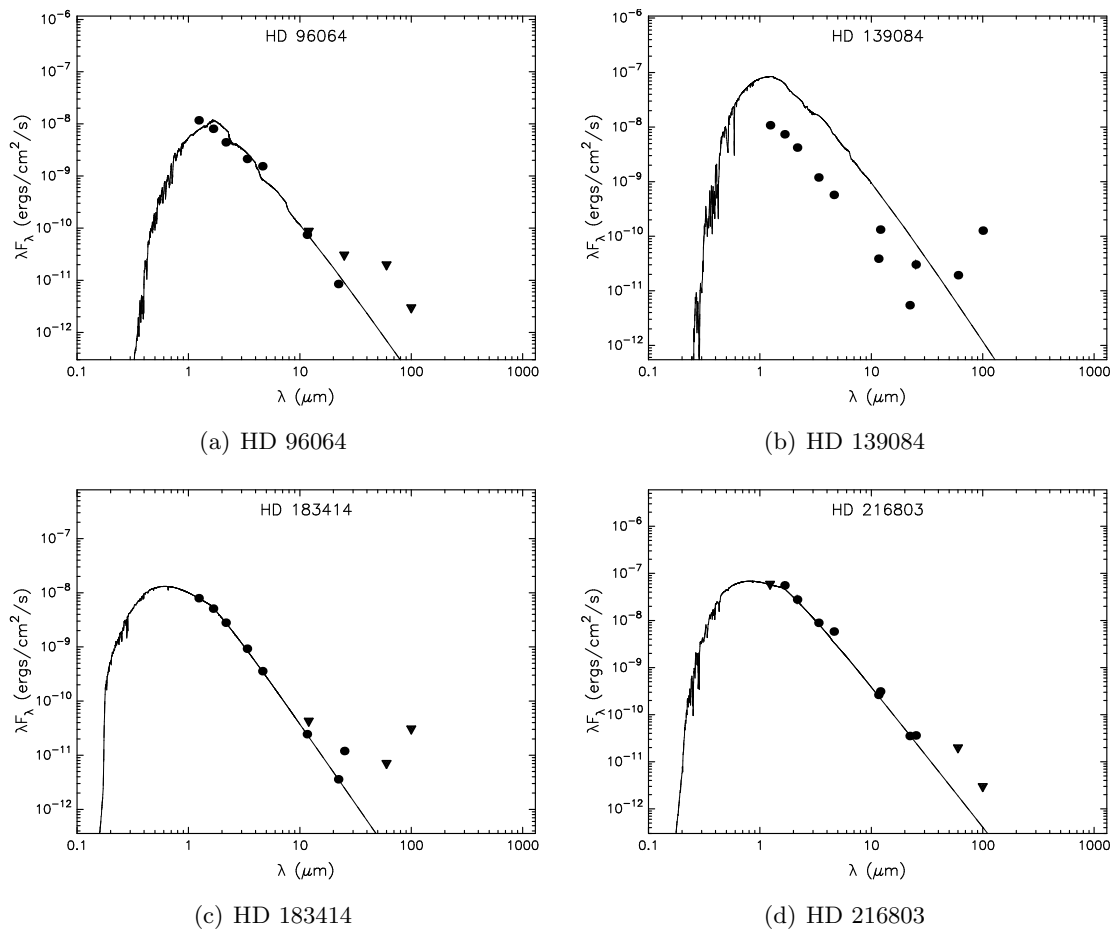


Figure C.1: SEDs of Group A targets including the best fitting stellar atmosphere model based on Kurucz models

Group B (targets, with > 5 initial FEROS data points):

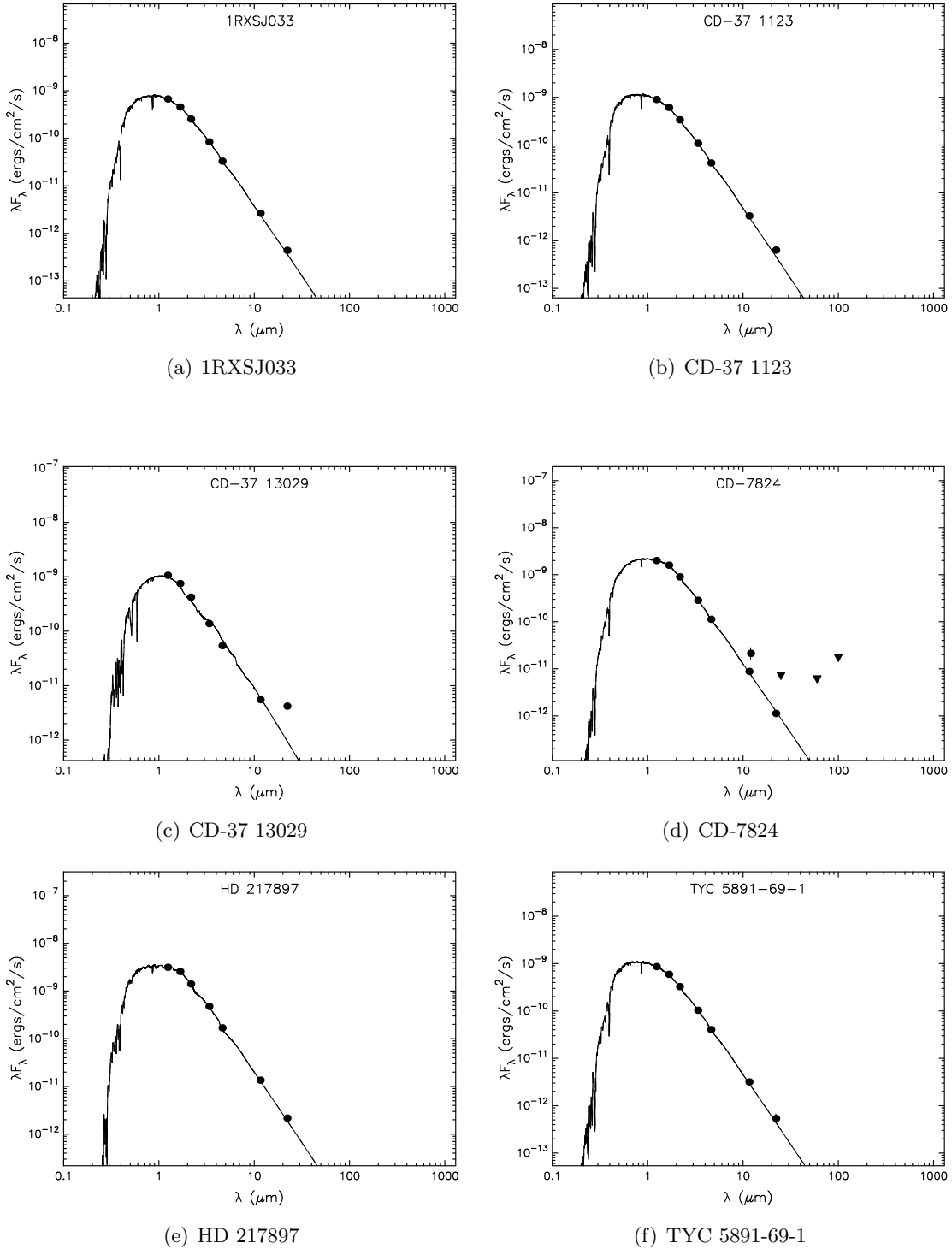


Figure C.2: SEDs of Group B targets including the best fitting stellar atmosphere model based on Kurucz models

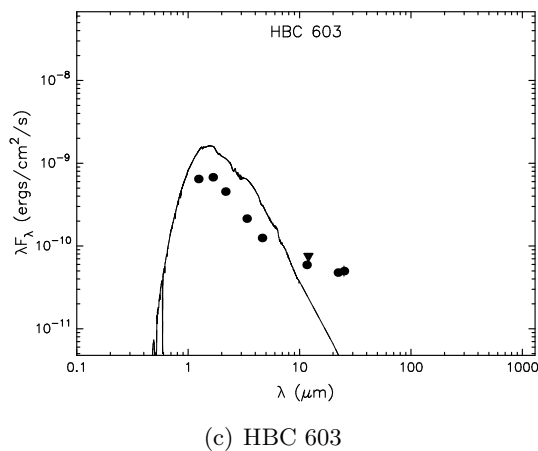
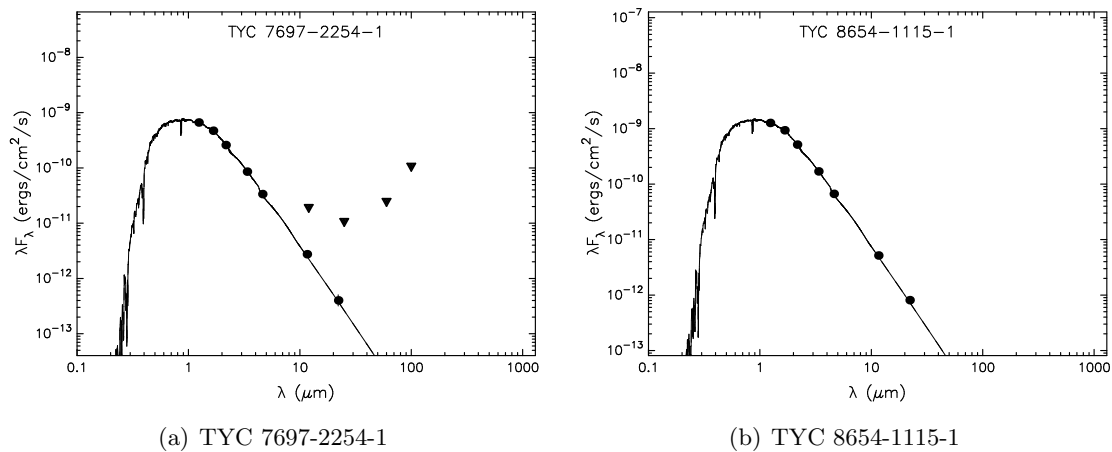


Figure C.3: SEDs of Group B targets including the best fitting stellar atmosphere model based on Kurucz models

Group C (targets, with < 5 initial FEROS data points):

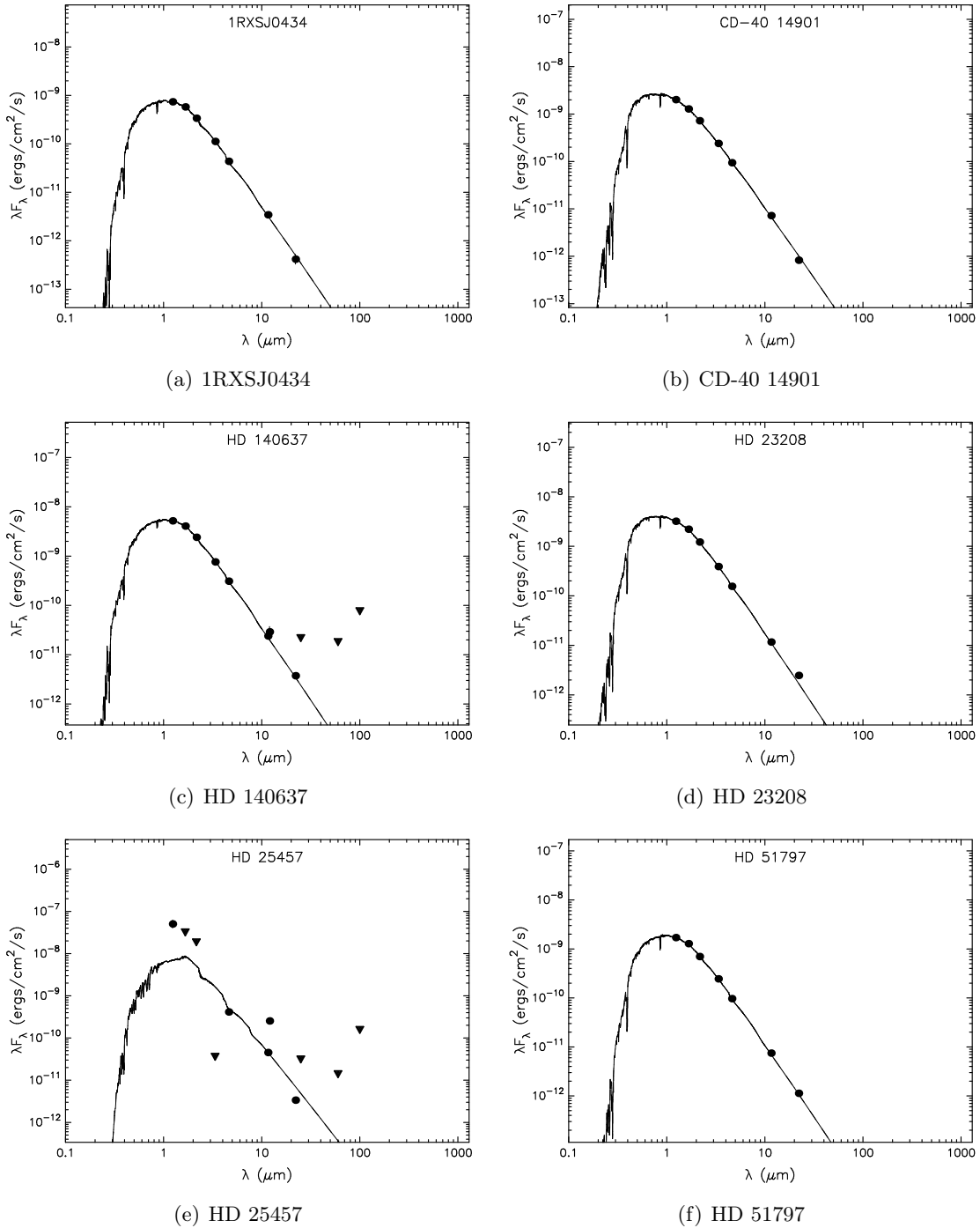


Figure C.4: SEDs of Group C targets including the best fitting stellar atmosphere model based on Kurucz models

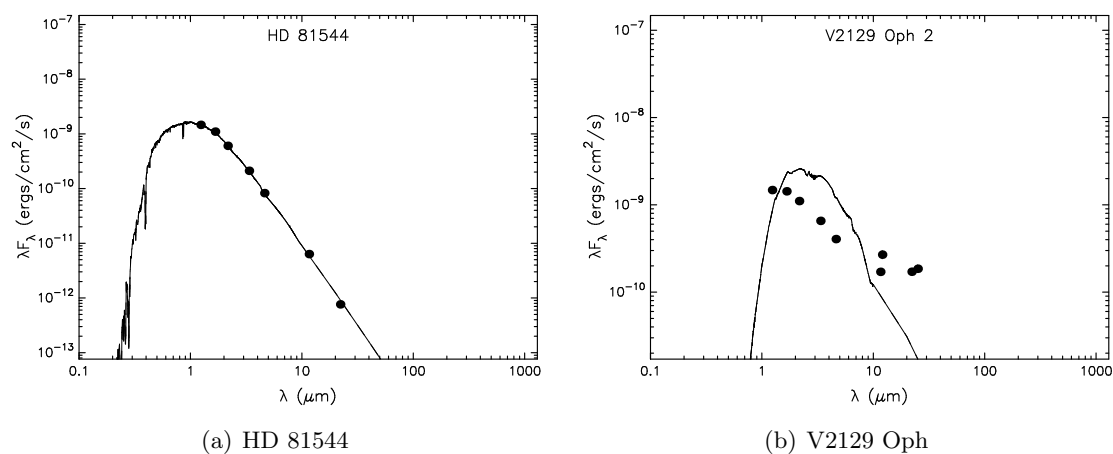


Figure C.5: SEDs of Group C targets including the best fitting stellar atmosphere model based on Kurucz models

Appendix D

RV periodograms

The analysis of the obtained RV results in terms of periodicities was executed with **GLS**. This appendix contains the generalised Lomb-Scargle periodograms of all targets including the corresponding window functions.

Furthermore, the plots of the sampling tests for seven targets, executed with a bootstrap analysis and the de-aliasing method of Dawson & Fabrycky (2010), respectively, are given.

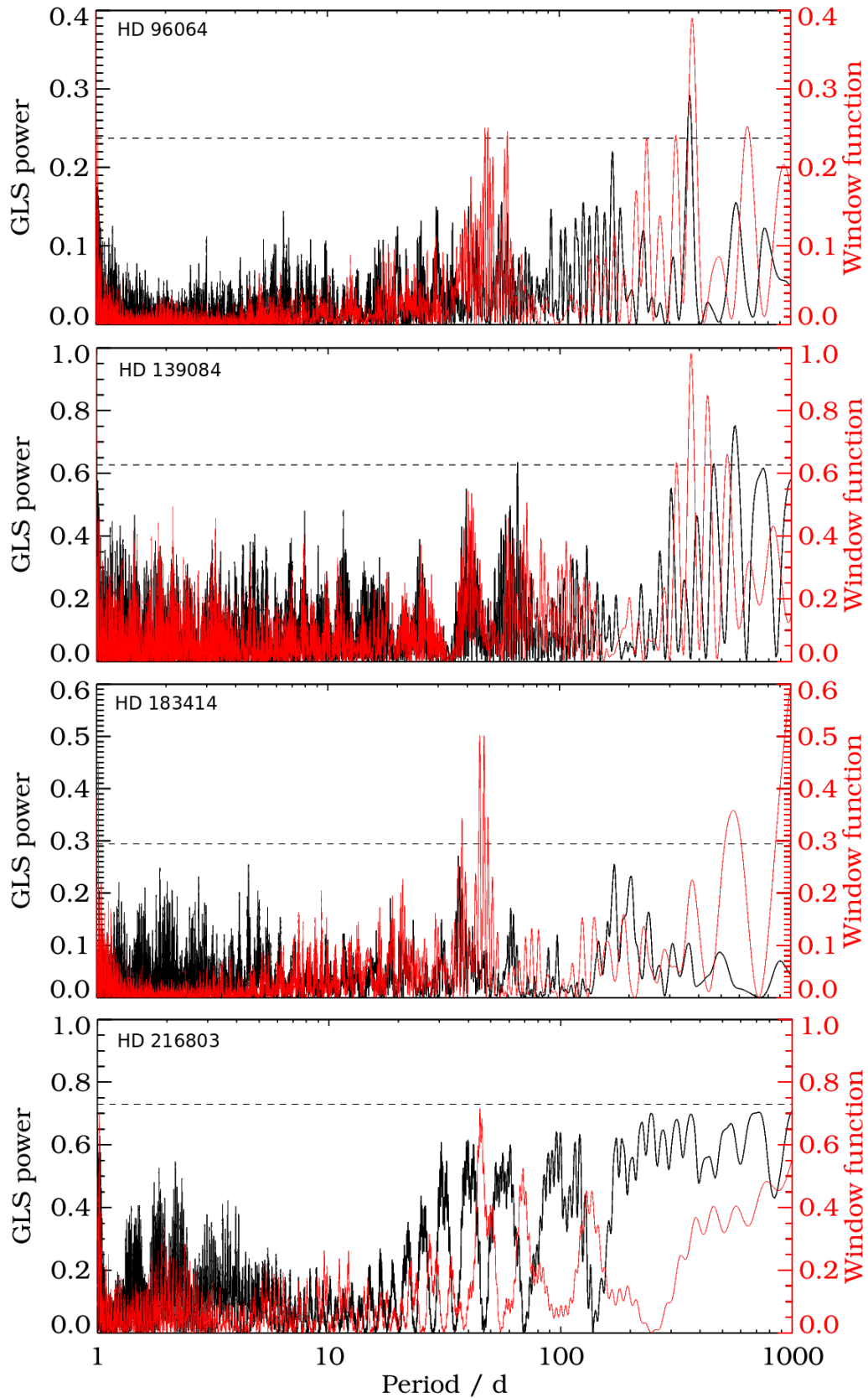


Figure D.1: RV GLS periodograms for the four targets of Group A. Black lines indicate the GLS power over period, while red lines mark the window function. The dashed line shows the 0.1% FAP level.

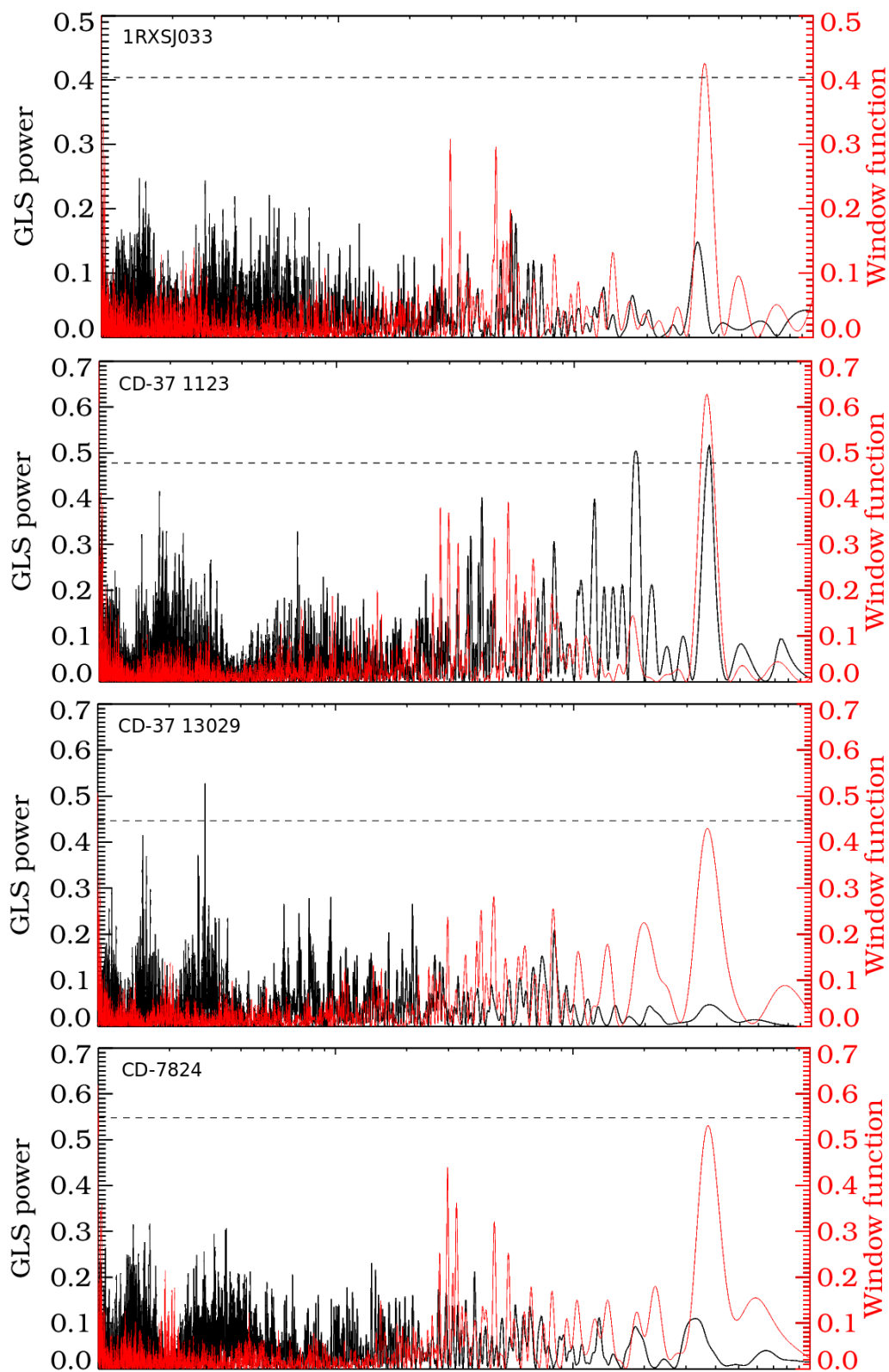


Figure D.2: RV GLS periodograms for four targets of Group B. Black lines indicate the GLS power over period, while red lines mark the window function. The dashed line shows the 0.1% FAP level.

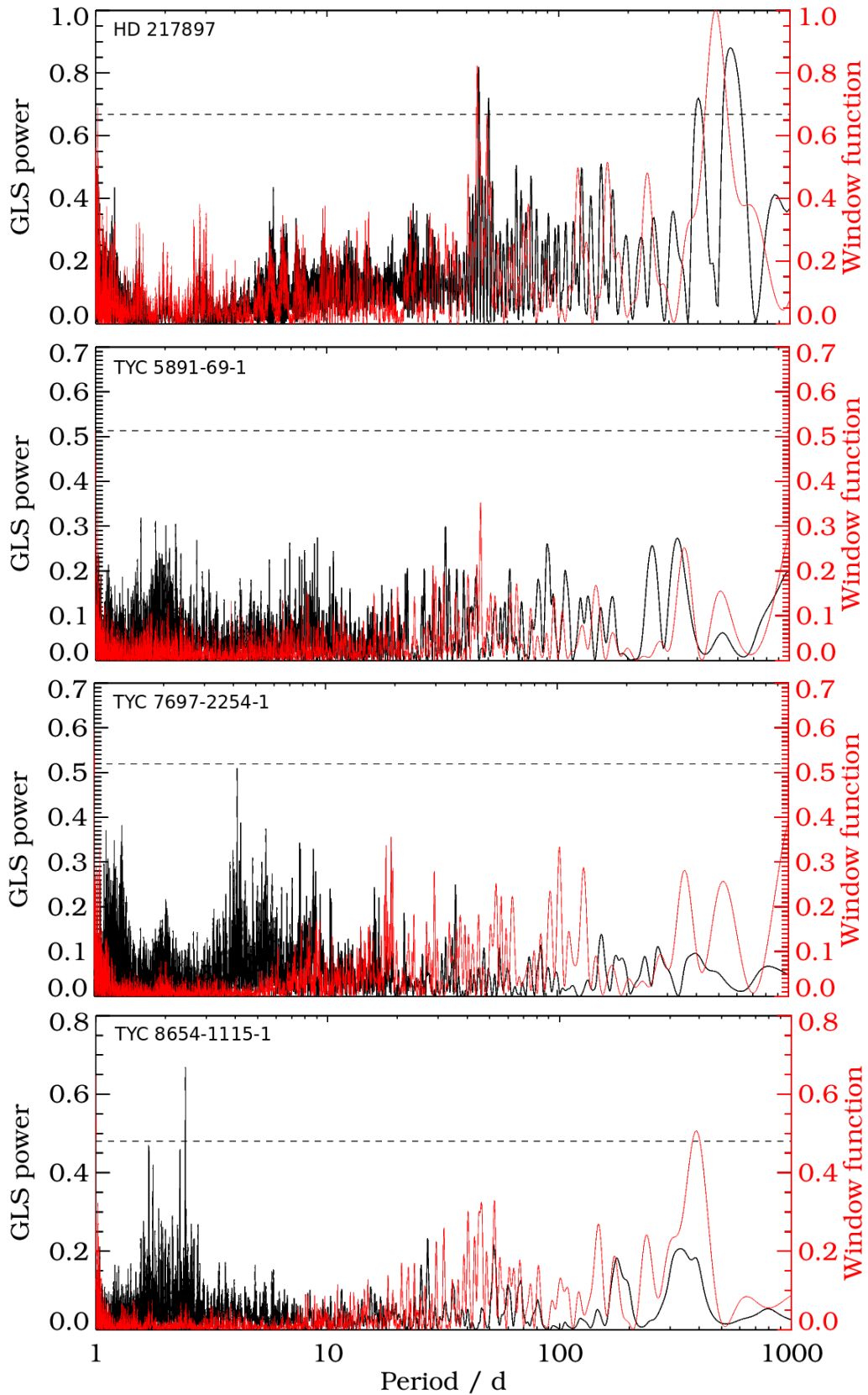


Figure D.3: RV GLS periodograms for four targets of Group B. Black lines indicate the GLS power over period, while red lines mark the window function. The dashed line shows the 0.1% FAP level.

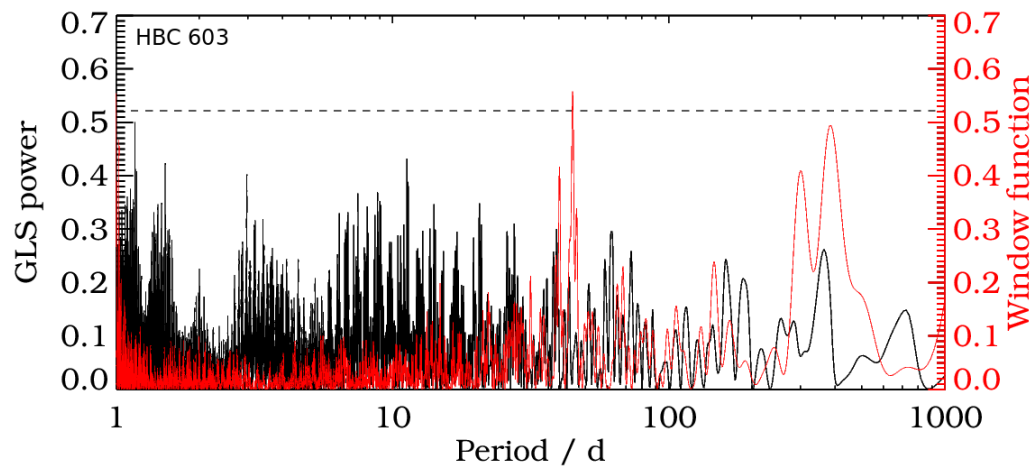


Figure D.4: RV GLS periodogram for one target of Group B. The black line indicates the GLS power over period, while the red line marks the window function. The dashed line shows the 0.1 % FAP level.

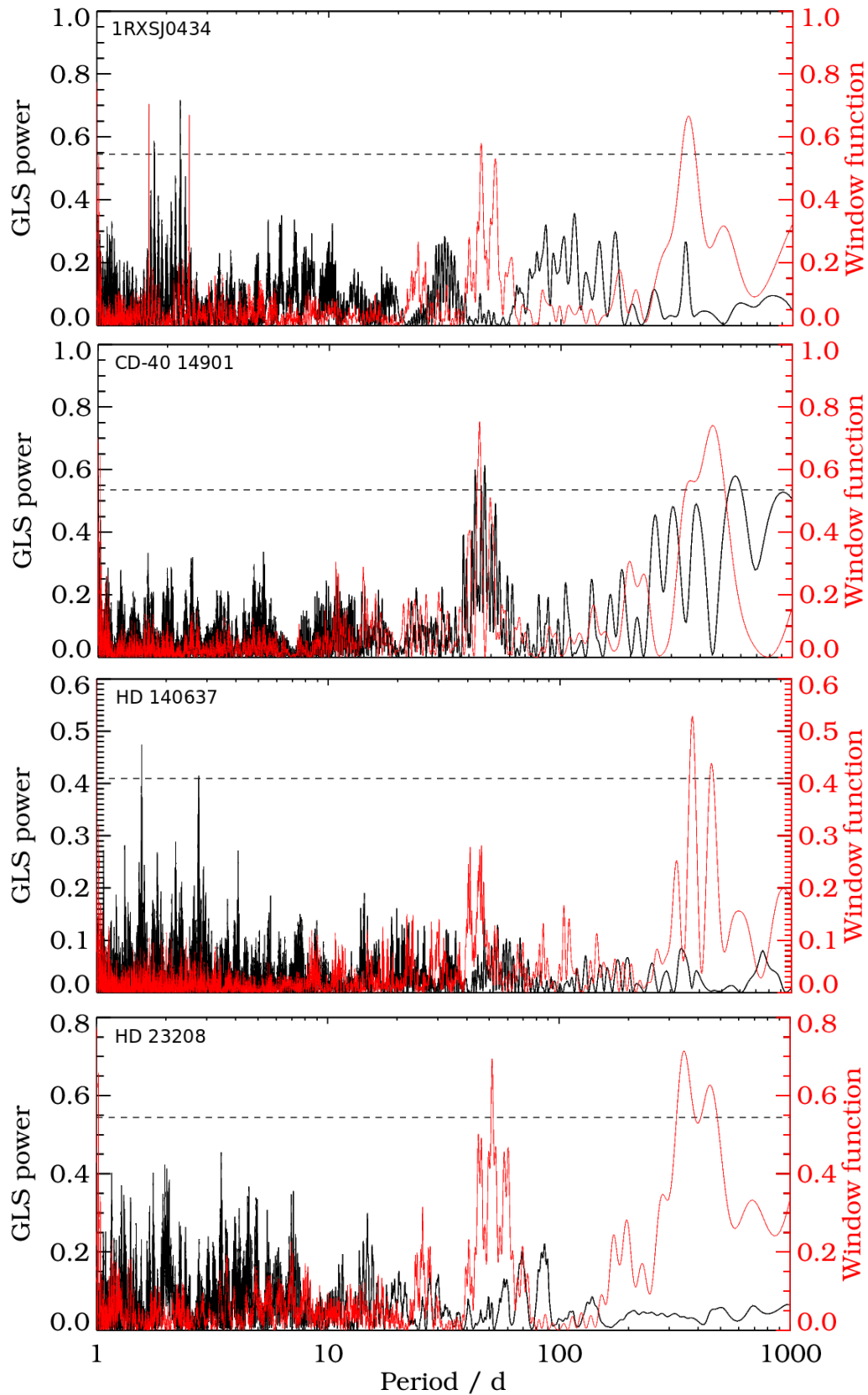


Figure D.5: RV GLS periodograms for four targets of Group C. Black lines indicate the GLS power over period, while red lines mark the window function. The dashed line shows the 0.1% FAP level.

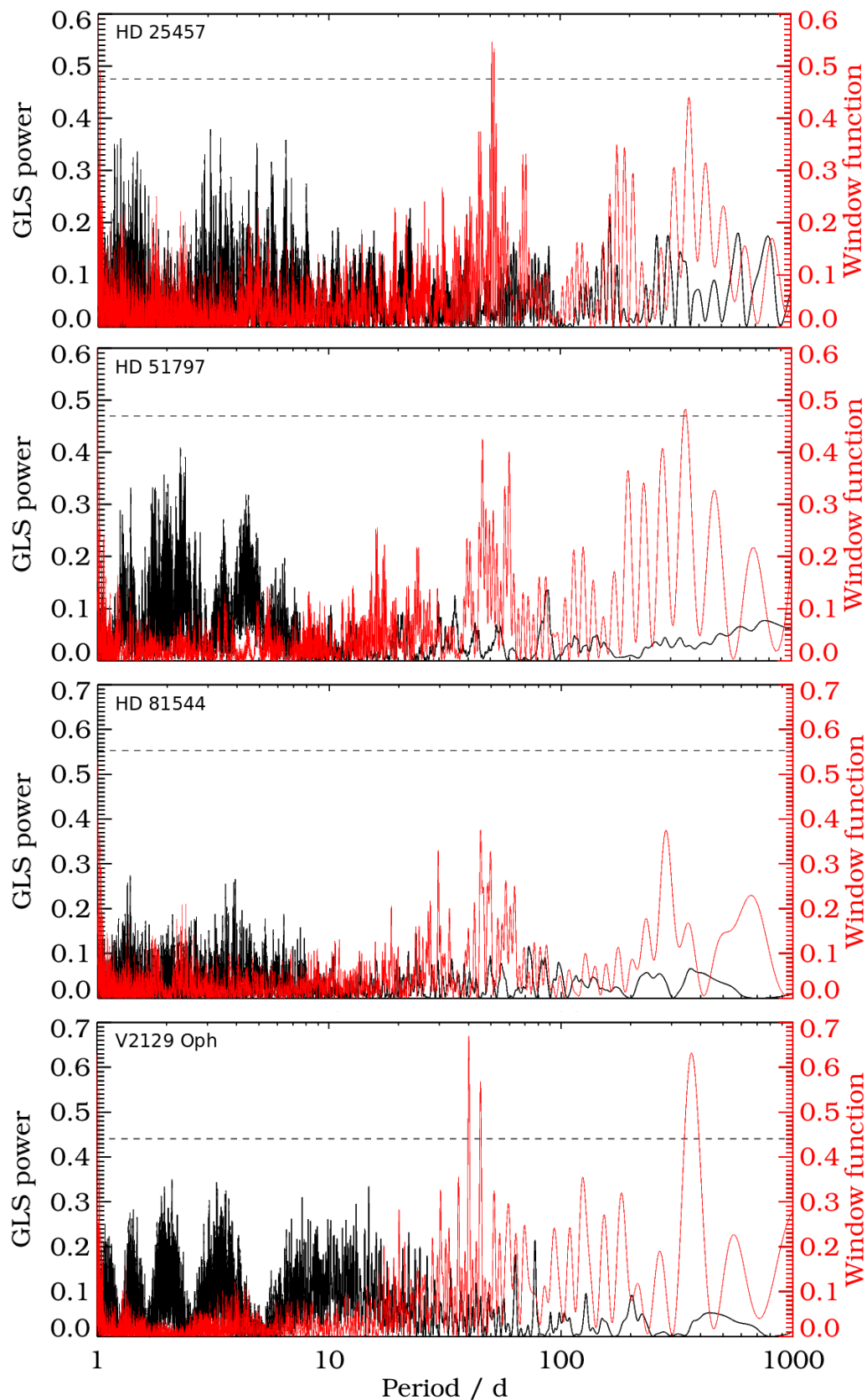


Figure D.6: RV GLS periodograms for four targets of Group C. Black lines indicate the GLS power over period, while red lines mark the window function. The dashed line shows the 0.1% FAP level.

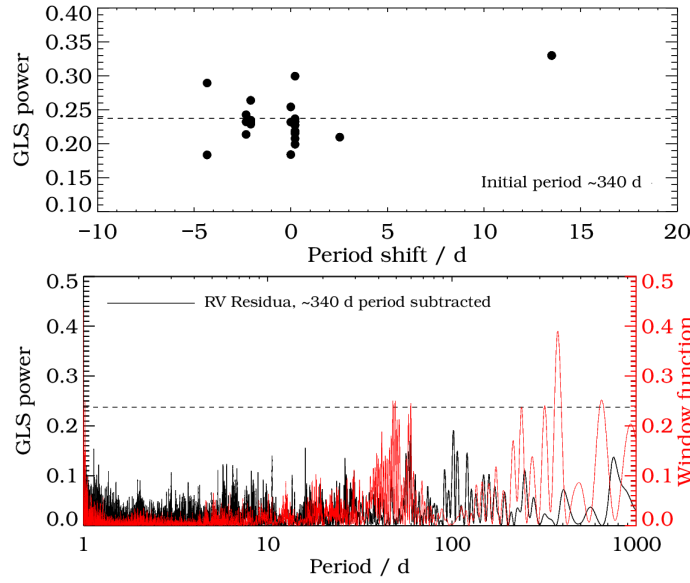


Figure D.7: Results for the measurement sampling test for HD 96064. Upper panel: Sampling test with GLS power over period shift for one initially significant period. Bottom panel: GLS periodogram for RV residua after subtracting the period of ~ 340 d.

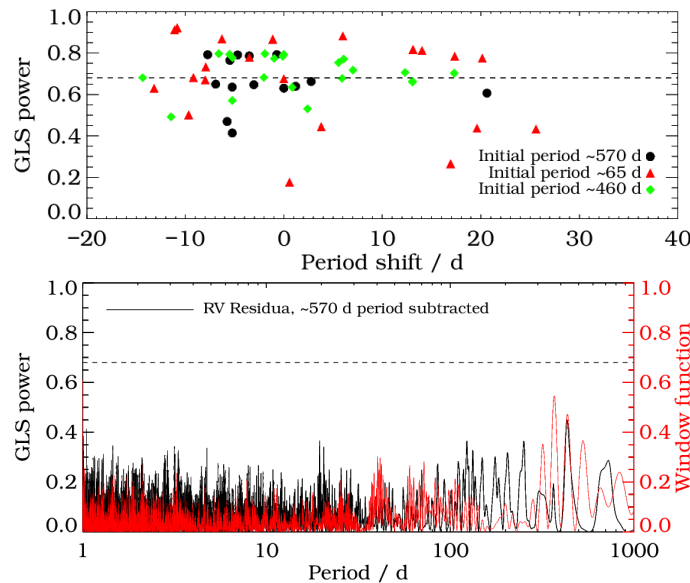


Figure D.8: Results for the measurement sampling test for HD 139084. Upper panel: Sampling test with GLS power over period shift for three initially significant periods. Bottom panel: GLS periodogram for RV residua after subtracting the strongest period of ~ 570 d.

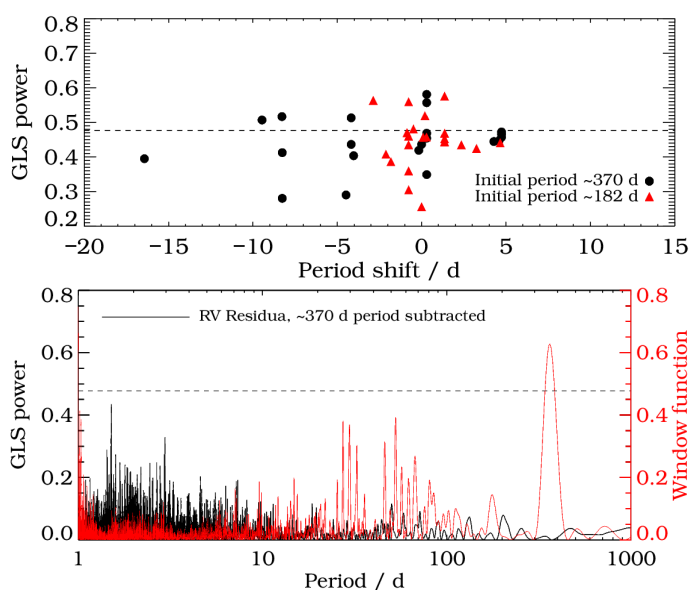


Figure D.9: Results for the measurement sampling test for CD-37 1123. Upper panel: Sampling test with GLS power over period shift for two initially significant period. Bottom panel: GLS periodogram for RV residua after subtracting the stronger period of ~ 370 d.

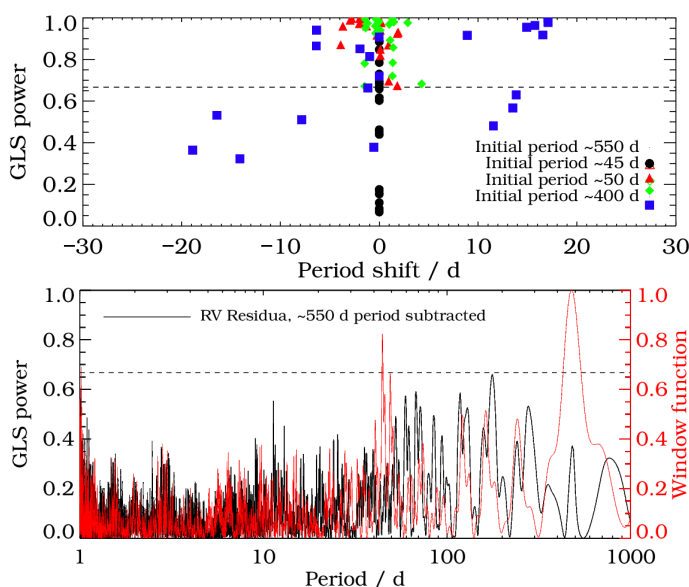


Figure D.10: Results for the measurement sampling test for HD 217897. Upper panel: Sampling test with GLS power over period shift for four initially significant periods. Bottom panel: GLS periodogram for RV residua after subtracting the strongest period of ~ 550 d.

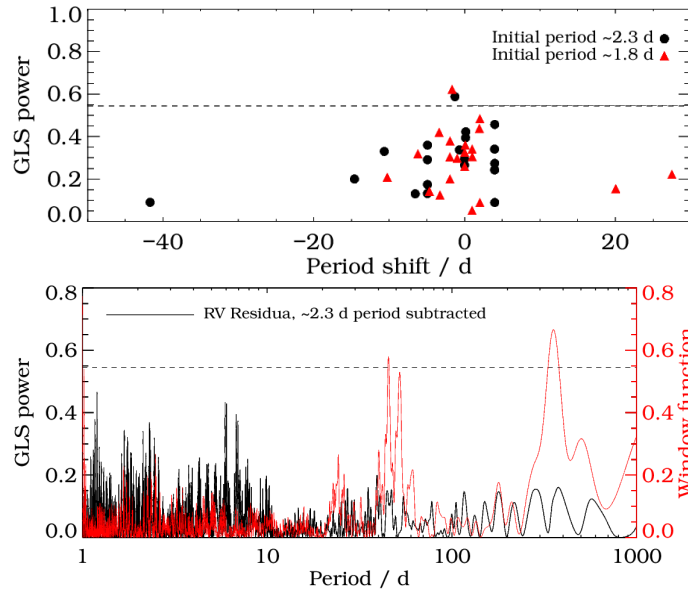


Figure D.11: Results for the measurement sampling test for 1RXSJ0434. Upper panel: Sampling test with GLS power over period shift for two initially significant period. Bottom panel: GLS periodogram for RV residua after subtracting the stronger period of ~ 2.3 d.

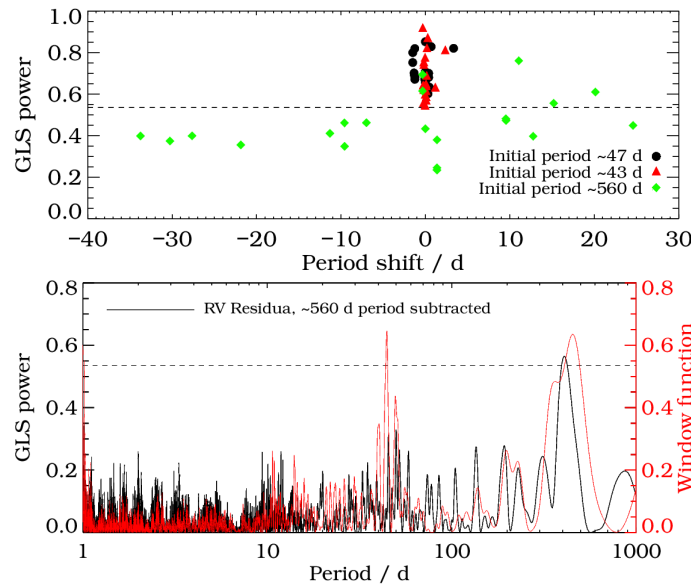


Figure D.12: Results for the measurement sampling test for CD-40 14901. Upper panel: Sampling test with GLS power over period shift for three initially significant periods. Bottom panel: GLS periodogram for RV residua after subtracting the period of ~ 560 d, which is apparently induced by the sampling function.

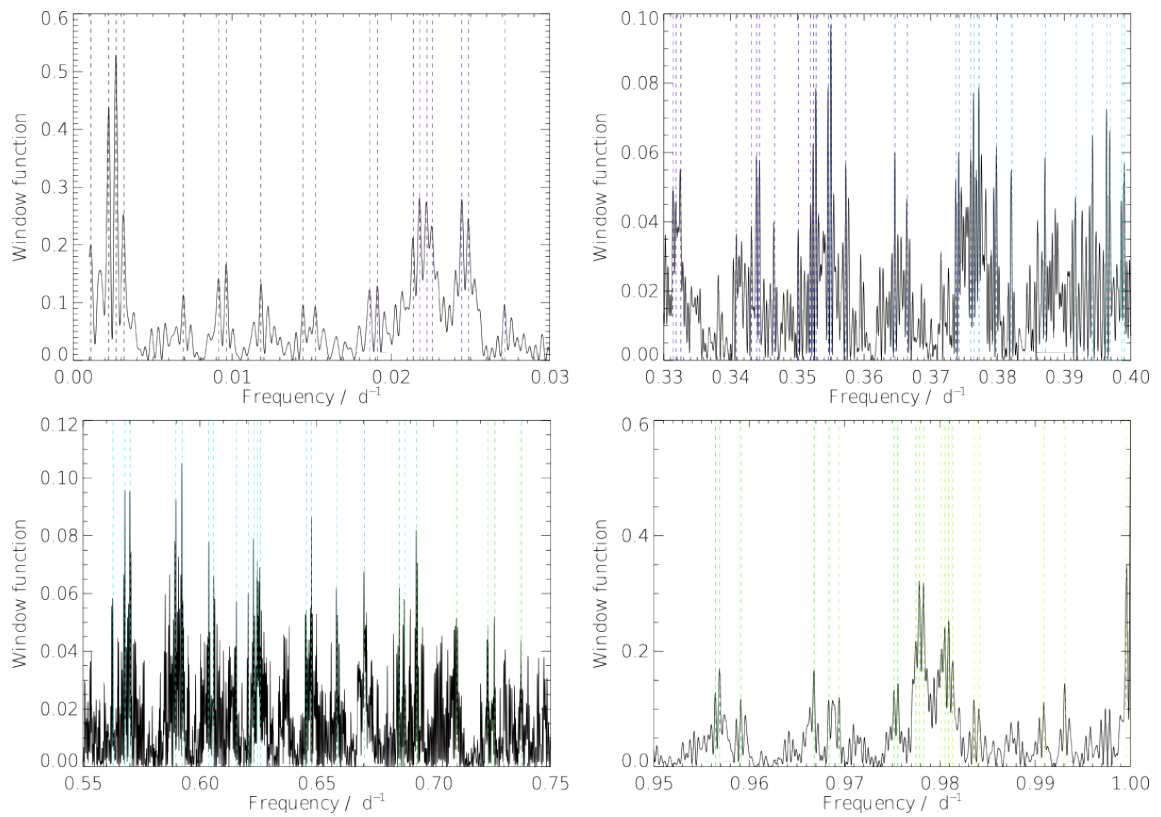


Figure D.13: Different regions in the window function of HD 140637. Colored lines mark selected strong frequency peaks $f_{s,i}$.

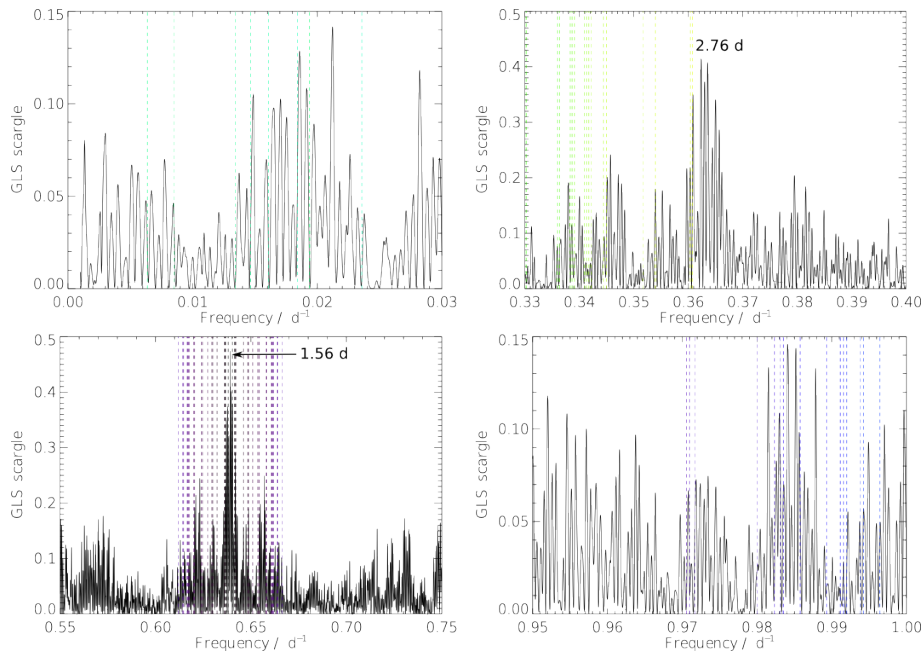
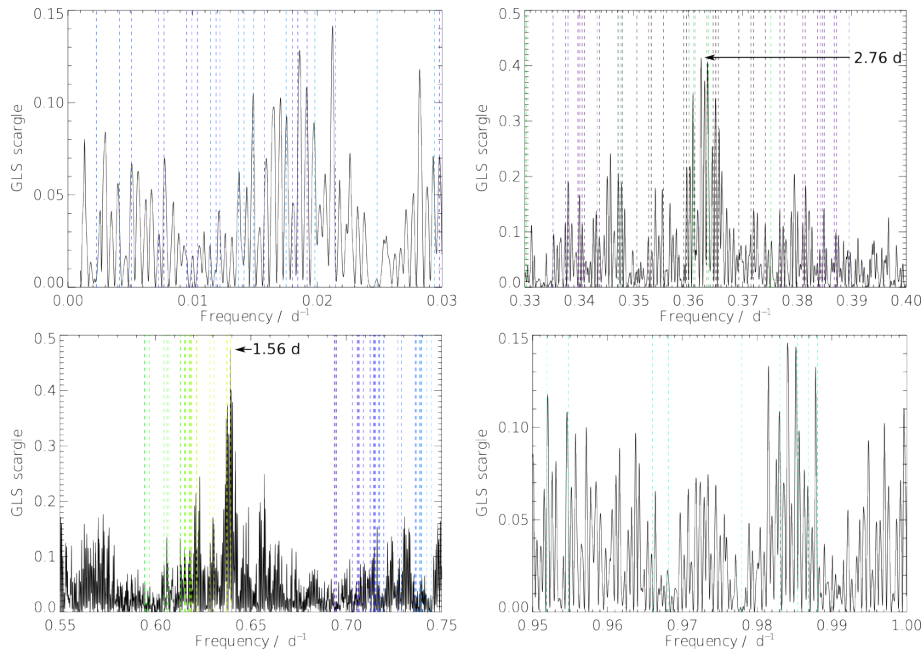
(a) $f_0 = 641.437 \cdot 10^{-3} \hat{=} 1.559$ d(b) $f_0 = 362.319 \cdot 10^{-3} \hat{=} 2.760$ d

Figure D.14: Different regions in the GLS scargle function of HD 140637 for two different f_0 . Colored lines mark calculated strong alias frequency peaks $f_{a,i}$ using selected strong sampling frequency peaks $f_{s,i}$ from the window function.

Bibliography

- ÁBRAHÁM, P., JUHÁSZ, A., DULLEMOND, C. P., KÓSPÁL, Á., VAN BOEKEL, R., BOUWMAN, J., HENNING, T., MOÓR, A. ET AL. (2009) Episodic formation of cometary material in the outburst of a young Sun-like star. *Nature*, **459**, 224–226.
- ABT, H. A. & LEVY, S. G. (1976) Multiplicity among solar-type stars. *ApJS*, **30**, 273–306.
- ALLARD, F., LAWLOR, T., ALEXANDER, D. R. & HAUSCHILDT, P. H. (1995) M Stars Model Atmospheres: Spectra and Colors. In *American Astronomical Society Meeting Abstracts*, vol. 27 of *Bulletin of the American Astronomical Society*.
- ALONSO, R., BARBIERI, M., RABUS, M., DEEG, H. J., BELMONTE, J. A. & ALME-NARA, J. M. (2008) Limits to the planet candidate GJ 436c. *A&A*, **487**, L5–L8.
- ALONSO, R., BROWN, T. M., TORRES, G., LATHAM, D. W., SOZZETTI, A., MANDUSHEV, G., BELMONTE, J. A., CHARBONNEAU, D. ET AL. (2004) TrES-1: The Transiting Planet of a Bright K0 V Star. *ApJ*, **613**, L153–L156.
- ALSUBAI, K. A., PARLEY, N. R., BRAMICH, D. M., WEST, R. G., SORENSEN, P. M., COLLIER CAMERON, A., LATHAM, D. W., HORNE, K. ET AL. (2011) Qatar-1b: a hot Jupiter orbiting a metal-rich K dwarf star. *MNRAS*, **417**, 709–716.
- ANDERSON, D. R., COLLIER CAMERON, A., GILLON, M., HELLIER, C., JEHIN, E., LENDL, M., MAXTED, P. F. L., QUELOZ, D. ET AL. (2012) WASP-44b, WASP-45b and WASP-46b: three short-period, transiting extrasolar planets. *MNRAS*, **422**, 1988–1998.
- ARMITAGE, P. J. (1999) Disc Dispersal Around Young Stars. In *Astrophysical Discs - an EC Summer School*, edited by J. A. Sellwood & J. Goodman, vol. 160 of *Astronomical Society of the Pacific Conference Series*.
- ASPIN, C., REIPURTH, B., HERCZEG, G. J. & CAPAK, P. (2010) The 2008 Extreme Outburst of the Young Eruptive Variable Star EX Lupi. *ApJ*, **719**, L50–L55.
- BAKOS, G., CSUBRY, Z., PENEV, K., AFONSO, C., BAYLISS, D., BEKY, B., CONROY, P., CSAK, B. ET AL. (2011) Hat-south: A Global Network Of Wide Angle Telescopes Searching For Transiting Extrasolar Planets Around Bright Stars. In *American Astronomical Society Meeting Abstracts #217*, vol. 43 of *Bulletin of the American Astronomical Society*.
- BAKOS, G. Á., CSUBRY, Z., PENEV, K., BAYLISS, D., JORDÁN, A., AFONSO, C., HARTMAN, J. D., HENNING, T. ET AL. (2013) HATSouth: A Global Network of Fully Automated Identical Wide-Field Telescopes. *PASP*, **125**, 154–182.

- BAKOS, G. Á., HARTMAN, J. D., TORRES, G., BÉKY, B., LATHAM, D. W., BUCHHAVE, L. A., CSUBRY, Z., KOVÁCS, G. ET AL. (2012) HAT-P-34b-HAT-P-37b: Four Transiting Planets More Massive than Jupiter Orbiting Moderately Bright Stars. *AJ*, **144**, 19.
- BAKOS, G. Á., TORRES, G., PÁL, A., HARTMAN, J., KOVÁCS, G., NOYES, R. W., LATHAM, D. W., SASSELOV, D. D. ET AL. (2010) HAT-P-11b: A Super-Neptune Planet Transiting a Bright K Star in the Kepler Field. *ApJ*, **710**, 1724–1745.
- BALONA, L. A. (1987) Radial velocities of calcium emission stars. I - Observations at Sutherland. *South African Astronomical Observatory Circular*, **11**, 1–12.
- BARAFFE, I. & CHABRIER, G. (2010) Effect of episodic accretion on the structure and the lithium depletion of low-mass stars and planet-hosting stars. *A&A*, **521**, A44.
- BARNES, J. W. (2009) Transit Lightcurves of Extrasolar Planets Orbiting Rapidly Rotating Stars. *ApJ*, **705**, 683–692.
- BARNES, S. A. (2007) Ages for Illustrative Field Stars Using Gyrochronology: Viability, Limitations, and Errors. *ApJ*, **669**, 1167–1189.
- BARROS, S. C. C., POLLACCO, D. L., GIBSON, N. P., HOWARTH, I. D., KEENAN, F. P., SIMPSON, E. K., SKILLEN, I. & STEELE, I. A. (2011) A lower mass for the exoplanet WASP-21b. *MNRAS*, **416**, 2593–2599.
- BASRI, G. & BATALHA, C. (1990) Hamilton echelle spectra of young stars. I - Optical veiling. *ApJ*, **363**, 654–669.
- BASRI, G., MOHANTY, S., ALLARD, F., HAUSCHILDT, P. H., DELFOSSE, X., MARTÍN, E. L., FORVEILLE, T. & GOLDMAN, B. (2000) An Effective Temperature Scale for Late-M and L Dwarfs, from Resonance Absorption Lines of Cs I and Rb I. *ApJ*, **538**, 363–385.
- BATALHA, N. M., ROWE, J. F., BRYSON, S. T., BARCLAY, T., BURKE, C. J., CALDWELL, D. A., CHRISTIANSEN, J. L., MULLALLY, F. ET AL. (2013) Planetary Candidates Observed by Kepler. III. Analysis of the First 16 Months of Data. *ApJS*, **204**, 24.
- BAYLISS, D., ZHOU, G., PENEV, K., BAKOS, G., HARTMAN, J., JORDÁN, A., MANCINI, L., MOHLER, M. ET AL. (2013) HATS-3b: An inflated hot Jupiter transiting an F-type star. *ArXiv e-prints*.
- BERDYUGINA, S. V. (2005) Starspots: A Key to the Stellar Dynamo. *Living Reviews in Solar Physics*, **2**, 8.
- BERNHARD, K., BERNHARD, C. & BERNHARD, M. (2009) Chromospherically active stars in the ASAS-3 database: Paper 1. 25 new variables. *Open European Journal on Variable Stars*, **98**, 1.
- BERTIN, E. & ARNOUTS, S. (1996) SExtractor: Software for source extraction. *A&AS*, **117**, 393–404.
- BERTOUT, C., BASRI, G. & BOUVIER, J. (1988) Accretion disks around T Tauri stars. *ApJ*, **330**, 350–373.

- BOISSE, I., BONFILS, X. & SANTOS, N. C. (2012) SOAP. A tool for the fast computation of photometry and radial velocity induced by stellar spots. *A&A*, **545**, A109.
- BOISSE, I., BOUCHY, F., HÉBRARD, G., BONFILS, X., SANTOS, N. & VAUCLAIR, S. (2011) Disentangling between stellar activity and planetary signals. *A&A*, **528**, A4.
- BONFILS, X., MAYOR, M., DELFOSSE, X., FORVEILLE, T., GILLON, M., PERRIER, C., UDRY, S., BOUCHY, F. ET AL. (2007) The HARPS search for southern extra-solar planets. X. A $m \sin i = 11 M_{\oplus}$ planet around the nearby spotted M dwarf <ASTROBJ>GJ 674</ASTROBJ>. *A&A*, **474**, 293–299.
- BOPP, B. W. & HEARNshaw, J. B. (1983) An H-alpha survey of southern hemisphere active chromosphere stars. *ApJ*, **267**, 653.
- BORUCKI, W. J., KOCH, D. & KEPLER SCIENCE TEAM (2010) Kepler Planet Detection Mission: Highlights of the First Results. In *AAS/Division for Planetary Sciences Meeting Abstracts #42*, vol. 42 of *Bulletin of the American Astronomical Society*.
- BORUCKI, W. J., KOCH, D. G., BASRI, G., BATALHA, N., BOSS, A., BROWN, T. M., CALDWELL, D., CHRISTENSEN-DALSGAARD, J. ET AL. (2011a) Characteristics of Kepler Planetary Candidates Based on the First Data Set. *ApJ*, **728**, 117.
- BORUCKI, W. J., KOCH, D. G., BASRI, G., BATALHA, N., BROWN, T. M., BRYSON, S. T., CALDWELL, D., CHRISTENSEN-DALSGAARD, J. ET AL. (2011b) Characteristics of Planetary Candidates Observed by Kepler. II. Analysis of the First Four Months of Data. *ApJ*, **736**, 19.
- BOUVIER, J., BERTOUT, C., BENZ, W. & MAYOR, M. (1986) Rotation in T Tauri stars. I - Observations and immediate analysis. *A&A*, **165**, 110–119.
- BRANDNER, W., ALCALA, J. M., KUNKEL, M., MONETI, A. & ZINNECKER, H. (1996) Multiplicity among T Tauri stars in OB and T associations. Implications for binary star formation. *A&A*, **307**, 121.
- BRAY, R. J. & LOUGHHEAD, R. E. (1974) *The solar chromosphere*.
- BRYAN, M. L., ALSUBAI, K. A., LATHAM, D. W., PARLEY, N. R., COLLIER CAMERON, A., QUINN, S. N., CARTER, J. A., FULTON, B. J. ET AL. (2012) Qatar-2: A K Dwarf Orbited by a Transiting Hot Jupiter and a More Massive Companion in an Outer Orbit. *ApJ*, **750**, 84.
- CALVET, N., BASRI, G. & KUHI, L. V. (1984) The chromospheric hypothesis for the T Tauri phenomenon. *ApJ*, **277**, 725–737.
- CARPENTER, J. M., BOUWMAN, J., MAMAJEK, E. E., MEYER, M. R., HILLENBRAND, L. A., BACKMAN, D. E., HENNING, T., HINES, D. C. ET AL. (2009) Formation and Evolution of Planetary Systems: Properties of Debris Dust Around Solar-Type Stars. *ApJS*, **181**, 197–226.
- CARROLL, B. W. & OSTLIE, D. A. (1996) *An Introduction to Modern Astrophysics*.
- CASSAN, A., KUBAS, D., BEAULIEU, J.-P., DOMINIK, M., HORNE, K., GREENHILL, J., WAMBSGANSS, J., MENZIES, J. ET AL. (2012) One or more bound planets per Milky Way star from microlensing observations. *Nature*, **481**, 167–169.

- CASTELLI, F. & KURUCZ, R. L. (2004) New Grids of ATLAS9 Model Atmospheres. *ArXiv Astrophysics e-prints*.
- CATALANO, S., BIAZZO, K., FRASCA, A. & MARILLI, E. (2002) Measuring starspot temperature from line depth ratios. I. The method. *A&A*, **394**, 1009–1021.
- CHABRIER, G., BARAFFE, I., ALLARD, F. & HAUSCHILDT, P. (2000) Deuterium Burning in Substellar Objects. *ApJ*, **542**, L119–L122.
- CHAUVIN, G., LAGRANGE, A.-M., BONAVIDA, M., ZUCKERMAN, B., DUMAS, C., BESSELL, M. S., BEUZIT, J.-L., BONNEFOY, M. ET AL. (2010) Deep imaging survey of young, nearby austral stars . VLT/NACO near-infrared Lyot-coronographic observations. *A&A*, **509**, A52.
- CHRISTIAN, D. J., POLLACCO, D. L., SKILLEN, I., IRWIN, J., CLARKSON, W. I., COLLIER CAMERON, A., EVANS, N., FITZSIMMONS, A. ET AL. (2006) The WASP project in the era of robotic telescope networks. *Astronomische Nachrichten*, **327**, 800.
- CLARET, A. (2004) A new non-linear limb-darkening law for LTE stellar atmosphere models III. Sloan filters: Calculations for $-5.0 \leq \log [M/H] \leq +1$, $2000 \text{ K} \leq T_{eff} \leq 5000 \text{ K}$ at several surface gravities. *A&A*, **428**, 1001–1005.
- CLARET, A., DIAZ-CORDOVES, J. & GIMENEZ, A. (1995) Linear and non-linear limb-darkening coefficients for the photometric bands R I J H K. *A&AS*, **114**, 247.
- COLLIER CAMERON, A. (1992) Modelling Stellar Photospheric Spots Using Spectroscopy (Invited). In *Surface Inhomogeneities on Late-Type Stars*, edited by P. B. Byrne & D. J. Mullan, vol. 397 of *Lecture Notes in Physics*, Berlin Springer Verlag.
- COLLIER CAMERON, A., GUENTHER, E., SMALLEY, B., McDONALD, I., HEBB, L., ANDERSEN, J., AUGUSTEIJN, T., BARROS, S. C. C. ET AL. (2010) Line-profile tomography of exoplanet transits - II. A gas-giant planet transiting a rapidly rotating A5 star. *MNRAS*, **407**, 507–514.
- CUMMING, A. (2004) Detectability of extrasolar planets in radial velocity surveys. *MNRAS*, **354**, 1165–1176.
- CUTISPOTO, G. (1993) Longterm Monitoring of Active Stars - Part Three - UBV Ri/c Photometry of 14 Southern Hemisphere Variables. *A&AS*, **102**, 655.
- CUTRI, R. M., SKRUTSKIE, M. F., VAN DYK, S., BEICHMAN, C. A., CARPENTER, J. M., CHESTER, T., CAMBRESY, L., EVANS, T. ET AL. (2003) 2MASS All-Sky Catalog of Point Sources (Cutri+ 2003). *VizieR Online Data Catalog*, **2246**, 0.
- CUTRI, R. M. E. (2012) WISE All-Sky Data Release (Cutri+ 2012). *VizieR Online Data Catalog*, **2311**, 0.
- DA SILVA, L., TORRES, C. A. O., DE LA REZA, R., QUAST, G. R., MELO, C. H. F. & STERZIK, M. F. (2009) Search for associations containing young stars (SACY). III. Ages and Li abundances. *A&A*, **508**, 833–839.
- DAWSON, R. I. & FABRYCKY, D. C. (2010) Radial Velocity Planets De-aliased: A New, Short Period for Super-Earth 55 Cnc e. *ApJ*, **722**, 937–953.

- DE GEUS, E. J., DE ZEEUW, P. T. & LUB, J. (1989) Physical parameters of stars in the Scorpio-Centaurus OB association. *A&A*, **216**, 44–61.
- DEEN, C. (2013) Modification of the MOOG spectral synthesis codes to account for Zeeman broadening of spectral lines. *ArXiv e-prints*.
- DÉSERT, J.-M., CHARBONNEAU, D., DEMORY, B.-O., BALLARD, S., CARTER, J. A., FORTNEY, J. J., COCHRAN, W. D., ENDL, M. ET AL. (2011) The Hot-Jupiter Kepler-17b: Discovery, Obliquity from Stroboscopic Starspots, and Atmospheric Characterization. *ApJS*, **197**, 14.
- DOPITA, M., HART, J., MCGREGOR, P., OATES, P., BLOXHAM, G. & JONES, D. (2007) The Wide Field Spectrograph (WiFeS). *Ap&SS*, **310**, 255–268.
- DUQUENNOY, A., MAYOR, M. & HALBWACHS, J.-L. (1991) Multiplicity among solar type stars in the solar neighbourhood. I - CORAVEL radial velocity observations of 291 stars. *A&AS*, **88**, 281–324.
- EVANS, II, N. J., DUNHAM, M. M., JØRGENSEN, J. K., ENOCH, M. L., MERÍN, B., VAN DISHOECK, E. F., ALCALÁ, J. M., MYERS, P. C. ET AL. (2009) The Spitzer c2d Legacy Results: Star-Formation Rates and Efficiencies; Evolution and Lifetimes. *ApJS*, **181**, 321–350.
- FERNÁNDEZ, D., FIGUERAS, F. & TORRA, J. (2008) On the kinematic evolution of young local associations and the Scorpius-Centaurus complex. *A&A*, **480**, 735–751.
- FRESSIN, F., TORRES, G., CHARBONNEAU, D., BRYSON, S. T., CHRISTIANSEN, J., DRESSING, C. D., JENKINS, J. M., WALKOWICZ, L. M. ET AL. (2013) The False Positive Rate of Kepler and the Occurrence of Planets. *ApJ*, **766**, 81.
- FUHRMANN, K. & CHINI, R. (2012) Multiplicity among F-type Stars. *ApJS*, **203**, 30.
- GALLET, F. & BOUVIER, J. (2013) Improved angular momentum evolution model for solar-like stars. *ArXiv e-prints*.
- GHEZ, A. M., MCCARTHY, D. W., PATIENCE, J. L. & BECK, T. L. (1997) The Multiplicity of Pre-Main-Sequence Stars in Southern Star-forming Regions. *ApJ*, **481**, 378.
- GHEZ, A. M., NEUGEBAUER, G. & MATTHEWS, K. (1993) The multiplicity of T Tauri stars in the star forming regions Taurus-Auriga and Ophiuchus-Scorpius: A 2.2 micron speckle imaging survey. *AJ*, **106**, 2005–2023.
- GLEBOCKI, R. & GNACINSKI, P. (2005) Catalog of Stellar Rotational Velocities (Glebocki+ 2005). *VizieR Online Data Catalog*, **3244**, 0.
- GOMES DA SILVA, J., SANTOS, N. C., BONFILS, X., DELFOSSE, X., FORVEILLE, T., UDRY, S., DUMUSQUE, X. & LOVIS, C. (2012) Long-term magnetic activity of a sample of M-dwarf stars from the HARPS program . II. Activity and radial velocity. *A&A*, **541**, A9.
- GRAS-VELÁZQUEZ, À. & RAY, T. P. (2005) Weak-line T Tauri stars: circumstellar disks and companions. I. Spectral energy distributions and infrared excesses. *A&A*, **443**, 541–556.
- GRAY, D. F. (1988) *Lectures on spectral-line analysis: F, G and K stars*.

- GRAY, D. F. (1994) Spectral line-depth ratios as temperature indicators for cool stars. *PASP*, **106**, 1248–1257.
- GRAY, D. F. (2008) *The Observation and Analysis of Stellar Photospheres*.
- GRAY, R. O. (1999) SPECTRUM: A stellar spectral synthesis program. Astrophysics Source Code Library.
- GRAY, R. O., CORBALLY, C. J., GARRISON, R. F., MCFADDEN, M. T., BUBAR, E. J., MCGAHEE, C. E., O'DONOGHUE, A. A. & KNOX, E. R. (2006) Contributions to the Nearby Stars (NStars) Project: Spectroscopy of Stars Earlier than M0 within 40 pc-The Southern Sample. *AJ*, **132**, 161–170.
- GREINER, J., BORNEMANN, W., CLEMENS, C., DEUTER, M., HASINGER, G., HONSBURG, M., HUBER, H., HUBER, S. ET AL. (2008) GROND - a 7-Channel Imager. *PASP*, **120**, 405–424.
- GUSTAFSSON, B., EDVARDSSON, B., ERIKSSON, K., JØRGENSEN, U. G., NORDLUND, Å. & PLEZ, B. (2008) A grid of MARCS model atmospheres for late-type stars. I. Methods and general properties. *A&A*, **486**, 951–970.
- HALL, J. C. (2008) Stellar Chromospheric Activity. *Living Reviews in Solar Physics*, **5**, 2.
- HANSEN, B. M. S. & BARMAN, T. (2007) Two Classes of Hot Jupiters. *ApJ*, **671**, 861–871.
- HARTIGAN, P., HARTMANN, L., KENYON, S., HEWETT, R. & STAUFFER, J. (1989) How to unveil a T Tauri star. *ApJS*, **70**, 899–914.
- HARTMAN, J. D., BAKOS, G. Á., BÉKY, B., TORRES, G., LATHAM, D. W., CSUBRY, Z., PENEV, K., SHPORER, A. ET AL. (2012) HAT-P-39b-HAT-P-41b: Three Highly Inflated Transiting Hot Jupiters. *AJ*, **144**, 139.
- HARTMAN, J. D., BAKOS, G. Á., TORRES, G., LATHAM, D. W., KOVÁCS, G., BÉKY, B., QUINN, S. N., MAZEH, T. ET AL. (2011) HAT-P-32b and HAT-P-33b: Two Highly Inflated Hot Jupiters Transiting High-jitter Stars. *ApJ*, **742**, 59.
- HELLIER, C., ANDERSON, D. R., COLLIER CAMERON, A., DOYLE, A. P., FUMEL, A., GILLON, M., JEHIN, E., LENDL, M. ET AL. (2012) Seven transiting hot Jupiters from WASP-South, Euler and TRAPPIST: WASP-47b, WASP-55b, WASP-61b, WASP-62b, WASP-63b, WASP-66b and WASP-67b. *MNRAS*, **426**, 739–750.
- HENRY, T. J., SODERBLOM, D. R., DONAHUE, R. A. & BALIUNAS, S. L. (1996) A Survey of Ca II H and K Chromospheric Emission in Southern Solar-Type Stars. *AJ*, **111**, 439.
- HERBIG, G. H. (1977) Eruptive phenomena in early stellar evolution. *ApJ*, **217**, 693–715.
- HERBIG, G. H. (2007) EX Lupi: History and Spectroscopy. *AJ*, **133**, 2679–2683.
- HERBIG, G. H. (2008) History and Spectroscopy of EXor Candidates. *AJ*, **135**, 637–648.
- HERBIG, G. H. & BELL, K. R. (1988) *Third Catalog of Emission-Line Stars of the Orion Population : 3 : 1988*.

- HERNÁNDEZ, J., HARTMANN, L., CALVET, N., JEFFRIES, R. D., GUTERMUTH, R., MUZEROLLE, J. & STAUFFER, J. (2008) A Spitzer View of Protoplanetary Disks in the γ Velorum Cluster. *ApJ*, **686**, 1195–1208.
- HOOGERWERF, R. (2000) OB association members in ACT+TRC Catalogs (Hoogerwerf, 2000). *VizieR Online Data Catalog*, **831**, 30043.
- HOWARD, A. W., MARCY, G. W., BRYSON, S. T., JENKINS, J. M., ROWE, J. F., BATALHA, N. M., BORUCKI, W. J., KOCH, D. G. ET AL. (2012) Planet Occurrence within 0.25 AU of Solar-type Stars from Kepler. *ApJS*, **201**, 15.
- HUGHES, J., HARTIGAN, P., KRAUTTER, J. & KELEMEN, J. (1994) The stellar population of the Lupus clouds. *AJ*, **108**, 1071–1090.
- HUSSER, T.-O., WENDE- VON BERG, S., DREIZLER, S., HOMEIER, D., REINERS, A., BARMAN, T. & HAUSCHILDT, P. H. (2013) A new extensive library of PHOENIX stellar atmospheres and synthetic spectra. *ArXiv e-prints*.
- JENKINS, J. S., RAMSEY, L. W., JONES, H. R. A., PAVLENKO, Y., GALLARDO, J., BARNES, J. R. & PINFIELD, D. J. (2009) Rotational Velocities for M Dwarfs. *ApJ*, **704**, 975–988.
- JOHNS-KRULL, C. M. & BASRI, G. (1997) The Spectral Variability of the T Tauri Star DF Tauri. *ApJ*, **474**, 433.
- KALAS, P., GRAHAM, J. R. & CLAMPIN, M. (2005) A planetary system as the origin of structure in Fomalhaut’s dust belt. *Nature*, **435**, 1067–1070.
- KANG, Y. W. & WILSON, R. E. (1989) Least-squares adjustment of SPOT parameters for three RS CVn binaries. *AJ*, **97**, 848–865.
- KAUFER, A. & PASQUINI, L. (1998) FEROS: the new fiber-linked echelle spectrograph for the ESO 1.52-m telescope. In *Society of Photo-Optical Instrumentation Engineers (SPIE) Conference Series*, edited by S. D’Odorico, vol. 3355 of *Society of Photo-Optical Instrumentation Engineers (SPIE) Conference Series*.
- KAUFER, A., WOLF, B., ANDERSEN, J. & PASQUINI, L. (1997) FEROS, the fiber-fed extended range optical spectrograph for the ESO 1.52-m telescope. *The Messenger*, **89**, 1–4.
- KEENAN, P. C. & MCNEIL, R. C. (1989) The Perkins catalog of revised MK types for the cooler stars. *ApJS*, **71**, 245–266.
- KENYON, S. J. & HARTMANN, L. (1987) Spectral energy distributions of T Tauri stars - Disk flaring and limits on accretion. *ApJ*, **323**, 714–733.
- KIPPING, D. M. (2012) An analytic model for rotational modulations in the photometry of spotted stars. *MNRAS*, **427**, 2487–2511.
- KIPPING, D. M., FOSSEY, S. J. & CAMPANELLA, G. (2009) On the detectability of habitable exomoons with Kepler-class photometry. *MNRAS*, **400**, 398–405.
- KÖHLER, R., NEUHÄUSER, R., KRÄMER, S., LEINERT, C., OTT, T. & ECKART, A. (2008) Multiplicity of young stars in and around R Coronae Australis. *A&A*, **488**, 997–1006.

- KÓSPÁL, Á., ÁBRAHÁM, P., GOTO, M., REGÁLY, Z., DULLEMOND, C. P., HENNING, T., JUHÁSZ, A., SICILIA-AGUILAR, A. ET AL. (2011) Near-infrared Spectroscopy of EX Lupi in Outburst. *ApJ*, **736**, 72.
- KÓSPÁL, Á., MOHLER-FISCHER, M., SICILIA-AGUILAR, A., ÁBRAHÁM, P., CURÉ, M., HENNING, T., KISS, C., LAUNHARDT, R. ET AL. (2013) Radial velocity variations in the young eruptive star EX Lup. *submitted to A&A*.
- KRAFT, R. P. (1967) Studies of Stellar Rotation. V. The Dependence of Rotation on Age among Solar-Type Stars. *ApJ*, **150**, 551.
- KROUPA, P. (1995) Inverse dynamical population synthesis and star formation. *MNRAS*, **277**, 1491.
- KUPKA, F. G., RYABCHIKOVA, T. A., PISKUNOV, N. E., STEMPELS, H. C. & WEISS, W. W. (2000) VALD-2 – The New Vienna Atomic Line Database. *Baltic Astronomy*, **9**, 590–594.
- LADA, C. J. (2006) Stellar Multiplicity and the Initial Mass Function: Most Stars Are Single. *ApJ*, **640**, L63–L66.
- LARSON, A. M., IRWIN, A. W., YANG, S. L. S., GOODENOUGH, C., WALKER, G. A. H., WALKER, A. R. & BOHLENDER, D. A. (1993) A CA II lambda 8662 index of chromospheric activity - The case of 61 Cygni A. *PASP*, **105**, 332–336.
- LAUNHARDT, R., QUELOZ, D., HENNING, T., QUIRRENBACH, A., DELPLANCKE, F., ANDOLFATO, L., BAUMEISTER, H., BIZENBERGER, P. ET AL. (2008) The ESPRI project: astrometric exoplanet search with PRIMA. In *Society of Photo-Optical Instrumentation Engineers (SPIE) Conference Series*, vol. 7013 of *Society of Photo-Optical Instrumentation Engineers (SPIE) Conference Series*.
- LEBRETON, Y. (2012) Ages of Exoplanet Host-stars from Asteroseismology: HD 17156, a Case Study. In *Progress in Solar/Stellar Physics with Helio- and Asteroseismology*, edited by H. Shibahashi, M. Takata & A. E. Lynas-Gray, vol. 462 of *Astronomical Society of the Pacific Conference Series*.
- LECONTE, J., LAI, D. & CHABRIER, G. (2011) Distorted, nonspherical transiting planets: impact on the transit depth and on the radius determination. *A&A*, **528**, A41.
- LI, S.-L., MILLER, N., LIN, D. N. C. & FORTNEY, J. J. (2010) WASP-12b as a prolate, inflated and disrupting planet from tidal dissipation. *Nature*, **463**, 1054–1056.
- LIU, H., ZHOU, J.-L. & WANG, S. (2011) Modeling Planetary System Formation with N-body Simulations: Role of Gas Disk and Statistics Compared to Observations. *ApJ*, **732**, 66.
- LOCKWOOD, G. W., SKIFF, B. A., HENRY, G. W., HENRY, S., RADICK, R. R., BALIUNAS, S. L., DONAHUE, R. A. & SOON, W. (2007) Patterns of Photometric and Chromospheric Variation among Sun-like Stars: A 20 Year Perspective. *ApJS*, **171**, 260–303.
- LOMB, N. R. (1976) Least-squares frequency analysis of unequally spaced data. *Ap&SS*, **39**, 447–462.

- LORENZETTI, D., ANTONIUCCI, S., GIANNINI, T., LI CAUSI, G., VENTURA, P., ARKHAROV, A. A., KOPATSKAYA, E. N., LARIONOV, V. M. ET AL. (2012) On the Nature of EXor Accretion Events: An Infrequent Manifestation of a Common Phenomenology? *ApJ*, **749**, 188.
- LYNDEN-BELL, D. & PRINGLE, J. E. (1974) The evolution of viscous discs and the origin of the nebular variables. *MNRAS*, **168**, 603–637.
- MAMAJEK, E. E. & HILLENBRAND, L. A. (2008) Improved Age Estimation for Solar-Type Dwarfs Using Activity-Rotation Diagnostics. *ApJ*, **687**, 1264–1293.
- MANCINI, L., SOUTHWORTH, J., CICERI, S., FORTNEY, J. J., MORLEY, C. V., DITTMANN, J. A., TREGLOAN-REED, J., BRUNI, I. ET AL. (2013) A lower radius and mass for the transiting extrasolar planet HAT-P-8 b. *A&A*, **551**, A11.
- MANDEL, K. & AGOL, E. (2002) Analytic Light Curves for Planetary Transit Searches. *ApJ*, **580**, L171–L175.
- MARCY, G., BUTLER, R. P., FISCHER, D., VOGT, S., WRIGHT, J. T., TINNEY, C. G. & JONES, H. R. A. (2005) Observed Properties of Exoplanets: Masses, Orbits, and Metallicities. *Progress of Theoretical Physics Supplement*, **158**, 24–42.
- MAXTED, P. F. L., ANDERSON, D. R., COLLIER CAMERON, A., GILLON, M., HELLIER, C., QUELOZ, D., SMALLEY, B., TRIAUD, A. H. M. J. ET AL. (2010) WASP-32b: A Transiting Hot Jupiter Planet Orbiting a Lithium-Poor, Solar-Type Star. *PASP*, **122**, 1465–1470.
- MAYOR, M., MARMIER, M., LOVIS, C., UDRY, S., SÉGRANSAN, D., PEPE, F., BENZ, W., BERTAUX, J. . ET AL. (2011) The HARPS search for southern extra-solar planets XXXIV. Occurrence, mass distribution and orbital properties of super-Earths and Neptune-mass planets. *ArXiv e-prints*.
- MAYOR, M., PEPE, F., QUELOZ, D., BOUCHY, F., RUPPRECHT, G., LO CURTO, G., AVILA, G., BENZ, W. ET AL. (2003) Setting New Standards with HARPS. *The Messenger*, **114**, 20–24.
- MAYOR, M. & QUELOZ, D. (1995) A Jupiter-mass companion to a solar-type star. *Nature*, **378**, 355–359.
- MCCULLOUGH, P. R., STYS, J. E., VALENTI, J. A., FLEMING, S. W., JANES, K. A. & HEASLEY, J. N. (2005) The XO Project: Searching for Transiting Extrasolar Planet Candidates. *PASP*, **117**, 783–795.
- MEIBOM, S., BARNES, S. A., LATHAM, D. W., BATALHA, N., BORUCKI, W. J., KOCH, D. G., BASRI, G., WALKOWICZ, L. M. ET AL. (2011) The Kepler Cluster Study: Stellar Rotation in NGC 6811. *ApJ*, **733**, L9.
- MESSINA, S., DESIDERA, S., LANZAFAME, A. C., TURATTO, M. & GUINAN, E. F. (2011) RACE-OC project: rotation and variability in the ϵ Chamaeleontis, Octans, and Argus stellar associations. *A&A*, **532**, A10.
- MESSINA, S., DESIDERA, S., TURATTO, M., LANZAFAME, A. C. & GUINAN, E. F. (2010) RACE-OC project: Rotation and variability of young stellar associations within 100 pc. *A&A*, **520**, A15.

- MIDDELKOOP, F. (1982a) Magnetic structure in cool stars. IV - Rotation and CA II H and K emission of main-sequence stars. *A&A*, **107**, 31–35.
- MIDDELKOOP, F. (1982b) Magnetic structure in cool stars. VI - CA II H and K fluxes from evolved stars. *A&A*, **113**, 1–8.
- MOHLER-FISCHER, M., MANCINI, L., HARTMAN, J. D., BAKOS, G. B., PENEV, K., BAYLISS, D., JORDAN, A., CSUBRY, Z. ET AL. (2013) HATS-2b: A transiting extrasolar planet orbiting a K-type star showing starspot activity. *ArXiv e-prints*.
- MONTES, D., LÓPEZ-SANTIAGO, J., GÁLVEZ, M. C., FERNÁNDEZ-FIGUEROA, M. J., DE CASTRO, E. & CORNIDE, M. (2001) Late-type members of young stellar kinematic groups - I. Single stars. *MNRAS*, **328**, 45–63.
- MOORE, C. E., MINNAERT, M. G. J. & HOUTGAST, J. (1966) *The solar spectrum 2935 Å to 8770 Å*.
- MORDASINI, C., ALIBERT, Y., GEORGY, C., DITTKRIST, K.-M., KLAHR, H. & HENNING, T. (2012a) Characterization of exoplanets from their formation. II. The planetary mass-radius relationship. *A&A*, **547**, A112.
- MORDASINI, C., ALIBERT, Y., KLAHR, H. & HENNING, T. (2012b) Characterization of exoplanets from their formation. I. Models of combined planet formation and evolution. *A&A*, **547**, A111.
- MÜLLER, A., ROCCATAGLIATA, V., HENNING, T., FEDELE, D., PASQUALI, A., CAFFAU, E., RODRÍGUEZ-LEDESMA, M. V., MOHLER-FISCHER, M. ET AL. (2013) Reanalysis of the FEROS observations of HIP 11952. *ArXiv e-prints*.
- NAEF, D., MAYOR, M., BEUZIT, J.-L., PERRIER, C., QUELOZ, D., SIVAN, J.-P. & UDRY, S. (2005) The ELODIE planet search: synthetic view of the survey and its global detection threshold. In *13th Cambridge Workshop on Cool Stars, Stellar Systems and the Sun*, edited by F. Favata, G. A. J. Hussain & B. Battrick, vol. 560 of *ESA Special Publication*.
- NEUGEBAUER, G., HABING, H. J., VAN DUINEN, R., AUMANN, H. H., BAUD, B., BEICHMAN, C. A., BEINTEMA, D. A., BOGGESS, N. ET AL. (1984) The Infrared Astronomical Satellite (IRAS) mission. *ApJ*, **278**, L1–L6.
- NOYES, R. W., HARTMANN, L. W., BALIUNAS, S. L., DUNCAN, D. K. & VAUGHAN, A. H. (1984a) Rotation, convection, and magnetic activity in lower main-sequence stars. *ApJ*, **279**, 763–777.
- NOYES, R. W., WEISS, N. O. & VAUGHAN, A. H. (1984b) The relation between stellar rotation rate and activity cycle periods. *ApJ*, **287**, 769–773.
- O'DONOVAN, F. T., CHARBONNEAU, D., MANDUSHEV, G., DUNHAM, E. W., LATHAM, D. W., TORRES, G., SOZZETTI, A., BROWN, T. M. ET AL. (2006) TrES-2: The First Transiting Planet in the Kepler Field. *ApJ*, **651**, L61–L64.
- PÄTZOLD, M., ENDL, M., CSIZMADIA, S., GANDOLFI, D., JORDA, L., GRZIWA, S., CARONE, L., PASTERNAKI, T. ET AL. (2012) Transiting exoplanets from the CoRoT space mission. XXIII. CoRoT-21b: a doomed large Jupiter around a faint subgiant star. *A&A*, **545**, A6.

- PEARSON, K. (1920) Notes on the history of correlation. *Biometrika*, **13**, 25–45.
- PENEV, K., BAKOS, G. Á., BAYLISS, D., JORDÁN, A., MOHLER, M., ZHOU, G., SUC, V., RABUS, M. ET AL. (2013) HATS-1b: The First Transiting Planet Discovered by the HATSouth Survey. *AJ*, **145**, 5.
- PERRYMAN, M. (2011) *The Exoplanet Handbook*.
- PERRYMAN, M. A. C. & ESA (eds.) (1997) *The HIPPARCOS and TYCHO catalogues. Astrometric and photometric star catalogues derived from the ESA HIPPARCOS Space Astrometry Mission*, vol. 1200 of *ESA Special Publication*.
- PONT, F., GILLILAND, R. L., MOUTOU, C., CHARBONNEAU, D., BOUCHY, F., BROWN, T. M., MAYOR, M., QUELOZ, D. ET AL. (2007) Hubble Space Telescope time-series photometry of the planetary transit of HD 189733: no moon, no rings, starspots. *A&A*, **476**, 1347–1355.
- POVICH, M. S., GIAMPAPA, M. S., VALENTI, J. A., TILLEMANN, T., BARDEN, S., DEMING, D., LIVINGSTON, W. C. & PILACHOWSKI, C. (2001) Limits on Line Bisector Variability for Stars with Extrasolar Planets. *AJ*, **121**, 1136–1146.
- PRESS, W. H., TEUKOLSKY, S. A., VETTERLING, W. T. & FLANNERY, B. P. (1992) *Numerical recipes in C. The art of scientific computing*.
- QUELOZ, D., HENRY, G. W., SIVAN, J. P., BALIUNAS, S. L., BEUZIT, J. L., DONAHUE, R. A., MAYOR, M., NAEF, D. ET AL. (2001) No planet for HD 166435. *A&A*, **379**, 279–287.
- QUELOZ, D., MAYOR, M., WEBER, L., BLÉCHA, A., BURNET, M., CONFINO, B., NAEF, D., PEPE, F. ET AL. (2000) The CORALIE survey for southern extra-solar planets. I. A planet orbiting the star Gliese 86. *A&A*, **354**, 99–102.
- RABUS, M., ALONSO, R., BELMONTE, J. A., DEEG, H. J., GILLILAND, R. L., ALMENARA, J. M., BROWN, T. M., CHARBONNEAU, D. ET AL. (2009a) A cool starspot or a second transiting planet in the TrES-1 system? *A&A*, **494**, 391–397.
- RABUS, M., DEEG, H. J., ALONSO, R., BELMONTE, J. A. & ALMENARA, J. M. (2009b) Transit timing analysis of the exoplanets TrES-1 and TrES-2. *A&A*, **508**, 1011–1020.
- REID, I. N., HAWLEY, S. L. & GIZIS, J. E. (1995) The Palomar/MSU Nearby-Star Spectroscopic Survey. I. The Northern M Dwarfs -Bandstrengths and Kinematics. *AJ*, **110**, 1838.
- REID, N. (2003) Activity and kinematics of members of the TW Hydrae association. *MNRAS*, **342**, 837–850.
- REINERS, A., JOSHI, N. & GOLDMAN, B. (2012) A Catalog of Rotation and Activity in Early-M Stars. *AJ*, **143**, 93.
- ROBITAILLE, T. P., WHITNEY, B. A., INDEBETOUW, R. & WOOD, K. (2007) Interpreting Spectral Energy Distributions from Young Stellar Objects. II. Fitting Observed SEDs Using a Large Grid of Precomputed Models. *ApJS*, **169**, 328–352.

- ROUAN, D., PARVIAINEN, H., MOUTOU, C., DELEUIL, M., FRIDLUND, M., OFIR, A., HAVEL, M., AIGRAIN, S. ET AL. (2012) Transiting exoplanets from the CoRoT space mission . XIX. CoRoT-23b: a dense hot Jupiter on an eccentric orbit. *A&A*, **537**, A54.
- RUSSELL, H. N. (1912) On the Determination of the Orbital Elements of Eclipsing Variable Stars. II. *ApJ*, **36**, 54.
- RUTTEN, R. G. M. (1984) Magnetic structure in cool stars. VII - Absolute surface flux in CA II H and K line cores. *A&A*, **130**, 353–360.
- SAHLMANN, J., HENNING, T., QUELOZ, D., QUIRRENBACH, A., ELIAS, N. M., LAUNHARDT, R., PEPE, F., REFFERT, S. ET AL. (2013) The ESPRI project: astrometric exoplanet search with PRIMA. I. Instrument description and performance of first light observations. *A&A*, **551**, A52.
- SANCHIS-OJEDA, R. & WINN, J. N. (2011) Starspots, Spin-Orbit Misalignment, and Active Latitudes in the HAT-P-11 Exoplanetary System. *ApJ*, **743**, 61.
- SANCHIS-OJEDA, R., WINN, J. N., HOLMAN, M. J., CARTER, J. A., OSIP, D. J. & FUENTES, C. I. (2011) Starspots and Spin-orbit Alignment in the WASP-4 Exoplanetary System. *ApJ*, **733**, 127.
- SANTOS, N. C., GOMES DA SILVA, J., LOVIS, C. & MELO, C. (2010) Do stellar magnetic cycles influence the measurement of precise radial velocities? *A&A*, **511**, A54.
- SCARGLE, J. D. (1982) Studies in astronomical time series analysis. II - Statistical aspects of spectral analysis of unevenly spaced data. *ApJ*, **263**, 835–853.
- SETIAWAN, J., HENNING, T., LAUNHARDT, R., MÜLLER, A., WEISE, P. & KÜRSTER, M. (2008) A young massive planet in a star-disk system. *Nature*, **451**, 38–41.
- SETIAWAN, J., PASQUINI, L., DA SILVA, L., VON DER LÜHE, O. & HATZES, A. (2003) Precise radial velocity measurements of G and K giants. First results. *A&A*, **397**, 1151–1159.
- SETIAWAN, J., WEISE, P., HENNING, T., LAUNHARDT, R., MÜLLER, A. & RODMANN, J. (2007) Evidence for a Planetary Companion around a Nearby Young Star. *ApJ*, **660**, L145–L148.
- SICILIA-AGUILAR, A., KÓSPÁL, Á., SETIAWAN, J., ÁBRAHÁM, P., DULLEMOND, C., EIROA, C., GOTO, M., HENNING, T. ET AL. (2012) Optical spectroscopy of EX Lupi during quiescence and outburst. Infall, wind, and dynamics in the accretion flow. *A&A*, **544**, A93.
- SILVA, A. V. R. (2003) Method for Spot Detection on Solar-like Stars. *ApJ*, **585**, L147–L150.
- SILVERSTONE, M. D., MEYER, M. R., MAMAJEK, E. E., HINES, D. C., HILLENBRAND, L. A., NAJITA, J., PASCUCCI, I., BOUWMAN, J. ET AL. (2006) Formation and Evolution of Planetary Systems (FEPS): Primordial Warm Dust Evolution from 3 to 30 Myr around Sun-like Stars. *ApJ*, **639**, 1138–1146.

- SING, D. K., PONT, F., AIGRAIN, S., CHARBONNEAU, D., DÉSSERT, J.-M., GIBSON, N., GILLILAND, R., HAYEK, W. ET AL. (2011) Hubble Space Telescope transmission spectroscopy of the exoplanet HD 189733b: high-altitude atmospheric haze in the optical and near-ultraviolet with STIS. *MNRAS*, **416**, 1443–1455.
- SIPOS, N., ÁBRAHÁM, P., ACOSTA-PULIDO, J., JUHÁSZ, A., KÓSPÁL, Á., KUN, M., MOÓR, A. & SETIAWAN, J. (2009) EX Lupi in quiescence. *A&A*, **507**, 881–889.
- SIVERD, R. J., BEATTY, T. G., PEPPER, J., EASTMAN, J. D., COLLINS, K., BIERYLA, A., LATHAM, D. W., BUCHHAVE, L. A. ET AL. (2012) KELT-1b: A Strongly Irradiated, Highly Inflated, Short Period, 27 Jupiter-mass Companion Transiting a Mid-F Star. *ApJ*, **761**, 123.
- SKUMANICH, A. (1972) Time Scales for CA II Emission Decay, Rotational Braking, and Lithium Depletion. *ApJ*, **171**, 565.
- SMALLEY, B., ANDERSON, D. R., COLLIER-CAMERON, A., DOYLE, A. P., FUMEL, A., GILLON, M., HELLIER, C., JEHIN, E. ET AL. (2012) WASP-78b and WASP-79b: two highly-bloated hot Jupiter-mass exoplanets orbiting F-type stars in Eridanus. *A&A*, **547**, A61.
- SNEDEN, C., BEAN, J., IVANS, I., LUCATELLO, S. & SOBECK, J. (2012) MOOG: LTE line analysis and spectrum synthesis. Astrophysics Source Code Library.
- SODERBLOM, D. R. (1983) Rotational studies of late-type stars. II - Ages of solar-type stars and the rotational history of the sun. *ApJS*, **53**, 1–15.
- SODERBLOM, D. R. (2010) The Ages of Stars. *ARA&A*, **48**, 581–629.
- SODERBLOM, D. R., DUNCAN, D. K. & JOHNSON, D. R. H. (1991) The chromospheric emission-age relation for stars of the lower main sequence and its implications for the star formation rate. *ApJ*, **375**, 722–739.
- SODERBLOM, D. R., KING, J. R., HANSON, R. B., JONES, B. F., FISCHER, D., STAUFFER, J. R. & PINSONNEAULT, M. H. (1998) The Problem of HIPPARCOS Distances to Open Clusters. II. Constraints from Nearby Field Stars. *ApJ*, **504**, 192.
- SOLANKI, S. K. (2003) Sunspots: An overview. *A&A Rev.*, **11**, 153–286.
- SONG, I., ZUCKERMAN, B. & BESSELL, M. S. (2003) New Members of the TW Hydrae Association, β Pictoris Moving Group, and Tucana/Horologium Association. *ApJ*, **599**, 342–350.
- SONG, I., ZUCKERMAN, B. & BESSELL, M. S. (2004) On Ca II Emission as an Indicator of the Age of Young Stars. *ApJ*, **614**, L125–L127.
- SONG, I., ZUCKERMAN, B. & BESSELL, M. S. (2012) New Members of the Scorpius-Centaurus Complex and Ages of Its Sub-regions. *AJ*, **144**, 8.
- SOUTHWORTH, J., DOMINIK, M., JØRGENSEN, U. G., RAHVAR, S., SNODGRASS, C., ALSUBAI, K., BOZZA, V., BROWNE, P. ET AL. (2011) A much lower density for the transiting extrasolar planet WASP-7. *A&A*, **527**, A8.

- SOUTHWORTH, J., HINSE, T. C., JØRGENSEN, U. G., DOMINIK, M., RICCI, D., BURGENDORF, M. J., HORNSTRUP, A., WHEATLEY, P. J. ET AL. (2009) High-precision photometry by telescope defocusing - I. The transiting planetary system WASP-5. *MNRAS*, **396**, 1023–1031.
- SOUTHWORTH, J., MANCINI, L., MAXTED, P. F. L., BRUNI, I., TREGLOAN-REED, J., BARBIERI, M., RUOCCO, N. & WHEATLEY, P. J. (2012) Physical properties and radius variations in the HAT-P-5 planetary system from simultaneous four-colour photometry. *MNRAS*, **422**, 3099–3106.
- STAHL, O., KAUFER, A. & TUBBESING, S. (1999) The FEROS spectrograph. In *Optical and Infrared Spectroscopy of Circumstellar Matter*, edited by E. Guenther, B. Stecklum & S. Klose, vol. 188 of *Astronomical Society of the Pacific Conference Series*.
- STEFFEN, J. H., FABRYCKY, D. C., AGOL, E., FORD, E. B., MOREHEAD, R. C., COCHRAN, W. D., LISSAUER, J. J., ADAMS, E. R. ET AL. (2013) Transit timing observations from Kepler - VII. Confirmation of 27 planets in 13 multiplanet systems via transit timing variations and orbital stability. *MNRAS*, **428**, 1077–1087.
- STRASSMEIER, K. G. (2009) Starspots. *A&A Rev.*, **17**, 251–308.
- STRUVE, O. & RUDKJØBING, M. (1949) Stellar Spectra with Emission Lines in the Obscuring Clouds of Ophiuchus and Scorpius. *ApJ*, **109**, 92.
- SZABÓ, G. M., SZABÓ, R., BENKŐ, J. M., LEHMANN, H., MEZŐ, G., SIMON, A. E., KÓVÁRI, Z., HODOSÁN, G. ET AL. (2011) Asymmetric Transit Curves as Indication of Orbital Obliquity: Clues from the Late-type Dwarf Companion in KOI-13. *ApJ*, **736**, L4.
- THOMANN, C., JAMES, D. J., BOBERG, O. M., CARGILE, P. & AARNIO, A. (2013) Photometric and Spectroscopic Analysis of Young, Nearby Open Cluster Collinder 70. In *American Astronomical Society Meeting Abstracts*, vol. 221 of *American Astronomical Society Meeting Abstracts*.
- TINETTI, G., BEAULIEU, J. P., HENNING, T., MEYER, M., MICELA, G., RIBAS, I., STAM, D., SWAIN, M. ET AL. (2012) EChO. Exoplanet characterisation observatory. *Experimental Astronomy*, **34**, 311–353.
- TOKOVININ, A. (2008) Comparative statistics and origin of triple and quadruple stars. *MNRAS*, **389**, 925–938.
- TONRY, J. & DAVIS, M. (1979) A survey of galaxy redshifts. I - Data reduction techniques. *AJ*, **84**, 1511–1525.
- TORRES, C. A. O., QUAIST, G. R., MELO, C. H. F. & STERZIK, M. F. (2008) *Young Nearby Loose Associations*. p. 757.
- TREGLOAN-REED, J., SOUTHWORTH, J. & TAPPERT, C. (2013) Transits and starspots in the WASP-19 planetary system. *MNRAS*, **428**, 3671–3679.
- TUSNSKI, L. R. M. & VALIO, A. (2011) Transit Model of Planets with Moon and Ring Systems. *ApJ*, **743**, 97.
- VALENTI, J. A. & PISKUNOV, N. (1996) Spectroscopy made easy: A new tool for fitting observations with synthetic spectra. *A&AS*, **118**, 595–603.

- VAN LEEUWEN, F. (2008) Hipparcos, the New Reduction (van Leeuwen, 2007). *VizieR Online Data Catalog*, **1311**, 0.
- VAUGHAN, A. H., PRESTON, G. W. & WILSON, O. C. (1978) Flux measurements of CA II H and K emission. *PASP*, **90**, 267–274.
- VERNAZZA, J. E., AVRETT, E. H. & LOESER, R. (1973) Structure of the Solar Chromosphere. Basic Computations and Summary of the Results. *ApJ*, **184**, 605–632.
- VERNAZZA, J. E., AVRETT, E. H. & LOESER, R. (1981) Structure of the solar chromosphere. III - Models of the EUV brightness components of the quiet-sun. *ApJS*, **45**, 635–725.
- VIANA ALMEIDA, P., SANTOS, N. C., MELO, C., AMMLER-VON EIFF, M., TORRES, C. A. O., QUAIST, G. R., GAMEIRO, J. F. & STERZIK, M. (2009) Search for associations containing young stars (SACY). II. Chemical abundances of stars in 11 young associations in the solar neighborhood. *A&A*, **501**, 965–971.
- VOGT, S. S., HATZES, A. P., MISCH, A. A. & KÜRSTER, M. (1999) Doppler Imagery of the Spotted RS Canum Venaticorum Star HR 1099 (V711 Tauri) from 1981 to 1992. *ApJS*, **121**, 547–589.
- WALLERSTEIN, G. & CONTI, P. S. (1969) Lithium and Beryllium in Stars. *ARA&A*, **7**, 99.
- WANG, H., APAI, D., HENNING, T. & PASCUCCI, I. (2004) FU Orionis: A Binary Star? *ApJ*, **601**, L83–L86.
- WANG, SHARON, X., WRIGHT, J. T., COCHRAN, W., KANE, S. R., HENRY, G. W., PAYNE, M. J., ENDL, M., MACQUEEN, P. J. ET AL. (2012) The Discovery of HD 37605c and a Dispositive Null Detection of Transits of HD 37605b. *ApJ*, **761**, 46.
- WEAVER, W. B. (1987) Anomalous distribution of axial inclinations of T Tauri stars. *ApJ*, **319**, L89–L92.
- WEISE, P. (2010) PhD thesis - *Search for planets around young stars with the radial velocity technique*, University of Heidelberg.
- WICHMANN, R., SCHMITT, J. H. M. M. & HUBRIG, S. (2003) Nearby young stars. *A&A*, **399**, 983–994.
- WILLIAMS, J. P. & CIEZA, L. A. (2011) Protoplanetary Disks and Their Evolution. *ARA&A*, **49**, 67–117.
- WILSON, O. C. (1963) A Probable Correlation Between Chromospheric Activity and Age in Main-Sequence Stars. *ApJ*, **138**, 832.
- WINDMARK, F., BIRNSTIEL, T., ORMEL, C. W. & DULLEMOND, C. P. (2012) Breaking through: The effects of a velocity distribution on barriers to dust growth. *A&A*, **544**, L16.
- WRIGHT, J. T. & HOWARD, A. W. (2009) Efficient Fitting of Multiplanet Keplerian Models to Radial Velocity and Astrometry Data. *ApJS*, **182**, 205–215.

- WRIGHT, N. J., DRAKE, J. J., MAMAJEK, E. E. & HENRY, G. W. (2011) The Stellar-activity-Rotation Relationship and the Evolution of Stellar Dynamos. *ApJ*, **743**, 48.
- YI, S., DEMARQUE, P., KIM, Y.-C., LEE, Y.-W., REE, C. H., LEJEUNE, T. & BARNES, S. (2001) Toward Better Age Estimates for Stellar Populations: The Y^2 Isochrones for Solar Mixture. *ApJS*, **136**, 417–437.
- ZACHARIAS, N., FINCH, C. T., GIRARD, T. M., HENDEN, A., BARTLETT, J. L., MONET, D. G. & ZACHARIAS, M. I. (2012) UCAC4 Catalogue (Zacharias+, 2012). *VizieR Online Data Catalog*, **1322**, 0.
- ZECHMEISTER, M. & KÜRSTER, M. (2009) The generalised Lomb-Scargle periodogram. A new formalism for the floating-mean and Keplerian periodograms. *A&A*, **496**, 577–584.
- ZECHMEISTER, M., KÜRSTER, M. & ENDL, M. (2009) The M dwarf planet search programme at the ESO VLT + UVES. A search for terrestrial planets in the habitable zone of M dwarfs. *A&A*, **505**, 859–871.
- ZEEMAN, P. (1897) On the Influence of Magnetism on the Nature of the Light Emitted by a Substance. *ApJ*, **5**, 332.
- ZHAO, J. K., OSWALT, T. D., ZHAO, G., LU, Q. H., LUO, A. L. & ZHANG, L. Y. (2013) Tracers of Chromospheric Structure. I. Ca II H&K Emission Distribution of 13,000 F, G, and K Stars in SDSS DR7 Spectroscopic Sample. *AJ*, **145**, 140.
- ZUCKERMAN, B. & SONG, I. (2004) Young Stars Near the Sun. *ARA&A*, **42**, 685–721.
- ZUCKERMAN, B., SONG, I. & BESSELL, M. S. (2004) The AB Doradus Moving Group. *ApJ*, **613**, L65–L68.
- ZUCKERMAN, B., SONG, I., BESSELL, M. S. & WEBB, R. A. (2001) The β Pictoris Moving Group. *ApJ*, **562**, L87–L90.

Acknowledgements

First of all, I would like to thank Thomas Henning, who gave me the chance to work on my PhD thesis at the MPIA. He always showed much interest in my research progress, assisted me in many ways and always had a sympathetic ear for my problems and concerns.

Furthermore, I want to thank Ralf Launhardt. I'm sure I wouldn't have managed my PhD easily in the predefined time without his uncountable very good counsels and his tireless efforts to look over proposals, papers and finally the thesis. We really had a lot of fun and I thank him for everything!

Moreover, many thanks to Andreas Quirrenbach for being my second advisor and the co-corrector of this thesis.

Another big 'Thank you!' goes to my awesome office mates: Tobias, Yu-Yen, Alex, Jiang, Mathias, Karsten, Bernhard and Thomas. The days at the institute wouldn't have been as much fun without you, folks!

The same goes to the old and new hands of the students coffee. Many names are already covered by the list of my office mates, but I don't want to forget Natalie, Tessel, Eduardo, Kai, Felix, Ilya, Taisiya, Michael and all the others! Don't forget to bring coffee ;-)

Also, I don't want to forget Christian Fendt and my whole IMPRS generation. This community made the social acclimatisation so much easier in the new town Heidelberg.

Many thanks to André Müller, Martin Kürster and Tom Robitaille, who really helped me a lot with all kind of questions.

The work with HATSouth (almost) always went swimmingly with such awesome colleagues! Thanks Luigi, Simona and Thomas for this very good teamwork. Special thanks go to Simona, who took over a lot of work from me while I was writing up this thesis and covered my back that way.

Thanks a lot Ian for taking over the thankless task to read over the grammar and spelling of my work.

Furthermore, many thanks to Eike Günther and Artie Hatzes for many good advices.

I guess my work wouldn't have been so smooth without the wonderful help of the people at the back of the stage: the people from the reception desk, Technischer Dienst, IT and library.

Of course I can't forget my dear friends, who sweetened regularly my small free time: Tobias, Karsten, Fredrik, Maria, László, Dario and Vesselina and their hero-aliases. We really put them in their places!

Of course I don't want to forget my dear husband and my family, who always supported me in my decisions. I wouldn't be there where I am now without you!

Last but not least I want to thank everyone who I forgot above and I bet these are a lot! Sorry and thank you all!